A COMPREHENSIVE INVESTIGATION ON THE ROLES OF AMINO ACID PROMOTERS ON GAS HYDRATE FORMATION

Kan Jeenmuang

A Dissertation Submitted in Partial Fulfillment of the Requirements
for the Degree of Doctor of Philosophy
The Petroleum and Petrochemical College, Chulalongkorn University
in Academic Partnership with
The University of Michigan, The University of Oklahoma,
and Case Western Reserve University
2026

A Comprehensive Investigation on the Roles of Amino Acid Promoters on Gas Hydrate Formation

Mr. Kan Jeenmuang

A Dissertation Submitted in Partial Fulfillment of the Requirements
for the Degree of Doctor of Philosophy in Petrochemical Technology
The Petroleum and Petrochemical College
Chulalongkorn University
Academic Year 2025

การศึกษาผลกระทบและความสัมพันธ์ของกรดอะมิโนต่อการก่อตัวของแก๊สไฮเดรต

นายกานต์ จีนเมือง

วิทยานิพนธ์นี้เป็นส่วนหนึ่งของการศึกษาตามหลักสูตรปริญญาวิทยาศาสตรดุษฎีบัณฑิต
สาขาวิชาเทคโนโลยีปิโตรเคมี
วิทยาลัยปิโตรเลียมและปิโตรเคมี จุฬาลงกรณ์มหาวิทยาลัย
ปีการศึกษา 2568

Thesis Title	A Comprehensive Investigation on the Roles of Amino Acid Promoters on Gas Hydrate Formation
By	Mr. Kan Jeenmuang
Field of Study	Petrochemical Technology
Thesis Advisor	Professor Pramoch Rangsunvigit, Ph.D.
Thesis Co Advisor	Professor Praveen Linga, Ph.D.
	Santi Kulprathipanja, Ph.D.

Accepted by The Petroleum and Petrochemical College, Chulalongkorn University in Partial Fulfillment of the Requirement for the Doctor of Philosophy

.... Dean of The Petroleum and Petrochemical College

(Professor Pramoch Rangsunvigit, Ph.D.)

DISSERTATION COMMITTEE

.... Chairman
(Professor Adrian Evan Flood, Ph.D.)

.... Thesis Advisor
(Professor Pramoch Rangsunvigit, Ph.D.)

.... Thesis Co-Advisor
(Professor Praveen Linga, Ph.D.)

.... Thesis Co-Advisor
(Santi Kulprathipanja, Ph.D.)

.... Examiner
(Professor Boonyarach Kitiyanan, Ph.D.)

.... Examiner
(Assistant Professor Uthaiporn Suriyapraphadilok, Ph.D.)

.... Examiner
(Tanate Danuthai, Ph.D.)

กานต์ จีนเมือง : การศึกษาผลกระทบและความสัมพันธ์ของกรดอะมิโนต่อการก่อตัวของแก๊สไฮเดรต. (A Comprehensive Investigation on the Roles of Amino Acid Promoters on Gas Hydrate Formation)
อ.ที่ปรึกษาหลัก : ศ. ดร.ปราโมช รังสรรค์วิจิตร
อ.ที่ปรึกษาร่วม: ศ. ดร.ปราวีน ลินกา, ดร.สันติ กุลประทีปัญญา

ในช่วงเวลาที่ผ่านมา กรดอะมิโนมีบทบาทสำคัญในการเพิ่มประสิทธิภาพการก่อตัวของแก๊สไฮเดรต อย่างไรก็ความเข้าใจถึงคุณสมบัติของกรดอะมิโนทั้ง 20 ชนิดยังมีความไม่ชัดเจน อาทิ ผลของกรดอะมิโนแต่ละชนิด งานวิจัยนี้จึงมุ่งเน้นศึกษาผลกระทบของความเป็นไฮโดโฟบิกของกรดอะมิโนชนิดต่างๆ ต่อการก่อตัวของมีเทนและคาร์บอนไดออกไซด์ไฮเดรต ซึ่งผลการศึกษาแสดงให้เห็นถึงการเร่งการก่อตัวที่สังเกตเห็นได้ในการก่อตัวของแก๊สไฮเดรตเมื่อเพิ่มความไฮโดโฟบิกของกรดอะมิโน นอกจากนี้ เมื่อวิเคราห์ผลจากการศึกษาด้านจลหพลศาสตร์ ลักษณะรูปร่างการก่อตัว และรามานสเปกโทรสโกปี แสดงให้เห็นถึงกลไกที่ทำให้กรดอะมิโนมีความสามารถในการเพิ่มทั้งปริมาณ และความเร็วในกระบวนการก่อตัวแก๊สไฮเดรต โดยการเพิ่มความเข้มข้นกรดอะมิโน เพิ่มประสิทธิภาพในการก่อตัวของคาร์บอนไดออกไซด์ไฮเดรตในน้ำเกลือโซเดียมคลอไลน์ ซึ่งส่งผลให้มีความเป็นไปได้ที่สูงขึ้นที่ในการกักเก็บแก๊สคาร์บอนไดออกไซต์ในรูปแบบแก๊สไฮเดตในพื้นที่ทะเลลึก การศึกษาได้พัฒนาแบบจำลองทางคณิตศาสตร์เพื่อทำนายผลการก่อตัวของแก๊สไฮเดรต และการศึกษาความคงทนของมีเทนไฮเดรต โดยผลการศึกษาแสดงว่าเทคโนโลยีนี้มีความสามารถในการกักเก็บไฮเดรตได้ที่อุณหภูมิสูง และยังสามารถเก็บรักษาไว้เป็นเวลานานได้เช่นกัน นอกจากนี้ สารละลายที่ใชในการก่อตัวแก๊สไฮเดรตสามารถใหม่ได้อีกครั้ง

สาขาวิชา เทคโนโลยีปิโตรเคมี
ปี การศึกษา2567

ลายมือชื่อนิสิต ....
ลายมือชื่อ อ.ที่ปรึกษาหลัก ....
ลายมือชื่อ อ.ที่ปรึกษาร่วม ....
ลายมือชื่อ อ.ที่ปรึกษาร่วม ....

6391001163 : MAJOR PETROCHEMICAL TECHNOLOGY
KEYWORD: Methane hydrate, Carbon dioxide hydrate, Hydrate formation, Hydrate stability, Amino acid, Solution reusability, Brine water, Raman spectroscopy, Response surface methodology, Crystallizer optimization

Kan Jeenmuang : A Comprehensive Investigation on the Roles of Amino Acid Promoters on Gas Hydrate Formation.
Advisor: Prof. Pramoch Rangsunvigit, Ph.D.
Co-advisor: Prof. Praveen Linga, Ph.D., Santi Kulprathipanja, Ph.D.

Hydrate-based technology has garnered significant attention within the scientific community due to its versatile applications, including energy storage (such as natural gas) and carbon dioxide capture. However, a comprehensive understanding of this technology is yet to be achieved, and it has not met the essential criteria for scalability. This underscores the pressing need for in-depth study, enhancement, and optimization, opening avenues to advance its efficacy and broaden its applicability. While amino acids have been extensively studied in the context of hydrate formation, a fundamental inquiry persists regarding the efficient mechanism governing their hydrophobicity, which spans the diverse spectrum of 20 amino acid types. This study primarily explores the impact of amino acid hydrophobicity on methane and carbon dioxide hydrate formation and dissociation. The results demonstrate a notable enhancement in hydrate formation with increased amino acid hydrophobicity. Moreover, by integrating kinetics, morphology, and in situ Raman investigation, the concealed molecular mechanism behind hydrophobic amino acids' ability to enhance both capacity and kinetics of hydrate formation was clarified. Despite the challenging conditions posed by NaCl, the addition of amino acids showcased effectiveness in CO_2 hydrate formation, particularly within brine, significantly improving the feasibility of CO_2 sequestration in deep-sea floors. Additionally, pivotal insights for scalability have been pursued, involving the optimization of crystallizer design and the prediction of hydrate formation models. Through methane hydrate stability investigation, stability at 283.2 K has been confirmed, while solution reusability tests have identified several amino acids suitable for reuse. These multifaceted efforts collectively aim to propel advancements in energy storage and carbon capture technologies, bridging critical knowledge gaps and laying a foundation for future research in hydrate-based technology.

Field of Study: Petrochemical Technology	Student's Signature ....
AcademicYear: 2024	Advisor's Signature ....
	Co-advisor's Signature ....
	Co-advisor's Signature ....

ACKNOWLEDGEMENTS

I would like to take this opportunity to sincerely thank my advisor, Prof. Pramoch Rangsunvigit, for his invaluable guidance, discussions, and supervision since the early stages of my research. His unwavering support and encouragement have been instrumental throughout my graduate thesis journey.

Special thanks are also due to my co-advisor, Prof. Praveen Linga, for his advice, guidance, and the opportunity to conduct my research in the Linga Lab at the National University of Singapore. I am also grateful to Dr. Santi Kulprathipanja for his insightful advice and willingness to share his expertise, which greatly contributed to shaping my ideas and research direction.

I extend my gratitude to Prof. Adrian Flood for graciously serving as the chairman of my final examination, and to Prof. Boonyarach Kitiyanan, Asst. Prof. Uthaiporn Suriyapraphadilok, and Dr. Tanate Danuthai for their valuable contributions as members of my thesis committee. Their suggestions and feedback have been invaluable in completing this thesis.

I am grateful for the Ph.D. scholarship and the opportunity to conduct research abroad provided by the Second Century Fund (C2F), Chulalongkorn University.

I am also thankful for the full scholarship and support provided by The Petroleum and Petrochemical College, Chulalongkorn University, for my thesis work.

I would like to acknowledge the assistance and guidance provided by Dr. Phuwadej Pornaroontham, Dr. Gaurav Bhattacharjee, and Dr. M. Fahed Qureshi, whose advice was immensely beneficial to my research.

I would like to thank the entire faculty and staff at The Petroleum and Petrochemical College for their kind assistance and cooperation.

Finally, I express my heartfelt gratitude to my entire family for instilling in me a love for intellectual pursuit since childhood, for their unwavering support, and for their deep understanding of every aspect of my academic journey.

Kan Jeenmuang

TABLE OF CONTENTS

LIST OF TABLES

Page

LIST OF FIGURES

Page

CHAPTER 1
INTRODUCTION

Gas hydrates, also known as clathrates, are ice-like solid compounds formed when water molecules create a cage-like lattice structure to trap gas molecules, typically methane, ethane, propane, etc., under conditions of low temperature and high pressure. The physical interaction, governed by Van der Waals forces, between small gas molecules and the surrounding water molecules creates cage-like structures where the gas molecules are captured and retained (Sloan Jr and Koh, 2007). Owing to these specific conditions, this distinct chemical phenomenon is frequently observed in cold environments, such as deep-sea sediments and polar regions, where temperatures are suitably low, and pressure intensifies with depth. CH_4 molecules, originating from either microbial or geological processes, permeate the water within sediment layers and become entrapped within the lattice structure, resulting in the formation of Natural Gas Hydrate (NGH). These formations pique significant interest due to their potential as a forthcoming energy source and their connection to climate change, as they possess the capability to release CH_4, a potent greenhouse gas, when destabilized (Makogon, 2007).

The interplay between guest gas molecules and the underlying water lattice structure dictates the formation and stability of gas hydrate cages, with changes in guest molecules leading to alterations in cage structures (Sloan Jr and Koh, 2007). The size and chemical characteristics of these molecules are instrumental in determining the specific type of hydrate structure that forms. Notably, three common hydrate structures exist: structure I (sI, primitive cubic), structure II (sII, face-centered cubic), and structure H (sH, hexagonal) (Englezos and Lee, 2005; Jager *et al.*, 1999; Khokhar *et al.*, 1998).

Gas hydrates, with their remarkable gas capture capacity, open up new possibilities for innovative applications based on hydrate technology. One such application is the solidified natural gas (SNG) technology, which offers long-term energy storage and transportation benefits. Indeed, SNG technology distinguishes itself by employing lower pressure and higher temperature conditions in contrast to conventional methods like compressed natural gas (CNG) and liquefied natural gas (LNG), which necessitate high pressure and lower temperature, respectively. This approach provides higher volumetric energy storage in a more compact form, operates at moderate temperature and pressure conditions, ensures nearly full retrieval of stored natural gas while demanding minimal energy input, and is considered one of the safest modes for natural gas storage, as highlighted by Veluswamy *et al.* (2018).Gas hydrates also have applications in carbon capture and storage, as they can sequester CO_2 by trapping it within their lattice structure, contributing to efforts in mitigating greenhouse gas emissions (Qureshi *et al.*, 2022b; Zheng *et al.*, 2020). Furthermore, hydrates can be used in gas separation processes, such as natural gas purification (Partoon *et al.*, 2018; Zheng *et al.*, 2019) and desalination (Seo *et al.*, 2019; Truong-Lam *et al.*, 2022), owing to their ability to selectively capture specific gas molecules within their cages.

Hydrate formation closely resembles crystallization, encompassing two pivotal stages: nucleation and growth (Khurana *et al.*, 2017). Nevertheless, hydrate nucleation necessitates specific conditions, and the process exhibits notably sluggish kinetics, often demanding low temperatures for both formation and storage, leading to elevated refrigeration expenses (Gudmundsson *et al.*, 1994; Lang *et al.*, 2010). So, enhancing hydrate formation is essential to bolster the feasibility and economic competitiveness of hydrate-based technology compared to conventional alternatives (Veluswamy *et al.*, 2018). This imperative arises from the need to harness the abundant energy and storage potential of gas hydrates in a more efficient and cost-effective manner. By improving the formation process, such as optimizing temperature and pressure conditions (Majid and Koh, 2021), and developing innovative techniques for controlled hydrate growth (Linga and Clarke, 2016), the full potential of gas hydrates for energy storage, carbon capture, and various industrial applications can then be realized.

Improving hydrate formation involves both thermodynamic and kinetic considerations. On the thermodynamic front, research aims to identify optimal pressure-temperature conditions and the use of thermodynamic inhibitors to promote hydrate formation at higher temperatures, reducing the need for energy-intensive refrigeration. Among the range of thermodynamic promoters (THPs), tetrahydrofuran

(THF) has showcased its remarkable efficacy in altering phase equilibria. It stands out for its ability to create the most substantial driving force for CH_4 and CO_2 hydrate formation and, notably, enables hydrate formation at moderate temperatures and pressures. (Beheshtimaal and Haghtalab, 2018; Lee *et al.*, 2012). Simultaneously, efforts in kinetic enhancement strategies focus on the advancement of nucleation and growth techniques aimed at increasing the mass transfer between the gas and liquid phases during the hydrate formation process (Du *et al.*, 2014; Zhang *et al.*, 2007). These techniques include the use of stirred reactors, spray reactors, and gas bubble reactors (Linga and Clarke, 2016). Additional approaches include the introduction of hydrate-forming surfactants, amino acids and various chemical promoters known as hydrate formation kinetic promoters (KHPs), all with the goal of accelerating the hydrate formation process (Majid and Koh, 2021). These strategies collectively aim to overcome the inherent challenge of slow kinetics, ultimately bolstering the viability and efficiency of hydrate-based applications.

Initially, surfactants served as effective KHPs; however, owing to environmental concerns and the issue of foam formation upon hydrate dissociation, amino acids have emerged as an alternative solution (Veluswamy *et al.*, 2016a). Amino acid, a protein-based compound, which have both hydrophobic and hydrophilic part as similar as surfactant. However, the presence of approximately 20 different amino acids has initially complicated the study, as their dual potential roles as both promoters and inhibitors in the hydrate formation process raised questions and challenges during the research. Numerous amino acids have been examined, yet no consistent trend has emerged across all 20 amino acids studied. Furthermore, the synergistic effects of combining THPs like THF with amino acids as KHPs have not been thoroughly explored. Therefore, gaining a better understanding of the capabilities of various amino acids and their synergistic interactions with other THPs holds the potential to significantly enhance the feasibility of hydrate-based technology across a range of applications, encompassing energy storage with CH_4 hydrates and the capture and sequestration of CO_2 through CO_2 hydrates deep within the Earth's subsurface.

This study aimed to comprehensively investigate the impact of various amino acids and their hydrophobic characteristics on both CH_4 and CO_2 hydrate formation systems, with the objective of enhancing the feasibility of technology related to energy storage and CO_2 capture and sequestration using the CH_4 and CO_2 hydrate formation. To achieve this, a range of amino acids with varying hydrophobicity were examined in both CH_4 and CO_2 hydrate formation processes. Various investigative methods were employed to gain a comprehensive understanding of the role of amino acids, encompassing assessments of hydrate formation and dissociation kinetics, morphological analyses, metastable zone analyses and the evaluation of the reusability of the recovered solution. To enhance the feasibility of hydrate-based technology, a synergistic approach was employed, combining amino acids as kinetic hydrate promoters (KHPs) with tetrahydrofuran (THF) as thermodynamic hydrate promoters (THPs) at near-room temperature, aimed at reducing energy consumption during the hydrate formation process. Simultaneously, the study delved into the optimization of the hydrate formation crystallizer, utilizing a Design of Experiment methodology with The Face-Centered Central Composite Design response surface method (FCCCD-RSM). This systematic approach facilitated the refinement of hydrate formation conditions, striking a harmonious balance between efficient crystallizer utilization and operational effectiveness. Moreover, to increase the competitiveness of hydrate-based technology, this study delved into the palletization of hydrates and assessed their stability for long-term storage applications. Finally, to assess CO_2 hydrate-based technology for CO_2 sequestration under conditions closely resembling real-world formation locations, 3.5 wt% NaCl was introduced into the hydrate formation process. The study also employed various specialized characterization instruments, such as in situ Raman spectroscopy, which introduced an innovative approach for monitoring CO_2 hydrate formation, and High-Performance Liquid Chromatography (HPLC), offering detailed composition analyses of reused hydrate solutions.

CHAPTER 2
LITERATURE REVIEW

2.1 Natural Gas

Natural gas is a hydrocarbon-based fossil fuel primarily composed of methane (CH_4) and is one of the cleanest-burning fuels used for various applications. It forms beneath the Earth's surface over millions of years through the decomposition of organic matter, such as ancient plants and microorganisms, under high pressure and temperature conditions. These organic materials get buried deep within the Earth, and the intense heat and pressure cause the carbon and hydrogen atoms within them to reconfigure, resulting in the formation of natural gas. Once formed, natural gas can migrate through porous rock layers and accumulate in underground reservoirs. It is typically extracted by drilling wells into these reservoirs, and after extraction, it is processed to remove impurities and transported through pipelines for various uses, including electricity generation, heating, and as a fuel source for vehicles as show on Figure 2.1 (U.S. Energy Information Administration, 2022).

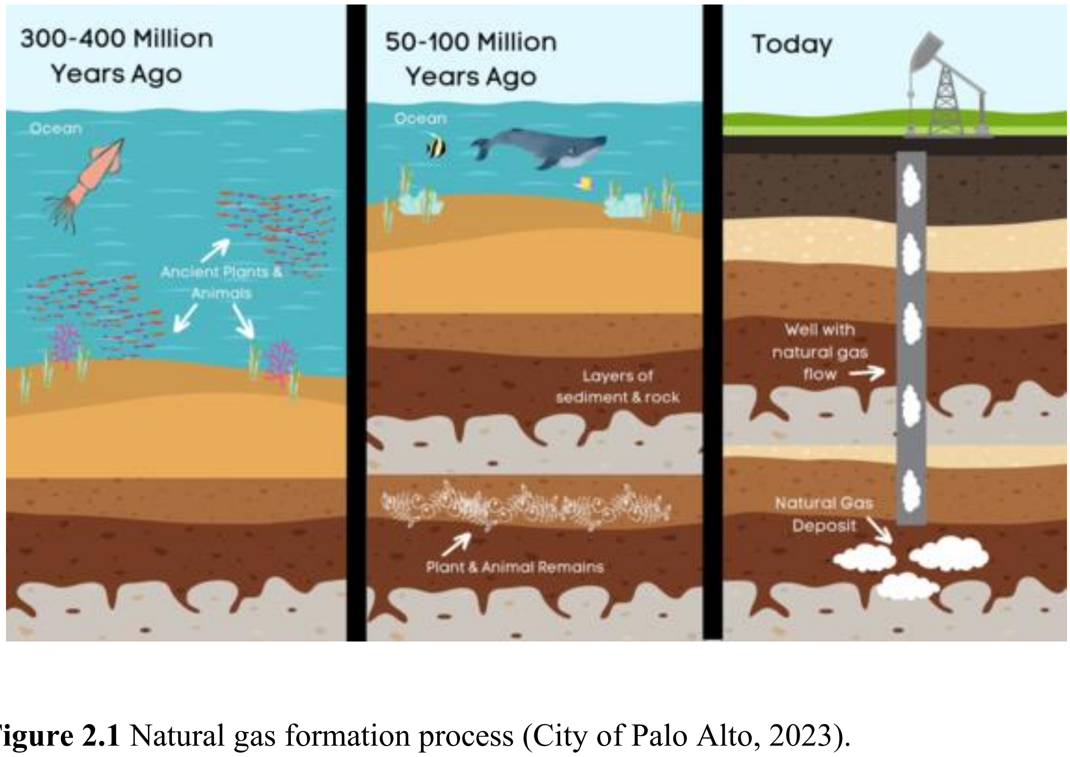

Figure 2.1 Natural gas formation process (City of Palo Alto, 2023).

Natural gas is often regarded as one of the cleanest fossil fuels when compared to other hydrocarbon energy sources. The combustion of natural gas, known for its relatively lower carbon content, primarily results in the generation of carbon dioxide (CO_2) and water vapor. This process produces significantly fewer harmful emissions, such as nitrogen oxides (NO_x) and sulfur dioxide (SO_2), in contrast to coal or oil, as illustrated in Figure 2.2 (Abdul *et al.*, 2019). Additionally, advancements in natural gas extraction and transportation technologies, like pipelines and liquefied natural gas (LNG), have made it an efficient and more environmentally friendly energy option. While it is not entirely free from environmental concerns, natural gas is often considered a transitional energy source toward cleaner and more sustainable energy alternatives. This perspective has contributed to the increased demand for natural gas. The International Energy Agency forecasts that global natural gas consumption will grow at an average annual rate of 0.8% from 2022 to 2025, reaching approximately 4,240 bcm by the end of 2025, Figure 2.3 (International Energy Agency, 2022).

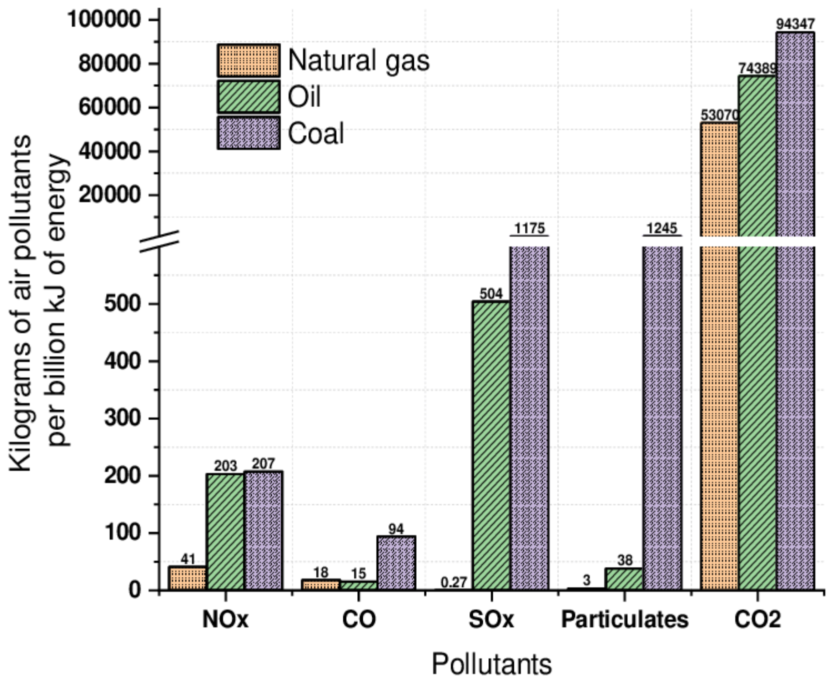

Figure 2.2 Analysis of emissions from natural gas compared to other available fossil fuels (Abdul *et al.*, 2019).

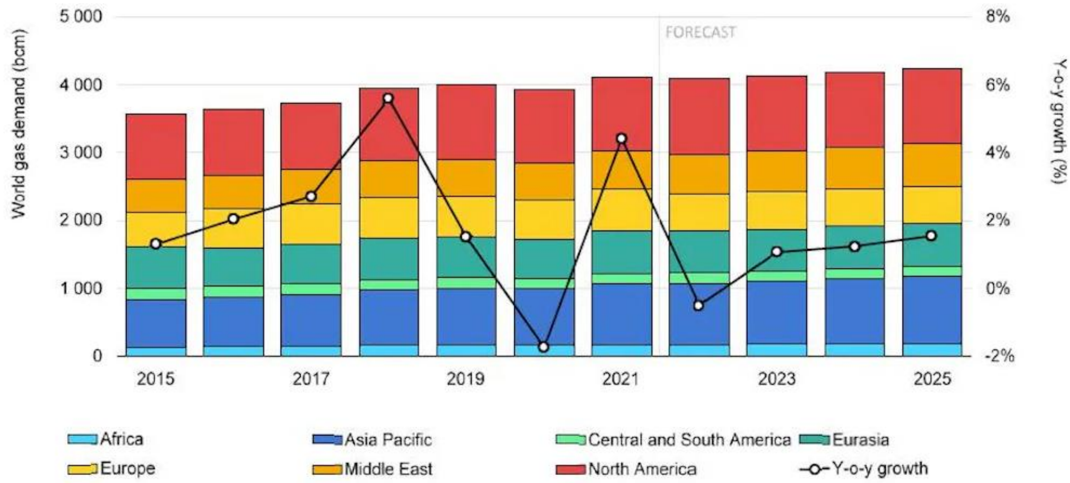

Figure 2.3 Global natural gas demand growth (International Energy Agency, 2022).

2.2 Natural Gas Storage and Transportation

The demand for energy is continually rising, and there are remote natural gas sources that need to be transported and stored to meet this demand report highlighted a substantial requirement for natural gas imports and exports, as depicted in Figure 2.4. Meeting this demand necessitates advanced transport technologies Figure 2.5 and a robust transportation chain, Figure 2.6.

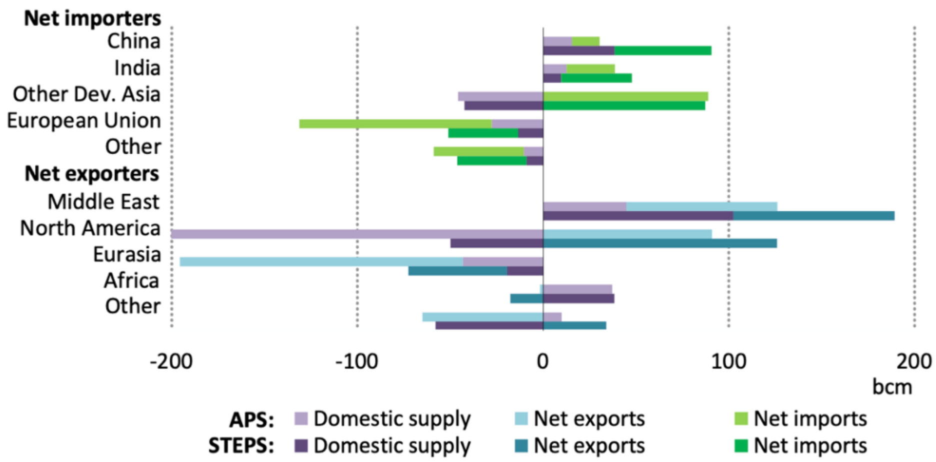

Figure 2.4 Change in natural gas supply balance by region in the Stated Policies and Announced Pledges scenarios, 2022-2030 (International Energy Agency, 2023).

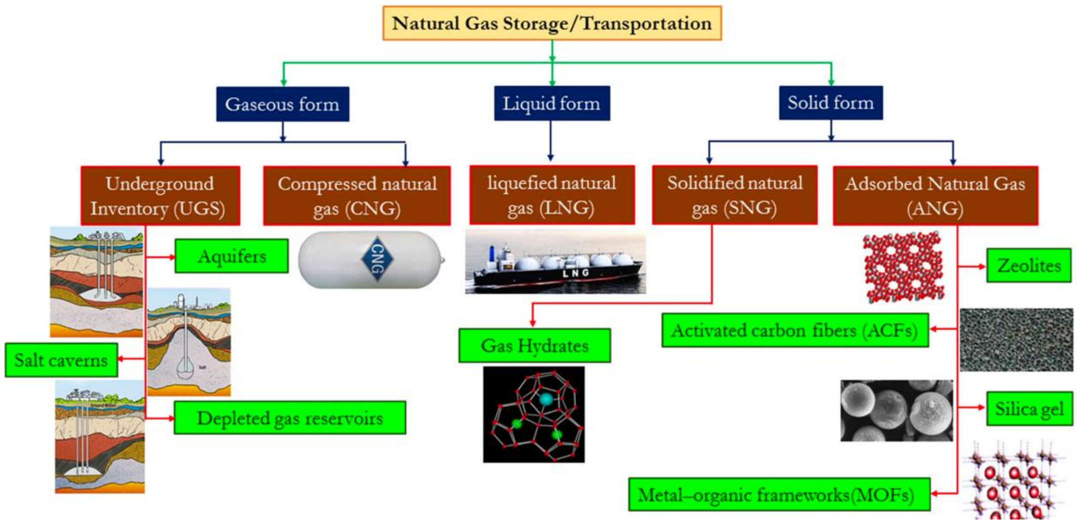

Figure 2.5 Pathways for natural gas storage and transportation (Veluswamy *et al.*, 2018).

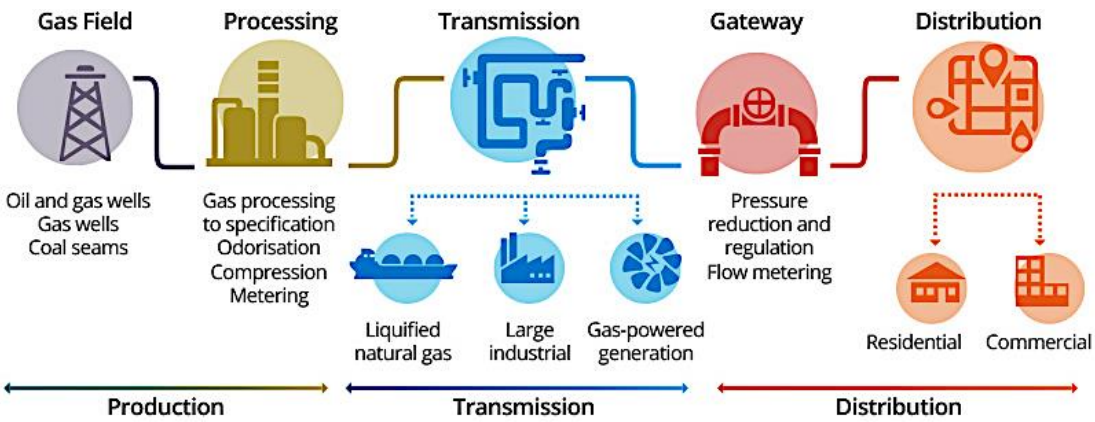

Figure 2.6 Natural gas transport chain (DTE Energy, 2019).

2.2.1 Compressed Natural Gas (CNG)

Compressed natural gas, or CNG, is a storage method for natural gas, primarily composed of methane, where the gas is stored in high-pressure tanks made of materials like aluminum, steel, or composites, while it remains in its gaseous state. These tanks maintain pressures around 20-25 MPa (200-250 bar or 3000-3600 psi). CNG is gaining prominence as a transportation fuel, especially for vehicles, due to its lower carbon emissions and cost-effectiveness. However, CNG does have some limitations, including its lower volumetric energy storage capacity compared to liquid fuels like gasoline. This means that larger storage tanks or more frequent refueling may be required for vehicles, which can be a practical consideration for long-haul transportation (Wang *et al.*, 2010).

2.2.2 Liquefied Natural Gas (LNG)

Liquefied natural gas (LNG) is a colorless and odorless liquid primarily consisting of methane (usually 85-95%) along with trace amounts of ethane, propane, butane, and nitrogen. The LNG production process involves cooling natural gas to a frigid temperature of -162°C under atmospheric pressure. This cryogenic cooling transition from gas to liquid results in a remarkable reduction in volume, making LNG much easier to store and transport. The process of liquefaction results in a considerable reduction in the volume occupied by natural gas, making it up to 600 times smaller. This significant reduction in volume is pivotal for efficient transportation and storage, as it enables large quantities of natural gas to be transported across great distances, even to regions lacking local natural gas reserves. However, LNG faces significant challenges, including the energy-intensive and costly process of cooling natural gas to cryogenic temperatures for liquefaction. Additionally, LNG storage and transportation can be affected by boil-off gas, which results in the evaporation of LNG over time and can lead to variations in the stored quantity of LNG (Veluswamy *et al.*, 2018).

2.2.3 Adsorbed Natural Gas (ANG)

Adsorbed Natural Gas (ANG) is an innovative approach to natural gas storage that involves the adsorption of gas molecules onto a solid adsorbent material, typically at high pressures. Unlike conventional CNG and LNG storage, ANG operates at lower pressures, usually in the range of 3.5 to 35 MPa, making it a safer and more practical option for onboard storage in vehicles. The adsorbent materials used, such as activated carbon, metal-organic frameworks (MOFs), or porous materials, have a high surface area and adsorption capacity. ANG offers advantages in terms of reduced storage pressure and temperature requirements, making it more suitable for various applications. Indeed, Adsorbed Natural Gas (ANG) technology has certain drawbacks, with one of the notable limitations being the requirement to transport adsorbent materials along with the stored natural gas. This inevitably results in additional weight, which can be considered an unwelcome burden, especially in transportation applications. ANG is still an evolving technology, and researchers are working on addressing these challenges by developing more efficient adsorbent materials and optimizing storage systems to minimize the negative effects of added weight and payload reduction (Energy Educatio University of Calgary, 2018).

2.3 Carbon Dioxide

Carbon dioxide (CO_2) is a colorless, odorless gas that consists of one carbon atom and two oxygen atoms. It is a naturally occurring chemical compound and a key component of Earth's atmosphere. Carbon dioxide is produced through various natural processes, such as respiration of living organisms, volcanic eruptions, and the decay of organic matter. It also plays a critical role in the Earth's carbon cycle.

2.3.1 Carbon Dioxide Emission

In recent decades, the concentration of carbon dioxide in the Earth's atmosphere has been increasing due to human activities, primarily the burning of fossil fuels (such as coal, oil, and natural gas) and deforestation. However, the combustion of these fossil fuels releases substantial quantities of CO_2 into the atmosphere, resulting in the accumulation of this greenhouse gas at alarming levels. Elevated CO_2 levels trap heat in the Earth's atmosphere, leading to global warming, more frequent extreme weather events, and other environmental challenges (Hannah *et al.*, 2020). Reducing CO_2 emissions has become a paramount goal to mitigate the impacts of climate change and secure a more sustainable future. In 2015, the Paris Agreement was established, marking a significant milestone in the global effort to combat climate change. This historic accord received support from nearly all nations around the world, representing the first unified strategy to reduce greenhouse gas emissions responsible for global warming (United Nations Framework Convention on Climate Change, 2016). By 2050, the goal is to significantly reduce greenhouse gas emissions, aiming for near-zero emissions, to help limit global warming to 1.5 degrees Celsius above pre-industrial levels (International Energy Agency, 2023).

In addressing this challenge, there is a growing emphasis on transitioning toward cleaner and more sustainable energy sources while implementing carbon capture and sequestration technologies. The strategy involves a phased approach, commencing with the elimination of new unabated coal plants and setting ambitious targets for annual increases in solar and wind power generation by 2030. These initiatives are directed at curbing CO_2 emissions stemming from industrial activities and power generation, Figure 2.7. Furthermore, it underscores the importance of research and development to facilitate the widespread adoption of emerging technologies. Despite the substantial investments required, this inclusivity is considered indispensable in pursuit of the net-zero emissions goal. The shift toward clean energy is projected to drive annual energy investments up to $5 trillion by 2030, contributing 0.4 percentage points to global GDP growth annually, while also generating numerous employment opportunities in the clean energy sector and its associated industries. According to the International Energy Agency (IEA), a comprehensive roadmap has been outlined to guide the global endeavor towards achieving net-zero emissions by 2050, Figure 2.8 *(International Energy Agency, 2023)*.

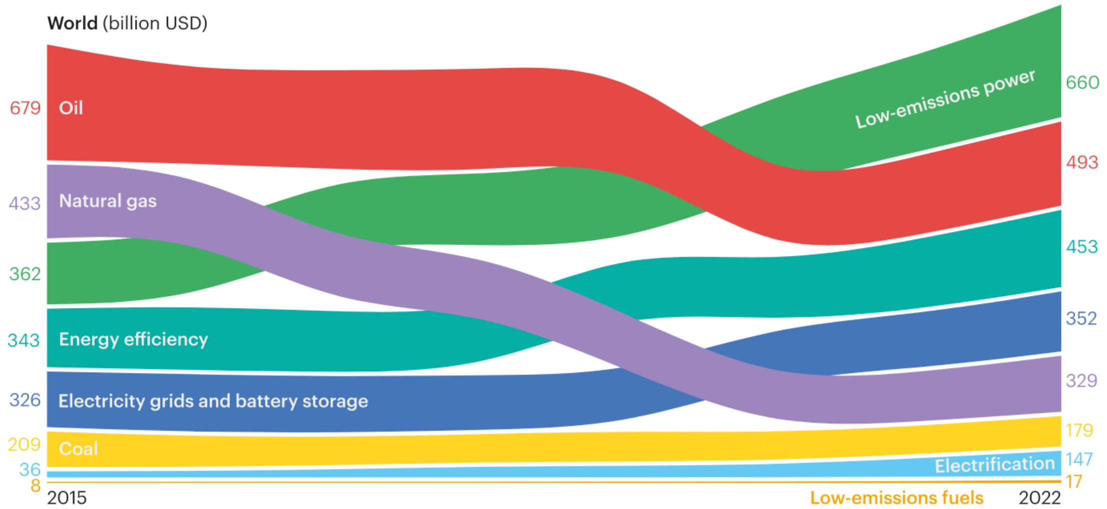

Figure 2.7 Investments flows on energy system (International Energy Agency, 2023).

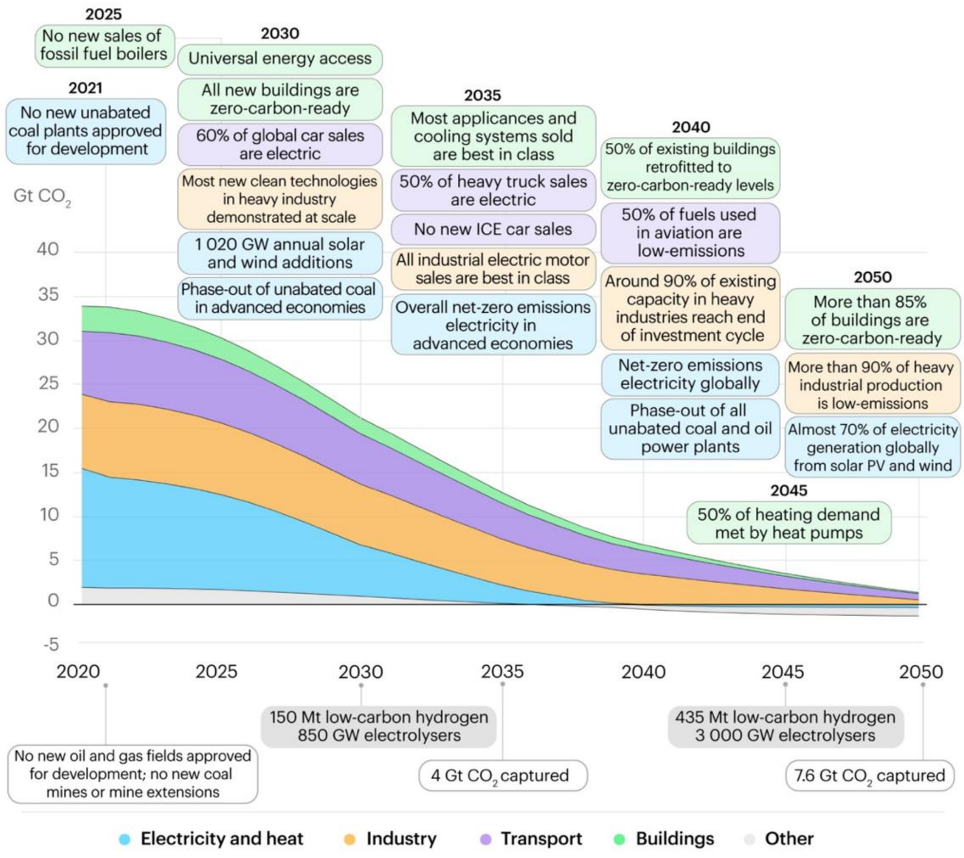

Figure 2.8 Roadmap to achieving net zero emissions by 2050 (International Energy Agency, 2023).

2.4 Carbon Capture, Transportation and Storage

In the pursuit of achieving net zero emissions by 2050, it becomes imperative to prioritize investments in carbon capture technology. Conventional carbon capture and storage (CCS) systems involve three primary phases: carbon capture, transportation, and storage. In the carbon capture phase, CO_2 is extracted from emissions generated by a variety of industrial processes and power generation methods, often employing techniques like post-combustion capture, pre-combustion capture, or oxy-fuel combustion. Following the capture, the CO_2 is transported to a designated storage site through pipelines or alternative means. In the storage phase, the CO_2 is injected deep underground into geological formations, such as depleted oil and gas reservoirs, saline aquifers, or unmineable coal seams, where it is securely stored.

2.4.1 Carbon Capture

CO_2 can be directly captured from industrial sources, employing techniques like post-combustion capture, pre-combustion capture, or oxy-fuel combustion.

(a) Post-combustion capture is a widely used method for capturing CO_2 from flue gas emissions produced by various industrial processes and power generation. In this method, the flue gas, which contains CO_2 along with other gases, is treated with a solvent or passed through a solid adsorbent to selectively capture the CO_2, Figure 2.9. Solvent-based post-combustion capture often employs a liquid solvent, such as monoethanolamide (MEA), which reacts with CO_2 to form a soluble compound. The CO_2-rich solvent can then be regenerated, releasing pure CO_2 for storage or utilization. In solid adsorption, materials like activated carbon or metal-organic frameworks selectively adsorb CO_2, which can be desorbed and collected for storage (Liang et al., 2015).

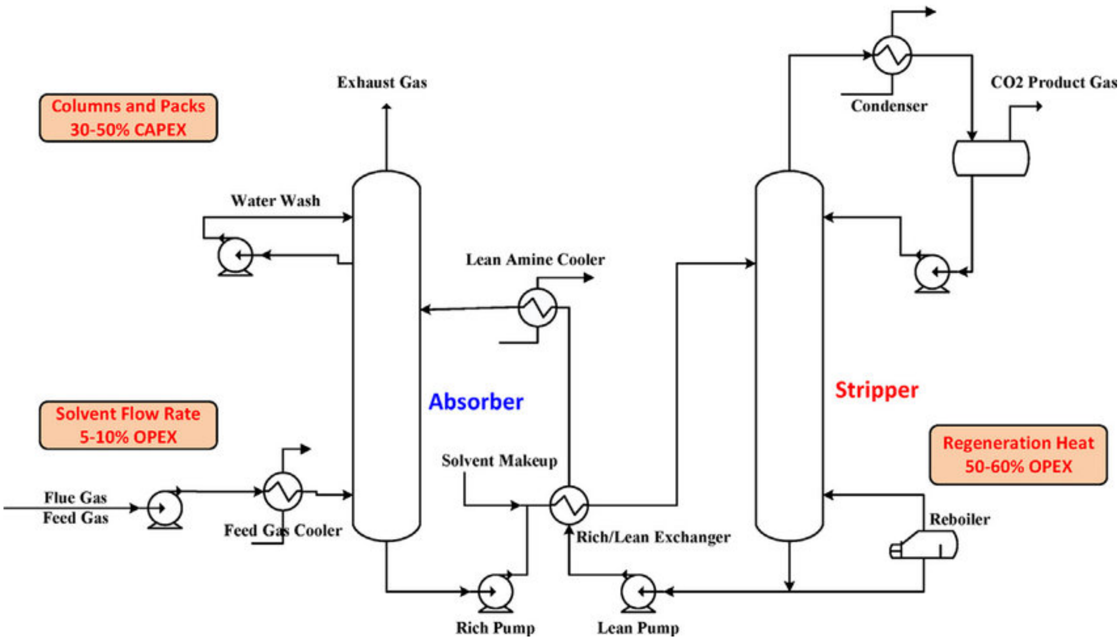

Figure 2.9 Process flow diagram of post-combustion carbon capture with reactive solvents (Liang *et al.*, 2015).

(b) Pre-combustion capture is typically applied in integrated gasification combined cycle (IGCC) power plants and other processes where fuel is gasified before combustion, Figure 2.10. In this method, the fuel (usually coal or natural gas) is gasified, producing syngas, a mixture of carbon monoxide (CO) and hydrogen (H_2), along with impurities. The CO_2 is separated from the syngas, typically using techniques like the Water-Gas Shift (WGS) reaction or amine-based solvents. After separation, the CO_2 is collected and can be further compressed for transport and storage (Theo *et al.*, 2016).

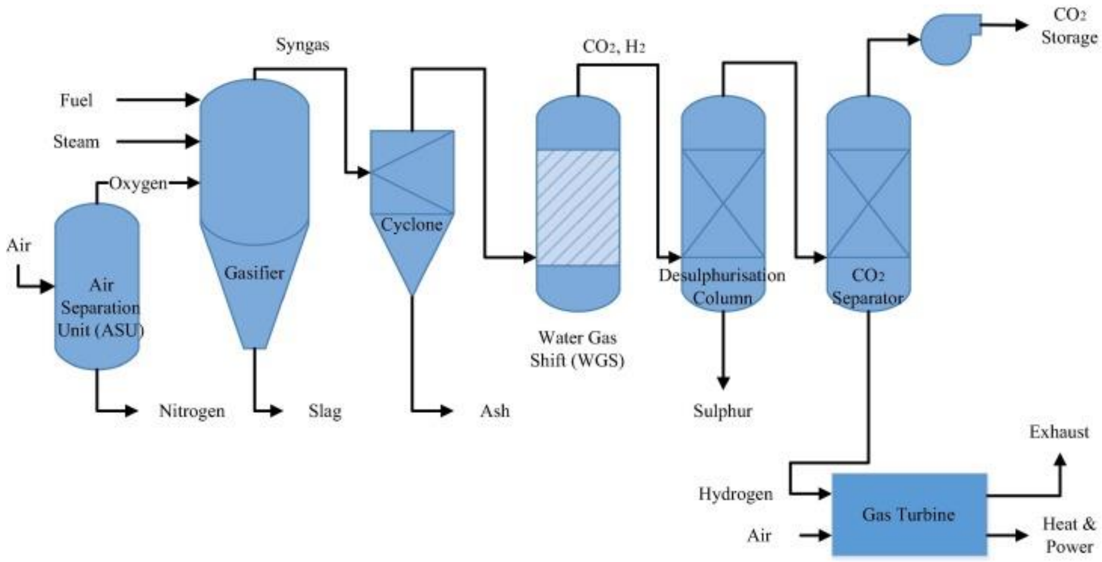

Figure 2.10 Process flow diagram of pre-combustion carbon capture system for gasification power plan (Theo *et al.*, 2016).

(c) Oxy-fuel combustion involves burning fuel in an oxygen-rich environment instead of air. This results in a flue gas primarily composed of CO_2 and water vapor, making the separation of CO_2 easier. The concentrated CO_2 stream can be captured directly from the flue gas by cooling and condensing the water vapor. Oxy-fuel combustion is often used in cement and power plants, where the high CO_2 concentration in the flue gas simplifies the capture process. The captured CO_2 can then be compressed and transported to storage sites, Figure 2.11 (Duan and Li, 2023).

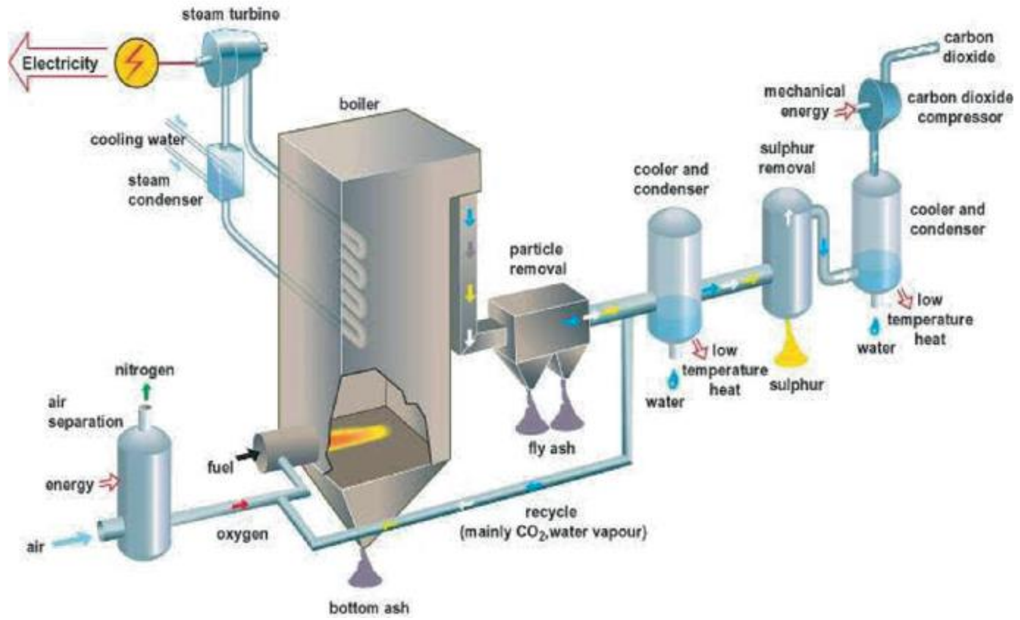

Figure 2.11 Process flow diagram of the oxy-fuel combustion (Duan and Li, 2023).

In addition to the mentioned technologies, Membrane Gas Separation uses semipermeable membranes to selectively allow CO_2 to permeate through, separating it from other gases in the mixture (Basile *et al.*, 2011). Gas Hydrate Formation relies on natural gas hydrates to capture CO_2 through high-pressure and low-temperature crystallization, but it's currently in experimental stages and less mature than other methods (Zheng *et al.*, 2020).

After capturing CO_2, it is compressed to a supercritical state for efficient transportation. Common methods include pipelines for longer distances and ships or trucks for shorter hauls. In term of Carbon Storage, CO_2 is stored underground in deep saline formations, depleted oil and gas reservoirs, or unmineable coal seams. Mineralization converts CO_2 into solid carbonates, while enhanced oil recovery (EOR) injects CO_2 into oil reservoirs, increasing production and storing the gas. These techniques contribute to preventing CO_2 emissions and reducing their impact on the global climate. However, conventional CCS technologies, while significant, face challenges related to cost, infrastructure, and public acceptance that need to be addressed for widespread adoption and achieving emissions reduction targets.

2.5 Gas Hydrates

Gas hydrates are fascinating crystalline compounds formed when water molecules trap gas molecules in a cage-like structure under specific conditions of low temperature and high pressure. While methane is the predominant gas within most naturally occurring gas hydrates, they can also encapsulate other gases such as ethane, carbon dioxide, and hydrogen sulfide. One notable aspect is that a single cubic meter of natural gas hydrates can yield a remarkable 160 cubic meters of natural gas upon dissociation (Veluswamy *et al.*, 2018). Due to the specific requirements of low temperature and high pressure, these gas hydrates are abundant and have been discovered beneath the seafloor, in polar regions, and even within certain permafrost areas. Their existence presents both distinctive challenges and opportunities, offering the potential as an unconventional energy source and playing a role in the dynamics of climate change (Lenz and Ojamae, 2011).

2.5.1 Gas Hydrate Structure

Through the utilization of X-ray diffraction techniques, Kirchner *et al.* (2004) contributed valuable insights into the intricate structures of gas hydrates. This method revealed the existence of three distinct methane hydrate structures, namely sI, sII, and sH hydrates. The structure type that forms is primarily determined by the size of the guest molecule. For instance, methane can fit into both the small and large cages of sI, while propane is too large to fit into the large cage of sI but can comfortably occupy the large cage of sII, thus forming sII hydrates. In each of these structures, water molecules form a cage that encapsulates methane, forming what is known as a pentagonal dodecahedron. It is the combination of these water cage structures and guest molecules that confers stability to these hydrates, allowing them to effectively store gas over extended periods. The geometrical parameters of the main hydrate crystal structures are summaries in Table 2.1(Gabitto and Tsouris, 2010; Kirchner *et al.*, 2004).

(a) Structure I (sI) exhibits a body-centered cubic arrangement and contains 46 water molecules with 8 potential gas sites consisting of 2 small and 6 large cages as illustrates in Figure 2.12. The symbol $5^{12}6^2$ specifies a water cage composed of twelve pentagonal and two hexagonal faces. It accommodates small-diameter molecules, typically ranging from 0.40 to 0.55 nm, such as methane or ethane, although it cannot host larger gases like propane. sI hydrates are commonly found in natural settings, especially in deep oceans where biogenic gases, primarily methane, carbon dioxide, and hydrogen sulfide, are prevalent.

(b) Structure II (sII) exhibits a diamond lattice within a cubic framework and comprises 136 water molecules with 24 potential gas sites (16 small and 8 large). This structure can accommodate relatively larger gas molecules, with diameters ranging from 0.6 to 0.7 nanometers. Typically, sII hydrates host larger guest molecules such as propane or iso-butane, and they may also contain combinations of methane gas.

(c) Structure H (sH) consists of 34 water molecules and has 6 potential gas sites (3 small, 2 medium and 1 large). It features a combination of both large and small molecules, with sizes typically falling in the range of 0.8 to 0.9 nm, such as methyl cyclohexane and methane. Within sH hydrates, there are small, medium-sized, and large cage. Notably, the formation of Type H hydrates requires the presence of two guest gases, one large and one small, to stabilize the sH structure.

Table 2.1 Geometric characteristics of key hydrate crystal structures (Gabitto and Tsouris, 2010)

	Structure I (sI)		**Structure II (sII)**		**Structure H (sH)**		
Cavity	small	large	small	large	small	medium	large
Description	5^{12}	$5^{12}6^{2}$	5^{12}	$5^{12}6^{4}$	5^{12}	$4^{3}5^{6}6^{3}$	$5^{12}6^{4}$
Cavities/unit cell	2	6	16	8	3	2	1
Average cavity radius (nm)	0.395	0.433	0.391	0.473	0.391	0.406	0.571
Coordination number	20	24	20	28	20	20	36
Water moleculesper unit cell	46		136		34		
Lattice type	Cubic		Face-centered cubic		Hexagonal		
Unit cell parameters (nm)	a = 1.2		a = 1.7		a = 1.21, c = 1.01		
Density (kg m^{-3})	912		940		1952		

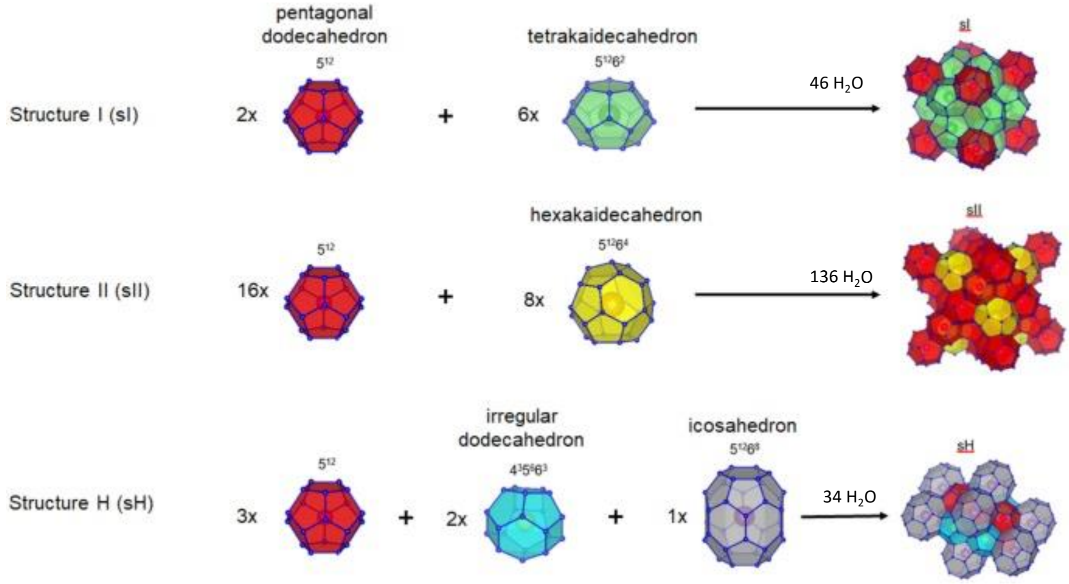

Figure 2.12 Structure types of gas hydrates (Schicks, 2022).

2.5.2 Gas Hydrates in Natural Resource

Gas hydrates are predominantly found in two geological environments: under permafrost in polar continental shelves and within sediment beneath the ocean floor, as indicated by the blue regions on the curves in Figure 2.13. These areas represent zones where the necessary conditions for hydrate formation are met, based on pressure-temperature phase equilibrium data and reflection seismic data. Moreover, these areas are rich in organic carbon, which serves as a source of methane production by microbes. Methane, whether produced by microbes or from deeper conventional gas reservoirs, can combine with sediment pore waters to form gas hydrates beneath the seafloor. While gas hydrates can also form on the seafloor in areas where fluids leak into the ocean at seep sites, these deposits are not a significant part of the global gas hydrate inventory. Within continental margin sediments, the thickness of the gas hydrate zone varies with natural pressure and temperature conditions, thinning out upslope and thickening downslope. Field studies have shown that only a small fraction, often less than 5 percent, of the sediments in these regions host gas hydrates, which may be concentrated in specific layers or fractures (Harrison, 2010).

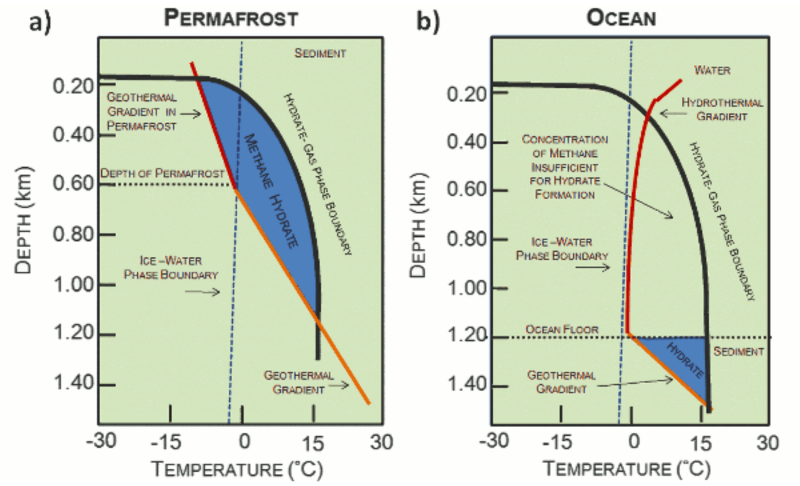

Figure 2.13 Phase diagram depicting stable gas hydrate conditions; (a) permafrost and (b) ocean environment (Harrison, 2010).

Gas hydrates are stable only within specific ranges of temperature and pressure. As average atmospheric and ocean temperatures increase, gas hydrates in permafrost and deep marine settings may break down and release the trapped methane. Methane that escapes from the seafloor into the ocean, as depicted in Figure 2.14, is commonly transformed into carbon dioxide by microorganisms. This conversion process raises the acidity of ocean waters and decreases oxygen levels. Additionally, some of the methane undergoes a transformation into carbonate rock, while a minor portion may find its way into the atmosphere as either methane or carbon dioxide (Suess, 2020).

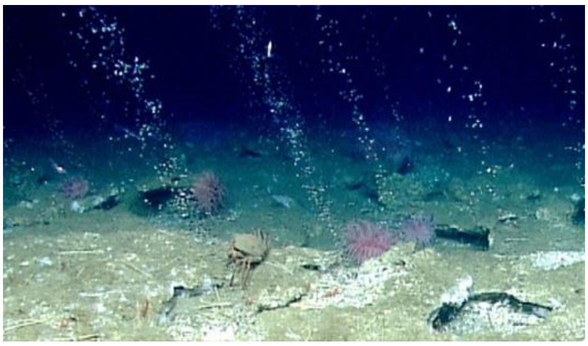

Figure 2.14 Methane bubble streams emanating from the sea floor (Schmidt Ocean Institute).

Currently, a vast reserve of gas hydrates is known to exist on Earth, estimated at over 15x10^{12} tonnes of oil equivalent (TOE). Even if we were to extract just 15 to 17% of this resource, it could provide a substantial energy supply for up to 200 years. Gas hydrate deposits are found both on land, particularly in polar regions, and offshore worldwide, with more than 220 gas hydrate deposits discovered across the globe. Figure 2.15 illustrates a map that indicates the presence of gas hydrates based on seismic data and highlights areas where drilling expeditions have successfully recovered gas hydrates, whether in permafrost or deep marine environments (Makogon, 2007). The production of gas hydrates has the potential to not only facilitate the continued economic development of individual countries but also to promote global political stability. Additionally, it offers the advantage of mitigating global warming by preventing the release of methane gas from hydrate structures, which can occur due to rising temperatures caused by global warming.

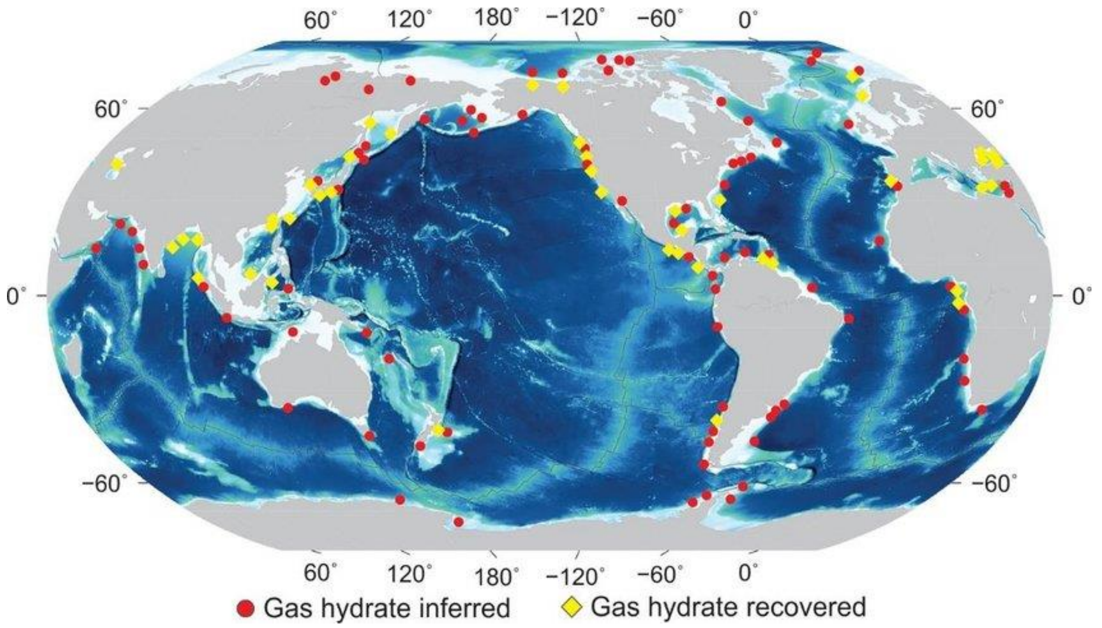

Figure 2.15 Map displaying the locations of discovered gas hydrate deposits and where gas hydrate has been successfully recovered (Villar-Muñoz, 2019).

2.6 Gas Hydrate Formation

The formation of natural gas hydrates follows a crystallization process that takes place under precise temperature and pressure conditions, determined by the specific combination of guest molecules, Figure 2.16. Under these specific conditions (high pressure driving force and high subcooling temperature), water molecules organize themselves into a crystalline lattice structure. Each water molecule establishes hydrogen bonds with neighboring water molecules, resulting in the formation of a network of cages or cavities. Subsequently, guest molecules like methane, carbon dioxide, or other small hydrocarbons enter and take up residence within these cavities within the water lattice. The hydrogen bonds in the lattice effectively imprison the gas molecules, resulting in the creation of gas hydrates (Sloan Jr and Koh, 2007).

Under the specific conditions for hydrate formation, the subcooling temperature and pressure driving force define what is known as the hydrate formation metastable zone (Bhamidi *et al.*, 2017). Within this zone, the hydrate structure is in a thermodynamically unstable state, meaning it should ideally transition to another phase or crystal structure under equilibrium conditions. However, kinetic barriers keep it in its current state, making it a region where the hydrate structure can temporarily exist in a less stable state (Mettler Toledo, 2023). To address this, the addition of mechanical agitation provides the necessary energy to initiate hydrate crystal nucleation by introducing nucleation sites and disrupting the kinetic barriers that keep the solution in the liquid phase. This process encourages the rapid growth of hydrate crystals and leads to the phase transition from a solution to a hydrates (Baek *et al.*, 2020). This concept is crucial for understanding and controlling hydrate formation processes.

The formation process consists of two main stages: nucleation and growth. During the nucleation phase, the initial formation of hydrate structures begins, usually taking place at the interface between the solution phase and gas phase. Once nucleation is successful, a thin hydrate film develops on this interface, serving as the foundation for further growth. The growth phase operates in a regime constrained by mass transfer limitations. Enhancements involving increased solubility of hydrate-forming gas molecules in water and the expansion of the contact area between hydrate formers and solution have been recognized as strategies to mitigate mass transfer resistance (Kumar *et al.*, 2015).

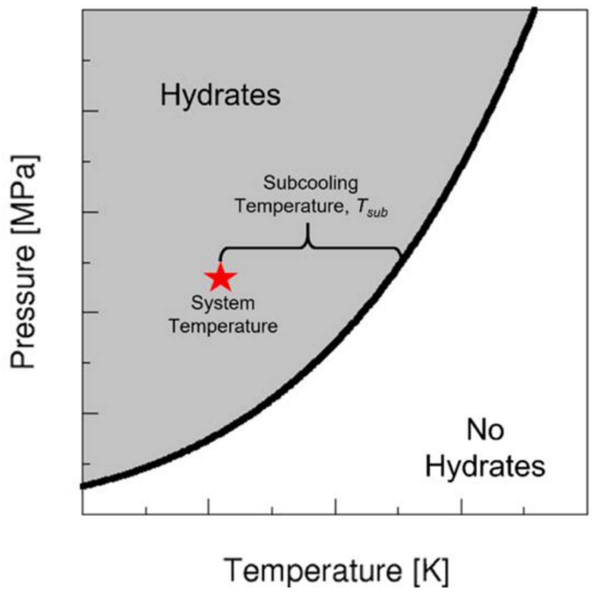

Figure 2.16 Typical hydrate equilibrium curve and hydrate stability region (Majid and Koh, 2021).

2.7 Gas Hydrate Dissociation

Gas hydrate dissociation is a process that involves breaking the hydrogen bonds between water molecules and the van der Waals interaction forces between guest molecules and water molecules within the hydrate lattice. Once this process is complete, the products of hydrate dissociation consist of water molecules (host molecules) and gas molecules (guest molecules). Various conventional methods have been suggested for extracting natural gas from hydrate reservoirs, such as depressurization, thermal stimulation, chemical inhibitor injection, or combinations of these techniques, Figure 2.17. Each method has its advantages and limitations, and the choice of which to use depends on factors like the geological and reservoir conditions, the energy source available, and the intended application (Sun *et al.*, 2016).

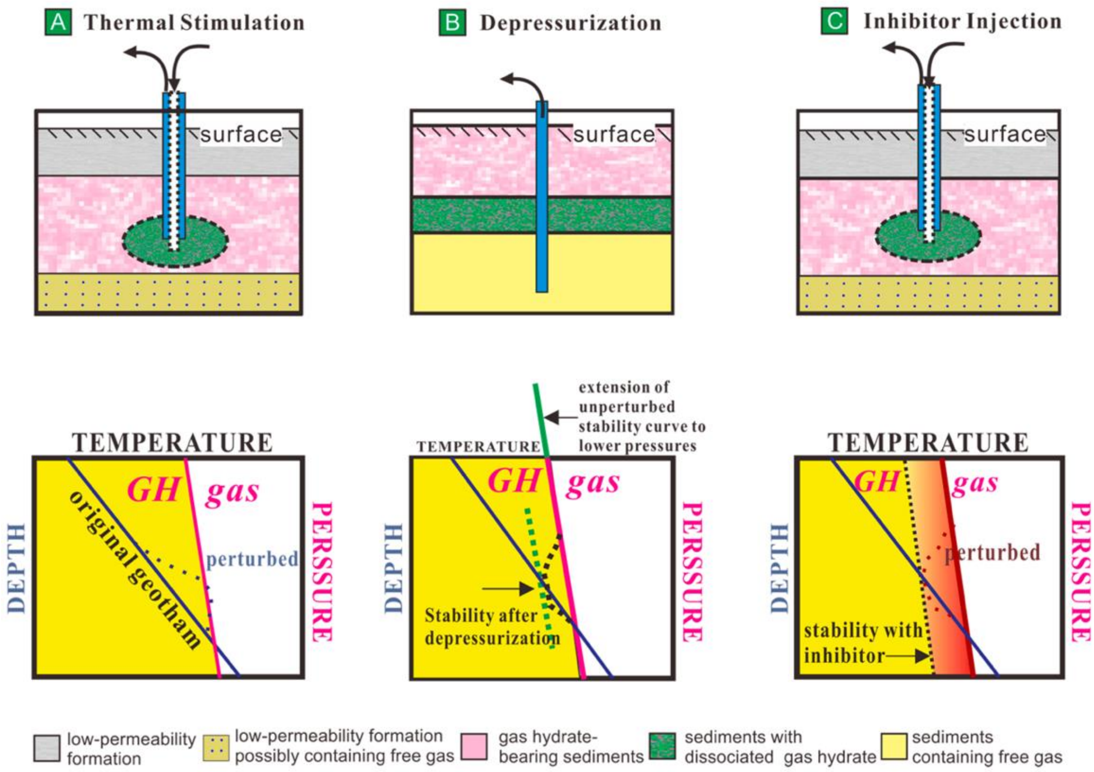

Figure 2.17 Mechanisms of the three primary hydrate dissociation methods: a) Thermal Stimulation, b) Depressurization, and c) Inhibitor Injection (Sun *et al.*, 2016).

2.7.1 <u>Depressurization</u>

Depressurization is the most common method used for gas hydrate dissociation. It involves reducing the pressure within the hydrate reservoir to levels below the hydrate stability zone. As the pressure decreases, hydrates dissociate into their constituent water and gas phases. While this method is effective, it can take time for the pressure to drop sufficiently, and it may require the extraction of large volumes of water along with the gas.

2.7.2 <u>Thermal Stimulation</u>

Thermal stimulation relies on increasing the temperature in the hydrate reservoir. By raising the temperature above the equilibrium temperature for natural gas hydrates at the prevailing pressure, the hydrates dissociate. This method can be faster than depressurization but often requires the input of substantial energy, typically in the form of heat. Care must be taken to ensure that the heat applied doesn't damage the surrounding geological formations.

2.7.3 Chemical Inhibitor Injection

Chemical inhibitor injection is a method that utilizes chemicals to prevent or slow down hydrate formation (Yin *et al.*, 2016). It can be further categorized into two types:

(a) Thermodynamic Inhibitors, such as methanol or glycols, work by altering the thermodynamic conditions of the system. They shift the phase equilibrium between water, hydrocarbons, and hydrates. By doing so, they make it more difficult for hydrates to form. This method is often used in preventing hydrate formation during oil and gas production or transportation.

(b) Kinetic Inhibitors hinder the kinetics of hydrate formation rather than thermodynamics. They work by slowing down the rate at which hydrates nucleate and grow. While they don't prevent hydrate formation entirely, they can significantly delay it. Kinetic inhibitors are often used in pipelines or equipment where the risk of hydrate formation is high.

2.8 Hydrate-Based Technology

As natural gas hydrates or clathrate hydrates are an ice-like solid, which can contain gas molecule, occupied in the cage of a water molecule. Gas hydrates, with their remarkable gas capture capacity, open up new possibilities for innovative applications based on hydrate technology. An example of these innovative applications is solidified natural gas (SNG) technology, which provides significant advantages in long-term energy storage and transportation. Gas hydrates also find applications in carbon capture and storage, playing a role in sequestering CO_2 by trapping it within their lattice structure. This contributes to global efforts to reduce greenhouse gas emissions (Qureshi *et al.*, 2022b; Zheng *et al.*, 2020). Additionally, hydrates are utilized in gas separation processes, including natural gas purification (Partoon *et al.*, 2018; Zheng *et al.*, 2019) and desalination (Seo *et al.*, 2019; Truong-

Lam *et al.*, 2022), leveraging their capacity to selectively capture particular gas molecules within their crystalline cages.

2.8.1 Energy Storage and Transportation

Energy storage using Solidified Natural Gas (SNG) technology is an innovative offering significant advantages for long-term energy storage and transportation. SNG technology stands out by employing lower pressure and higher temperature conditions, in contrast to conventional methods like CNG and LNG, which necessitate high pressure and low temperature. CNG involves compressing natural gas to 20-30 MPa but comes with safety risks due to high pressure. LNG, on the other hand, is costly to produce, with significant investments in cooling systems to lower the temperature to 113 K, converting it into cryogenic liquid natural gas. In contrast, SNG technology not only offers higher volumetric energy storage in a more compact form but also operates under moderate temperature and pressure conditions, ensuring efficient natural gas storage and transportation. This approach provides higher volumetric energy storage in a more compact form, operates at moderate temperature and pressure conditions, ensures nearly full retrieval of stored natural gas while demanding minimal energy input, and is considered one of the safest modes for natural gas storage (Veluswamy *et al.*, 2018). Figure 2.18 illustrates the sequential process for storing natural gas using hydrate-based technology (SNG). It encompasses four key steps: the formation of natural gas hydrates, the dewatering process to eliminate unreacted water, the palletization step to create hydrate pellets, and the final cooling and depressurization phase to achieve the required storage conditions. Figure 2.19 Displays the Hydrate Pellet Machine (HPM) and the resultant hydrate pellets developed by Mitsui Engineering & Shipbuilding, Japan (Mimachi *et al.*, 2015).

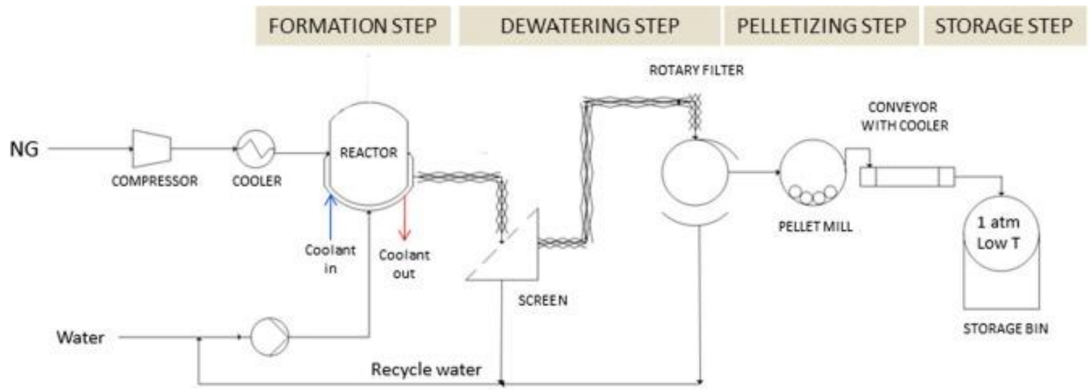

Figure 2.18 Flowchart of a natural gas production and storage chain utilizing hydrate technology (Veluswamy *et al.*, 2018).

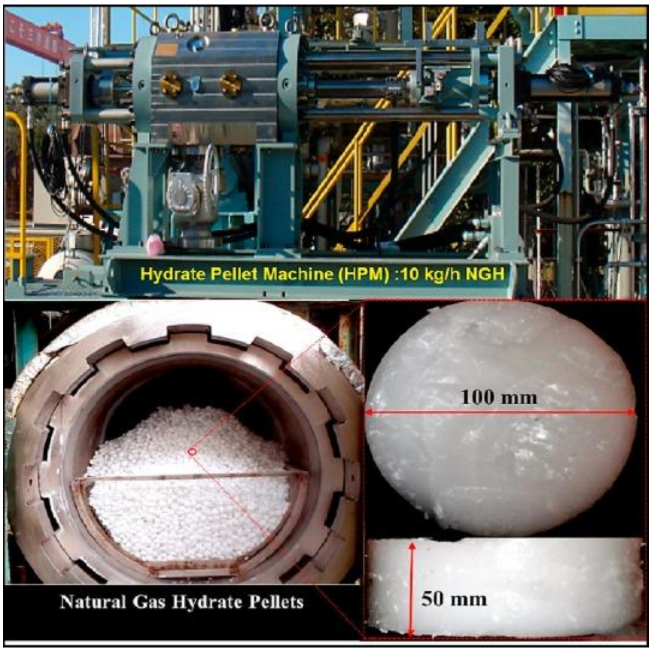

Figure 2.19 Hydrate pellet machine developed by Mitsui Engineering & Shipbuilding, Japan, used for pelletizing natural gas hydrate (Mimachi *et al.*, 2015).

2.8.2 Carbon Capture, Storage and Sequestration

The capture and storage of CO_2 is a critical endeavor in the quest to mitigate the impacts of climate change. Conventional carbon capture and storage (CCS) technologies, while reliable, often face significant economic challenges, particularly in the high costs associated with the capture stage. To make carbon capture more economically feasible, alternative technologies have been explored. Among these, hydrate-based carbon capture (HBCC) has emerged as a promising option. HBCC offers a promising avenue for CO_2 capture, storage, and sequestration. By trapping carbon dioxide within its lattice structure, gas hydrates can play a vital role in mitigating greenhouse gas emissions. HBCC offers advantages such as the potential for energy savings, impurity tolerance, and ease of transport in unit processes. Additionally, the use of gas hydrates for carbon capture offers several advantages, such as the efficient and compact storage of CO_2 and the potential for application in a wide range of carbon capture and storage projects, supporting the global transition to a more sustainable and eco-friendly energy landscape (Nguyen *et al.*, 2022). Figure 2.20 illustrates the concept of hydrate-based CO_2 capture from flue gas (CO_2 + N_2) or syngas (CO_2 + H_2). It is still in the early stages of research and development, but it has garnered significant scientific interest due to its unique characteristics.

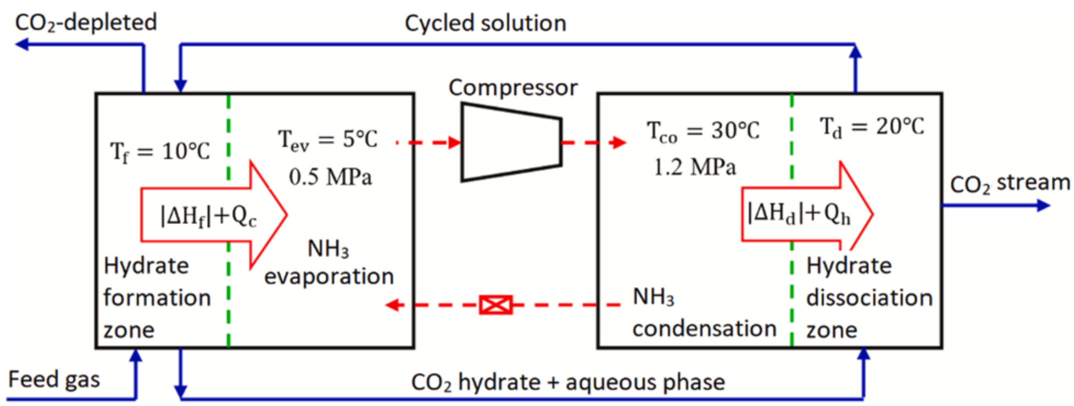

Figure 2.20 Schematic illustration of various approaches of CO_2 sequestration as clathrate hydrates (Nguyen *et al.*, 2022).

Hydrate-based technology presents an intriguing possibility for the transformation of CO_2 gas into CO_2 hydrate, which can be stored beneath the subsea level for long-term CO_2 sequestration. CO_2 hydrates offer several favorable attributes for carbon sequestration (Zheng *et al.*, 2020):

(a) They possess a higher density, ranging from 1040 kg/m³ to 1160 kg/m³, compared to seawater, resulting in a negative buoyancy effect.

(b) CO_2 hydrates can remain stable at moderate oceanic or permafrost depths where temperatures are below 10 °C.

(c) Storing CO_2 in solid hydrate form is less susceptible to disturbances in fluid flow, such as passing eddies and gas fluxes.

(d) When stored as gas hydrates within porous media, such as ocean floor sediments or permafrost, CO_2 hydrates can effectively cement the porous sediments, similar to how methane hydrates operate.

(e) The dissolution of CO_2 from hydrates into the surrounding water occurs at a significantly slower rate compared to liquid CO_2 lakes.

Figure 2.21 illustrates the various methods for storing CO_2 in the form of clathrate hydrates. After capturing CO_2 from emission sources, it can be transported to storage sites. Potential storage sites for CO_2 hydrates encompass deep oceanic basins, sub-seafloor saline formations, depleted natural gas hydrate reservoirs, existing natural gas hydrate reservoirs, permafrost regions with unfrozen water, and depleted oil and gas reservoirs partially saturated with water (Zheng *et al.*, 2020).

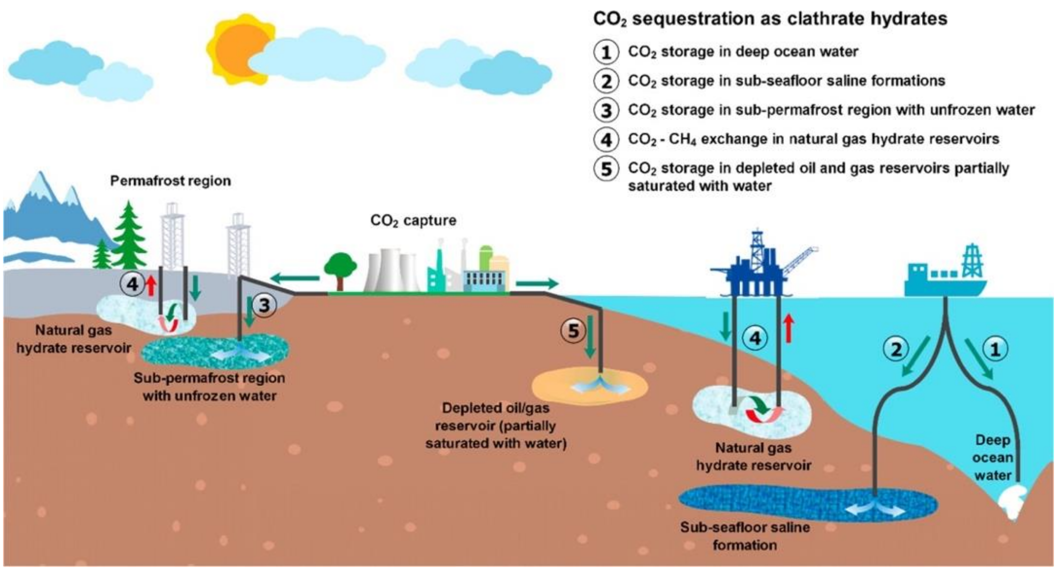

Figure 2.21 Schematic illustration of various approaches of CO_2 sequestration as clathrate hydrates (Zheng *et al.*, 2020).

Another approach to CO_2 storage involves injecting CO_2 or CO_2-containing gas into natural gas hydrate reservoirs to achieve simultaneous CO_2 sequestration and methane production. Figure 2.22 illustrates the stability zones of CH_4 and CO_2 hydrates in hypothetical oceanic and permafrost regions. In specific regions of the pressure-temperature chart, the equilibrium pressure for CH_4 hydrate formation is higher than that for CO_2 hydrate formation at the same temperature. This indicates that CO_2 hydrates are more stable than CH_4 hydrates under these conditions, justifying the CO_2-CH_4 exchange process (Zheng *et al.*, 2020).

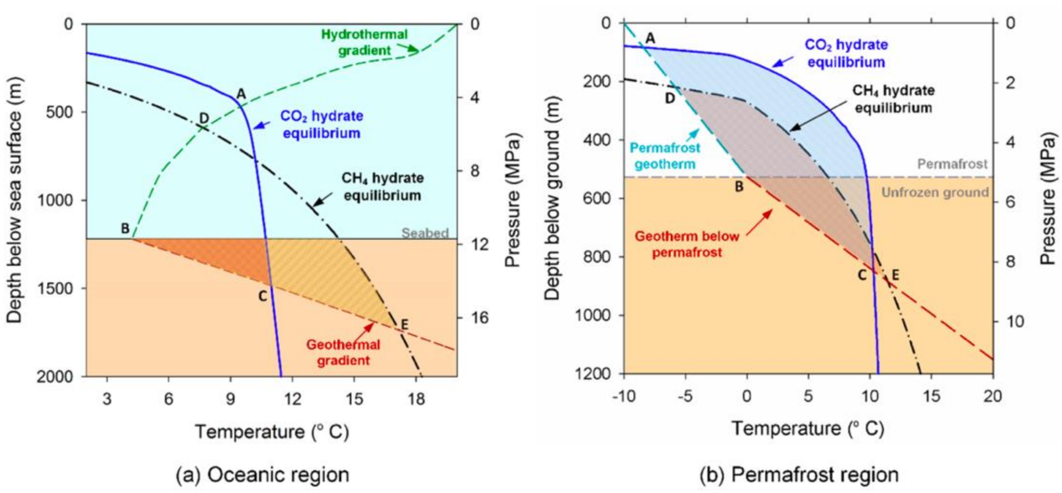

Figure 2.22 Comparison of the stability zones for CH_4 and CO_2 hydrates in hypothetical oceanic (a) and permafrost (b) regions (Zheng *et al.*, 2020).

2.8.3 Separation Process

Hydrate-based technology extends its application to separation processes, encompassing gas separation and water purification, particularly in desalination. Gas separation utilizing gas hydrate-based technology capitalizes on the crystalline structure of gas hydrates, which forms when water molecules trap gas molecules under specific temperature and pressure conditions. This innovation allows the selective capture of specific gases from mixtures, proving beneficial in reducing greenhouse gas emissions, purifying natural gas, and facilitating efficient gas storage and transportation, as well as applications in carbon capture and storage (CCS) (Partoon *et al.*, 2018; Zheng *et al.*, 2019).

In the domain of water purification, desalination, the process of removing salts from seawater, plays a pivotal role in addressing the global water scarcity issue. Clathrate hydrate-based desalination has emerged as a promising technology. When seawater or a salt solution encounters a hydrate-forming agent under suitable temperature and pressure conditions, it results in the formation of a solid phase known as a clathrate hydrate. This process effectively excludes dissolved ions and salts from the hydrate crystals, enabling the separation of pure water from an electrolyte solution. Furthermore, the hydrate crystals can be mechanically separated from the brine. After removal, these crystals can be decomposed through depressurization or thermal stimulation. This dissociation releases the water and the hydrate-forming molecules, which can be recovered and recycled (Babu *et al.*, 2018; Truong-Lam *et al.*, 2022).

2.9 Gas Hydrate Promoter

While hydrate-based technology has shown considerable promise and success, there is still room for improvement to enhance its feasibility and cost-effectiveness, especially when compared to challenging conventional technologies. To reduce operational costs, it’s essential for hydrates to form at higher temperatures and lower pressures while also having a fast hydrate formation kinetics (Veluswamy *et al.*, 2018). The addition of various chemical promoters that influence the structure of hydrates and Can shift the hydrate thermodynamic phase equilibrium to higher temperatures and lower pressures has been introduced. Changing the hydrate phase equilibrium also leads to an increase in the temperature and pressure driving force, which enhances hydrate nucleation and accelerates the rate of hydrate formation. However, altering the hydrate phase equilibrium is not the only way to enhance hydrate formation kinetics; increasing mass transfer between the gas phase and liquid phase can also boost the formation kinetics (Du *et al.*, 2014; Zhang *et al.*, 2007). Improving reactor configuration to provide more contact area and incorporating chemical promoters to reduce the interfacial tension of the solution are additional methods that can be employed to improve both the kinetics and the gas capacity of hydrate formation.

2.9.1 Thermodynamic Promoter (THPs)

Increasing the temperature at which hydrate formation occurs can be achieved through the utilization of thermodynamic promoters (THPs). These are substances or compounds integrated into the system with the objective of optimizing or modifying the thermodynamic conditions, thereby adjusting the equilibrium curve that governs the formation and stability of gas hydrates (Sloan Jr and Koh, 2007; Veluswamy *et al.*, 2018). The mechanism of THP molecules revolves around prompting the creation of hydrate cages, effectively entrapping their own molecules within the hydrate structure. This cage formation results in a shift of the hydrate equilibrium curve towards conditions of lower pressure and higher temperature, thereby broadening the range of temperature and pressure within which gas hydrates remain stable (Mech *et al.*, 2016; Seo *et al.*, 2003; Seo *et al.*, 2001). In a system that combines gases with thermodynamic promoters (THPs), the relatively larger size of THPs typically leads them to form within the larger hydrate cages. Thanks to the extended stable window of THPs, they consistently form before the small guest gas occupies the smaller hydrate cages (Khurana *et al.*, 2017). Due to the combination of small and large cages within the hydrate structure, concentration plays a significant role. In most cases, the best hydrate formation in terms of capacity occurs at stoichiometric concentration, which corresponds to the specific concentration at which the maximum number of large cages within the hydrate structure is filled, balance large and small cages hydrate formation (Al-Sowadi *et al.*, 2019).

However, it’s important to note that the effect of THPs on hydrate structure can vary based on their specific chemical properties. This modification may or may not result in a change in the hydrate structure, potentially transitioning from Structure I to Structure II, Structure H, or even a semi-clathrate hydrate (Veluswamy *et al.*, 2018). Moreover, variations in the chemical properties of THPs can impact their capacity to induce hydrate cage formation and their concentration, resulting in changes in the number of large cages formed and leading to varying degrees of expansion within the hydrate phase.

2.9.1.1 Methane + Thermodynamic Promoter (THPs)

Numerous studies have explored the addition of thermodynamic promoters (THPs) in methane hydrate formation, focusing on various hydrate structures such as sII, sH , and semi-clathrate. However, due to the limited stability windows of sH hydrates (Hütz and Englezos, 1996; Lee *et al.*, 2005; Tsuji *et al.*, 2004), as well as their reduced storage capacity and the compact nature of hydrate products in semi-clathrate hydrates (Chanakro *et al.*, 2020; Li *et al.*, 2007; L. Shi *et al.*, 2017), sII hydrates have attracted the most attention. They have been the subject of research for many years because of their potential for high-temperature methane hydrate formation (Majid and Koh, 2021; Veluswamy *et al.*, 2018). In the context of sII hydrates, research conducted by Lee *et al.* (2012), de Deugd *et al.* (2001), and Mainusch *et al.* (1997) investigated the methane hydrate phase equilibriums of solutions containing 1,3 dioxane, tetrahydropyran (THP), acetone, and tetrahydrofuran (THF). The results, as shown in Figure 2.23, reveal that cyclic ethers like tetrahydrofuran (THF), tetrahydropyran (THP), and 1,3-dioxolane (DIOX) have the potential to enable pure methane hydrate formation at temperatures near room temperature and lower pressures. Among these, THF exhibited the most significant effect in shifting the hydrate phase equilibrium to lowest pressure and highest temperature.

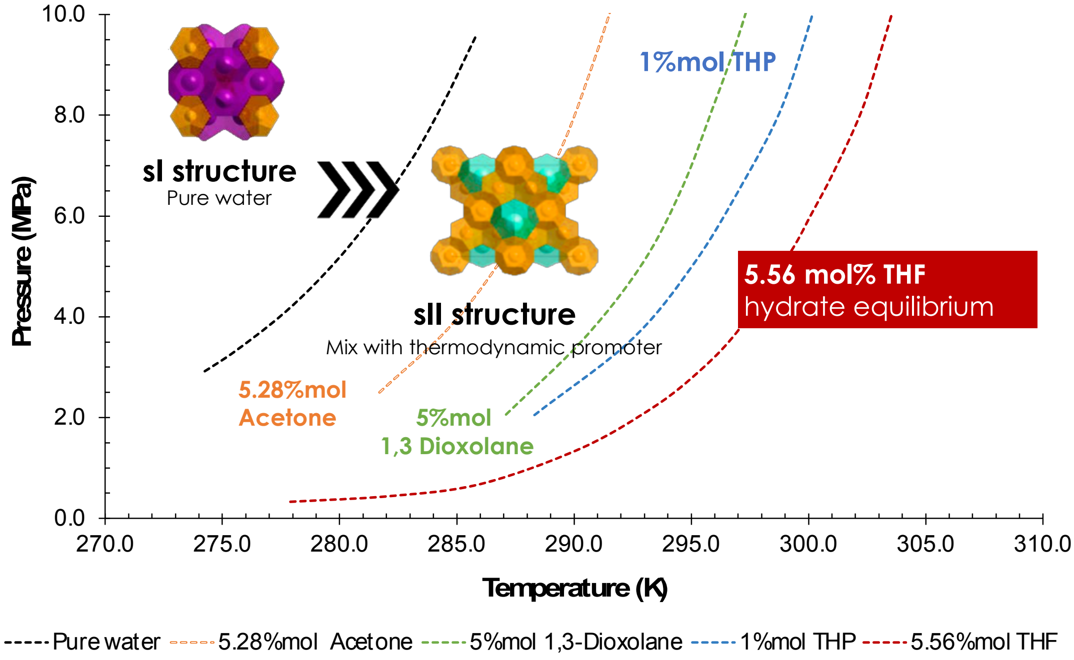

Figure 2.23 Phase equilibriums of methane hydrates in solutions containing 1,3-dioxane, THP, acetone, and THF (de Deugd *et al.*, 2001; Lee *et al.*, 2012; Mainusch *et al.*, 1997).

As previously mentioned, the concentration of THPs plays a critical role on hydrate phase. According to Al-Sowadi *et al.* (2019), a concentration of 5.56 mol% is identified as the stoichiometric concentration of sII hydrates, determined by the displacement of ethylene by THF molecules. Experiments conducted across varying THF concentrations consistently demonstrated that an increase in THF concentration results in a reduction in the number of encapsulated ethylene molecules within the hydrate structure, as depicted in Figure 2.24. Consequently, a THF concentration of 5.56 mol% is regarded as the optimal stoichiometric concentration for sII hydrate formation. a THF concentration of 5.56 mol% served as the stoichiometric level that extended the hydrate phase equilibrium most effectively, Figure 2.25 (Majid and Koh, 2021) and resulted in the highest hydrate formation, as demonstrated by the methane uptake, Figure 2.26 (Beheshtimaal and Haghtalab, 2018; Lin *et al.*, 2018).

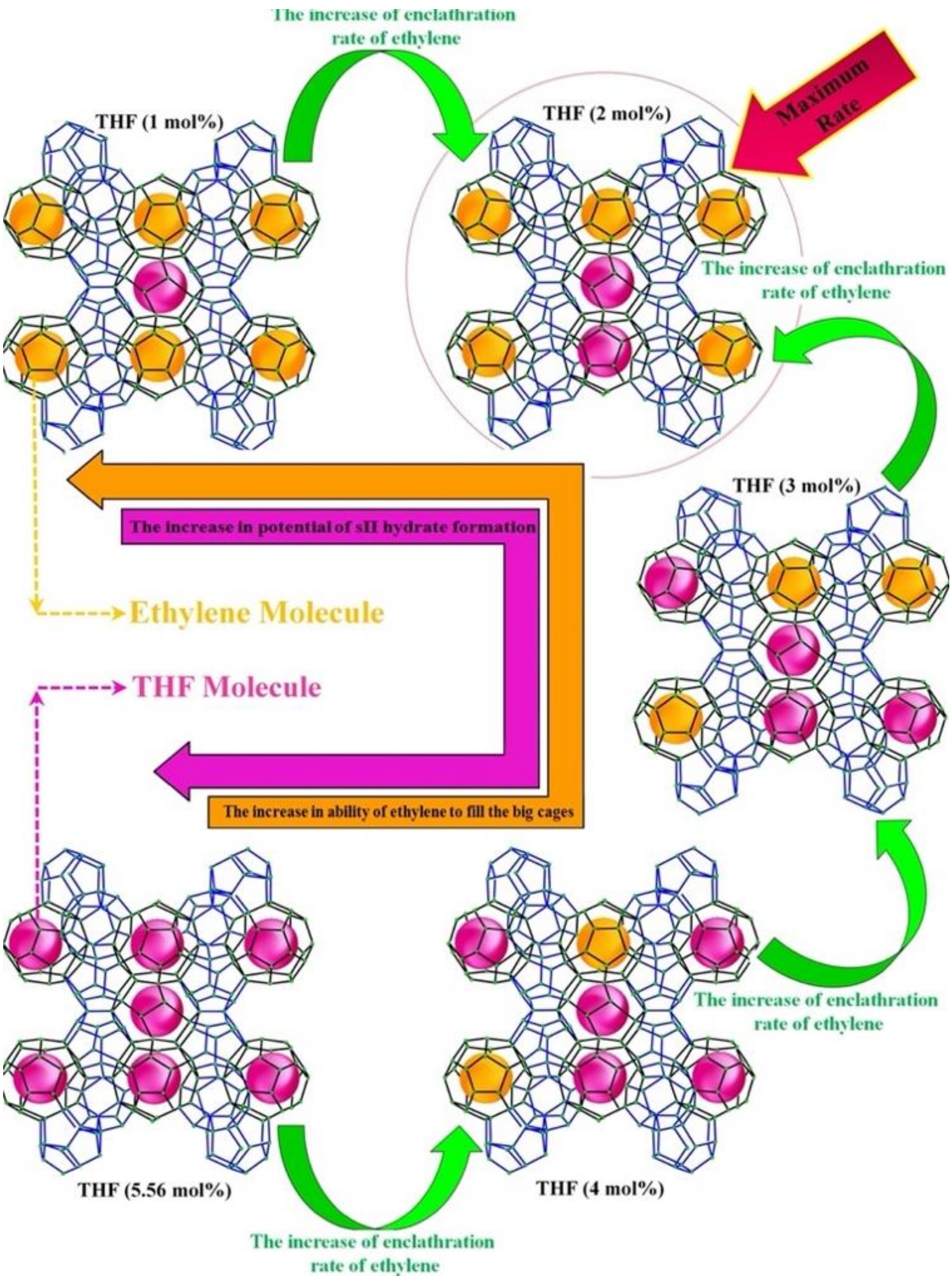

Figure 2.24 Kinetic behavior of formed hydrate in an ethylene-THF-water system based on THF concentration in aqueous solution (Al-Sowadi *et al.*, 2019).

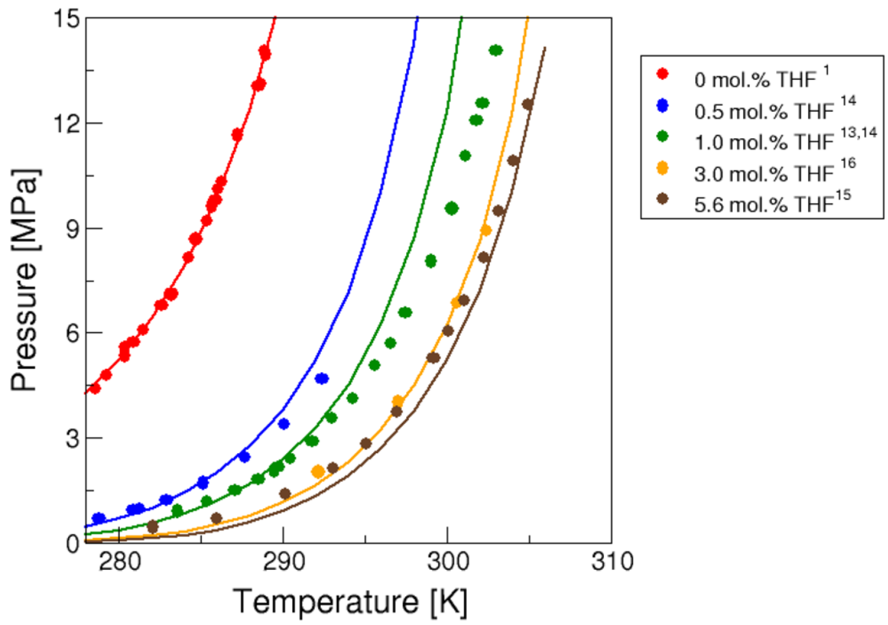

Figure 2.25 Methane-THF hydrate phase equilibrium (Majid and Koh, 2021).

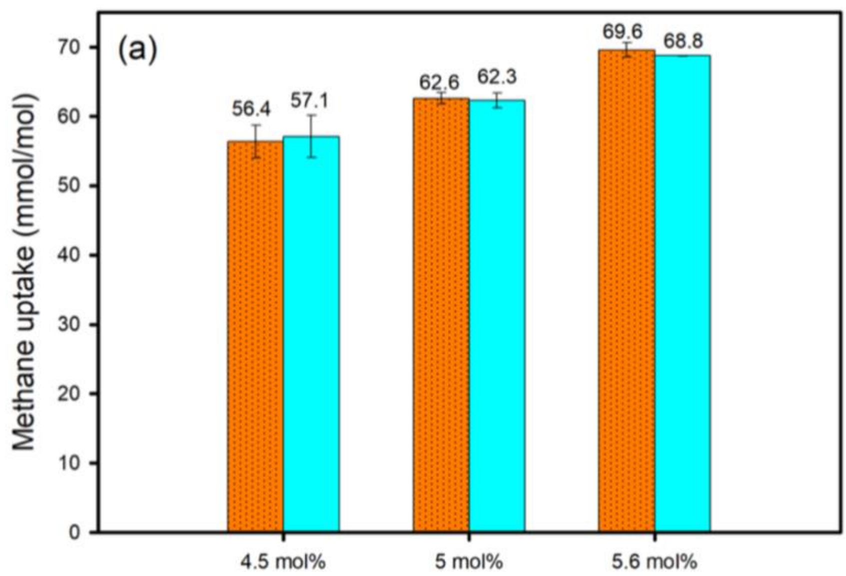

Figure 2.26 Methane uptake in different THF concentrations (Lin *et al.*, 2018).

As previously mentioned, extending the hydrate phase equilibrium has the additional benefit of increasing the temperature and pressure driving force, which, in turn, enhances hydrate nucleation and accelerates the rate of hydrate formation. In a study conducted by Veluswamy *et al.* (2016c), the effects of a

5.56 mole% THF as a thermodynamic promoter (THP) were examined at 283.2 K and 7 MPa, in comparison to pure methane at 9.5 MPa and 272 K for hydrate formation. Both systems were subject to a similar driving force. As depicted in Figure 2.27, the inclusion of 5.56 mole% THF led to a notable increase in the rate of hydrate formation, resulting in an 11.66-fold enhancement in methane uptake compared to pure methane. Therefore, the introduction of promoters like THF can enhance both thermodynamic and kinetic performance. This enhancement paves the way for the development of a cost-effective and energy-efficient solid natural gas technology using clathrate hydrates for natural gas storage.

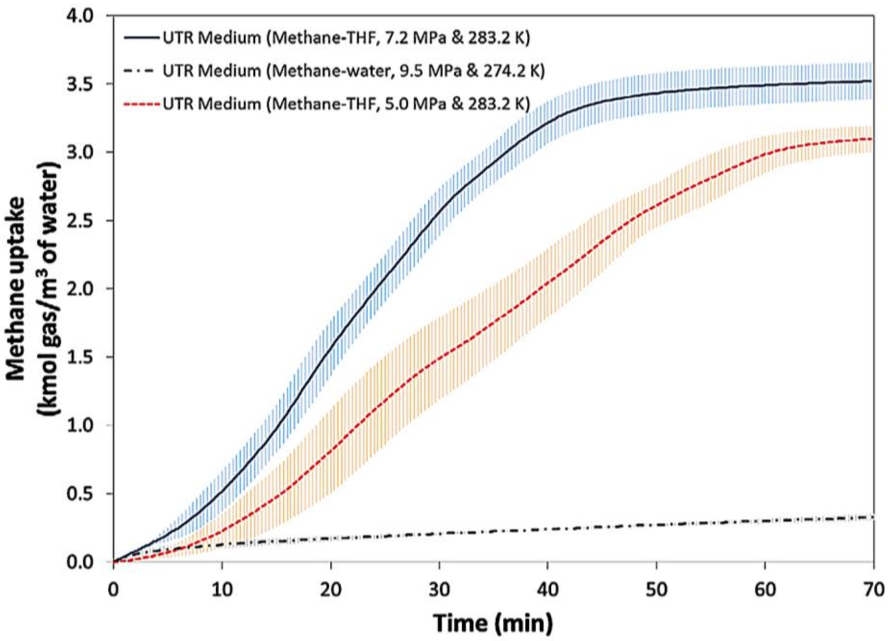

Figure 2.27 Methane uptake in the presence and absence of 5.56 mol% THF (Veluswamy *et al.*, 2016c).

By shifting the hydrate phase equilibrium through the addition of THPs, it becomes feasible to increase the formation temperature and decrease the formation pressure, Figure 2.28 (Inkong et al., 2019a). Veluswamy *et al.* (2016b) investigated the impact of temperature on mixed methane with 5.56 mol% THF hydrate formation kinetics, exploring three different temperatures (283.2 K, 288.2 K, and 293.2 K). At the specified experimental temperatures and pressure conditions, only sII hydrates were formed, and there was no opportunity for the formation of pure sI methane hydrates. The findings suggested that there was no significant difference in methane uptake at the various temperatures (283.2 K, 288.2 K, and 293.2 K). Nevertheless, an increase in temperature was observed to lead to a decrease in the rate of formation and an increase in the hydrate induction time, as well as the time taken for 90% completion, as shown in Table 2.2. Regarding the decrease in hydrate formation pressure, adverse effects on hydrate formation kinetics were also observed. However, it was noted that the methane uptake decreased under these conditions, as shown in Table 2.3.

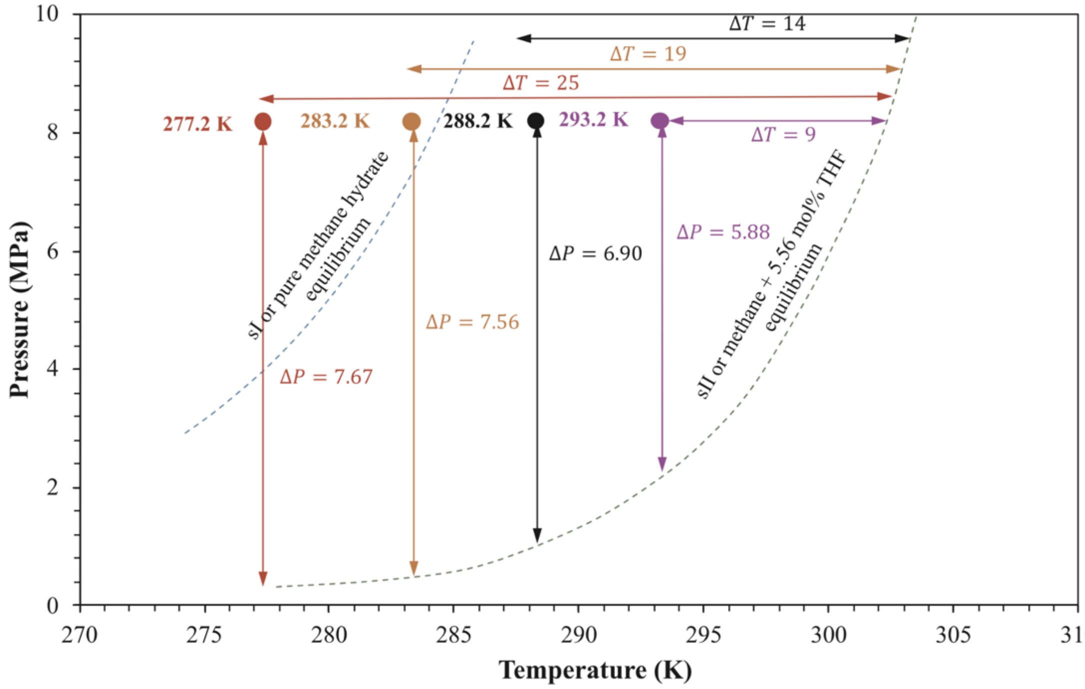

Figure 2.28 Temperature and pressure driving forces for mixed methane-THF hydrate formation were maintained at 8.0 MPa and various temperatures, 277.2 (ΔT = 25 K, ΔP =7.67), 283.2 (ΔT = 19 K, ΔP =7.56), 288.2 (ΔT = 14 K, ΔP =6.90), and 293.2 K (ΔT = 9 K, ΔP =5.88) (Inkong *et al.*, 2019a).

Table 2.2 Hydrate formation parameter for experiments conducted at 7.2 MPa and different temperatures (Veluswamy *et al.*, 2016b)

No.	Experimental temperature (K)	Induction time, IT (min)	Time taken for 90% completion, t_{90} (min)	Methane uptake[a] (kmol/mol)	Rate of methane uptake, NR_{30} (kmol m^3 h^{-1})		
					Stage 1	Stage 2	Stage 3
A1-A3	283.2	5.55 (±9.05)	46.22 (±1.39)	3.82 (±0.166)	5.500 (±0.208)	-	-
B1-B3	288.2	1.11 (±0.70)	112.44 (±3.15)	3.68 (±0.166)	1.840 (±0.276)	2.098 (±0.144)	-
C1-C3	293.2	25.80 (±17.72)	402.05 (±96.25)	3.81 (±0.082)	0.204 (±0.077)	0.530 (±0.093)	1.005 (±0.155)

[a] Methane uptake for experiments A1–A3 and B1–B3 reported at 3 h of hydrate growth while gas uptake for C1–C5 reported at 8 h of hydrate growth.

Table 2.3 Hydrate formation parameter for experiments conducted at 283.2 K and different pressure (Veluswamy *et al.*, 2016b)

No.	Experimental temperature (K)	Induction time, IT (min)	Time taken for 90% completion, t_{90} (min)	Methane uptake[a] (kmol/mol)	Rate of methane uptake, NR_{30} (kmol m^3 h^{-1})	
					Stage 1	Stage 2
D1-D3	7.2	0.83 (±1)	40.5 (±11.2)	4.34 (±0.31)	7.50 (±1.65)	-
E1-E3	5	11.6 (±13.1)	41.4 (±3.0)	3.98 (±0.06)	4.62 (±0.81)	-
F1-F3	3	17.8 (±7.5)	79.2 (±14.2)	3.52 (±0.13)	1.31 (±0.04)	4.34 (±0.31)

[a] Methane uptake for all experiments reported at 2 h of hydrate growth.

2.9.1.2 Carbon Dioxide + Thermodynamic Promoter (THPs)

Numerous studies have investigated the impact of adding thermodynamic promoters (THPs) on CO_2 hydrate formation. Figure 2.29 illustrates the influence of various THPs, including cyclopentane (CP), THF, and tetrabutylammonium bromide (TBAB), on CO_2 hydrate phase equilibrium (Choi *et al.*, 2021). However, it appears that THPs are not significantly effective in the context of CO_2 hydrate formation, as evidenced by low CO_2 uptake and limited hydrate conversion observed with various THPs, such as cyclopentane (CP) (Zhang *et al.*, 2023), THF (Liu *et al.*, 2023), and 1,3-dioxolane (DIOX) (Yao *et al.*, 2023), as shown in Figure 2.30. The effectiveness of THPs in promoting CO_2 hydrate formation seems to be influenced by complex interactions and specific conditions, which warrant further research to better understand and enhance their performance in this context.

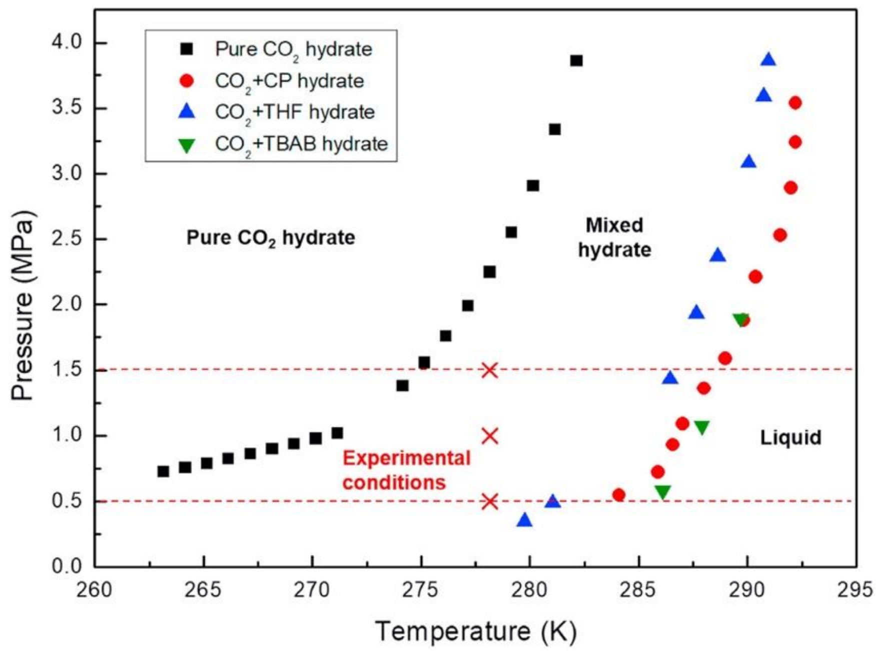

Figure 2.29 Hydrate phase equilibrium of CO_2 hydrate with and without THPs at a concentration of approximately 3.0 mol%.

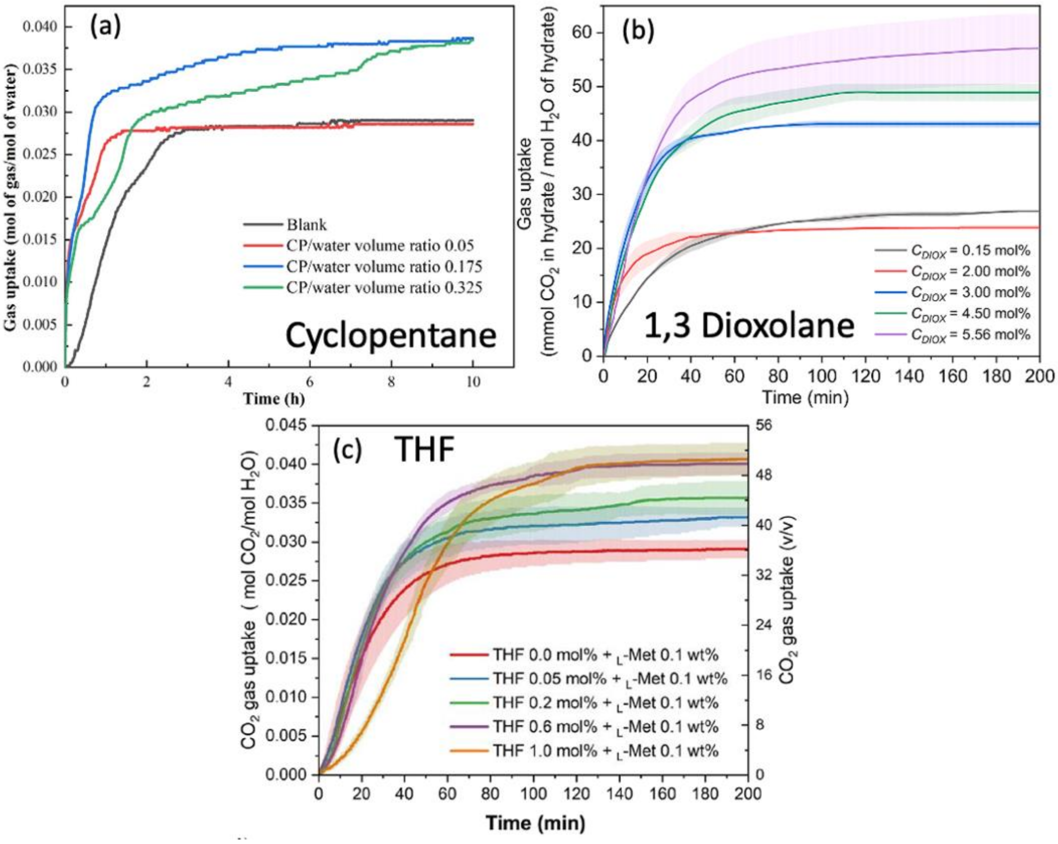

Figure 2.30 CO_2 uptake profiles during CO_2 hydrate formation with various additions of THPs: cyclopentane (CP) (Zhang *et al.*, 2023), THF (Liu *et al.*, 2023), and 1,3-dioxolane (DIOX) (Yao *et al.*, 2023).

2.9.2 Kinetic Promoter (KHPs)

While extending the phase equilibrium through THPs contributes to kinetic enhancement, when the temperature and pressure driving force decreases, additional promoters come into play. Unlike thermodynamic hydrate promoters (THPs), kinetic hydrate promoter molecules (KHPs) do not become part of the hydrate structure, as illustrated in Figure 2.31. Therefore, introducing kinetic hydrate promoters (KHPs) into the system does not lead to a substantial shift in the hydrate equilibrium curve. To effectively tackle the challenges of slow hydrate nucleation and formation rates, it becomes essential to improve mass transfer between the gas and liquid phases during the entire hydrate formation process (Du et al., 2014; Zhang et al., 2007).

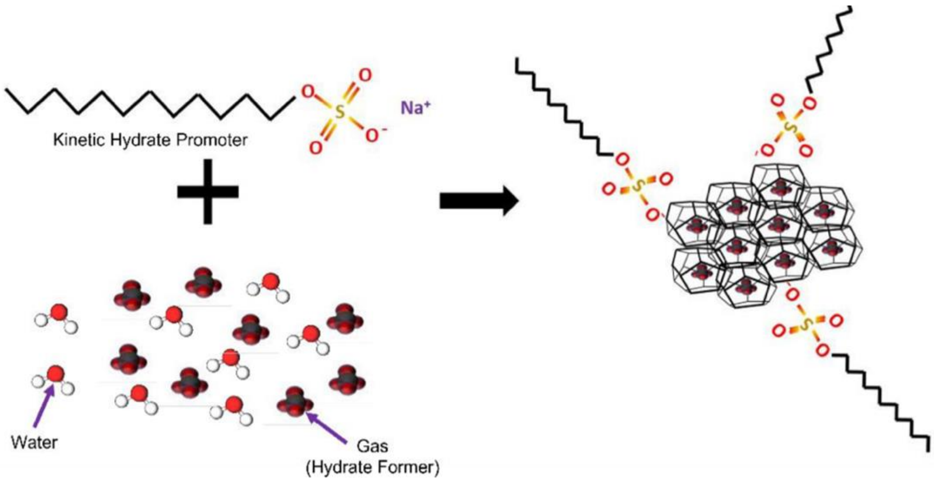

Figure 2.31 Formation of gas hydrates in the presence of a KHP (Majid and Koh, 2021).

Numerous chemicals have been explored in the quest to enhance hydrate formation kinetics. The timeline presented here showcases the initial reports on various materials from the literature that aimed to improve the kinetics of methane hydrate formation, including activated carbon, zeolite, silica sand, hollow silica, and more, Figure 2.32. Among these materials, surfactants showed promise as kinetic promoters. However, due to certain drawbacks, there has been a growing interest in environmentally friendly alternatives like amino acids.

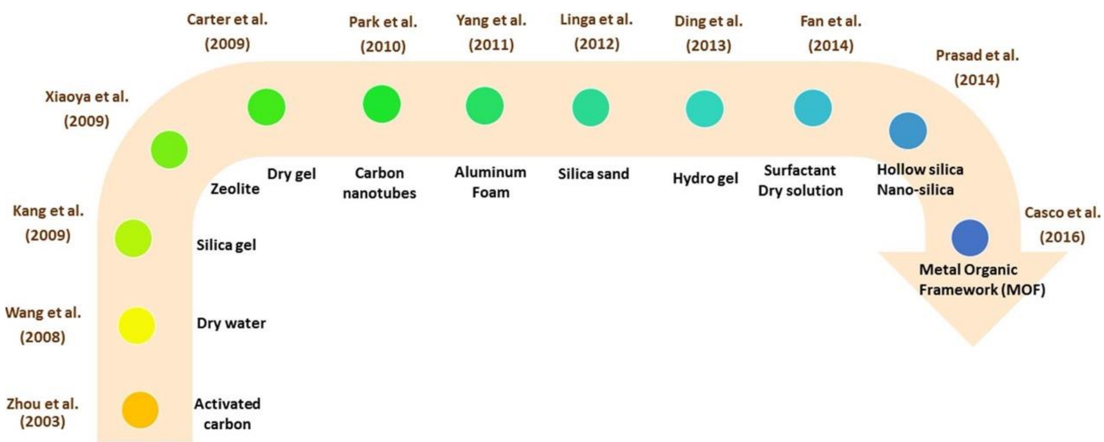

Figure 2.32 Timeline of reports on various materials used to improve methane hydrate formation kinetics (Veluswamy *et al.*, 2018).

2.9.2.1 Surfactant

Surfactants are well-recognized chemicals employed to accelerate gas hydrate formation kinetics. Their chemical properties, which include hydrophobic tails and hydrophilic heads, play a crucial role. These properties enable surfactant micelles to act as nucleation sites for hydrates, resulting in shorter nucleation times (induction times) and faster growth, Figure 2.33 (a). Surfactants are effective at reducing solution interfacial tension, leading to improved gas dissolution. This reduction in interfacial tension facilitates solution movement within the hydrate structure through capillary effects, as depicted in Figure 2.33 (b). Moreover, surfactants' capacity to adsorb onto the surfaces of hydrate particles creates a new layer within the gas-liquid interfacial area, often the initial site for hydrate formation, Figure 2.33 (c), (He *et al.*, 2019; Pan *et al.*, 2020).

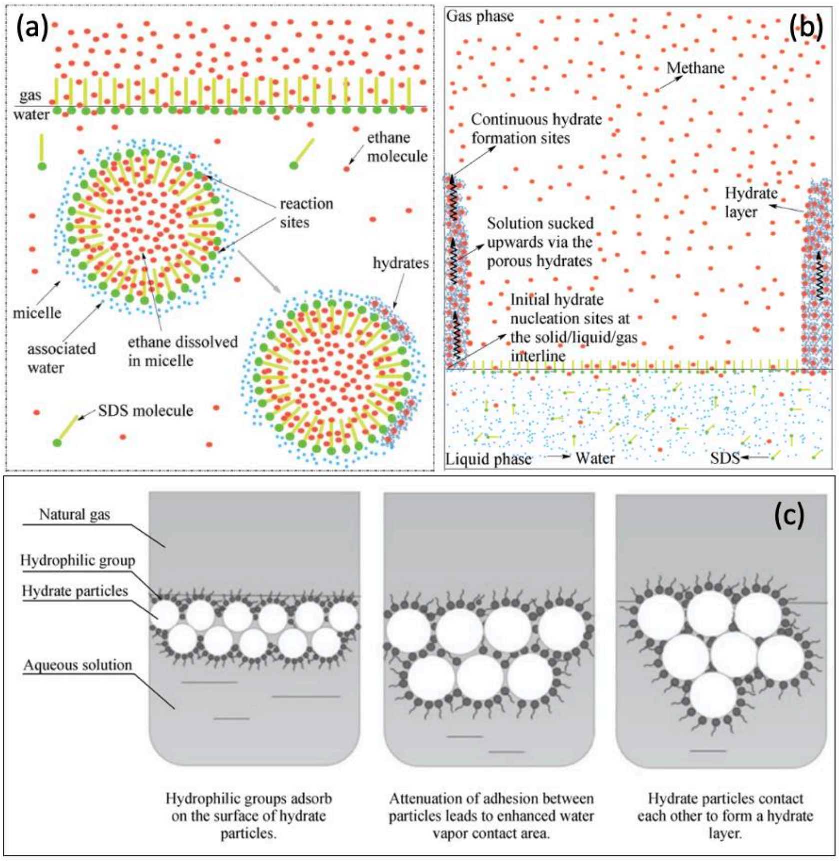

Figure 2.33 Possible mechanism of surfactants in enhancing gas hydrate formation (He *et al.*, 2019; Pan *et al.*, 2020).

Three common types of surfactants, anionic, cationic, and nonionic, can be classified based on their electrical properties. Each class of surfactants serves distinct roles in facilitating hydrate formation. Nevertheless, all types of surfactants have an impact on both hydrate storage capacity and formation rate as summarized in Table 2.4.

Among surfactants, anionic surfactants have been identified as the most effective in enhancing kinetic performance. In a study conducted by Ganji *et al.* (2007) under conditions of 276.2 K, 8.3 MPa, and a stirring speed of 200 rpm, the influence of sodium dodecyl sulfate (SDS) was examined. The results revealed that at an SDS concentration of 0.05 wt%, the hydrate formation rate exceeded that of the SDS-free solution by more than 35 times, significantly reducing the induction time. The hydrate reached a stable state in approximately 1 hour, as illustrated in Figure 2.34.

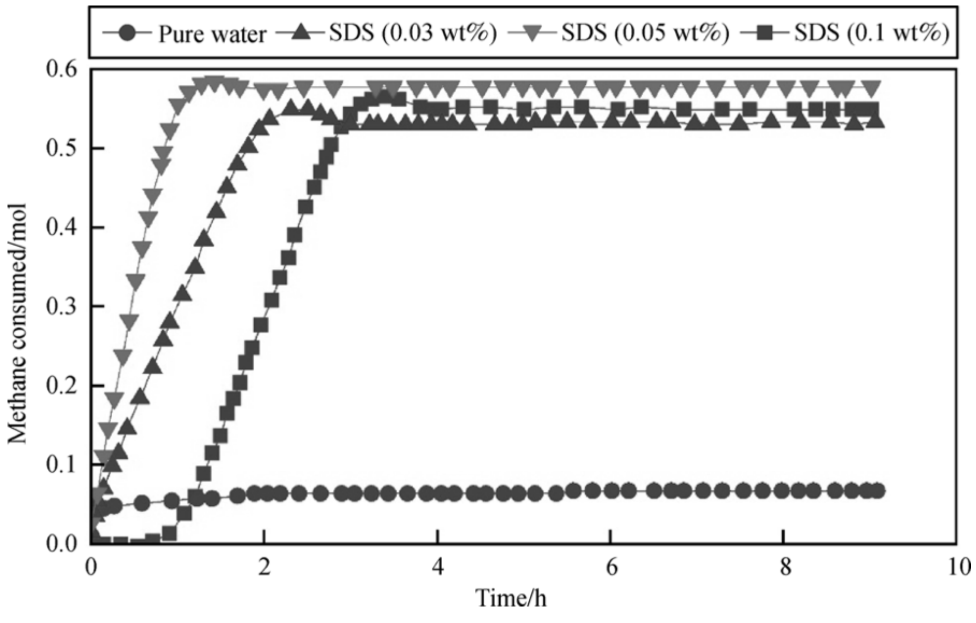

Figure 2.34 Methane uptake profiles of SDS solution (Ganji *et al.*, 2007).

Table 2.4 Hydrate formation parameter for experiments conducted at 283.2 K and different pressure (Veluswamy et al., 2016b)

Number	Surfactant	Type	Concentration range/(wt%)	Conclusion
1	APG	nonionic	0–0.16	Among them, at higher concentrations (0.08–0.16 wt%), the formation rate of hydrate in APG solution was very fast, the induction time was shortened to about 15min, and the induction time at 0.02 wt% in SDBS system was 25–30 min
	SDBS	anionic	0–0.2	
2	SDS	anionic	0.01, 0.02, 0.05, 0.07, 0.09, 0.12	All three reduced the phase equilibrium point and induction time of the hydrate
	CTAB	cationic	0.02, 0.03, 0.05, 0.07, 0.09	
	P123	nonionic	0.01, 0.03, 0.05, 0.09	
3	SDS	anionic	0.03, 0.05, 0.1	SDS effectively accelerated the rate of hydrate formation at three concentrations. LABS increased the rate of hydrate formation at 0.05 wt% and 0.1 wt%, but decreased at 0.03 wt%. In addition, CTAB and ENP promoted the hydrate formation at 0.01 wt%, and weaken at 0.03 and 0.05 wt%
	LABS	anionic		
	CTAB	cationic		
	ENF	nonionic		
4	SDS	anionic	0.03, 0.05	Compared to pure water, the induction time of hydrate formation in the presence of surfactant was reduced.
	HTABr	cationic	0.03, 0.05, 0.07	
	Brij-58	nonionic	0.03, 0.05, 0.07	
5	PVP	nonionic	0.005, 0.01	PVP showed a dual effect of promoting and inhibiting hydrate nucleation in the test
6	SDS	anionic	0.008, 0.0125, 0.1, 0.2, 0.4	SDS at 0.1 wt% or above was quite effective for increasing hydrate formation rate and gas conversion rate. STS was less effective to promot hydrate formation
	STS	anionic	0.0007, 0.0035, 0.01, 0.04, 0.06	
	SHS	anionic	0.0003, 0.001, 0.002, 0.004, 0.016	
7	LABSA	anionic	0.005, 0.01, 0.1, 1	With the addition of LABSA, the rate of hydrate formation increased; low concentrations of ETHOXALATE also increased the rate of hydrate formation. DAM has the weakest promotion ability of the three
	DAM	cationic		
	ETHOXALATE	nonionic		
8	Aerosol-OT/AOT	anionic	0.038	According to the analysis of infrared spectrum, SDS had obvious acceleration effect on hydrate formation, and CPC had no effect on its formation
	SDS	anionic		
	CPC	cationic		
9	SDS	anionic	0.5	Upon addition of the surfactant, a higher hydrate density was obtained and hydrate formation was accelerated
	PEG400	cationic		
10	SDS	anionic	0.05, 0.07, 0.09, 0.11	As the amount of surfactant increased, the rate of hydrate formation increased and the induction time decreased. The effect of anionic SDS on hydrate formation rate was the most significant, and cation HTABr had the greatest influence on induction time
	HTABr	cationic		
	Tritonx-405	nonionic		
11	SDS	anionic	0.1–0.4	When using SDS and SDSN, all reaction times were reduced to less than 40 min. While using SDBS, it took several hours to achieve pressure balance
	SDSN	anionic		
	SDBS	anionic		
12	SDS	anionic	0, 0.1, 0.2, 0.3	The addition of DTAC had little effect on the formation of methane hydrate. SDS, DAH and DN_2Cl had obvious promoting effects on methane hydrate formation. SDS had a higher hydrate formation rate than the other two, but at 0.1 and 0.2 wt%, DN_2Cl had a better methane uptake than SDS
	DAH	cationic		
	DTAC	cationic		
	DN_2Cl	nonionic		

Another noteworthy anionic surfactant is Methyl Ester Sulfonate (MES), which is derived from bio-based sources. Inkong *et al.* (2019b) conducted a study where they observed that increasing the MES concentration from 1 mM to 8 mM at 277.2 K and 8 MPa led to a reduction in gas hydrate formation induction times and an increase in the gas hydrate formation rate, as depicted in Figure 2.35 (a) and 2.35 (b), respectively. Despite MES being low in toxicity and environmentally friendly, it has a tendency to generate foam during gas hydrate dissociation, as shown in Figure 2.36. This foaming phenomenon is the primary reason for gas loss and renders MES a single-use solution.

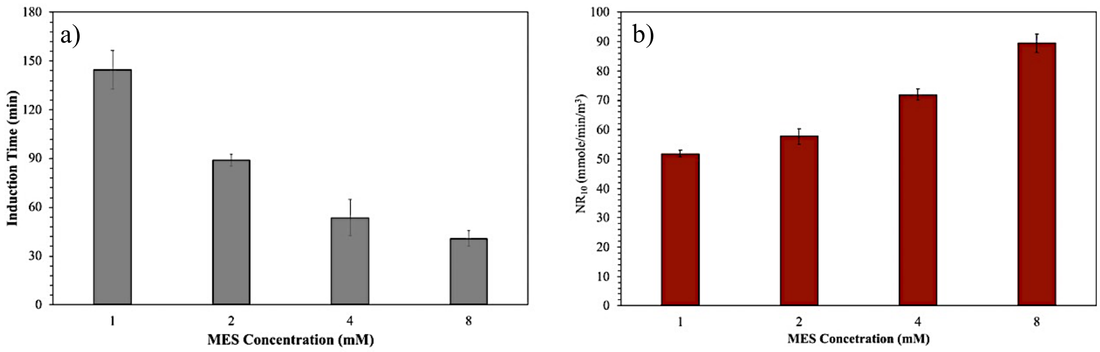

Figure 2.35 Gas hydrate formation induction time (a) and the normalized rate of gas hydrate formation (NR_{30}) at various MES concentrations (Inkong *et al.*, 2019b).

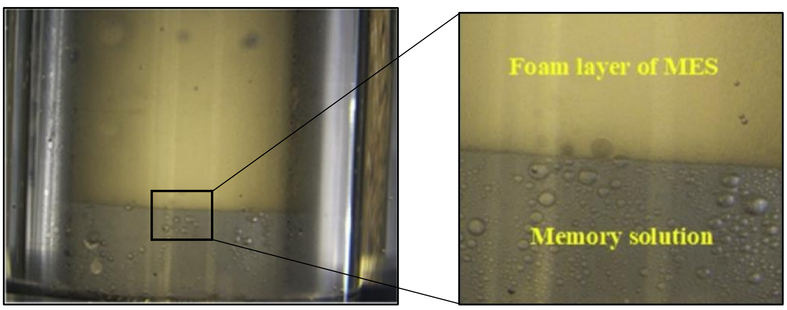

Figure 2.36 Foam formation after gas hydrate dissociation. (Inkong *et al.*, 2019b).

To address the issue of foam formation, researchers explored several nonionic surfactants, including Polyoxyethylene (n) lauryl ether, (EO3), (EO5), and Alkyl polyglycol ether (APG). When combined with SDS, these nonionic surfactants effectively reduced foam formation during hydrate dissociation, as illustrated in Figure 2.37. However, it's important to note that using only nonionic surfactants, methane hydrate could not be formed (Viriyakul *et al.*, 2021).

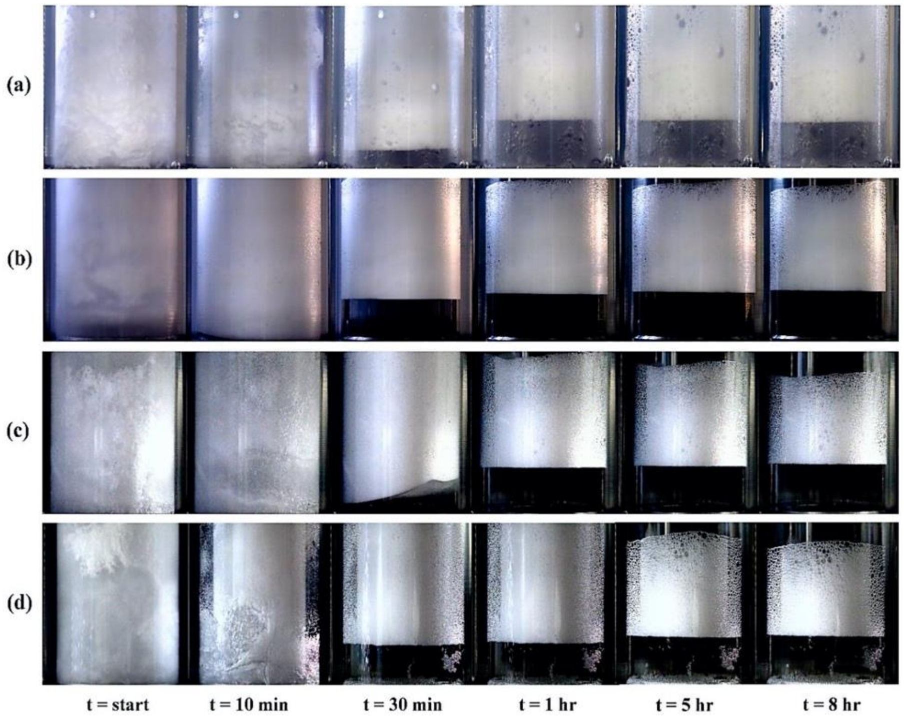

Figure 2.37 Foam formation during hydrate dissociation from hydrates formed in the presence of (a) 0.25 wt% SDS; (b) 0.25/0.25 wt% EO3/SDS; (c) 0.25/0.25 wt% EO5/SDS; (d) 0.25/0.25 wt% APG/SDS (Viriyakul et al., 2021).

2.9.2.2 Amino Acids

Due to the environmental toxicity and foam generation problems related to conventional surfactants, alternative solutions are sought, with amino acids emerging as a promising option. Amino acids, which possess surfactant-like properties due to their dual nature, featuring both a hydrophobic side chain and hydrophilic functional groups, have gained attention as a potential replacement for enhancing gas hydrates, Figure 2.38 (Bhattacharjee and Linga, 2021).

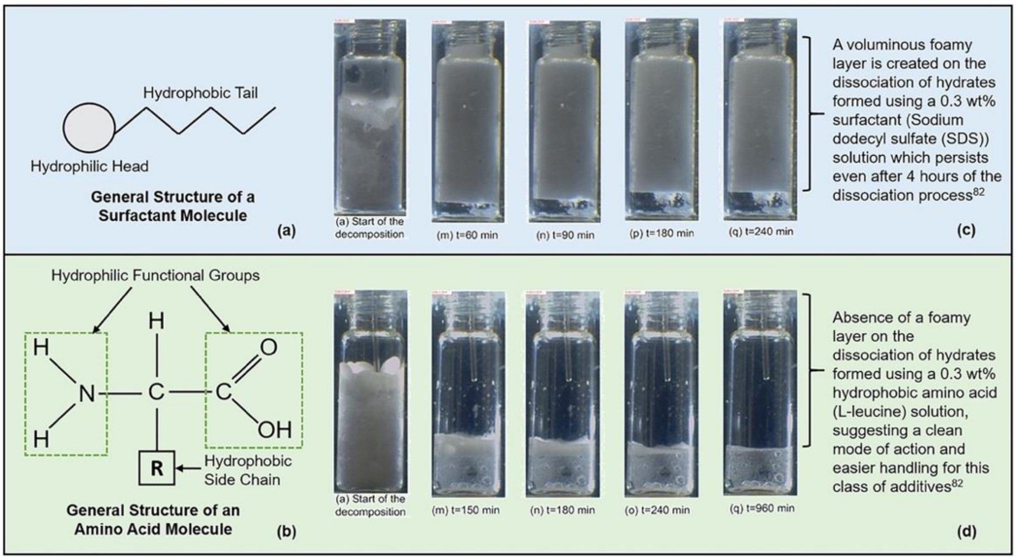

Figure 2.38 Hydrophobic amino acids vs. surfactants - molecular similarities and foam generation: (a) surfactant molecule, (b) hydrophobic amino acid, (c) foam from 0.3 wt% sds hydrate dissociation, (d) foam-free 0.3 wt% l-leucine hydrate dissociation (Bhattacharjee and Linga, 2021).

Nature encompasses over 500 amino acids, but the human genetic code directly encodes only 20 of them. These 20 amino acids serve as the building blocks for all proteins in your body. This graphic illustrates the structure of each of these amino acids and provides notation details for their representation, Figure 2.39 (Brunning, 2014). Among these 20 amino acids, several have been examined for their role in both methane and carbon dioxide hydrate formation, as outlined in Table 2.5 (Majid and Koh, 2021). However, the underlying mechanism or reasons for the varying performance of different amino acids have not been fully understood.

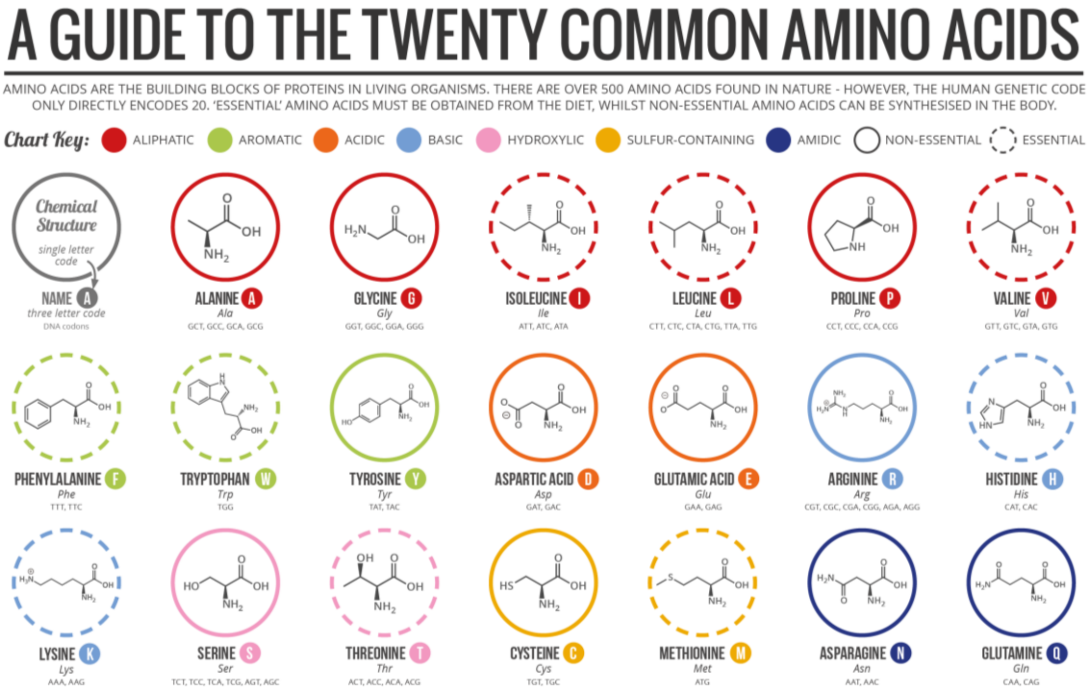

Figure 2.39 Twenty common amino acids and their distinct chemical properties (Brunning, 2014).

Table 2.5 Summary of studies on amino acid effects on hydrate formation kinetics (Majid and Koh, 2021)

amino acid	hydrate former	pressure (MPa)	temperature (K)
L-leucine, $C_6H_{13}NO_2$	methane	7.5	273
L-methionine, $C_5H_{11}NO_2S$	methane	5.3	275
	carbon dioxide	3.3	275
	methane/carbon dioxide	3.3	275
L-phenylalanine, $C_9H_{11}NO_2$	methane	5.3	275
	carbon dioxide	3.3	275
	methane/carbon dioxide	3.3	275
L-histidine, $C_6H_9N_3O_2$	methane	9.0–10.0	270–273
L-isoleucine, $C_6H_{13}NO_2$	methane	9.5	273
L-trytophan, $C_{11}H_{12}N_2O_2$	methane	10.0	275
	carbon dioxide	3.4–3.8	273–277
	methane/carbon dioxide	3.5–5.0	274

In terms of kinetic enhancement, amino acids demonstrate a similar potential for hydrate formation as surfactants. Veluswamy *et al.* (2016a) conducted a study investigating the impact of amino acid concentrations ranging from 0.1 to 0.5 wt%. Figure 2.40 illustrates methane uptake profiles and hydrate formation kinetic data at various leucine concentrations. Remarkably, leucine exhibits a distinct inflection point, beyond which the hydrate formation rate significantly increases compared to the initial nucleation rate.

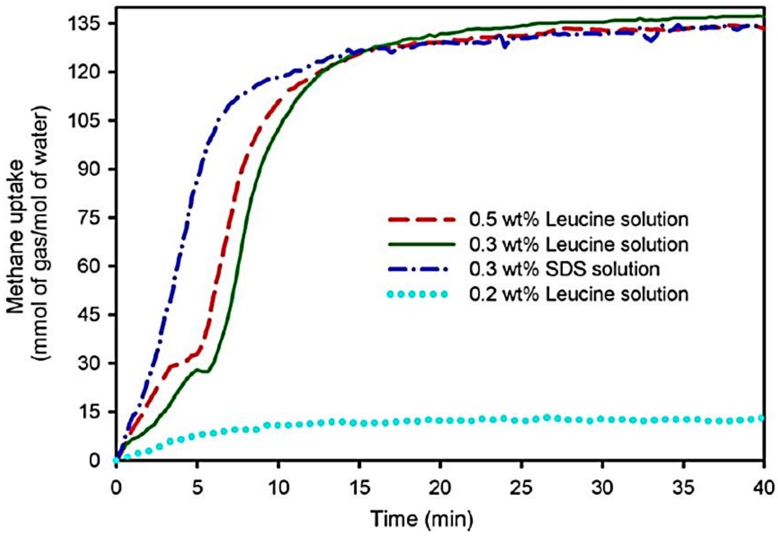

Figure 2.40 Methane uptake profiles in various solution systems, including SDS and amino acids at different concentrations (Veluswamy *et al.*, 2016a).

Hydrophobic amino acids have been suggested as potential candidates for Kinetic Hydrate Promoters (KHPs). Their hydrophobic side chains are believed to enhance gas dissolution, resulting in faster hydrate formation, as proposed by (Nguyen and Nguyen, 2017). When water mixes with hydrophobic amino acid, amino acid creates hydrophobic zones that prompt nearby water molecules align strongly to avoid these hydrophobic areas, creating localized water ordering akin to an empty cage or clathrate-like hydration shell. This setup attracts nonpolar gas molecules like methane, leading to increased gas density in these regions. This high density, coupled with the localized water, forms spots conducive to rapid hydrate formation as illustrate in Figure 2.41 (Bhattacharjee and Linga, 2021).

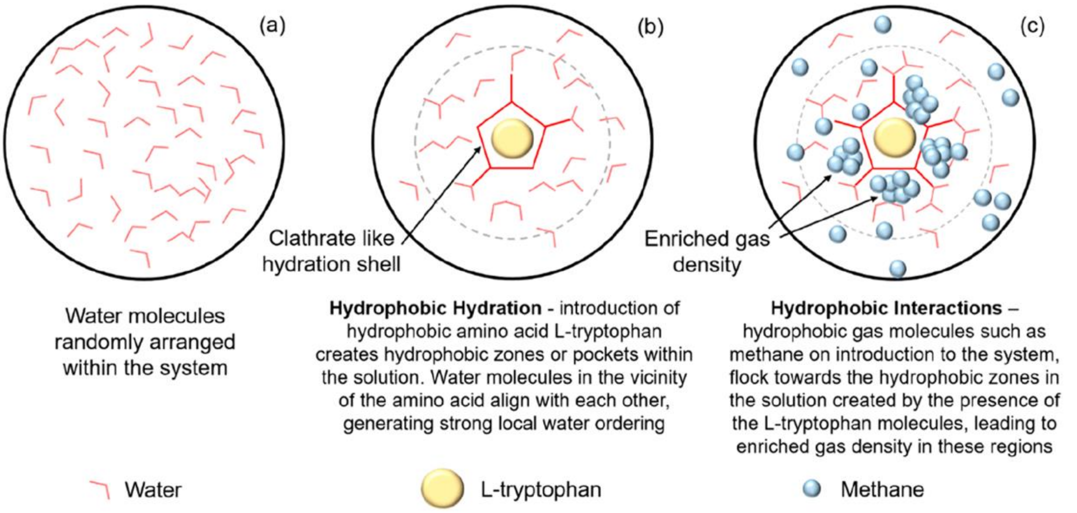

Figure 2.41 Hypothesis of the hydrophobic effect plays a significant role in promoting gas hydrate formation when a hydrophobic additive is presented (Bhattacharjee and Linga, 2021).

Hydrophobic amino acids can be classified based on their hydropathy index, which serves as a measure of hydrophobicity. A higher index value indicates increased hydrophobicity. Table 2.6 presents the hydropathy index values for different amino acids published by Kyte and Doolittle (1982).

Table 2.6 Hydropathy index of amino acids (Kyte and Doolittle, 1982)

Amino acid	Hydropathy index
Isoleucine	4.5
Valine	4.2
Leucine	3.8
Phenylalanine	2.8
Cysteine/ cystine	2.5
Methionine	1.9
Alanine	1.8
Glycine	-0.4
Threonine	-0.7
Tryptophan	-0.9
Serine	-0.8
Tyrosine	-1.3
Proline	-1.6
Histidine	-3.2
Glutamic acid	-3.5
Glutamine	-3.5
Aspartic acid	-3.5
Asparagine	-3.5
Lysine	-3.9
Arginine	-4.5

CHAPTER 3
EXPERIMENTAL

3.1 Objectives

1. To comprehensively investigate the impact of various amino acids and their hydrophobic characteristics on both CH_4 and CO_2 hydrate formation and dissociation kinetics, morphological analyses, and the evaluation of the reusability of the recovered solution.

2. To enhance the feasibility of hydrate-based technology related to energy storage and carbon capture and sequestration using CH_4 and CO_2 hydrate formation.
   (a) To form and store CH_4 hydrate at higher temperatures through the combination of THF and amino acids, aimed at reducing energy consumption during the hydrate formation process.
   (b) To optimize the hydrate formation crystallizer using a Design of Experiment methodology with the Face-Centered Central Composite Design response surface method (FCCCD-RSM) to strike a harmonious balance between efficient crystallizer utilization and operational effectiveness.
   (c) To resemble real-world CO_2 sequestration locations, 3.5 wt% NaCl was introduced into the hydrate formation process.

3.2 Materials and Equipments

3.2.1 Chemicals

1. Ultra-high purity CH_4 gas (99.99% from Linde Public Company, Thailand)
2. High–purity carbon dioxide gas (99.9% from Air Liquide Singapore Private Limited, Singapore)

3. Tetrahydrofuran (AR grade from ACL Labscan, Thailand)
4. Amino acid including L–Tryptophan (Trp), L–Methionine (Met), L–Leucine (Leu), L–Valine (Val), and L–Glutamic acid (Glu) (reagent grade, >98% (HPLC) from Sigma-Aldrich, Singapore)
5. sodium chloride (NaCl) (reagent grade, ≥99.0% from Sigma-Aldrich, Singapore)
6. Deionized water (Merck Millipore, U.S.A.)

3.2.2 Equipments

1. High Pressure Crystallizer (CR)
2. Personal Computer (PC)
3. Gas Supply Reservoir ®; Swagelok, Thailand
4. Pressure Transmitter (PT) with a 0.13 % accuracy within the range of 0 – 21 MPa; Cole Parmer®, model 68073-68074, Singapore
5. K-type Thermocouple with a 1.0 K accuracy; SL heater, Thailand
6. External Refrigerator (ER); Daeyang, Model RC-20, Korea
7. Data Logger (DL); Wisco Industrial Instruments, AI210, Thailand
8. Video camera (VC); OPTIKA® ITALY, Model C-HP, Italy
9. Real–time in situ Raman Instrument; W2 inovations, Sraman–532, U.S.A.

3.2.3 Softwares

1. AI-Utility and OD04; Wisco Industrial Instruments
2. Pro View; OPTIKA
3. SpectraSoft; W2 inovations
4. Origin Pro 2021b SR2; OriginLab Corporation
5. IBM SPSS 28; IBM
6. Design-Expert software V13.0; Stat-Ease Inc.

3.3 Experimental Apparatus and Procedures

3.3.1 Experimental Apparatus

Four different experimental setups were employed in this study, each serving various investigation objectives, including:

(1) CH_4 and CO_2 hydrate formation and dissociation kinetics and morphological studies, metastable zone analyses, and the evaluation of the reusability of the recovered solution.

(2) Hydrate palletization.

(3) Hydrate pallet stability for long-term storage.

(4) In situ Raman investigation.

In brief, the gas hydrate experimental setup consisted of a stainless-steel crystallizer equipped with or without a crystal-clear sapphire window. Additionally, a supply gas reservoir was connected to the hydrate crystallizer to enhance gas availability. The system's temperature was controlled using a circulating mixed glycol/water solution regulated by an external refrigerator. Pressure and temperature were monitored using pressure transmitters and thermocouples, and the data were recorded by a data logger system connected to a personal computer. Further details for each investigation are provided in the respective sections of this study.

3.3.2 Hydrate Formation of Kinetics and Morphological Studies

As mentioned earlier, there are different hydrate formation setups depending on the study objectives. In summary, for the hydrate formation process, various mixed solutions and solution volumes were loaded into the investigation crystallizers. Several experiment setups included the use of magnetic bars to create a stirring system inside the hydrate formation chamber. To prevent unwanted gas in the study system, methane gas was purged three times. Subsequently, the crystallizer was then cooled to the desired temperature. Once the temperature stabilizes, the study gases were introduced into the system until it reaches desirable pressure. Most of the experiments were carried out under constant conditions, with fixed solution and gas in the system. Real-time pressure and temperature were monitored and recorded for 10 hours until the pressure drop did not exceed 50 kPa for an hour. During hydrate formation, the pressure inside the crystallizer reduced due to gas consumption, and the temperature increased due to the observed exothermic reaction. In the morphological study, videos showing hydrate formation were recorded during the experiments. Additionally, in the in situ Raman investigation, a real-time in situ Raman instrument with an integration time of 3.0 seconds was connected to the reactor, providing ongoing data on hydrate formation. All experiments were repeated at least three times to confirm reproducibility. Additional specifics for each investigation can be found within the corresponding sections of this study.

The pressure and temperature data were employed to calculate the moles of gas consumed during the hydrate formation process ($\Delta n_{H,\downarrow}$) using Equation 3.1 (Babu *et al.*, 2013; Veluswamy and Linga, 2013).

$$\Delta n_{H,\downarrow} = n_{H,0} - n_{H,t} = \left(\frac{PV}{zRT}\right)_{G,0} - \left(\frac{PV}{zRT}\right)_{G,t} \tag{3.1}$$

The equation employs the following variables: $n_{H\ t}$, the moles of hydrate at time t; $n_{H,0}$, the moles of hydrate at time 0; P, the pressure of the crystallizer in kPa; T, the temperature of the crystallizer in Kelvin; V, the volume of the gas phase within the crystallizer in cm^3; Z, the compressibility factor based on Pitzer's correlation (Smith *et al.*, 2005); and R, the universal gas constant at 8314 $cm^3 \cdot kPa/mol \cdot K$. The subscripts G,0 and G,t correspond to the gas phase at time zero and time t, respectively.

To quantify the quantity of gas integrated into the hydrate structure relative to the volume of water in the system, the gas uptake and the conversion of water to hydrate was determined using Equation 3.2 and 3.3.

$$\text{Gas uptake (mol of gas /mole of water)} = \frac{\left(\Delta n_{H,\downarrow}\right)_t}{n_{H_2O}} \tag{3.2}$$

$$\text{water to hydrate conversion (\%)} = \frac{\left(\Delta n_{H,\downarrow}\right)_t \times \text{Hydration number}}{n_{H_2O}} \times 100 \tag{3.3}$$

In the context of the system, n_{H_2O} represents the moles of water present (in moles), while $\Delta n_{H,\downarrow}$, signifies the moles of gas consumed during hydrate formation. The hydration number denotes the quantity of water molecules necessary for each gas molecule to participate in the formation of the hydrate structure. In the case of the sII mixed CH_4-THF hydrate structure produced in our experiments, this value is determined to be approximately 5.67 (Veluswamy *et al.*, 2016c). Conversely, for the sI CO_2 hydrate, the hydration number is reported as 7.03 (Khandelwal *et al.*, 2020).

Three kinetic parameters were examined for the hydrate formation process, including the induction time (IT), which signifies the time needed for the initial hydrate nucleation to become observable through a temperature spike inside the crystallizer. The normalized hydrate formation rate (NR_t) for the first t minutes following the start of IT was calculated using Equation 3.4 (Veluswamy *et al.*, 2015).

$$NR_t \text{ (mmol/mol·min) or (v/v·hr)} = \frac{R_t}{V_{water}} \tag{3.4}$$

In the provided equation, V_{water} represents the volume of water (m^3 or mole) introduced into the crystallizer, and R_t is the rate of hydrate formation (expressed in m^3/hr, mmol/min,). This rate is computed by fitting the average methane uptake attributable to hydrate growth at each experimental condition against time for the initial t minutes subsequent to IT, utilizing the least squares method. The specific time duration of t minutes, yielding the optimal fit, is selected for rate quantification based on the gas uptake profiles associated with hydrate formation in all conducted experiments.

Variations in the quantity of hydrate formation can lead to distinct t_{90} values. To ensure comparability, a normalized time to reach 90% completion of hydrate formation, called $t_{90,norm}$, was calculated using Equation 3.5.

$$t_{90,norm} \text{ (min/(mmol/mol) or (min/(v/v)} = \frac{t_{90}}{\text{Gas Uptake}_{\text{at } 90\%}} \tag{3.5}$$

3.3.3 Hydrate Dissociation of Kinetics and Morphological Studies

Following the formation of methane hydrates, the dissociation process was initiated using thermal stimulation. The temperature was incrementally raised from the experimental temperature to the desired dissociation temperature, specifically reaching 308.2 K for sII CH_4-THF hydrate and 293.2 K for CO_2 hydrates. This marked the starting point, denoted as time zero, for the hydrate dissociation experiments. During the experiments, temperature and pressure were constantly monitored until all the hydrates had completely melted. These data were used to calculate the mole gas release at any time during the hydrate dissociation ($\Delta n_{H,\uparrow}$) utilizing Equation 3.6. (Siangsai *et al.*, 2015).

$$\Delta n_{H,\uparrow}\ (\text{mole}) = n_{G,t}\text{-}n_{G,0}=\left(\frac{PV}{zRT}\right)_{G,t} - \left(\frac{PV}{zRT}\right)_{G,0} \quad (3.6)$$

$n_{H\,t}$, the moles of hydrate at time t; $n_{H,0}$, the moles of hydrate at time 0. The subscripts G,0 and G,t correspond to the gas phase at time zero and time t, respectively.

Gas recovery was determined over time for each dissociation experiment using Equation 3.7,

$$\text{Gas recovery (\%)} = \frac{(\Delta n_{H,\uparrow})}{(\Delta n_{H,\downarrow})_{End}} \times 100 \quad (3.7)$$

In this equation, $\Delta n_{H,\uparrow}$ represents the moles of gas released from the hydrate structure during the dissociation process at any specific time, while $(\Delta n_{H,\downarrow})_{End}$ signifies the moles of gas consumed during the hydrate formation at the end of the experiments.

Differences in the amount of hydrate formation can result in varying times required for complete hydrate dissociation. To facilitate comparisons, a normalized time to achieve 90% completion of hydrate dissociation, denoted as $t_{90d,norm}$, was computed using Equation 3.5.

$$t_{90d,norm}\ (\text{min/\%})= \frac{t_{90d}}{\text{Total water to hydrate conversion}} \quad (3.8)$$

3.3.4 Hydrate Stability Test

The initial steps mirrored those of the previous hydrate formation section. However, once the hydrates had fully developed, the excess gas was vented out, and the system's temperature was lowered to 273.2 K to prevent hydrate dissociation during the transfer phase. The obtained hydrates were subsequently compacted into pellets using an electric hydraulic pump. These hydrate pellets were then placed within a pre-cooled stainless-steel vessel, which was loaded into a refrigeration system. The storage conditions were established at 283.2 K and atmospheric pressure. Temperature and pressure fluctuations during the storage period were continually monitored and recorded at 1-minute intervals for a duration of 30 days. The calculation for gas release was the same as hydrate dissociation.

3.3.5 in situ Raman Spectroscopy Investigation

The Raman spectra obtained during the hydrate formation and dissociation experiments were collected with an integration time of 3.0 seconds and a time interval of 5.0 minutes. The analysis of the Raman spectra was carried out using the Origin Pro 2021b SR2 software, made available through the National University of Singapore's license. The Raman spectra were first processed by correcting the baselines. The study then concentrated on specific wavenumber ranges to investigate gases and water molecules. In the case of water molecules, the spectra revealed five sub-bands that were observed and subsequently deconvoluted using a Gaussian function. Because the shape and position of the O–H stretching spectra can be affected by changes in the hydrogen bond network, a thorough analysis was carried out to examine the intensity and wavenumber of these sub-bands. Similarly, the study delved into the investigation of peak intensity and wavenumber for gases spectra. Furthermore, the introduction of ratios between various specific bands aimed to enhance the understanding of the changes in Raman spectra during the hydrate formation and dissociation processes. Additional details regarding each investigation can be found in the respective sections of this study.

3.3.6 Optimizing Hydrate Formation with Design of Experiments (DOE)

To enhance the research framework and economize on process expenses, we constructed an RSM model employing a Face-Centered Central Composite Design (FCCCD). The selection of FCCCD was driven by its cost-effectiveness, versatility in accommodating both linear and nonlinear relationships, and its effectiveness in optimizing results while reducing the need for a large number of experimental runs. This optimization process was executed using Design-Expert software V13.0 (Stat-Ease Inc). The experimental setup revolved around three critical factors: gas-liquid interface areas, solution volume, and the percentage of excess gas. To overcome certain limitations, we transformed the study's variables into adjustable parameters for more precise control, namely, (A) crystallizer length, (B) solution volume to crystallizer volume ratio (V_S/V_R), and (C) volume of supplementary gas reservoir (V_{res}). Further specific details were written in corresponding sections of this study.

3.3.7 High-Performance Liquid Chromatography (HPLC) Investigation

A 1 mL standard solution containing 5.56 mol% THF, both with and without 0.25 wt% methionine, were initially prepared using the same procedure employed for hydrate formation. while 1 mL of reused solution was sampling from each cycle of hydyrate formation. Subsequently, these solutions underwent dilution and filtration through a 0.22 µm filter to remove unwanted particles for calibration and application. Then a 50 µL injection of a prepared solution containing the amino acid mixture was chromatographed onto a C18 column using the setup chromatographic conditions. Further specific details were written in corresponding sections of this study.

CHAPTER 4
ROLES OF AMINO ACID HYDROPHOBICITY ON METHANE-THF HYDRATES IN THE CONTEXT OF STORAGE AND STABILITY

4.1 Abstract

This report reveals the success of the formation of mixed methane-THF hydrates at room temperature (298.2K) and a pressure of 9.2 MPa equipped with a hybrid stirring in the presence of amino acids as kinetic promoters. Five different amino acids in increasing order of hydrophobicity: glutamic acid, valine, leucine, methionine, and tryptophan, were used to investigate their effects on methane uptake, formation, and dissociation kinetics. The addition of hydrophobic amino acids (tryptophan, methionine, and leucine) promotes the hydrate formation to completion, which doubly increases the methane uptake compared to that without amino acids and with hydrophilic amino acids (glutamic acid and valine) at the same condition. The results indicate that the hydrophobicity has a positive contribution to the methane uptake by creating a hydrophobic area, enhancing hydrate growth to completion. Moreover, the time taken to complete hydrate by 90 percent has a negative correlation to the molecular weight of the amino acids. The morphological studies demonstrate that the hydrates with hydrophobic amino acids were more consolidated than the addition of hydrophilic amino acids. Lastly, the hydrates with hydrophobic amino acids show excellent stability for 30 days even if they are stored at a temperature higher than their equilibrium temperature at atmospheric pressure. The small amount of gas lost was due to intrinsic loss only. This opens the possibility for cost-reduction for methane hydrate in commercialization.

Keywords: Solidified Natural Gas, Hydrate Formation, Amino acid, Hydrophobicity, and Stability.

4.2 Introduction

The demand for natural gas (NG) has been rapidly expanding. Natural gas usage is expected to rise 15% over the next decade, according to the International Energy Agency (International Energy Agency, 2021). The fundamental reason for this is that NG emits 30% to 50% less carbon dioxide per unit of energy output than coal and fuel oil (U.S. Energy Information Administration, 2021). However, both in terms of safety and cost, natural gas storage and transportation are difficult. At a high pressure of 20 to 30 MPa, NG can be compressed into compressed natural gas (CNG). However, due to the high pressure, it poses a safety risk (Veluswamy *et al.*, 2018). In addition, the production of liquefied natural gas (LNG) is an expensive process. The majority of LNG investments are made in the cooling system. The temperature is lowered to 113 K, resulting in cryogenic natural gas liquid. Furthermore, the recovery of gas is harmed by the change in gas quantity caused by boil-off gas, which makes LNG challenging for long-term storage (Veluswamy *et al.*, 2018). Solidified natural gas technology (SNG) has been developed as a strong and feasible alternative to avoid the above concerns. SNG has advantages in terms of storage energy requirements because it may be stored at milder conditions than other technologies. SNG also demonstrates the ease of gas recovery as well as safety against pressure issues. As the result, SNG has emerged as a promising natural gas storage option (Veluswamy *et al.*, 2018).

SNG works on the principle that suitable pressure and temperature induce the hydrogen bond of water molecules creating ice cages with molecules of gas trapped inside (Sloan Jr and Koh, 2007). Surprisingly, this idea has been brought from the blockage of natural hydrate issue found in the transportation of NG through the pipelines. Thus, previous studies focused on inhibiting natural hydrate formation. Recently, the paradigm has been shifted to form hydrate synthetically. Because of its high capacity, it may be used in a variety of applications, including gas separation (Partoon *et al.*, 2018; Sun *et al.*, 2014), energy storage (Siažik and Malcho, 2017), CO_2 capture (Babu *et al.*, 2014; Dashti *et al.*, 2015), and desalination (Babu *et al.*, 2018; Kang *et al.*, 2014; Seo *et al.*, 2019). The hydrate can store up to 170 volumes of gas per volume of hydrate for energy storage. The operational conditions, however, are still pricey. To have adequate formation driving force for hydrate nucleation, it must be compressed up to 10 MPa and chilled to 274.2 K (Khurana *et al.*, 2017). The ability to scale up hydrate technology to an industrial level still has to be improved.

The most often seen hydrate structures are sI, sII, and sH. sII has been demonstrated to be a hydrate structure capable of formation at temperatures close to ambient and at lower pressures than sI hydrate (Veluswamy *et al.*, 2018). The formation of sII hydrates can be facilitated by the addition of a thermodynamic promoter capable of extending the hydrate phase equilibrium. Tetrahydrofuran (THF) has been shown as a good promoter for shifting the phase equilibrium, resulting in the strongest hydrate formation driving force and the ability to form at higher temperatures (Beheshtimaal and Haghtalab, 2018; Lee *et al.*, 2012). This beats sI hydrates in terms of gas uptake, rate of formation, and energy consumption at high temperatures of hydrate formation. However, forming sII at temperatures close to ambient temperature reduces the kinetics (induction time (IT), hydrate formation rate (NR_{30}), and the time required to complete 90% of the hydrate formation (t_{90})) due to the decrease in the gas dissolution. To address this issue, the solubility of the gas in a solution must be increased (Veluswamy *et al.*, 2016b). One possibility is to maximize gas and liquid mass transfer mechanically. Increasing the contact duration and area of contact between liquid and gas can be accomplished by a reactor design (Englezos and Lee, 2005; Luo *et al.*, 2007; Mech *et al.*, 2016; Verrett *et al.*, 2012; Vysniauskas and Bishnoi, 1983; Zhong *et al.*, 2015). Nonetheless, the mechanical method is weakened by its energy needs (B.-H. Shi *et al.*, 2017). Another way is to add a kinetic promoter into the solution. This decreases the interfacial tension between gas and liquid, allowing more gas dissolution resulting in accelerating nucleation (Bavoh *et al.*, 2018; Chaturvedi *et al.*, 2018; Okutani *et al.*, 2008; Veluswamy *et al.*, 2016a). Sodium dodecyl sulfate (SDS), the most often used anionic surfactant, enhances the kinetics of hydrate formation (Veluswamy *et al.*, 2016b). Nonetheless, the unwanted foam is formed after hydrate decomposition (Inkong *et al.*, 2019b; Pandey *et al.*, 2018). As the result, alternative foam-free kinetic promoters are now being studied.

Recently, amino acids have garnered attention, as they are protein-based compounds and also have hydrophobic and hydrophilic components similar to surfactants. Amino acids share many of the same advantages as surfactants, but they are biocompatible and biodegradable without foam formation (Asheesh Kumar *et al.*, 2019a; Sa *et al.*, 2013). The addition of amino acids shortens the induction time of 5.56 mol% THF mixed methane hydrates and accelerates the rate of hydrate formation at ambient temperature (Jeenmuang *et al.*, 2021). Previous research reported that the side chain of amino acids plays an important role in the hydrate formation. Hydrophobic amino acids promote the rate of methane hydrate formation (Cai *et al.*, 2017), while hydrophilic amino acids slow down the kinetics (Bhattacharjee and Linga, 2021; Liu *et al.*, 2015). However, the suitable order of the amino acid hydrophobicity and other properties that might affect the hydrate formation has not been fully explained.

In this work, mixed methane-THF hydrate formation was reported at room temperature (298.2 K) and 9.2 MPa with 5.56 mol% THF as a thermodynamic promoter incorporated with amino acids as a kinetic promoter in a hybrid stirred reactor configuration. Five different amino acids, glutamic acid, valine, leucine, methionine, and tryptophan were used. The effects of amino acid hydrophobicity on the mixed-promoter methane hydrate forming system were clarified. The kinetic and morphological studies of hydrate formation and dissociation were elucidated. In addition, a 30-day stability test was performed on the synthetic hydrates at a storage temperature of 283.2 K.

4.3 Experimental

4.3.1 Materials

Ultra-high purity methane (99.99 %) supplied by Linde Public Company, Thailand was used for hydrate formation with distilled deionized water. Tetrahydrofuran (THF), AR grade, from RCI Labscan, Thailand, was utilized as the promoter. Amino acids as kinetic promoters were purchased from Sigma-Aldrich, Singapore. The following list in Table 4.1 contains the potential amino acids that were used in this experiment.

Table 4.1 Structure of the candidate amino acids

Name	Abbreviation	Molecular Structure	Molecular Weight	Purity
L-Glutamic acid	Glu	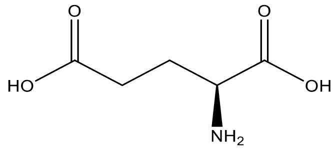	147.13	≥ 99%
L-Valine	Val	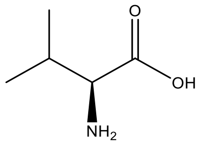	117.15	≥ 98%
L-Leucine	Leu	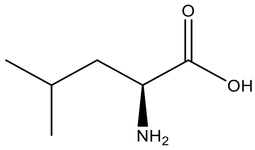	131.17	≥ 98%
L-Methionine	Met	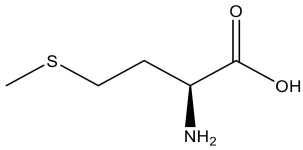	149.21	≥ 98%
L-Tryptophan	Trp	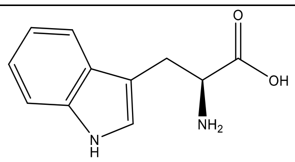	204.22	≥ 98%

4.3.2 Hydrate Formation and Dissociation for Kinetic and Morphological Studies

Two different crystallizers were used in this work. First, a stainless-steel crystallizer was used to investigate the kinetics of hydrate formation and dissolution. Second, a sapphire crystallizer was used in the hydrate morphological study. The equipment and procedure were modified from the previous work (Jeenmuang *et al.*, 2021). In short, an aqueous solution containing 5.56 mol% THF with the addition of amino acid was placed in a batch-type crystallizer equipped with a stirring system. The operating temperature was set at 298.2 K, with excess methane feed set at 9.2 MPa (Bhattacharjee *et al.*, 2020b; Veluswamy *et al.*, 2017a). To induce the hydrate nucleation, the hybrid stirred configuration was added. Stirring started at the beginning of the methane feed, and it was stopped when the first hydrate nucleation was observed (Bhattacharjee *et al.*, 2020b; Veluswamy *et al.*, 2017a). After the hydrate formation, the system temperature was then increased to 308.2 K to dissociate the hydrate structure. The temperature and pressure were monitored and recorded for 10 hours until the pressure drop was not over 100 kPa for an hour. Each experiment was triplicated to ensure reproducibility. In the morphological study, the video showing hydrate formation and dissociation were recorded during the experiments.

4.3.2 Hydrate Stability Test

The hydrate stability investigation was separated into two sections: the production of SNG hydrate pellets and the 30-day stability test. To begin, the hydrate pellets were formed with 100 cm^3 of 5.56 mol% THF and amino acids at 298.2 K and 9.2 MPa using a 370-cm^3 hydrate pelletizing crystallizer as shown in Figure 4.1 (a). The temperature was controlled by the external refrigerator (ER, Model NESLAB RTE7, Thermo Fisher Scientific, U.S.A.), which circulated the coolant, mixed ethylene glycol, and water, through the crystallizer jacket. The temperature and pressure were detected using a K-type thermocouple (TC) with a 1.0 K accuracy and a pressure transmitter (PT) with 1% accuracy within the range of 0 to 10 MPa (Model ZG-PT9200, ZEGA, Thailand). The thermocouple and pressure transducer were both connected to a data logger (DL, 4xthermocouple Phidget and VINT Hub Phidget, Phidget, Canada) that was connected to a personal computer (PC). The record was continued until the pressure was stable or until 5 hours of the experiment. After complete hydrate formation, the excess methane was then vented out, while the system temperature was decreased to 273.2 K to prevent the hydrate dissociation during the transfer step. The obtained hydrates were then pelletized using an electric hydraulic pump equipped with a piston (Model L42078A1, Hiwin Mikrosystem Corp., Taiwan). The mass of the hydrate pellet was about 100.0 ± 5.0 g with a size of 4.0 cm in diameter and 9.5 ± 0.5 cm long. Subsequently, the hydrate pellet was placed in a 290 cm^3 stainless steel vessel, which was pre-cooled to 273.2 K. The vessel was loaded into a refrigeration system. The storage condition was set at 283.2 K and atmospheric pressure, Figure 4.1 (b). The temperature and pressure changes during the storage were monitored and recorded at 1-minute interval for 15 days using the same model equipment as in previous work (Jeenmuang *et al.*, 2021). Moles of gas released and percentage loss were calculated using equations (4.1) and (4.2) respectively:

Mole of gas released at any given time ($\Delta n_{H,\uparrow}$)

$$\Delta n_{H,\uparrow} = n_{H,t} - n_{H,0} = \left(\frac{PV}{zRT}\right)_{G,t} - \left(\frac{PV}{zRT}\right)_{G,0} \tag{4.1}$$

$$\%\ \text{methane released} = \frac{(\Delta n_{H,\uparrow})}{(\Delta n_{H,\downarrow})_{End}} \times 100 \tag{4.2}$$

where $\Delta n_{H,\uparrow}$ is moles of released gas from hydrates during the hydrate stability test at any given time. $(\Delta n_{H,\downarrow})_{End}$ is moles of gas consumption at the end of hydrate formation. V is the volume of gas phase available inside the storage vessel. T and P are the measured temperature and pressure at time 0 and time t in the crystallizer. The compressibility factor, z, can be obtained from Pitzer's correlation.

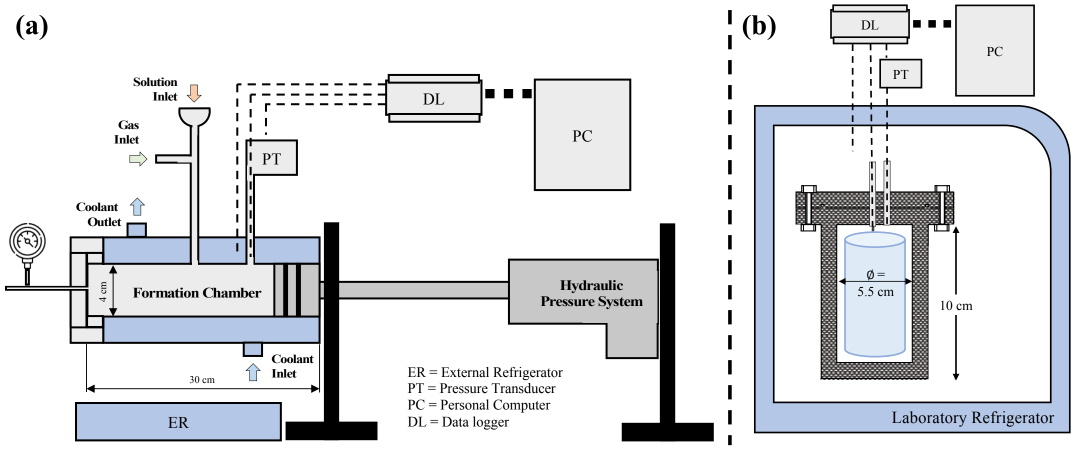

Figure 4.1 Schematic of stability experiment system; (a) hydrate pelletizing crystallizer and (b) the refrigerating system for stability test.

4.3.4 Methane Solubility at Different Pressures Measurements

The equipment and procedure of the solubility measurement were modified from the previous work (Bhattacharjee *et al.*, 2017). The experiments were performed in a 163-mL batch-type reactor equipped with a stirring system. A pressure transducer and data logger system were installed in the system to record the pressure drop caused by gas solubility in an aqueous solution. 100 mL of aqueous solution (pure water or 0.03 wt% tryptophan solution) was placed in a reactor and kept undisturbed for 30 min in order for the system to reach thermal equilibrium (experiments were carried out at room temperature, 298.2 K). Methane gas was then passed into the reactor at a relatively constant flow rate and time until the desired experimental pressure was reached. The dissolution of gas in an aqueous solution was then facilitated by stirring at 900 rpm. When the pressure inside the reactor stabilized, i.e., the pressure drop stopped, it was assumed that the solution had been saturated with methane gas, and the final pressure was recorded as the equilibrium pressure. The equilibrium pressure and concentration of methane in solution phase was then plotted and fitted to obtain Henry's constant.

The methane solubility (S_g) (mol/dm^3) can be calculated by equation (4.3)

$$S_g = \frac{\text{moles methane dissolved (mol)}}{\text{Volume of solution (dm}^3\text{)}} \tag{4.3}$$

Henry's constant (K_H) for methane (mol/dm^3·MPa) is obtained from equation (4.4)

$$K_H = \frac{S_g}{P_g} \tag{4.4}$$

where P_g is an equilibrium pressure of methane in gas phase (MPa), which also equals the slope of the graph plotted between equilibrium pressure (P_g) and methane solubility (S_g).

4.4 Result and Discussion

Room-temperature (298.2 K) methane hydrate formation is firstly conducted with a mixture of 5.56 mol% THF in water at 8 MPa. Figure 4.2 (a) shows that there is no methane uptake during 10 hours of operation. This might be due to an insufficient driving force to form hydrates. The operating pressure is then increased to 9.2 MPa at the same temperature to increase the driving force; however, the same result is observed. The forming system is modified by the installation of the hybrid stirring system using a magnetic stirrer with a speed of 500 rpm. The intention is to increase the gas-liquid mass transfer, which speeds up the hydrate nucleation (Veluswamy *et al.*, 2017a). As the result, the mixed methane-THF hydrates are successfully formed at 298.2 K and 9.2 MPa, as shown in Figure 4.2 (b). The methane uptake is at 50.69 ± 2.51 volume of gas (STP)/volume of water (v/v), which is equivalent to 62.72 ± 1.46 % water to hydrate conversion. This is half of that from a system operating at 293.2 K and 8 MPa without stirring (101.91 ± 1.40 v/v and 92.44 ± 0.80 % water to hydrate conversion), as described in Figure 4.3 (Veluswamy *et al.*, 2016b). This difference is caused by the different driving forces applied from 9.25 K and 5.88 MPa to 5.00 K and 4.77 MPa, Figure 4.4. This decrease in temperature and pressure driving forces directly reduces methane dissolution in the mixed THF water solution (He *et al.*, 2017; LibreTexts, 2022). Moreover, hydrate formation is an exothermic process (Sloan Jr, 2003), increasing the formation temperature favors a reverse reaction resulting in lower hydrate formation. To address this issue, a kinetic promoter is introduced. Five different amino acids are used as kinetic promoters, including glutamic acid (Glu), valine (Val), leucine (Leu), methionine (Met), and tryptophan (Trp). Their effects on the mixed methane-THF hydrate formation, hydrate morphology, and stability are presented below.

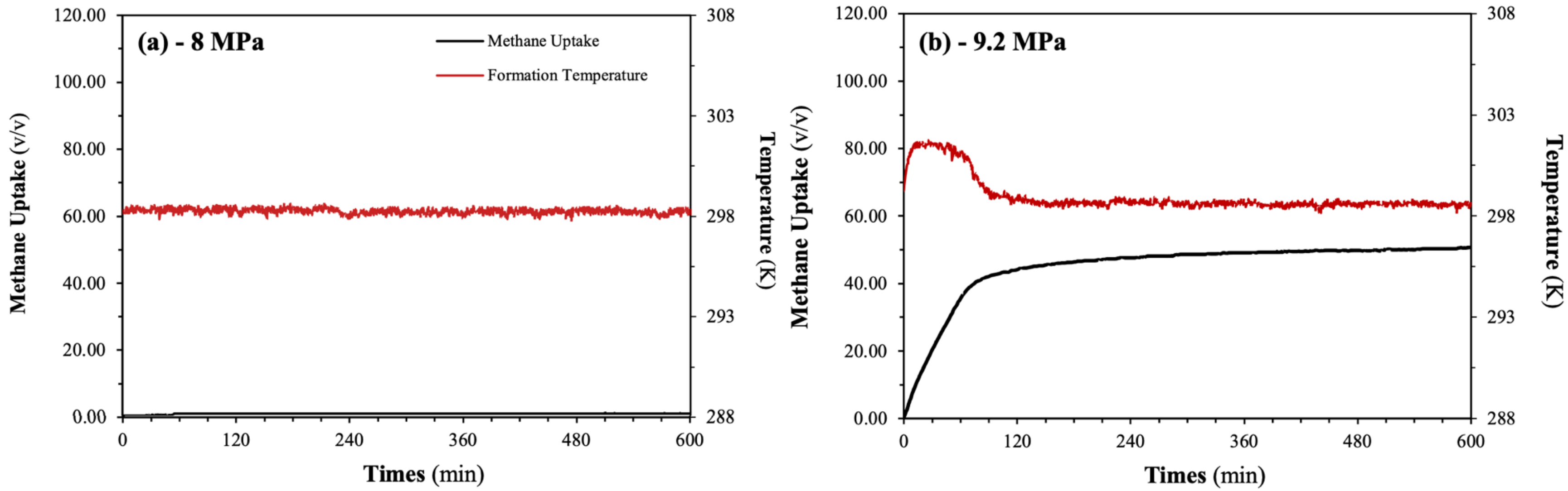

Figure 4.2 Methane uptake and temperature profile of the hydrate formation system consisting of 5.56 mol% THF at (a) 298.2 K and 8 MPa and (b) 298.2 K and 9.2 MPa with a stirring system.

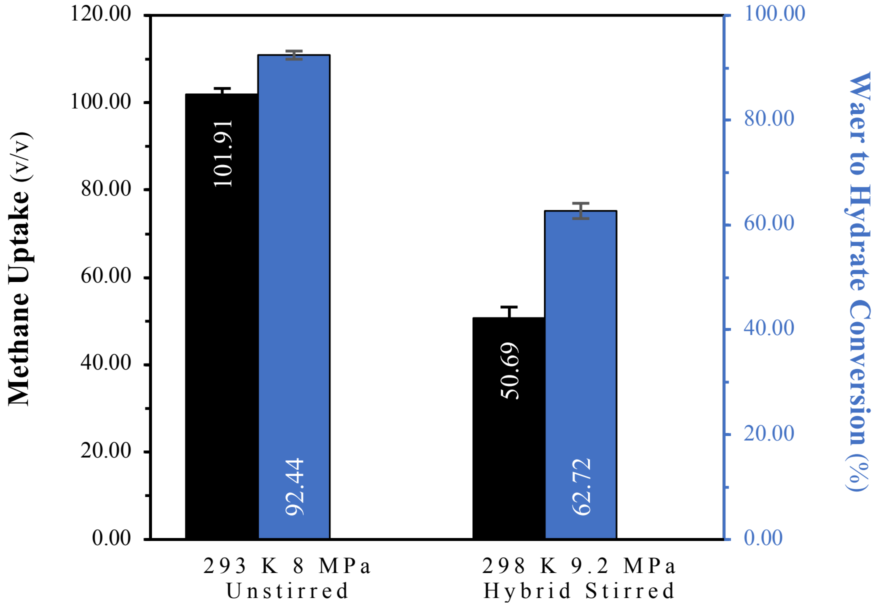

Figure 4.3 Comparison of methane uptake and water to hydrate conversion of hydrate formation systems consisting of 5.56 mol% THF at 293.2 K and 8 MPa without stirring and at 298.2 K and 9.2 MPa with a stirring system (Jeenmuang *et al.*, 2021).

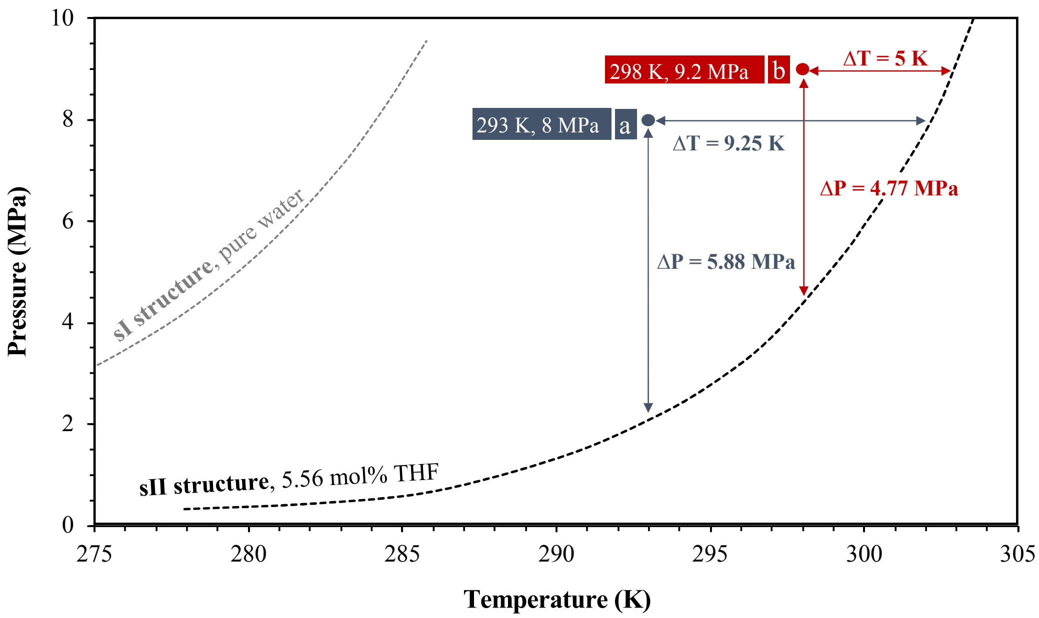

Figure 4.4 Pressure and temperature plot showing driving forces used at different formation conditions of (a) 293 K and 8 MPa and at (b) 298 K and 9.2 MPa.

4.4.1 Effects of Amino Acids on Mixed Methane Hydrate Formation

A stainless-steel crystallizer was used to investigate the effect of amino acids on the methane hydrate formation, including the methane uptake and the formation kinetics. Different concentrations of amino acids were added to a mixture of 5.56 mol% THF in deionized water. The operating condition was set at 298.2 K and 9.2 MPa with a 500-rpm hybrid stirring, which was applied until the first nucleation was observed.

4.4.1.1 Methane Uptake

The methane uptake and water to hydrate conversion of the hydrates formed by the addition of five amino acids at different concentrations were calculated. The mean and standard deviation of triplicated experiments are presented in Figure 4.5 (a). The methane uptake and water to hydrate conversion with the addition of glutamic acid (Glu) in Figure 4.5 (a1) show that the Glu concentration has no effect on the methane uptake. The addition of 0.125, 0.25, and 0.5 wt% Glu results in 48.70 ± 1.47, 46.52 ± 2.24, and 48.22 ± 2.23 v/v, respectively. These methane uptakes are about 60% water to hydrate conversion, which is similar to that of the system with only 5.56 mol% THF. Changing Glu to valine (Val) hardly affects the results much. Figure 4.5 (a2) shows that the conversions at all Val concentrations are about 60%, which is indistinguishable from that without the amino acid. Similarly, the addition of leucine (Leu) (Figure 4.5 (a3)) at 0.125 wt% does affect the methane uptake and the conversion. Increasing the Leu concentration to 0.25 wt%, surprisingly, enhances the conversion to about 90%. However, a further increase in the Leu concentration to 0.5 wt% loses the promoting effect. This suggests that a suitable concentration of Leu is essential. Too low Leu concentration does not have enough promoting effect, while too high also has a detrimental effect. This behavior is consistent with the previous report (Jeenmuang *et al.*, 2021) and other kinetic promoters (e.g., sodium dodecyl sulfate (SDS)) reported by Veluswamy *et al.* (2016b). Likewise, the addition of low methionine (Met) concentration (0.125 wt%) does not enhance the conversion much, 68.56 ± 0.63%, while, at higher concentrations (0.25 wt% and 0.5 wt%), the conversions are in the range of 93-94%, Figure 4.5 (a4). Note that tryptophan (Trp) concentration is used at 0.03, 0.05, and 0.125 wt%, different from the other amino acids, which are at 0.125, 0.25, and 0.5

wt%. The reason is that the concentration of Trp higher than 0.125 wt% does not show any difference in the methane uptake and the conversion. Therefore, the lower concentrations are used, Figure 4.5 (a5). Remarkably, Trp promotes both methane uptake and conversion at all concentrations. The conversions are achieved at 95.56 ± 0.29, 95.26 ± 0.13, and 95.33 ± 0.28% for the concentrations at 0.03, 0.05, and 0.125 wt%, respectively.

The effect of amino acids on methane uptake is plotted in Figure 4.5 (b). It shows that the methane uptakes from the addition of amino acids with different concentrations are separated into two groups. The methane uptake of the first group (Group A) is clearly higher than that of THF. On the other hand, the methane uptake of the other group (Group B) is comparable to that of THF. Group A consists of all concentrations of Trp, 0.25 wt% Leu, and 0.25 and 0.5 wt% of Met, while there are 0.125 and 0.5 wt% of Leu, 0.125 wt% of Met, and all concentrations of Glu and Val in Group B. The means of the methane uptake of the amino acids in Group B are close to that of THF but the deviation (SD) of each amino acid is different. It is questionable whether the addition of amino acids in Group B affects the methane uptake. A statistical test of Turkey-Kramer test was then utilized to confirm the effects of the amino acids in Group B. The test is to compare the methane uptake means of every amino acid to the means of the experiments with THF. The methane uptake means differences between each amino acid and THF, standard error, and P-value are presented in Table 4.2. Note that, a positive value of mean difference means the uptake mean of the system with THF is higher than that with an amino acid, while the opposite is true for a negative value. The methane uptake with THF is higher than that with Glu and Val, 2.88 and 0.01 v/v, whereas that with Leu or Met is lower, 3.50 and 10.07 v/v. The P-values are also provided in the table. The methane uptakes with Glu, Val, and Leu have P-values higher than 0.05, implying that their methane uptake means are not significantly different from those with THF at the confidence level of 95%. Only Met has a P-value lower than 0.05, referring to a statistically significant difference in the methane uptake means compared to that with THF. This confirms that the addition of 0.125 wt% Met does promote methane uptake, while the rest does not.

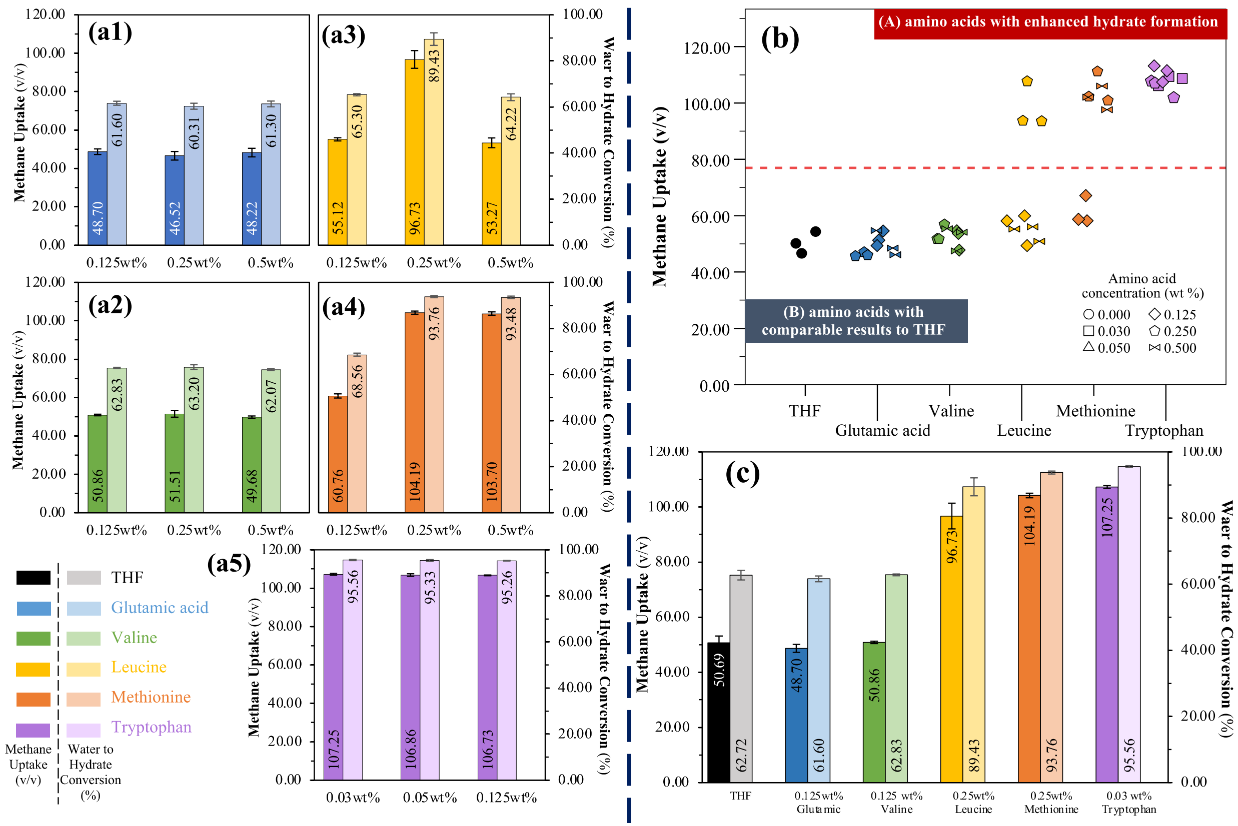

Figure 4.5 Methane uptake and water to hydrate conversion on the 298.2 K and 9.2 MPa hydrate forming systems with different amino acids and concentrations at 600 min after hydrate nucleation: (a1) Glu, (a2) Val, (a3) Leu, (a4) Met, and (a5) Trp. Comparison between 5.56 mol% THF with 5.56 mol% THF + amino acids at all concentrations (b). Comparison between 5.56 mol% THF with 5.56 mol% THF + amino acids with their optimum concentration (c).

Table 4.2 Statistical results of the test on mean differences between methane uptakes of THF and different amino acids in group B (Glu and Val at all concentrations, 0.125 and 0.5 wt% Leu and 0.125 wt% Met) by Tukey-Kramer test

Comparison		Mean Difference	Standard Error	*P*-value
THF	Glutamic acid	2.88	1.40	0.270
	Valine	0.01	1.40	1.000
	Leucine[a]	-3.50	1.48	0.159
	Methionine[b]	-10.07	1.71	<0.001*

Based on observed means, the error term is Mean Square (Error) = 4.402.

* The mean difference is significant at the 0.05 level.

[a] Leucine at 0.125 and 0.5 wt%

[b] Methionine at 0.125 wt%

In contrast, Group A consists of amino acids that promote the methane uptake. To further see whether each promoter affects the uptake to a different extent, the Turkey-Kramer test was again applied to differentiate their effects. Table 4.3 shows the result of the Turkey-Kramer test. The mean of the methane uptake with Leu is lower than that with Met or Trp, about 7.22 and 10.34 v/v, while that with Met is lower than Trp. Their methane uptake means are significantly different from each other, confirmed by their P-values lower than 0.05. Therefore, the effect of amino acids on the methane uptake can be arranged in increasing order of Leu, Met, and Trp.

Table 4.3 Statistical results of the test on mean differences between methane uptakes of amino acids in group A (0.25 wt% leucine, 0.125 and 0.25 wt% methionine and tryptophan at all concentrations) by Tukey-Kramer test

Comparison		Mean Difference	Standard Error	*P*-value
Leucine	Methionine	-7.22	1.55	0.001*
	Tryptophan	-10.34	1.46	<0.001*
Methionine	Tryptophan	-3.12	1.15	0.041*

Based on observed means, the error term is Mean Square (Error) = 4.788.

* The mean difference is significant at the 0.05 level

[a] Leucine at 0.125 and 0.5 wt%

[b] Methionine at 0.125 wt%

In summary, the addition of Glu and Val does not affect the methane uptake regardless of their concentrations. The addition of 0.25 wt% Leu has the promoting effect. The addition of Met and Trp promotes the methane uptake at all studied concentrations. The methane uptakes from the experiments without and with amino acids at their best condition (the highest methane uptake for Leu, Met, and Trp while the lowest concentration for Glu and Val) are plotted in ascending order of their promoting effect (methane uptake), as shown in Figure 4.5 (c).

To rationalize the effect of amino acids on the methane uptake, the hydrophobicity ranked by Trinquier and Sanejouand (1998) is introduced. Their hydrophobicity was made from the statistical analysis using an averaged-and-weighted-score calculation from 43 different methods on the data collected from literatures. It is more reliable than the other hydrophobicities (Kyte and Doolittle, 1982; Moon and Fleming, 2011; Wimley and White, 1996), which may have inconsistent measurements. The promoting effects of five different amino acids in Figure 4.5 (c) are followed the hydrophobicity in ascending order, starting from Glu, Val, Leu, Met, and Trp.

The role of amino acid in the sI methane hydrate formation has been proven as a kinetic promoter as it does not occupy the cavity of hydrates (Lee *et al.*, 2012). So, it would not shift an equilibrium curve on a phase diagram as a thermodynamic promoter does. To make sure that it behaves in the same manner in the sII hydrate formation, the equilibrium data from the forming systems with two different amino acids, Glu and Trp, are plotted in order to compare with the data obtained from the methane-5.56%THF-water system, Figure 4.6. The figure shows that there is no significant difference in the equilibrium data between with and without amino acid systems. This is in good agreement with the previous reports (Bhattacharjee and Linga, 2021; Lee *et al.*, 2012) confirming that the amino acid acts as a kinetic promoter for this specific methane hydrate forming system.

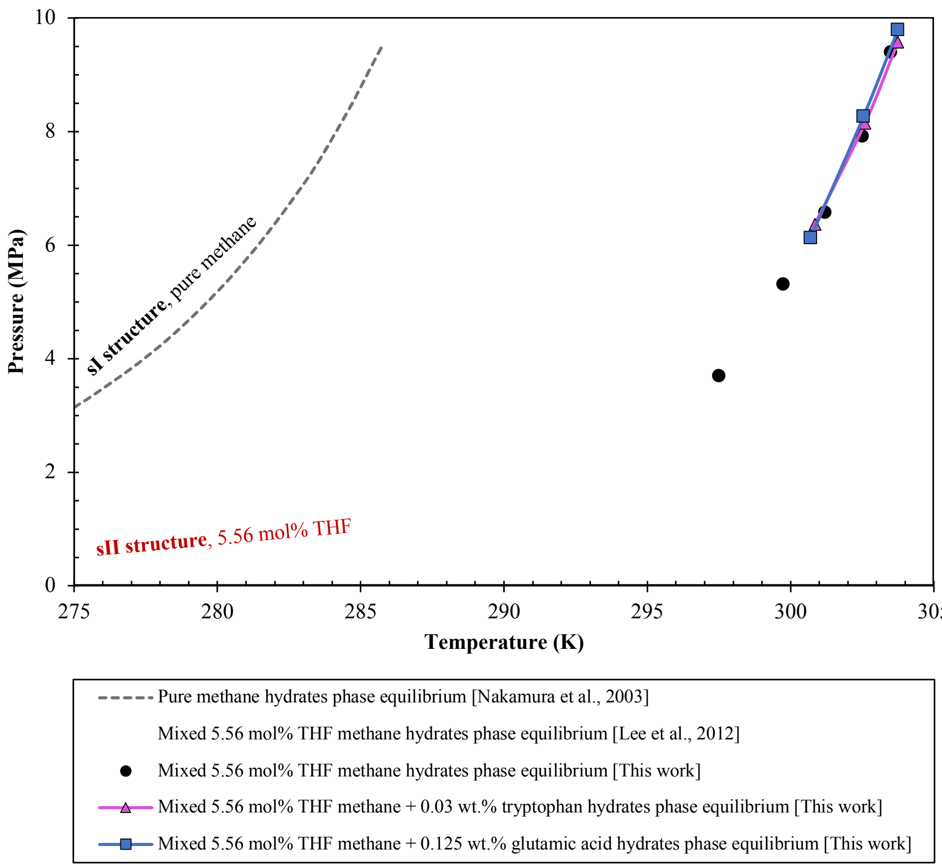

Figure 4.6 Hydrate phase equilibrium of methane hydrates at different systems collected from literatures (Lee *et al.*, 2012; Nakamura *et al.*, 2003) and experimental data from this study.

For a better understanding of the role of amino acid hydrophobicity as a kinetic promoter, the following mechanism, Figure 4.7, is proposed. First, the presence of amino acid alters the solution property (i.e., surface tension) (Atta *et al.*, 2021; Raza *et al.*, 2019) enhancing the dissolution of methane gas into water Figure 4.7, insert I. This is in good agreement with the methane solubility measurement, as shown in Figure 4.8, where the Henry's constant of the system with amino acid is greater than that of the system without amino acid. This implies the enhancement of methane dissolution by the addition of amino acids. The hydrophobic amino acid (Trp) creates a hydrophobic area with a cluster of methane molecules via hydrophobic-hydrophobic interactions Figure 4.7, insert II. The water molecules are prevented from this area making them localized by hydrogen bonds between water molecules, Figure 4.7, insert II (b). The presence of THF, a thermodynamic promoter, induces the formation of large cage of sII hydrates resulting in embryo nucleation, Figure 4.7, insert II (a) (Guo and Zhang, 2021; A. Kumar *et al.*, 2019; Asheesh Kumar *et al.*, 2019b). At the interface between the hydrophobic area formed by the hydrophobic amino acid and the area with localized water molecules, methane is adsorbed on the large cage embryo. Subsequently, the water molecules form and grow small cages of sII hydrates on the embryo. This is then followed by the crystal growth to form complete methane hydrates, leading to more methane being taken in. In contrast, a hydrophilic amino acid (Glu and Val) interacts with water molecules and inserts itself between the water molecules disrupting the water-water interactions. In conclusion, the hydrophobic amino acid enhances the methane uptake as well as the water to hydrate conversion nearly to the theoretical value. In contrast, the hydrophilic amino acid does not show any significant effect on the hydrate formation.

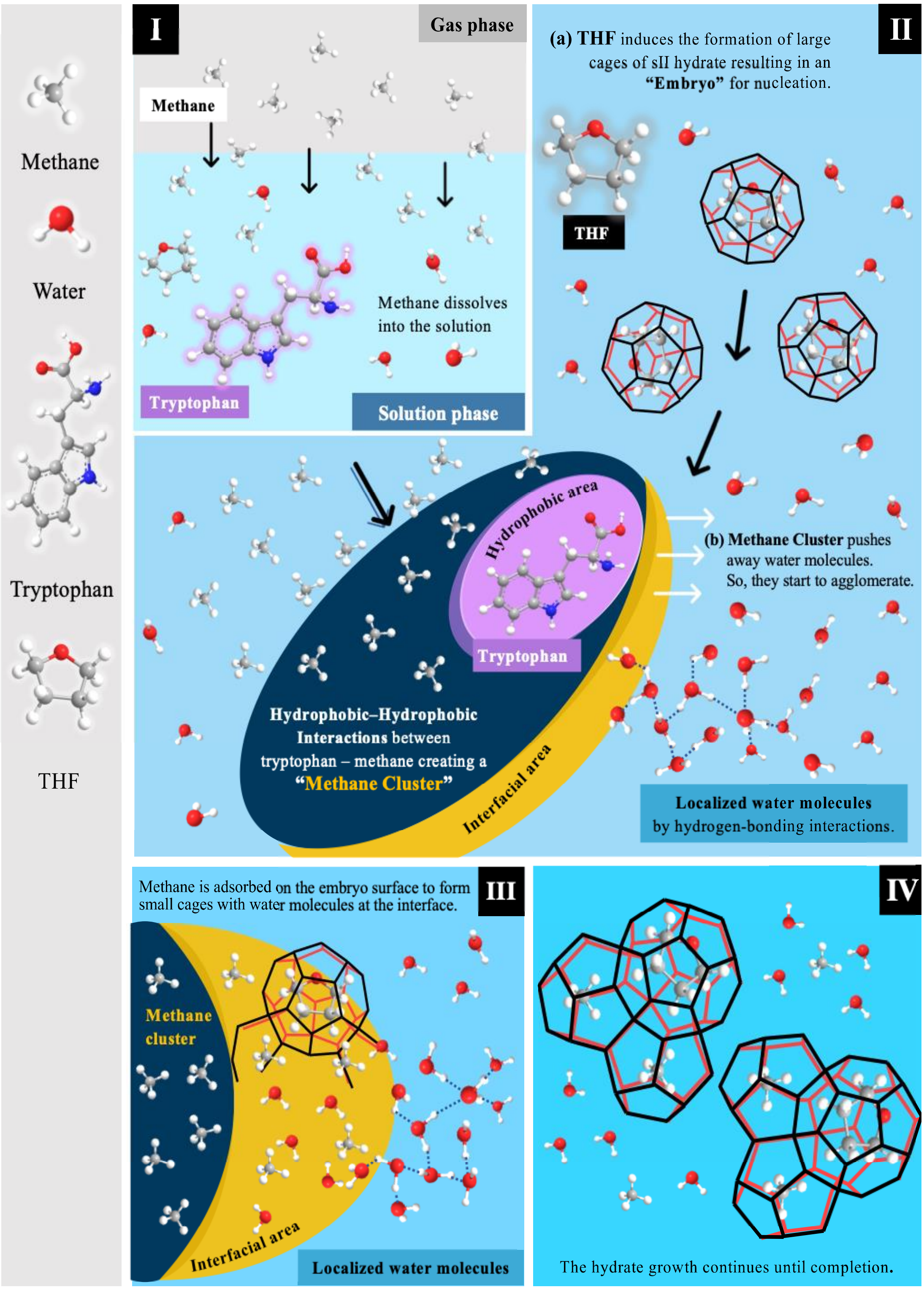

Figure 4.7 Proposed mechanism explaining the role of hydrophobic amino acid on the mixed methane-THF hydrate formation.

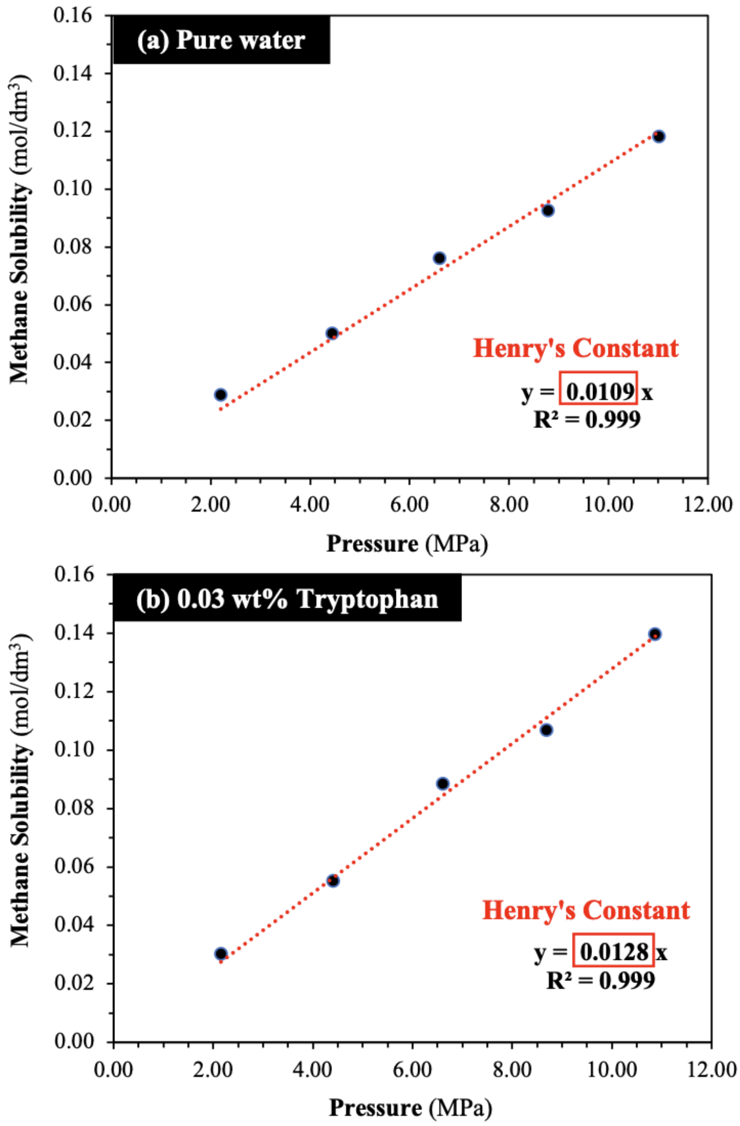

Figure 4.8 Methane solubility at different pressures and Henry's constant of the solutions containing (a) pure water and (b) 0.03 wt% Trp.

4.4.1.2 Methane Hydrate Formation Kinetics

The other crucial factor for hydrate formation is its kinetics, which is quantitatively expressed by the normalized rate of hydrate formation 30 minutes after the first nucleation (NR_{30}), the time to reach 90% of methane uptake (t_{90}), and the hydrate formation induction time. It is interesting that the amino acid hydrophobicity also affects the hydrate formation kinetics.

Figure 4.9 shows the methane uptake profiles from the system with the optimal concentration of amino acids during hydrate growth. The figure clearly shows different hydrate growth patterns and methane uptakes from the addition of amino acids. The hydrate growth patterns with THF, 0.125 wt% Glu, and 0.125 wt% Val experiments are similar. They achieve approximately the same methane uptake at 50 v/v. However, methane uptakes are higher with Leu, Met, and Trp. Despite the different methane uptakes, the rates of hydrate formation for the first 30 minutes are the same, as shown in Figure 4.9, insert I. Moreover, amino acid concentrations hardly affect the NR_{30}, Figure 4.10. It might be possible that this particular configuration is assisted by the stirring, which plays a more important role in the hydrate formation than the promoters. In addition, for the hydrate growth after 30 minutes, the hydrate formation rates are different, Figure 4.9, insert II. In the experiments with THF, Glu, and Val, the methane uptakes reach at about 50 v/v, while those with Leu, Met, and Trp, further increase and reach as high as 100 v/v. Hydrophobic amino acids boost methane uptake, as explained previously.

t_{90} or the time taken for hydrates to reach 90% of methane uptake with each amino acid, Figure 4.11 (a), is in ascending order of amino acid hydrophobicity at different concentrations. There is no clear trend observed in terms of hydrophobicity and t_{90}. It is noted that THF, Glu, and Val have lower t_{90} than Leu, Met, and Trp. Since there are different methane uptakes, t_{90} should be normalized by their methane uptake for a fair comparison. The normalized t_{90} (norm t_{90}) of each amino acid at different concentrations is summarized in Figure 4.11 (b). There is no significant difference in the norm t_{90} with the increase in the hydrophobicity from Glu, Val, and Leu. However, further increasing the hydrophobicity to Met and Trp decreases the norm t_{90}. With Trp, the most hydrophobic amino acid, the norm t_{90} is the lowest.

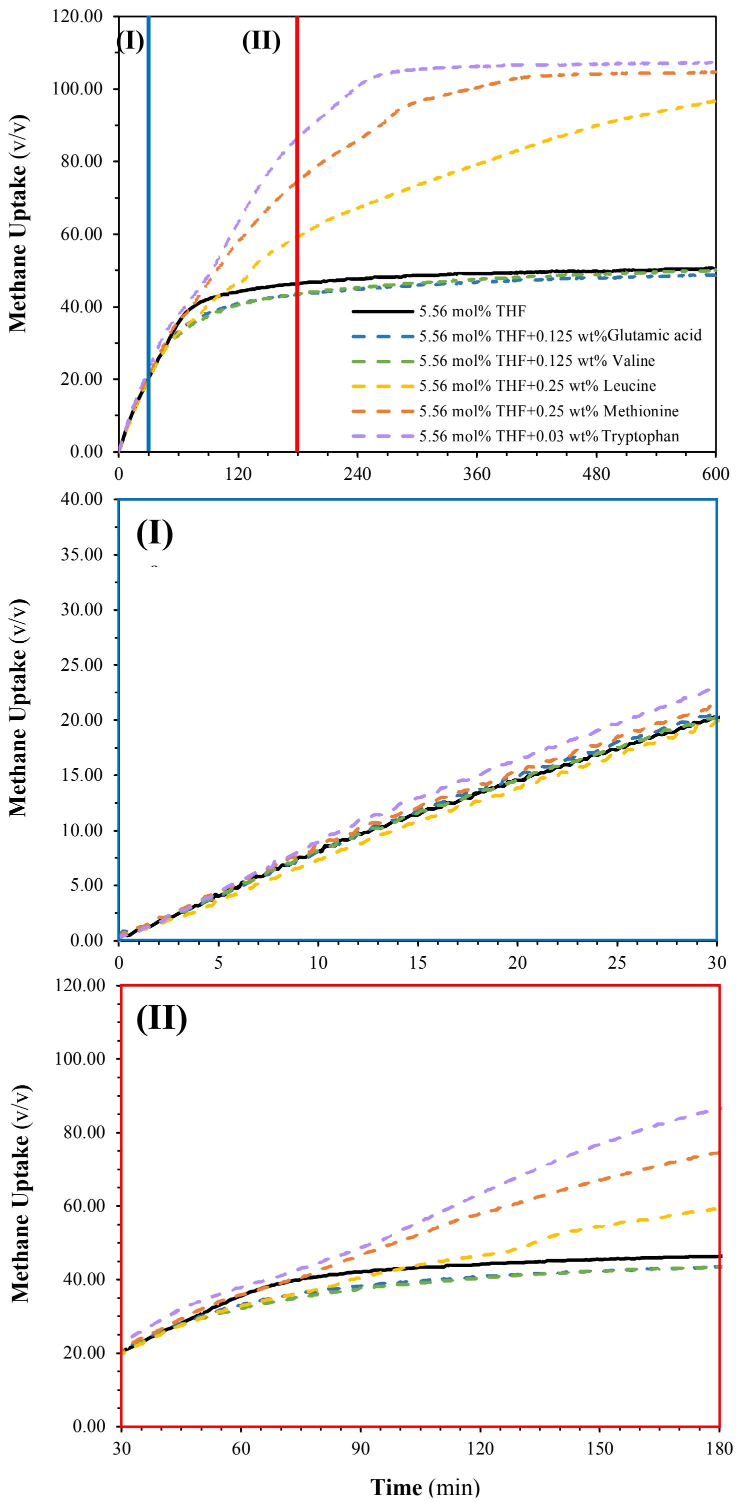

Figure 4.9 Plots of methane uptake against time of each amino acids at its selected concentration, magnified scale; insert I, the methane uptake during the first 30 minutes and insert II, the methane uptake after 30 minutes until 180 minutes after hydrate nucleation.

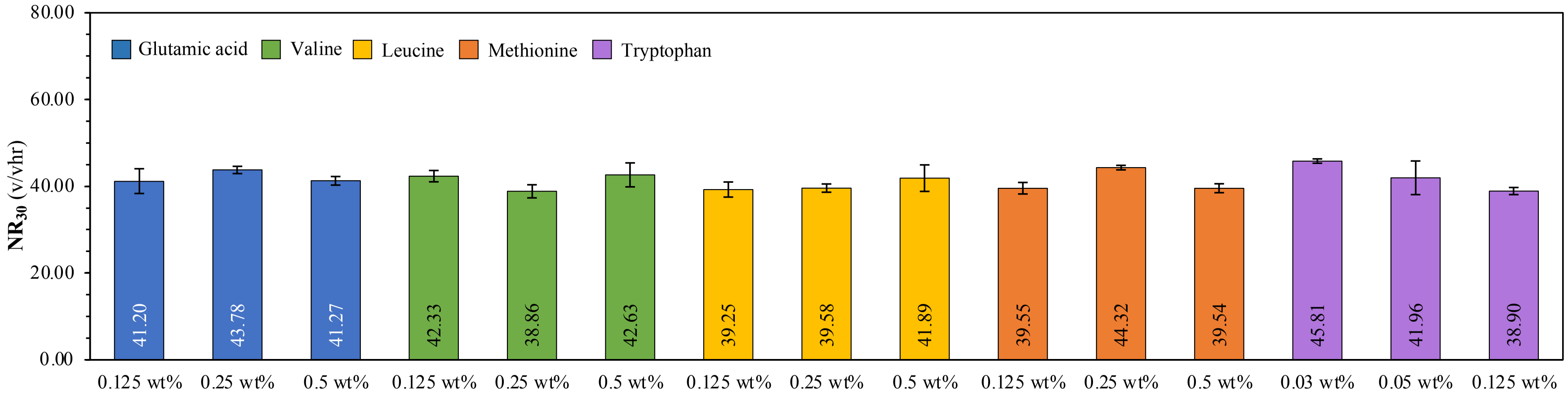

Figure 4.10 NR_{30} of hydrate forming systems using different amino acids at various concentrations at 298.2 K and, 9.2 MPa with a hybrid stirring system.

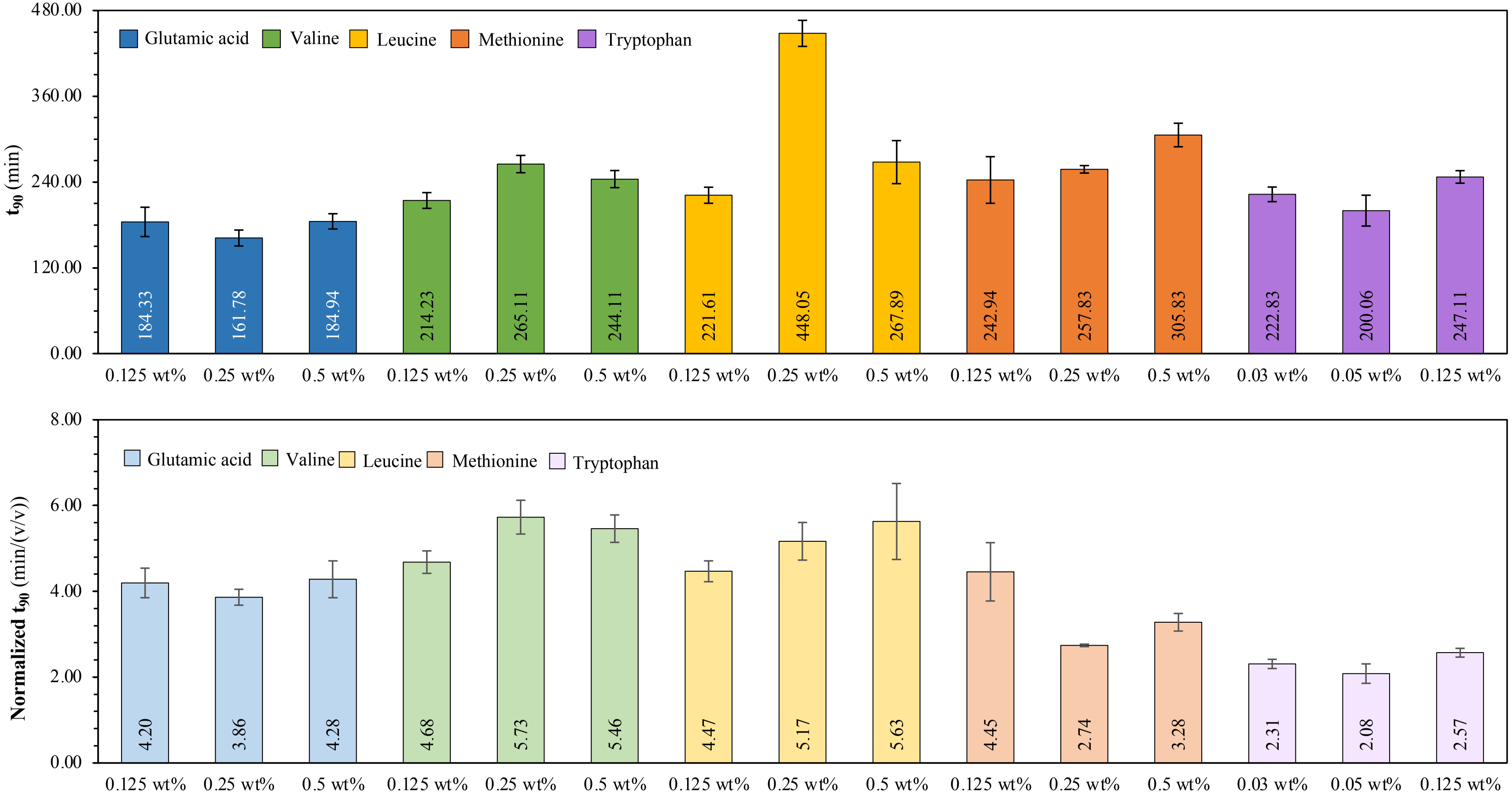

Figure 4.11 t_{90} (a) and normalized t_{90} (b) obtained from different hydrate forming systems at 298.2 K and, 9.2 MPa with a hybrid stirring system.

For better understanding, the norm t_{90} of each amino acid at different concentrations is plotted against the quantitative chemical descriptors of amino acids calculated from the RDKit, an open-source cheminformatics software. The selected descriptors are molecular weight (MW), solvent accessible surface area (SA), polar area to total surface area (PSA/SA), and logarithmic octanol/water partition coefficient (LogP). The correlation between features is presented in the correlation heatmap, Figure 4.12 (a). By considering the correlation coefficient (R), the norm t_{90} has a strong negative correlation with MW and SA of amino acids (R = -0.84 and -0.82, respectively). However, these two features are highly collinear with each other with R = 0.99. The amino acids with high MW tend to have a high surface area as well (Miller *et al.*, 1987). Therefore, only one feature, which is the MW, is selected to plot with the norm t_{90}. A jitter scatter plot showing the negative correlation of norm t_{90} against MW of amino acids is presented in Figure 4.12 (b). This brings to the possible insight that the time taken for the completion of hydrate formation is affected by the MW of the amino acids. Since the magnitude of MW implies the total number of electrons in that molecule, inferring the strength of London dispersion forces of an amino acid molecule, intermolecularly interacts with its neighboring molecules. When an amino acid is dissolved in water, new interactions between the amino acid and water must be stronger than the amino acid–amino acid interaction and water-water interaction. So that amino acid molecules can be separated from each other and also the hydrate. However, increasing the MW of amino acids leads to an increase in the strength of London dispersion forces between amino acid molecules. The amino acids with higher MWs tend to be less soluble, less surrounded by water molecules, and less inhibiting the hydrate growth. So, Trp, the highest MW amino acid, results in the fastest hydrate completion (lowest norm t_{90}) followed by Met and Leu, the lower MW, respectively. This MW concept is consistent with the concept of hydrophobicity that was purposed earlier. In addition, though Glu has the third-highest MW among these amino acids, its side group can dissociate into ions when dissolved in water. This makes Glu the least hydrophobic amino acid in the ranking.

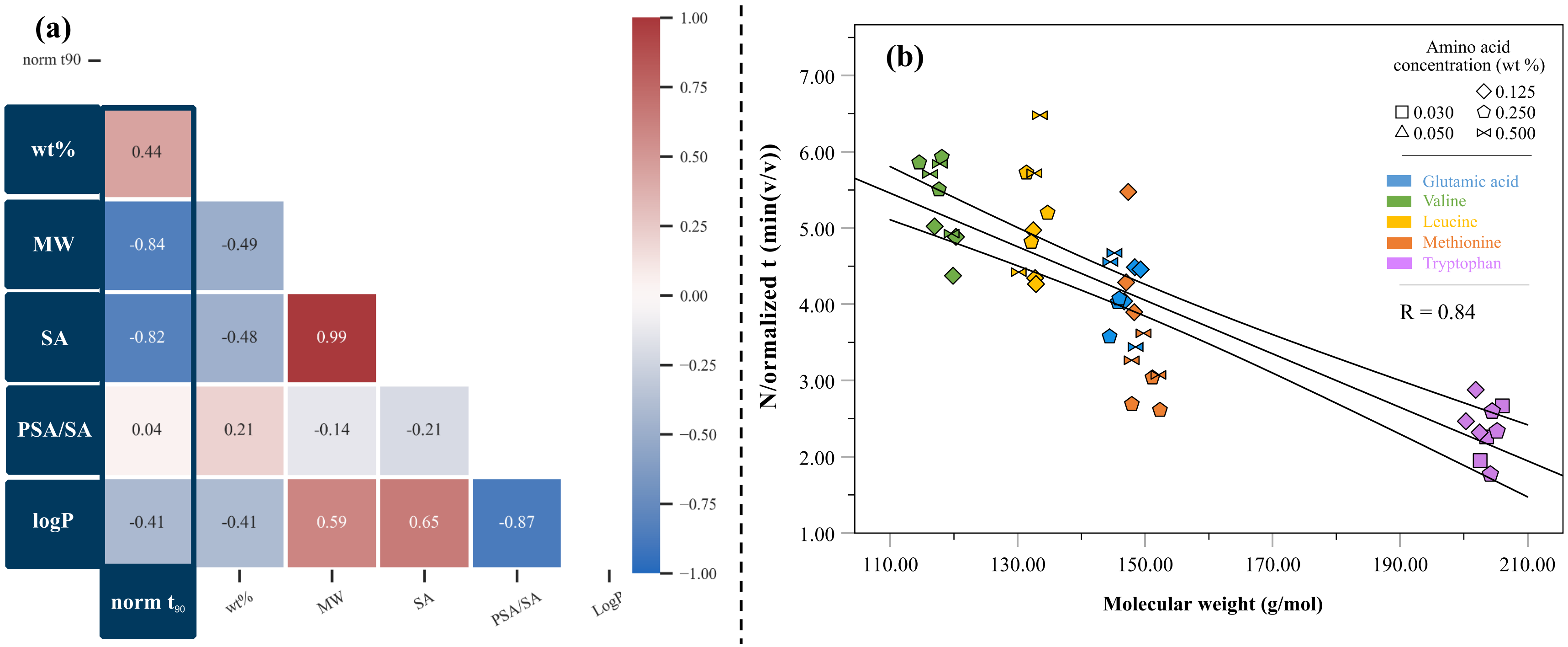

Figure 4.12 Correlation heatmap of the norm t_{90} of each amino acid against the quantitative chemical descriptors of the amino acid (a) and jitter scatter plot showing a negative correlation between the normalized t_{90} and MW of amino acids (b).

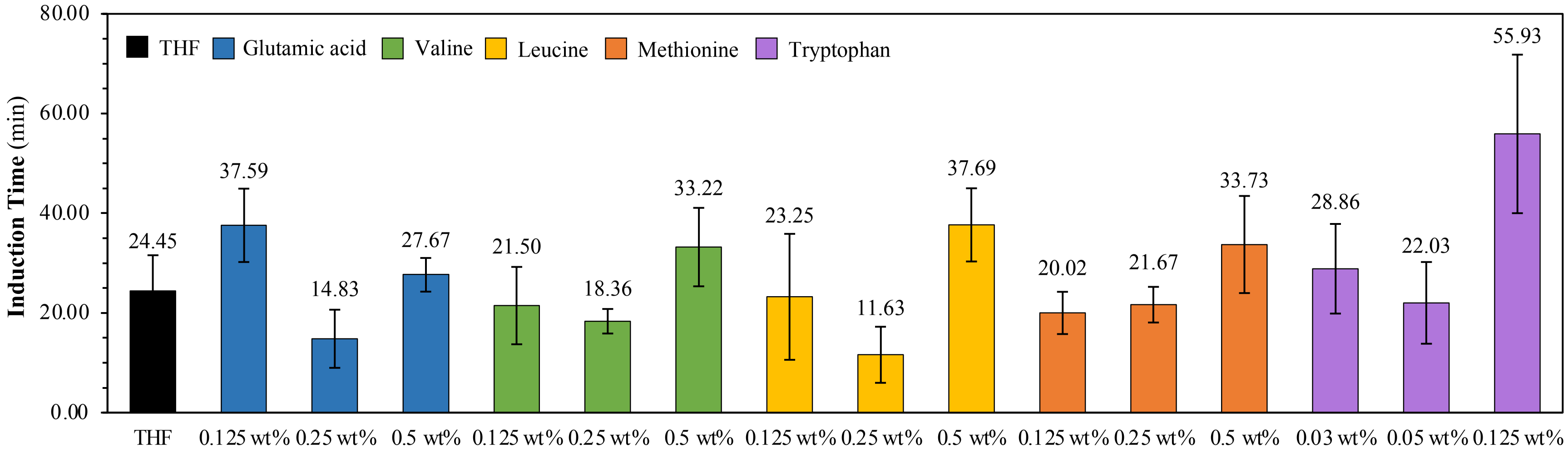

Figure 4.13 Induction time of the mixed methane-THF hydrate formation with the addition of amino acids and their concentration at 298 K, 9.2 MPa.

For the induction time, the time taken for the first nucleation, the mean and error bar of the induction time of the formation with different amino acids and concentrations are shown in Figure 4.13 The mean induction time of each amino acid at different concentrations is not significantly different from that of THF, confirmed by P-values from the Tukey Kramer test, which is higher than 0.05 at the confidence level of 95%, shown in Table 4.4. Exceptionally, the mean of 0.125 wt% Trp is different from the induction time mean of THF (P-value < 0.05) that slows down the induction time to about 1 hour, which is not preferable. Therefore, the addition of Trp at 0.03 wt% is preferred due to its highest methane uptake and fast induction time.

Table 4.4 Statistical results of the test on induction time mean differences between each amino acid at different concentrations by Turkey-Kramer's test

	Comparison	**Mean Difference**	**Standard Error**	***P*-value**
THF	Glu 0.125 wt %	-13.13	8.10	0.952
	Glu 0.25 wt %	9.62	8.10	0.997
	Glu 0.5 wt %	-3.22	8.10	1.000
	Val 0.125 wt %	2.95	8.10	1.000
	Val 0.25 wt %	6.09	8.10	1.000
	Val 0.5 wt %	-8.77	8.10	0.999
	Leu 0.125 wt %	1.21	8.10	1.000
	Leu 0.25 wt %	12.83	8.10	0.960
	Leu 0.5 wt %	-13.24	8.10	0.949
	Met 0.125 wt %	4.44	8.10	1.000
	Met 0.25 wt %	2.78	8.10	1.000
	Met 0.5 wt %	-9.27	8.10	0.998
	Trp 0.03 wt %	-4.41	8.10	1.000
	Trp 0.05 wt %	2.43	8.10	1.000
	Trp 0.125 wt %	-31.48	8.10	0.033*

Based on observed means, the error term is Mean Square (Error) = 98.469.

* The mean difference is significant at the 0.05 level.

4.4.2 Morphological Studies on Mixed Methane Hydrate Formation

The morphology study for the mixed methane-THF hydrate formation can shed light on how hydrates grow in a reactor. The hydrate formation experiment was carried out in a sapphire crystallizer equipped with a camera for video recording. The formation condition is the same as in the experiment for kinetic study (298 K, 9.2 MPa with a stirring system). The snapshots taken at different times during hydrate formation are presented in Figure 4.14. The hydrate growth patterns for each experiment are similar. For better visualization, a small amount of dye was added into the solution before the formation. Figure 4.15 shows the dyed hydrate growth patterns in THF, which are selected as the controlled experiment (Figure 4.15 (a)), an experiment with the addition of Glu, a hydrophilic amino acid in Group B (Figure 4.15 (b)), and experiment with Trp, a hydrophobic amino acid in Group A, (Figure 4.15 (c)), respectively. The patterns of hydrate formation with 5.56 mol% THF can be described as follows: At the start of the experiment, the solution is transparent, and a small vortex is seen due to the stirring by the magnetic bar (Figure 4.15 (a1)). When it reaches its nucleation, the solution becomes cloudier because of the nuclei of hydrates (Figure 4.15 (a2)). Afterward, the stirring is stopped, and the hydrates start growing from the interface of the gas and liquid phases (Figure 4.15 (a3)). The hydrates grow upward by bringing the liquid from the solution phase to the gas phase through the hydrate structure via the capillary effect (Mitarai *et al.*, 2015), as shown in Figure 4.15 (a4). In addition, as the concentration of methane in the gas phase is greater than in the solution phase, this increases the adsorption of methane on the surface of the hydrates, resulting in faster hydrate growth in the gas phase than in the solution phase. At a certain point, the hydrates start to sink together with the upward growth until it covers the entire reactor, 10 minutes after the nucleation (Figures 4.15 (a5) – (a7)). Hydrates continue to grow to the completion. This can be confirmed by the methane uptake profile, Figure 4.16. The morphology at the end of the experiment, Figure 4.15 (a8), does not present a significant difference from the earlier snapshot at 10 minutes, Figure 4.15 (a7).

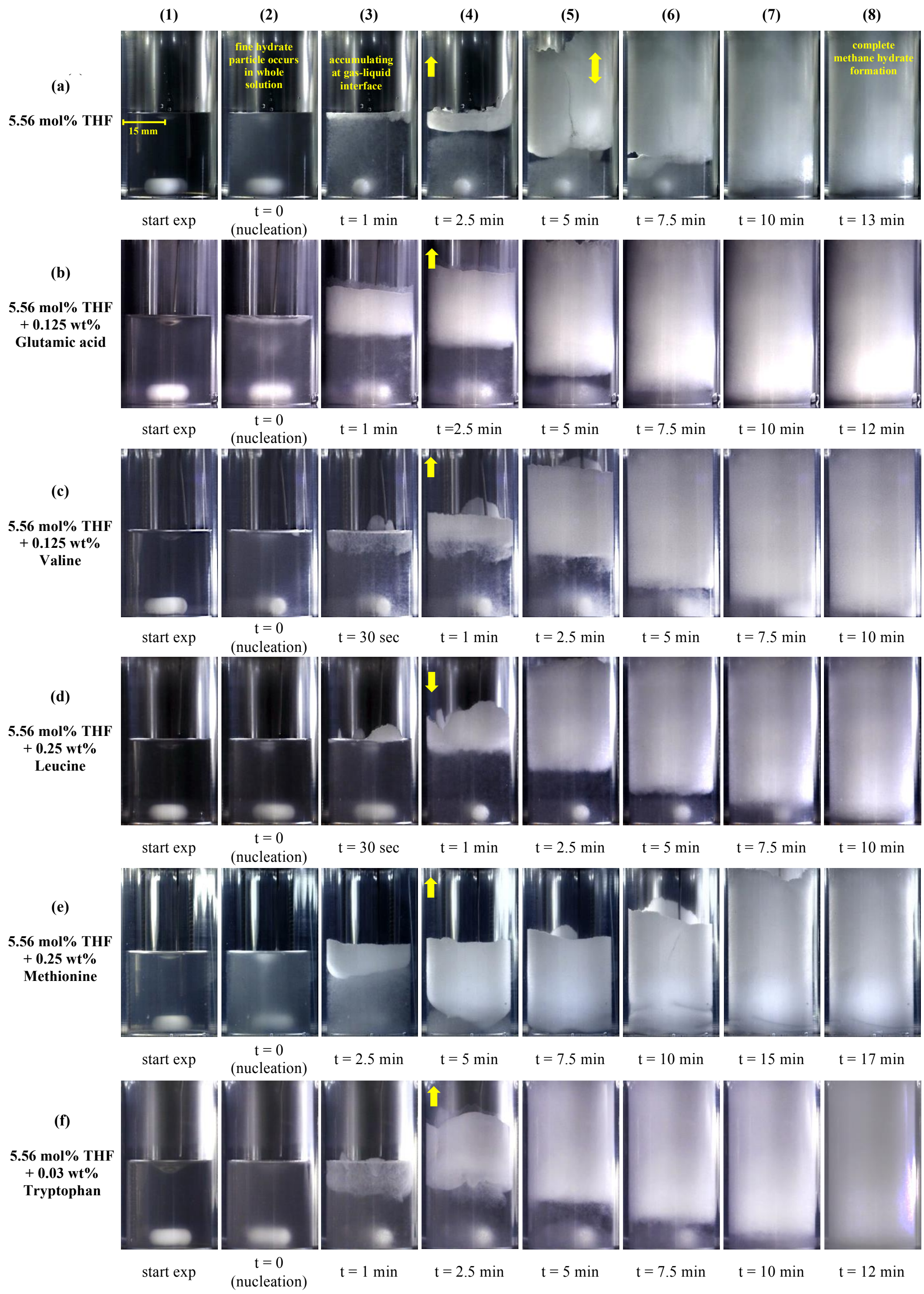

Figure 4.14 Morphology images of methane hydrate formation using different solutions (a) 5.56 mol% THF (b) 5.56 mol% THF + 0.125 wt.% glutamic acid (c) 5.56 mol% THF + 0.125 wt% valine (d) 5.56 mol% THF + 0.25 wt% leucine and (e) 5.56 mol% THF + 0.25 wt% methionine (f) 5.56 mol% THF + 0.03 wt.% tryptophan, at 298.2 K and 9.2 MPa with a hybrid stirring system.

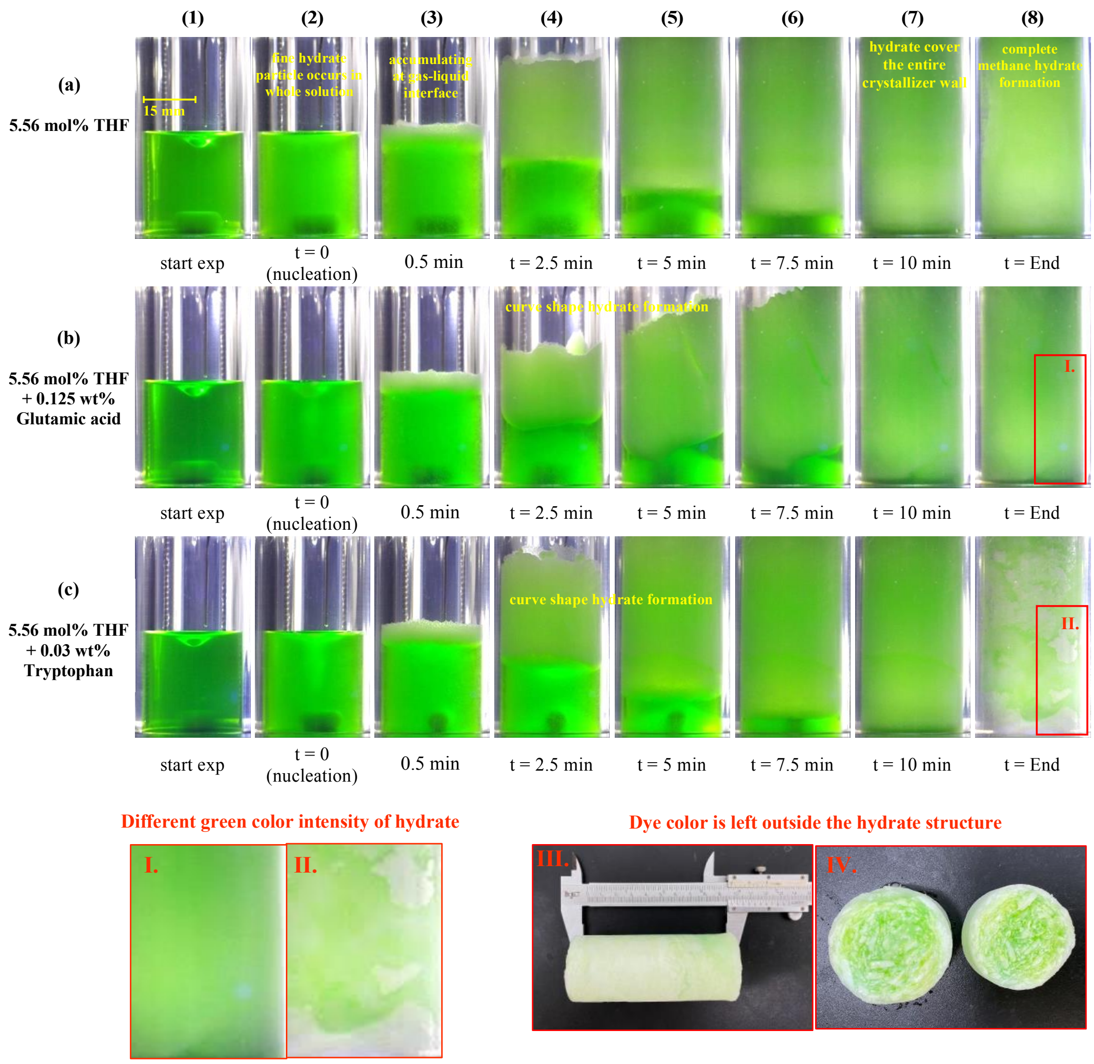

Figure 4.15 Morphology of dyed mixed methane hydrate formation with (a) 5.56 mol% THF (b) 5.56 mol% THF + 0.125 wt.% Glu and (c) 5.56 mol% THF + 0.03 wt.% Trp at 298 K and 9.2 MPa with hybrid stirred configuration.

The morphology of hydrate growth in the experiments with Glu and Trp is slightly different from THF (Figure 4.15 (b) and Figure 4.15 (c) respectively). The hydrate growth patterns at t = 2.5 and 5 minutes are in a curve formed, whereas that of THF is a flat one. This phenomenon is also found in the hydrate formation with the presence of Leu in the previous reports (Jeenmuang *et al.*, 2021; Veluswamy *et al.*, 2016a). The complete hydrates with a hydrophilic amino acid, Glu, are similar to those of THF, where the hydrates are homogenously green (Figure 4.15, insert I), while the hydrates with the hydrophobic amino acid, Trp, are disorderly green (Figure 4.15, insert II). This implies that the complete hydrates at the end of the experiment with Trp seem to be denser than those of the others. Apart from the color disorder, the color intensity of hydrates with THF and Glu is higher than that of Trp. This is because the green color used is made up of two coloring agents, brilliant blue FCF ($C_{37}H_{34}N_2Na_2O_9S_3$) and tartrazine ($C_{16}H_9N_4Na_3O_9S_2$). These molecules are much bigger than the cavity of sII hydrates. So, they are unable to stay in the hydrate structure, making hydrates colorless. The white color of hydrates formed in the presence of Trp means that most water molecules in the system are used to form hydrates, pushing dye molecules out of the hydrate structure, resulting in disorderly green color. This is visually confirmed by the photographs of the cross-sectional hydrate pellet in Figure 4.15, inserts III and IV. The green color is around the center of hydrates, while the white is around the cortex. This is because hydrates formed from the wall of the reactor before the core. In contrast, the hydrates in the presence of THF and Glu could not form complete hydrates, leaving color molecules dissolving in the remaining water and spreading all over the hydrates resulting in uniform-green hydrates. This is consistent with the results of hydrate conversion, where THF and Glu achieve around 60%, while that of Trp is at 95%.

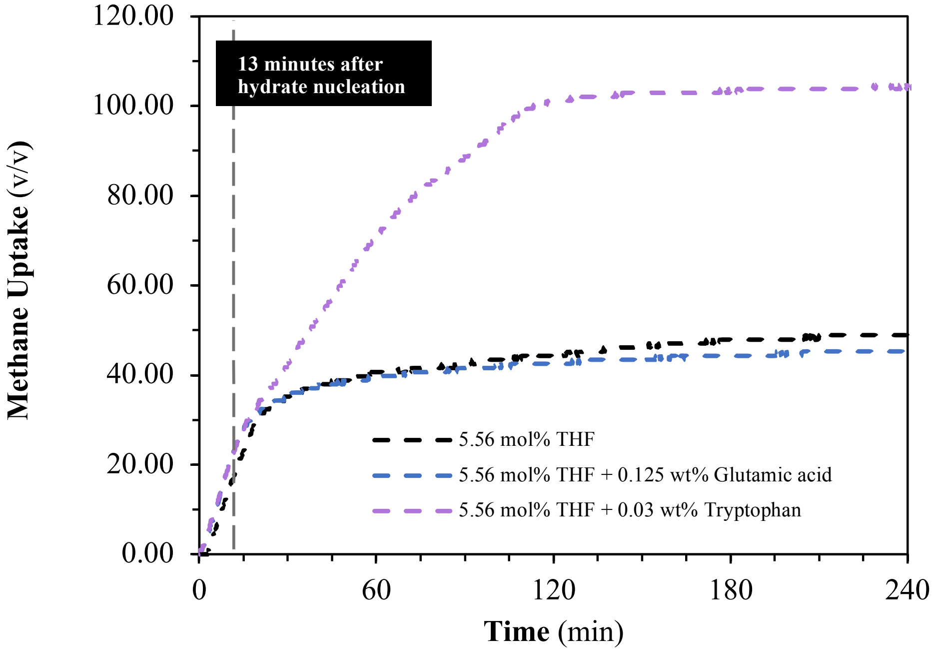

Figure 4.16 Methane uptake profile obtained from the morphological studies using a sapphire crystallizer.

4.4.3 Hydrate Dissociation Studies

After the completion of the mixed hydrate formation in the stainless-steel crystallizer, the dissociation of the fabricated hydrates was studied subsequently. The obtained hydrates were heated to 308.2 K, while the temperature and pressure changes were monitored. The pressure inside the crystallizer increased as methane dissociated from the hydrates. The pressure difference was then used to calculate the number of moles of methane recovered and percentage recovery. Figure 4.17 shows the percentage of methane recovered from the hydrates formed with different solutions. Most methane can be recovered from the hydrates without significant loss. All experiments with different amino acids show indifferent methane recovery compared to that of THF, meaning that the addition of amino acids does not affect the methane recovery. This is preferable in the gas storage technology.

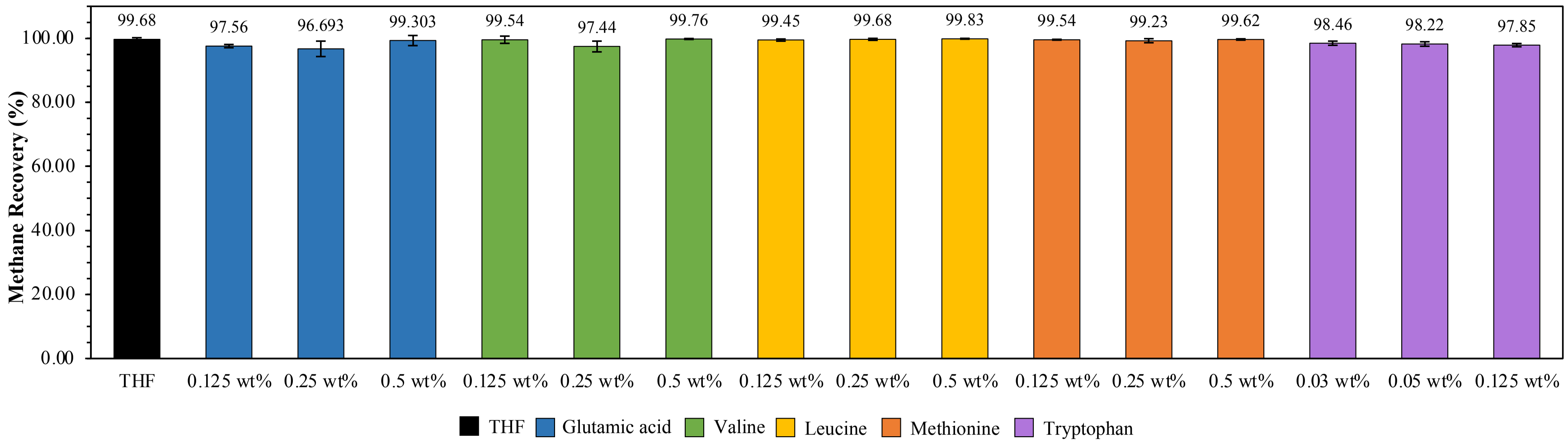

Figure 4.17 Methane recovery after hydrate dissociation of hydrates from different forming systems.

To gain an insight into the dissociation kinetics, the normalized methane recoveries from the hydrate formed with 5.56 mol% THF and five different amino acids at their optimal concentration are plotted against time. The average normalized methane recovery and its standard deviation are shown by the dashed line and the shaded area in Figure 4.18. THF, Glu, and Val completely dissociate at about 60 minutes, whereas Leu, Met, and Trp are about 110 minutes. The former group has faster dissociation than the latter because of the incomplete hydrate formation (about 60% water to hydrate conversion). The dissociation patterns can be separated into 2 groups following the water to hydrate conversion at about 60% and 95%. The higher the water to hydrate conversion, the higher extent of hydrate consolidation. More consolidated hydrates are likely to have a lower rate of dissociation than unconsolidated hydrates. This implies that the dissociation kinetics depends on the completion of the hydrates, not the type of amino acids.

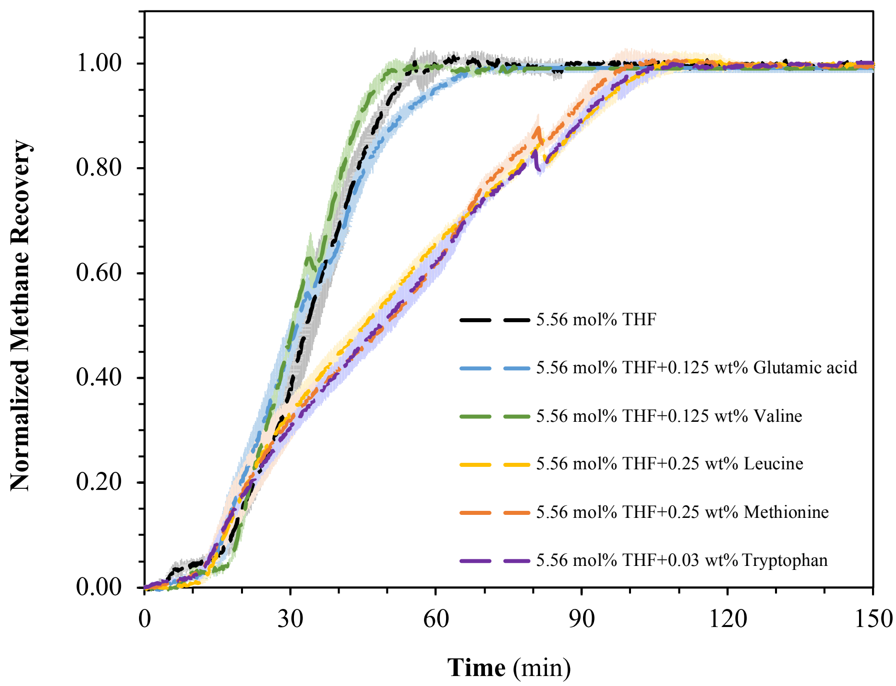

Figure 4.18 Normalized methane recovery against time of the hydrates obtained from different solutions dissociating at 308.2 K.

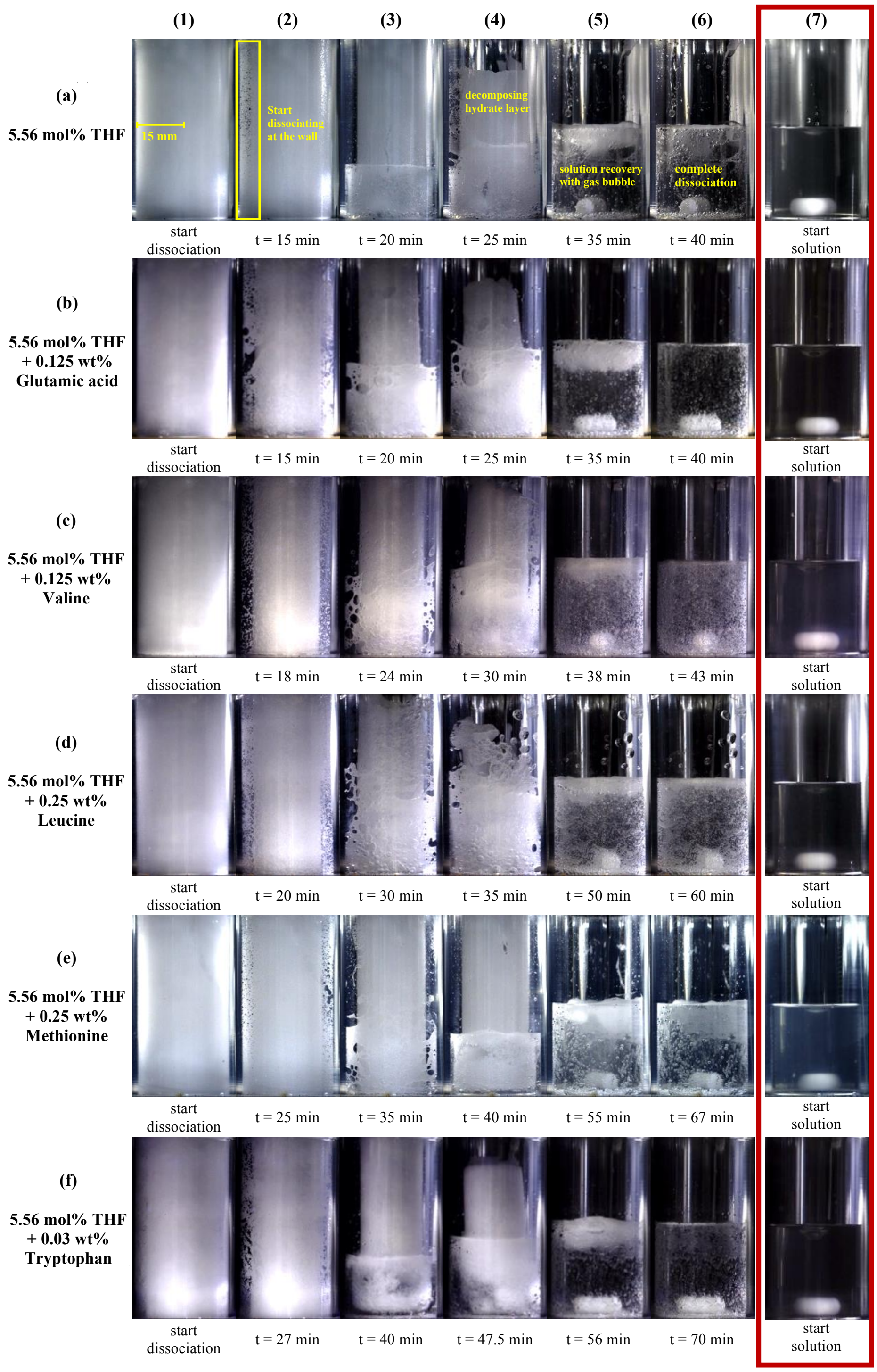

Figure 4.19 Dissociation morphology of the hydrates obtained from different solutions of (a) 5.56 mol% THF, (b) 5.56 mol% THF + 0.125 w.% Glu, (c) 5.56 mol% THF + 0.125 wt.% Val, (d) 5.56 mol% THF + 0.25 wt% Leu, (e) 5.56 mol% THF + 0.25 wt.% Met, and (f) 5.56 mol% THF + 0.03 wt% Trp.

The morphology of the hydrates during dissociation in the sapphire crystallizer is shown in Figure 4.19. For the hydrates formed with THF, Figure 4.19 (a), the dissociation firstly occurs at the wall of the crystallizer, Figure 4.19 (a2), followed by melting, Figure 4.19 (a3) – 4.19 (a5). The methane gas is released from the solution as small bubbles, which can be observed in Figures 4.19 (a5) and 4.19 (a6). After complete dissociation, the level of solution is the same as it was before the formation (Figure 4.19 (a7)). This implies that the dissociation conserves the amount of solution, leading to the possibility of multi-cycle use. The hydrates formed with different amino acids dissociate following the same pattern as THF does (Figures 4.19 (b) – 4.19 (f)), except for the rate and the time to complete dissociation. The hydrophilic amino acids (Glu and Val) have a similar dissociation rate to THF, but they are faster than those of the hydrophobic amino acids (Leu, Met, and Trp). Moreover, there was no foam formation during dissociation, emphasizing the advantage of the amino acid as a kinetic promoter over surfactant.

4.4.4 Hydrate Stability Test

The stability of gas hydrates is an important factor for SNG technology. A pelletizing crystallizer was used to form mixed methane-THF hydrates under the same condition as in earlier studies, which was then compressed into a packed pellet. To validate the reproductivity of the pelletizing crystallizer, the methane uptake, and the water to hydrate conversion of the hydrates from different solutions obtained from the pelletizing crystallizer are compared with those from the stainless-steel crystallizer. Figure 4.20 shows the consistency within the methane uptake and the percentage of water to hydrate conversion of the hydrates obtained from different crystallizers. Based on the results, the hydrates formed with THF are in the form of slurry, as shown in Figure 4.21, due to the liquid water disrupting the hydrates to be pelletized. The same observation can be seen in the hydrates formed with a hydrophilic amino acid (Glu and Val). In contrast, a hydrophobic amino acid (Leu, Met, and Trp) forms hydrates that can be pelletized, giving a 4.0-cm-diameter pellet, 9.5 ± 0.5 cm long, with a weight of 100 ± 5 g. In addition, the system was pre-cooled to 273.2 K before the pelletizing process. Later, the hydrate pellet is transferred to a closed stainless-steel storage vessel, which is then stored in a refrigerator at 283.2 K under atmospheric pressure. The temperature and pressure inside the storage vessel are monitored continuously for 30 days. Since the storing temperature is higher than the equilibrium temperature of the sII hydrates in the presence of THF at atmospheric pressure, which is at 277 K, some of the gases are released to re-establish the equilibrium, making the pressure in the storage vessel rise. The change in the pressure over that range indicates the unstable hydrates, which could not preserve the gas inside their cavities.

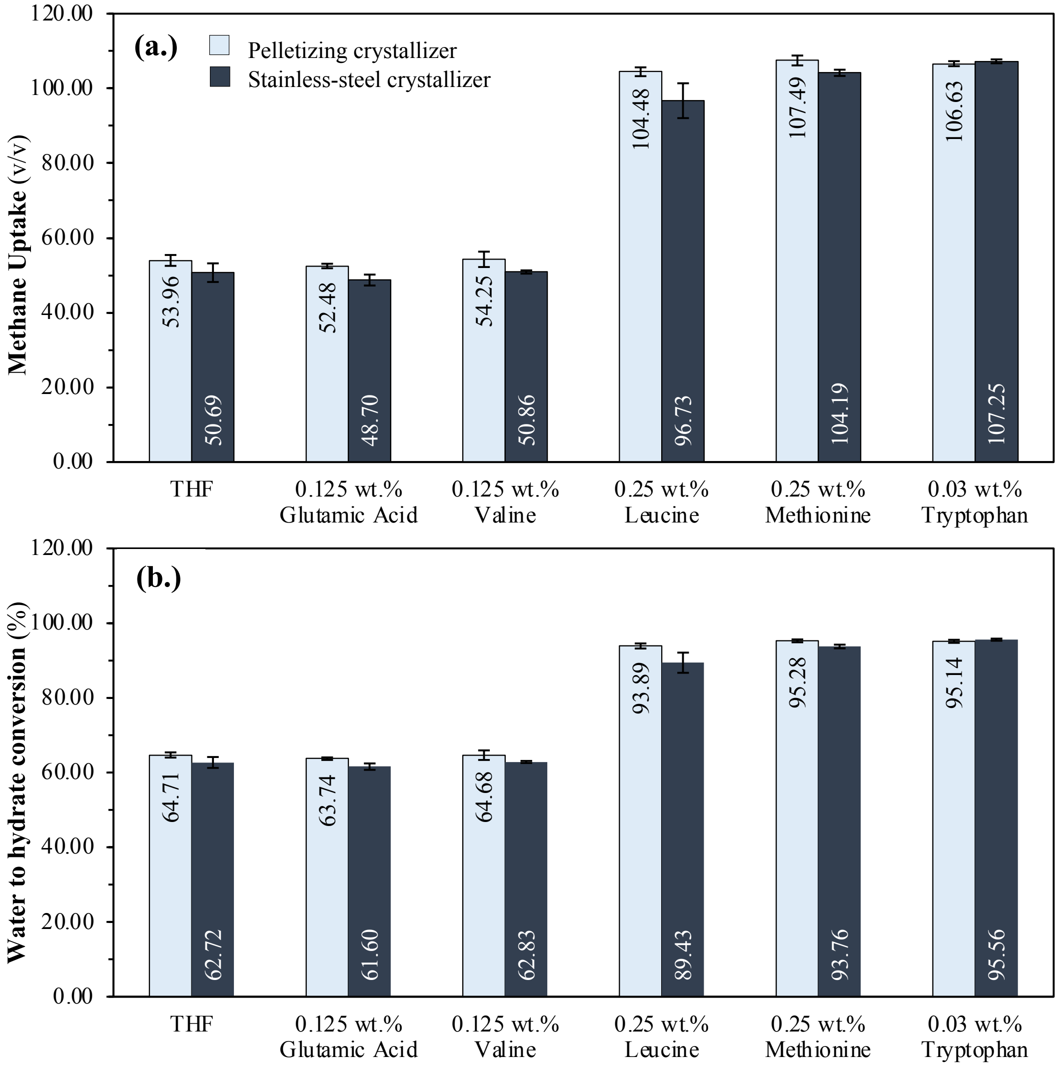

Figure 4.20 Methane uptake (a) and water to hydrate conversion (b) of different forming systems using different crystallizers.

Figure 4.21 Pictorial image demonstrating a slurry hydrate obtained from the forming system with 5.56 mol% THF only at 298.2 K and 9.2 MPa.

The mass and the size of the hydrate pellet obtained from a solution containing 0.03 wt% Trp (Run-1) are 99.87 g and 9.5 cm long, which is equivalent to 0.4991 moles of methane trapped inside the hydrate pellet, Figure 4.22 (a). Figure 4.22 (b) demonstrates the temperature and pressure profiles of the hydrate pellet during storage. Both the hydrate pellet and the storage vessel were cooled to 273.2 K before the hydrate pellet was moved from the crystallizer to the storage vessel. This caused the temperature of the storage vessel to rise at first. After that, the temperature remains at 283.2 K for the entire period. The methane gas dissociated from the hydrate pellet results in an increase in the pressure of the storage vessel. The pressure inside the storage vessel increases for the first day to 374.33 kPa. Then it slows down and becomes stable after the first 15 days at 663.91 kPa and finally reaches up to 684.59 kPa at the end of 30 days. The hydrate pellet released 0.0312 moles, or 6.25% methane loss, on the first day and released up to 0.0556 moles (11.14%) of cumulative methane loss after 15 days. At the end of the 30 days, only 0.0574 moles of methane were released (11.50%), which is slightly greater than on the 15th day. The major methane loss is from the first 15 days, which is 96.86% of the total loss, and the total loss in the latter is only 3.14%. The mass of the remnant hydrate pellet is 97.76 g at the end of the test. The stability tests on the other hydrate pellets were conducted only for 15 days due to insignificant changes in pressure and methane loss after 15 days.

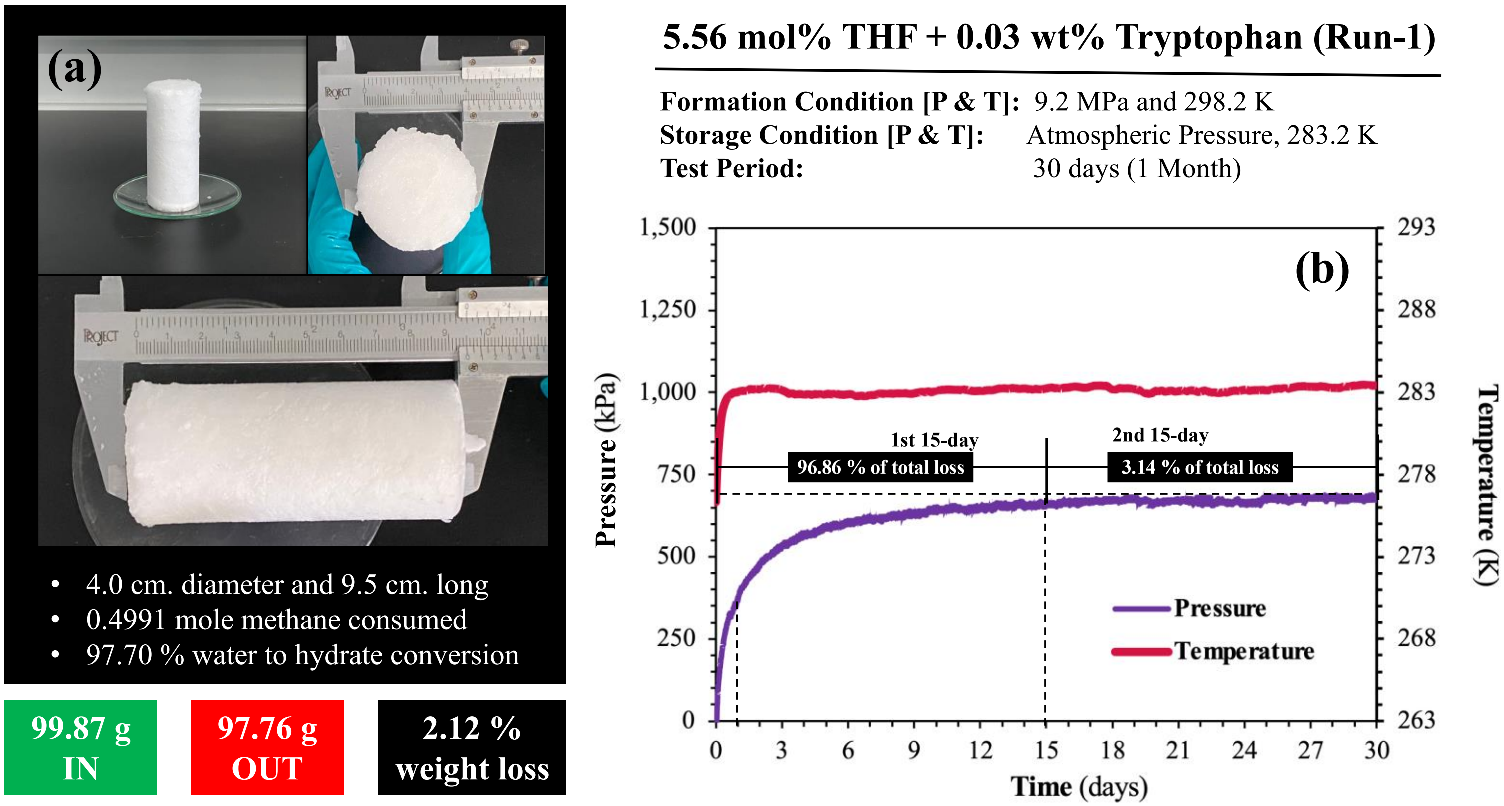

Figure 4.22 Results of the 30-day stability test at atmospheric pressure and 283.2 K of the hydrate pellet made from a solution containing 5.56 mol% THF and 0.03 wt% Trp (Run-1) (a), temperature and pressure profiles of the hydrate pellet during storage (b).

The stability test is repeated on the hydrate pellet made from different solutions for 15 days. Note that the condition to form a 5.56 mol% THF hydrate pellet is different from the others because at that condition it is unable to form complete hydrates. Therefore, it is carried out at 8 MPa and 293.2 K instead, which results in almost complete hydrate formation (Jeenmuang *et al.*, 2021). Moreover, the second run of stability tests on the pellet made from Trp is repeated (Run-2) in order to compare the mass of the hydrate pellet obtained after 15 days to those of the others. The 15-day stability test results are summarized in Table 4.5. All hydrates made from different solutions show similar results in terms of total methane release, which is about 12%. The major methane release is from the first day, which is greater than 50% of the total release.

Surprisingly, all hydrate pellets reach a final pressure release higher than the equilibrium pressure of mixed methane-THF hydrates at 283.2 K, which is 485 kPa (Lee *et al.*, 2012). Theoretically, the pressure released from the dissociation stops increasing at the equilibrium pressure. This further increase in the pressure over its equilibrium pressure could be explained by the difference in the hydrate-to-vessel volume ratio. For a small hydrate-to-vessel volume ratio, the gas is released to build up pressure, reaching the equilibrium pressure slowly. While there might be an overshoot in the pressure increase at the larger volume ratio. Further reducing the hydrate-to-vessel volume ratio lower than a certain value, all hydrates will be fully dissociated since it is impossible to release the gas to make up the equilibrium pressure.

Table 4.5 Comparison of the 15-day stability results of the hydrate pellets made from different solutions

Storage Condition [P & T]: Atmospheric Pressure and 283.2 K
Test Period: 15 Days

Solution	Mole gas consume (mol)	Water to hydrate conversion (%)	Pellet weight [IN] (g)	Pellet weight [OUT] (g)	% Weight Loss	After 24 hours			After 15 days		
						Pressure rise (kPa)	Mole gas loss (mol)	% Gas loss	Pressure rise (kPa)	Mole gas loss (mol)	% Gas loss
Formation Condition [P & T]: *298.2 K and 9.2 MPa*											
0.25 wt.% Leucine	0.4696	93.89	102.42	100.54	1.83	461.25	0.0385	8.18	649.48	0.0546	11.62
0.25 wt.% Methionine	0.4877	96.23	99.98	96.86	3.12	402.56	0.0337	6.88	680.50	0.0574	11.71
0.03 wt.% Tryptophan (Run-2)	0.4976	97.51	98.66	96.94	1.75	455.86	0.0381	7.71	669.13	0.0570	11.77
Formation Condition [P & T]: *293.2 K and 8 MPa*											
5.56 mol% THF	0.4315	88.97	100.55	98.98	1.56	469.53	0.0392	9.06	593.37	0.0497	11.53

4.5 Conclusion

The effect of the hydrophobicity of amino acid as a kinetic promoter in a mixed methane hydrate forming system with 5.56 mol% THF was clarified in this work. Five different amino acids, which are Glu, Val, Leu, Met, and Trp, were used. The addition of a hydrophobic amino acid (Leu, Met, and Trp) at its suitable concentration to a forming system promotes the water to hydrate conversion to completion, whereas a hydrophilic amino acid did not show any significant contributions compared to that without addition. The addition of a hydrophobic amino acid allowed a mixed methane-THF hydrates to form completely at room temperature (298.2 K) and 9.2 MPa. Trp, the most hydrophobic amino acid in the series, was found to be the best at promoting both gas uptake and the kinetics of the hydrate formation at a concentration of about 37-fold less than the others. Moreover, the addition of Trp has 2.85% and 9.81% higher methane uptake and18.61% and 123.81% lower normalized time to reach 90% of methane uptake compared to other hydrophobic amino acids. The addition of amino acid did not significantly alter the induction time of hydrate formation because stirring played a major contribution. The statistical analysis found a negative correlation between the normalized t_{90} and the MW of the amino acid. Furthermore, the addition of a hydrophobic amino acid did not only promote the kinetics but there was no foam formation during dissociation. This can overcome the drawback of using the conventional kinetic promoter, surfactants. Lastly, the stability of the hydrates was tested for 30 days. The hydrate pellet can stabilize itself at temperatures higher than the melting point of water and the equilibrium temperature at the atmospheric pressure of the hydrates. The overall methane loss was about 12%, which is the intrinsic loss due to its thermodynamics. It is believed that the hydrophobic amino acid is a game-changer for methane hydrate formation, which might further increase the chance of taking the SNG technology to commercialization within foreseeable time frames.

4.6 CRediT Authorship Contribution Statement

Kan Jeenmuang: Conceptualization, Methodology, Data curation, Formal analysis, Writing - review & editing, Visualization. **Phuwadej Pornaroontham:** Validation, Formal analysis, Writing - review & editing, Visualization. **Gaurav Bhattacharjee:** Validation, Writing - review & editing. **Santi Kulprathipanja:** Conceptualization, Supervision. **Praveen Linga:** Conceptualization, Supervision, Validation, Writing - review & editing. **Pramoch Rangsunvigit:** Conceptualization, Funding acquisition, Supervision, Validation, Writing - review & editing.

4.7 Acknowledgments

The authors acknowledge the financial support provided by the following organizations: Second Century Fund (C2F), Chulalongkorn University, and Thailand Science Research and Innovation Fund Chulalongkorn University CU_FRB65_ind (17)_203_63_05, Thailand. The authors also extend their sincere thanks to The Petroleum and Petrochemical College (PPC), Chulalongkorn University, Thailand; and The Department of Chemical and Biomolecular Engineering, Faculty of Engineering, National University of Singapore. Phuwadej Pornaroontham thanks the Ratchadapiseksomphote Endowment Fund for Postdoctoral Fellowship, Chulalongkorn University; Moreover, Pramoch Ransungvigit thanks Thailand Science Research and Innovation Fund Chulalongkorn University; Ratchadaphiseksomphot Endowment Fund, Chulalongkorn University, Thailand.

CHAPTER 5
MICRO KINETIC ANALYSIS OF THE CO_2 HYDRATE FORMATION AND DISSOCIATION WITH L-TRYPTOPHAN IN BRINE VIA HIGH PRESSURE IN SITU RAMAN SPECTROSCOPY FOR CO_2 SEQUESTRATION

5.1 Abstract

Hydrate-based CO_2 sequestration (HBCS) is widely recognized as a promising, long-term, and stable approach for CO_2 sequestration, but its slow formation kinetics in saline systems poses a significant challenge. In order to address this challenge, this experimental study investigated the potential of L–Tryptophan (L–Trp) as a CO_2 hydrate kinetic promoter in deionized water (DI) and brine systems. A high-pressure reactor coupled with in situ Raman spectroscopy was used to examine macro-level kinetics and micro-level Raman spectra. The CO_2 hydrate formation experiments were conducted at 3.5 MPa and 275.15 K with different L–Trp concentrations (0-3000 ppm) in both systems. Raman spectra were monitored throughout the hydrate formation process, identifying distinct peaks corresponding to dissolved CO_2, CO_2 hydrates, and water activity. The experimental results indicate that the addition of 1000 ppm L–Trp in DI significantly enhances the CO_2 uptake by 3.6–fold and promotes hydrate formation kinetics by 3.3–fold compared to the system without L–Trp. In the brine system (3.5 wt% NaCl), the optimal L–Trp concentration was found to be 2000 ppm, leading to a 1.5-fold increase in the CO_2 uptake. Remarkably, L–Trp not only enhances the formation kinetics but also facilitates dissociation and CO_2 recovery in DI. Nevertheless, the presence of NaCl hinders the promoting effect of L–Trp on the dissociation kinetics. These findings represent a significant advancement in feasible HBCS technology for CO_2 sequestration.

Keywords: Clathrate Hydrate; Carbon storage; Carbon dioxide; L–Tryptophan; Amino Acid, Raman Spectroscopy; Kinetic Promoter.

5.2 Introduction

The rise in global greenhouse gas emissions, primarily anthropogenic carbon dioxide (CO_2), has presented a pressing challenge in the form of climate change. In order to address this issue, the Paris Agreement aims to limit global warming to 1.5°C, necessitating a 50% reduction in CO_2 emissions by 2030 and the eventual establishment of a zero–carbon economy by 2050 (McGlade and Ekins, 2015; Zhao *et al.*, 2022). In this context, the utilization of CO_2 capture and storage through gas hydrates in deep oceanic sediments has garnered considerable attention due to their exceptional theoretical storage capacity of 180 v/v at standard temperature and pressure CO_2 (Pandey *et al.*, 2022). Gas hydrates are non-stoichiometric crystalline compounds formed when small gas molecules get trapped within water molecules at suitable pressure and temperature conditions (Sloan Jr and Koh, 2007). While hydrate–based CO_2 capture and sequestration offer numerous advantages, such as high storage capacity and reduced environmental impact, there are specific challenges that need to be addressed. Notably, the slow kinetics of CO_2 hydrate formation in bulk saline and freshwater systems due to mass transfer limitations at the gas–liquid interface (Xu *et al.*, 2020).

In recent years, the use of kinetic hydrate promoters, including amino acids and protein–based compounds possessing hydrophobic and hydrophilic moieties, has emerged as a promising strategy to enhance the kinetics of hydrate formation (Altamash *et al.*, 2017; M. F. Qureshi *et al.*, 2020). Prior research has demonstrated the significant influence of the hydrophobicity index of amino acid side chains on hydrate nucleation and growth (Jeenmuang *et al.*, 2023). Hydrophobic amino acids, such as L–tryptophan (L–Trp) and L–methionine, have been shown to accelerate the formation of methane hydrates (Veluswamy *et al.*, 2017b). In contrast, hydrophilic amino acids tend to impede kinetics (Sa *et al.*, 2016). Additionally, L–Trp and L–methionine have exhibited potential as CO_2 hydrate promoters, leading to improved formation kinetics (Cai *et al.*, 2017; Khandelwal *et al.*, 2020). L–Trp, in particular, has garnered attention as acost–effective, environmentally friendly, and low–dosage chemical agent (Motahari *et al.*, 2013; Tomé *et al.*, 2010). Notably, studies have indicated that the inclusion of L–Trp can enhance CO_2 gas uptake up to 4 times and increase water to hydrates conversion from 22% to 78% compared to systems without the promoter (Qureshi *et al.*, 2022a). However, it should be noted that the majority of research above has focused on freshwater systems, and there is a lack of experimental studies conducted in brine systems. Furthermore, despite the insights provided by gas uptake profiles and kinetics, there remains a scarcity of in situ spectroscopic investigations concerning the effect of L–Trp on CO_2 hydrate formation in both freshwater and brine systems. In nature, oceanic water is saline, and the presence of salinity is likely to affect the performance of L-Trp and the kinetics of CO_2 hydrate formation. This is a significant challenge, and it limits the application of L-Trp. In order to address this challenge, experiments are required to understand the potentials and limitations of L-Trp in brine systems (3.5 wt% NaCl) at macro and micro scales. These microscopic studies are essential to understand the functioning of L-Trp as a promoter and comprehend the changes occurring in hydrate structure, cage occupancy, gas-dissolving activity, and spectral behavior during CO_2 hydrate formation for both non-brine and brine systems in the presence of gas hydrate promoters like L-Trp.

Raman spectroscopy has gained significant attention in gas hydrate research due to its capability for in situ analysis, non–destructive nature, and ease of operation. This technique offers valuable insights into various aspects of a substance, such as its composition and molecular orientation (Jin *et al.*, 2014). Furthermore, confocal Raman spectroscopy quantifies gas concentrations (CO_2 and CH_4) in aqueous solutions across diverse temperature and pressure ranges, correlating with the intensity of active Raman species (Caumon *et al.*, 2014). It is a crucial tool for monitoring CO_2 particles injected into the deep ocean for carbon sequestration, enabling the observation of variations in Raman strength and frequency of CO_2 molecules (Pasteris *et al.*, 2004).

In the context of CO_2 hydrate, Raman spectroscopy identifies characteristic peaks at 1276.6 cm^{-1} and 1380.4 cm^{-1}, whereas in CO_2 dissolved form, the peaks are observed at 1276.0 cm^{-1} and 1383.5 cm^{-1} in pure aqueous solutions (Chen *et al.*, 2015). Notably, the CO_2 Raman peak positions in hydrates, aqueous solutions, and vapor phases exhibit similarities, causing a distinct band shift with CO_2 phase accumulation. Water molecules' O–H stretching band, integral for observing Raman spectrum changes, undergoes alterations during hydrate formation, impacting the hydrogen-bonded network (Zhao and London, 2006). Therefore, understanding the O–H stretching band can explain changes in hydrate structure during CO_2 hydrate formation (Perchard, 2001; Schicks *et al.*, 2005). in situ Raman spectroscopy, employed by Yao *et al.* (2023) investigated the promotion of CO_2 hydrate formation using low-dose dioxolane (DIOX). Their findings on the CO_2/DIOX Raman peak intensity ratio provided molecular insights, indicating an increase in the CO_2 fraction in the binary hydrate.

In this study, real–time in situ Raman spectroscopy was employed to monitor the formation of a significant quantity of CO_2 hydrates at 275.15 K and 3.5 MPa in the presence of L–Trp as a kinetic promoter, both in deionized water (DI) and brine containing salt ions (NaCl). The kinetics and morphological characteristics of CO_2 hydrate formation were investigated with different dosages of L–Trp (0–3000 ppm) and NaCl (0–3.5 wt%). The impact of these chemicals on carbon sequestration applications was also elucidated. Changes in the intensity, pattern, and position of the Raman spectra for CO_2 and the O–H stretching band of water were observed and analyzed. Furthermore, the relationship between the ratio of peak intensities and the results of hydrate formation kinetics was analyzed to propose the mechanism of CO_2 hydrate formation.

5.3 Experimental

5.3.1 Materials and Apparatus

The experimental setup for the study involved the use of specific materials and equipment as follows: high–purity carbon dioxide gas (99.9%) was purchased from Air Liquide Singapore Private Limited, while reagent–grade L–tryptophan (L–Trp, ≥98% purity) and sodium chloride (NaCl, ≥99.0% purity) were obtained from Sigma–Aldrich, Singapore. All trials utilized ultrapure deionized water (DI) acquired through reverse osmosis and purified by bactericidal ultraviolet light technology in conventional equipment supplied by Merck Millipore.

Figure 5.1 illustrates the experimental setup, which consisted of a 225–cm^3 full stainless–steel crystallizer with a cooling jacket and a magnetic bar stirring system (model: MIXdrive, 2mag magnetic motion) connected to a refrigerated bath circulator (model: SD07R-20, Polyscience). A 300–cm^3 supply vessel was linked to the crystallizer to increase the available amount of CO_2 for hydrate formation. Real–time pressure and temperature monitoring were conducted using a pressure transducer (model: A-10, WIKA) and thermocouples (Type T, Omega) connected to a National Instruments Data Acquisition (DAQ) system, which was then connected to a computer running LabVIEW software. Additionally, a real–time in situ Raman instrument (Model: SRaman–532, W2 Innovations, Inc) was connected to the reactor, providing ongoing data on hydrate formation and dissociation. The Raman probe, positioned in the reactor at a specific location submerged in the solution, allowed precise laser targeting to a designated area in front of the probe. The Raman instrument utilized a 532 nm Nd:YAG laser with a power of 42 mW, covering a spectral range of 150–4490 cm^{-1} with a resolution of 2.8 cm^{-1}/pixel at 2200 cm^{-1}. The integration time for acquiring Raman spectra during the hydrate formation experiments was set to 3.0 seconds. It featured an SF18 Spectrograph, a front-illuminated CCD, a 2-meter-long fiber cable of 100 mm diameters, and a Raman Probe at a laser wavelength of 532 nm. The Raman probe was inserted through the reactor and positioned at a specific location submerged in the solution. The laser was then directed to a specific area of solution in front of the probe inside the reactor. The incorporation of Raman investigation offers insights into the micro-level hydrogen bond network of water cages and the behavior of CO_2 molecules during CO_2 hydrate formation. Furthermore, the CO_2 hydrate ratio obtained through Raman investigation proves to be a potentially valuable indicator for assessing CO_2 hydrate formation.

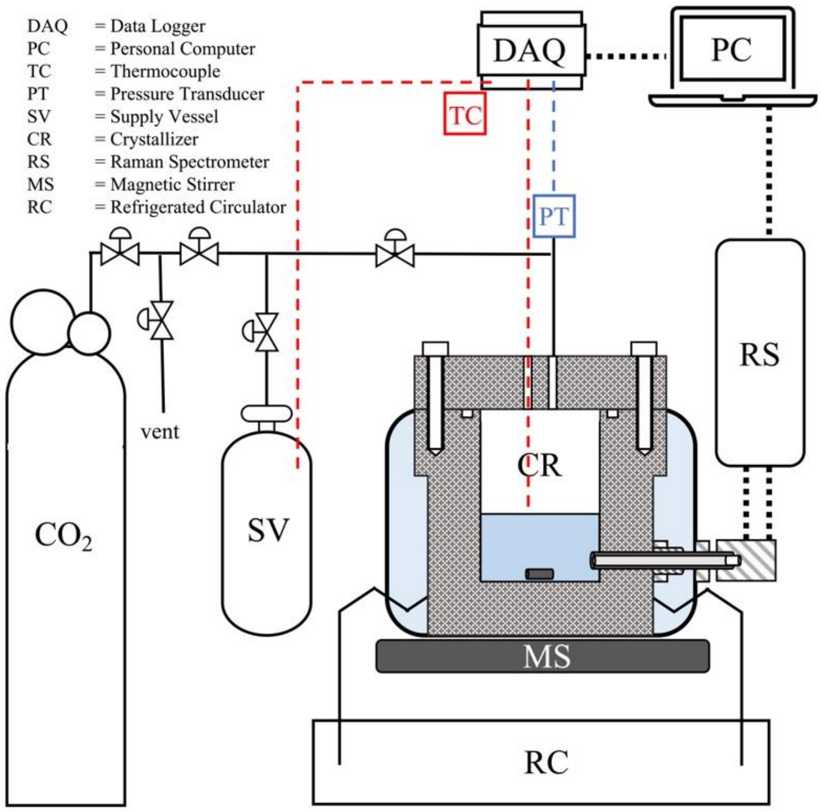

Figure 5.1 Experimental set–up schematic.

5.3.2 Hydrate Formation and Dissociation Procedures

A batch–type crystallizer equipped with a Raman spectrometer and a stirred reactor configuration was employed. Initially, a 50 cm^3 aqueous solution of L–Trp at varying concentrations was loaded into the crystallizer. Three CO_2 purges were carried out to prevent the ingress of undesired gases. The working temperature was maintained at 275.2 K, and an excess CO_2 feed pressure of 3.5 MPa was applied. After initiating the CO_2 feed, stirring at 700 rpm, and initiating the hydrate formation process, the system was allowed to reach equilibrium for a minimum of 5 minutes. The stirring system remained active until the completion of hydrate formation and was halted just before the initiation of hydrate dissociation. Throughout the experiment, the temperature and pressure were continuously monitored until the pressure drop remained below 50 kPa for one hour. After the completion of hydrate formation, the temperature of the crystallizer was raised to 308.2 K to initiate dissociation. The temperature and pressure were consistently recorded until all the hydrates were molten.

In the experiment conducted with brine water, the same procedure was replicated, except for replacing the L–Trp aqueous solution with a mixture of NaCl and L-Trp at varying concentrations. In order to ensure the reliability of the results, each experiment was repeated three times. The calculations of CO_2 hydrate formation and dissociation parameters are provided in the supporting information, and these values were derived from previous research (Khandelwal *et al.*, 2020). Meanwhile, a new parameter was explored to assess CO_2 hydrate formation from a different perspective.

The normalized time required to achieve 90% completion of hydrate formation, referred to as $t_{90,norm}$, was determined using equation (5.1).

$$t_{90,norm}\ (\text{min/(mmol/mol)}) = \frac{t_{90}\ (\text{min})}{CO_2\ \text{uptake}_{\text{at } 90\%}\ (\text{mmol/mol})} \quad (5.1)$$

To evaluate the dissociation performance, the CO_2 recovery was measured by monitoring the pressure buildup in the system during the dissociation process. The time required to achieve 90% of CO_2 recovery, normalized by its conversion, was calculated as $t_{90d,norm}$ using the following equation (5.2).

$$t_{90d,norm}\ (\text{min/\%}) = \frac{t_{90d}\ (\text{min})}{\text{total water to hydrate conversion (\%)}} \quad (5.2)$$

5.3.3 <u>in situ Raman Spectroscopy of CO_2 Hydrate Formation and Dissociation</u>

The Raman spectra obtained during the hydrate formation and dissociation experiments had an integration time of 3.0 seconds with a time interval of 5.0 minutes. The Raman spectra were analyzed using the Origin Pro 2021b SR2 license provided by the National University of Singapore. Initially, the baselines of the Raman spectra were corrected. The study focused on two specific ranges: 1250 – 1425 cm^{-1} for CO_2 dissolution and CO_2 in hydrates and 2800 – 3800 cm^{-1} for the stretching of O–H bond in water molecules, as depicted in Figure 5.2. During the formation of CO_2 hydrates, changes in the CO_2 concentration were observed through two distinct bands: a lower wavenumber band ($CO_{2,lo}$) around 1270 – 1280 cm^{-1} and an upper wavenumber band ($CO_{2,up}$) around 1375 – 1381 cm^{-1}. The peak intensity and wavenumber of both CO_2 spectra were investigated. Regarding water molecules, the Raman spectrum displayed two broad overlapping bands ranging from 2800 to 3800 cm^{-1}. Within these bands, five sub–bands were observed and subsequently deconvoluted using a Gaussian function. The constraints on peak position and their Full Width at Half Maximum (FWHM) for the deconvolution of water O–H bands were analyzed based on the methodologies outlined by Sun (2013) and Choe *et al.* (2016). The constant values employed in this study are presented in Table 5.1. Given that the shape and position of the O–H stretching spectra can be affected by variations in the hydrogen bond network, careful analysis was conducted to investigate the intensity and wavenumber of these sub–bands.

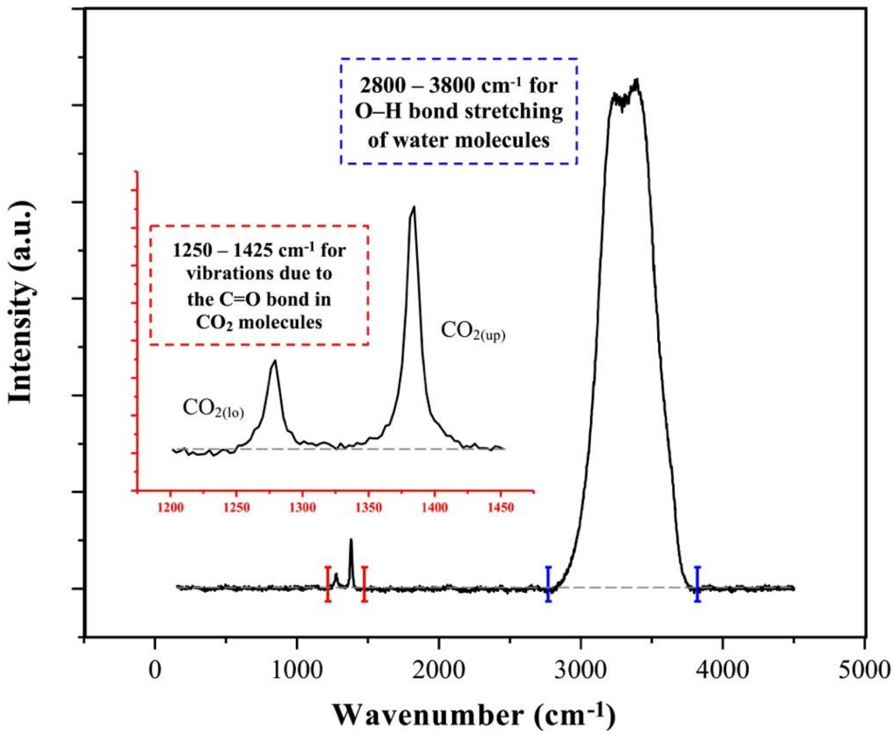

Figure 5.2 Raman spectra showing peak positions of CO_2 and H_2O molecules at different wavenumbers.

Table 5.1 Constant values for the Raman spectrum of water in the O–H stretching region based on the methodologies outlined in Sun (2013) and Choe *et al.* (2016)

MODE	275 K	
	Frequency	FWHM
DAA-OH	2990 - 3010	0 - 150
DDAA-OH	3200 - 3250	0 - 235
DA-OH	3400 - 3450	0 - 225
DDA-OH	3550 - 3600	0 - 150
FREE OH	3600 - 3650	0 - 115

5.4 Result and Discussion

5.4.1 Effect of L–Trp on CO_2 Hydrate Formation in DI Water Systems

5.4.1.1 Promoting Effect of L–Trp on CO_2 Hydrate Formation

A controlled experiment was initially conducted using DI water to facilitate CO_2 hydrate formation at a temperature of 275.2 K and a pressure of 3.5 MPa. The CO_2 uptake was continuously monitored over time, and the temperature profile during the experiment is illustrated in Figure 5.3 (a). Following the introduction of CO_2 gas into the system, the uptake of CO_2 gradually increases until reaching a plateau at approximately 35.16 mmol of gas per mole of water (mmol/mol), which is equivalent to 24.72% water to CO_2 hydrate conversion. The highest temperature change observed is about 2 K. Interestingly, the rise in the gas uptake exhibited two distinct steps, as indicated by the temperature spikes observed in the profile. The first spike, which occurs approximately 8 minutes after the introduction of CO_2, is likely due to the dissolution of CO_2 and CO_2 hydrate nucleation, referred to as stage–I. The second spike indicates hydrate formation, stage–II. Both processes are exothermic in nature, leading to an increase in temperature. The time taken from the start until the CO_2 hydrate nucleation is denoted as the induction time (t_{ind}). The temperature returns to the set value after 75 minutes, implying the hydrate formation is over. The duration of the experiment is extended to

300 minutes to validate the progress of hydrate formation. However, no changes is observed during this period. The conversion is far from completion, indicating that not all water molecules are fully utilized. This observation is supported by a photograph in Figure 5.4 (a), which clearly shows the presence of wet hydrates. A similar observation was reported earlier by Khandelwal *et al.* (2020) in a freshwater (deionized) system.

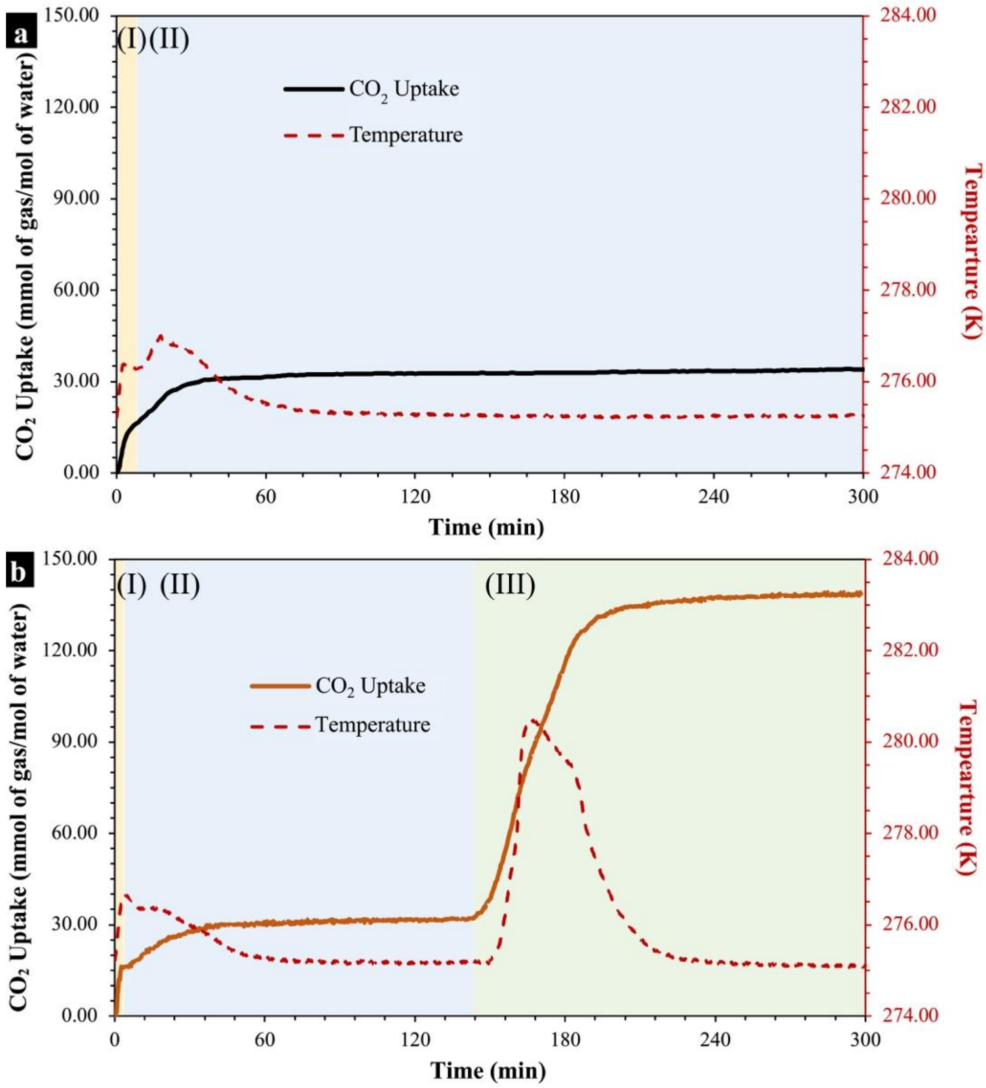

Figure 5.3 Profiles of CO_2 uptake and temperature during CO_2 hydrate formation in DI water: (a) in the absence of L–Trp and (b) with the addition of 500 ppm L–Trp. The background colors and the Roman numerals represent the stages of hydrate formation; yellow (stage I), blue (stage II) and green (stage III).

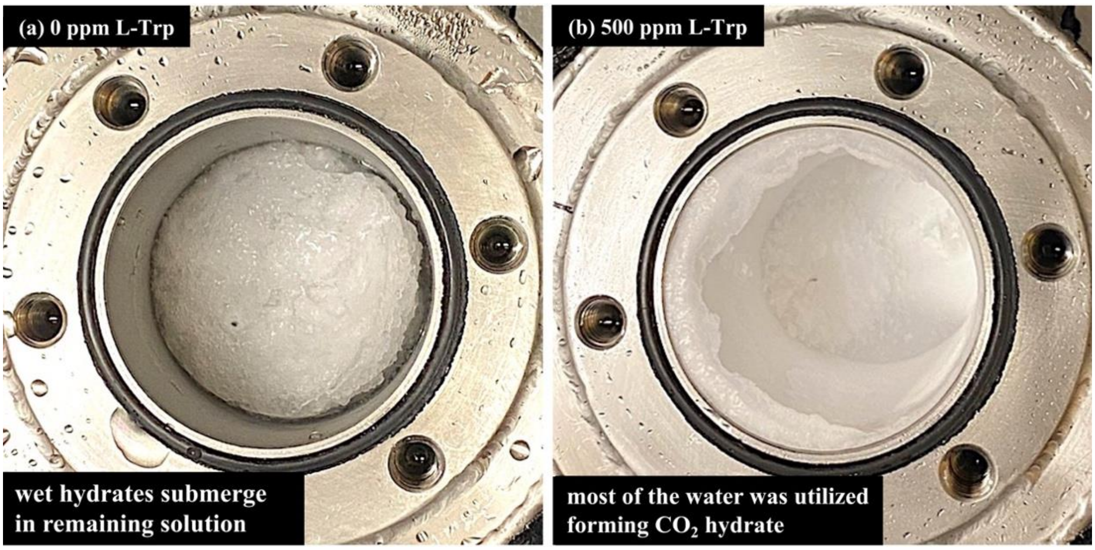

Figure 5.4 Morphological photographs of CO_2 hydrates formed at 275.2 K and 3.5 MPa (a) without L–Trp and (b) with 500 ppm L–Trp.

To address this issue, L–Tryptophan (L–Trp), a kinetic promoter, was introduced to the system at a concentration of 500 ppm. A similar concentration (500 ppm) was used by Qureshi *et al.* (2022a), and they reported an enhancement in the overall water to hydrate conversion from 82 to 98% and a reduction in the overall hydrate formation process time by 2.5 times using liquid CO_2. This motivated us to use the same concentration for this work. The hydrate formation experiment process was then conducted again, and the results are depicted in Figure 5.3 (b). In the presence of 500 ppm L–Trp in DI water, the CO_2 uptake initially follows a similar pattern as observed in the previous experiment, gradually increasing until reaching a plateau of approximately 32.27 mmol/mol, which corresponds to 22.68% conversion, after 75 minutes of CO_2 introduction. The temperature increases by around 1.5 K during this process. Even after t = 143 min, the hydrate formation continues, accompanied by a significant temperature increase of 5.5 K. This indicates a secondary growth of hydrates, stage–III. The hydrate formation concludes at t = 225 min when a total hydrate conversion of 97.13% (138.17 mmol/mol) is achieved. This indicates that most of the water is utilized in the process, as observed in Figure 5.4 (b).

L-Trp was selected as a promoter due to its amphiphilic properties and amino acids environmentally benevolent nature (Qureshi *et al.*, 2021; Zheng *et al.*, 2020). The actual mechanism by which L-Trp provides a promotional effect is still not clear. However, it has been widely reported that the hydrophilic carboxylic and amine groups of L-Trp are likely to attract more CO_2 molecules, increasing their local concentration and forming CO_2 pockets within the solutions (Bhattacharjee and Linga, 2021; Qureshi *et al.*, 2022b). Water near these pockets may tend to avoid the hydrophobic end of L-Trp, resulting in local water ordering in the form of empty cages. When this local ordering water combines with a higher concentration of CO_2 in the solution, a faster rate of CO_2 hydrate kinetics is likely to occur (Dhamu *et al.*, 2023; Fahed Qureshi *et al.*, 2022). Further insights into the mechanism have been provided by Bhattacharjee et al. (Bhattacharjee and Linga, 2021).

To gain microscopic insights into CO_2 hydrate formation, in situ Raman spectra were examined during the hydrate formation process with and without L–Trp. Two specific wavenumber ranges are of interest: 1250 - 1425 cm^{-1}, representing vibrations due to the C=O bond in CO_2 molecules and 2800 - 3800 cm^{-1}, representing vibrations of the O–H bond in water molecules.

In the absence of L–Trp, CO_2 in the system exhibit two distinct sharp Raman bands, $CO_{2,lo}$ and $CO_{2,up}$, as shown in Figure 5.5 (a1). The intensity of both CO_2 Raman bands increases during CO_2 hydrate formation, indicating an increased amount of CO_2 in the system. The peak shifting can be observed in Figure 5.5 (a2). For ease of visualization, the dashed lines at 1276.3 and 1381.4 cm^{-1} represent the peak position of dissolved CO_2 that is confirmed by the dissolution of CO_2 at different temperatures 275.2 and 278.2 K, at the same pressure of 3.5 MPa (Figure 5.6). Initially, during the CO_2 nucleation and formation stage (stage-II), distinct peaks corresponding to $CO_{2,lo}$ and $CO_{2,up}$ bands are observed at 1276.3 and 1381.4 cm^{-1}, respectively (t = 15 min). As the CO_2 hydrate formation progresses, the Raman bands for both $CO_{2,lo}$ and $CO_{2,up}$ exhibit a noticeable shift towards lower wavenumbers, specifically to 1273.2 and 1378.3 cm^{-1}, respectively, as observed at t = 30, 45, and 60 min. Interestingly, after the completion of CO_2 hydrate formation, a reversible shift in the CO_2 Raman peaks is observed, with the bands returning to their original positions at t = 300 min.

The reversibility of peak shift may be due to the dynamic interaction between CO_2 molecules and water cages during different stages of CO_2 hydrate formation and CO_2 gas dissolution. In the initial stages, where the rate of hydrate formation exceeds the dissociation rate, CO_2 molecules are preferentially captured within the water cages, resulting in a strong interaction between CO_2 and the surrounding water molecules. This interaction may restrict the movement of CO_2 molecules, leading to weaker vibrations of the C=O bond and the observed red shift in the Raman peaks (Le *et al.*, 2020; Rodriguez Machine, 2021). However, as the system reaches equilibrium at a conversion of 24.72% after 60 minutes, a reversible shift occurs, indicating a change in the distribution of CO_2 molecules between the hydrate and solution phases. The observed behavior might be explained by the migration of hydrate structures within the crystallizer. The low conversion results in hydrates floating towards the surface, displacing the solution phase towards the bottom where the Raman probe is placed. Consequently, the probe primarily detects CO_2 molecules in the solution phase.

For the system with 500 ppm L–Trp, the peaks corresponding CO_2 start shifting from 1276.3 and 1381.4 cm^{-1} (t = 15 min) to lower wavenumbers of 1273.2 and 1378.3 cm^{-1} at t = 180 min, shown by Figure 5.5 (b1–2). This shift indicates the predominant phase of secondary hydrate growth. The peaks then remain at the same position until the end of the experiment at t = 300 min. As the conversion reaches 97.13%, the crystallizer predominantly contains hydrates, and the reversibility of peak shifting cannot be observed.

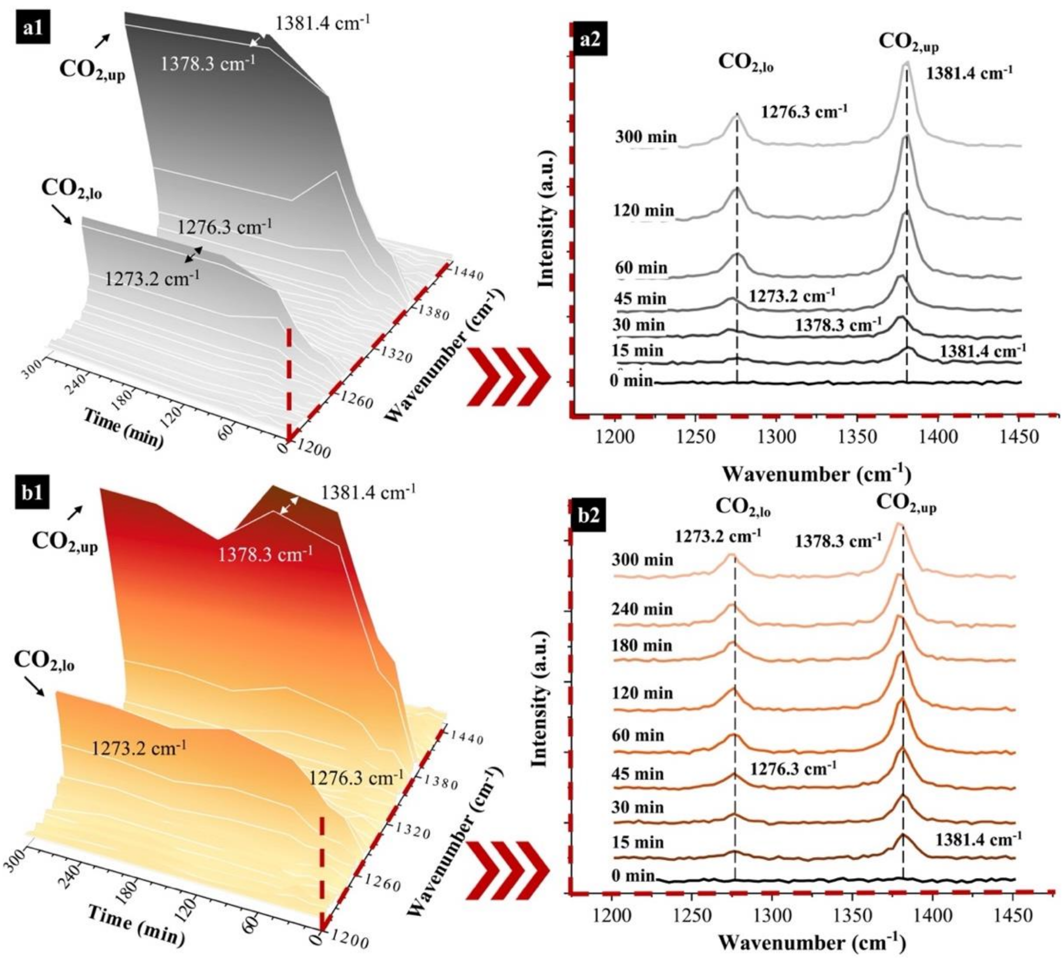

Figure 5.5 3D and 2D Plots representing the two distinct Raman bands ($CO_{2,lo}$ and $CO_{2,up}$) of the C=O bond Raman spectra in CO_2 molecules during CO_2 hydrate formation at 275.2 K and 3.5 MPa: (a) without L–Trp and (b) with 500 ppm L–Trp.

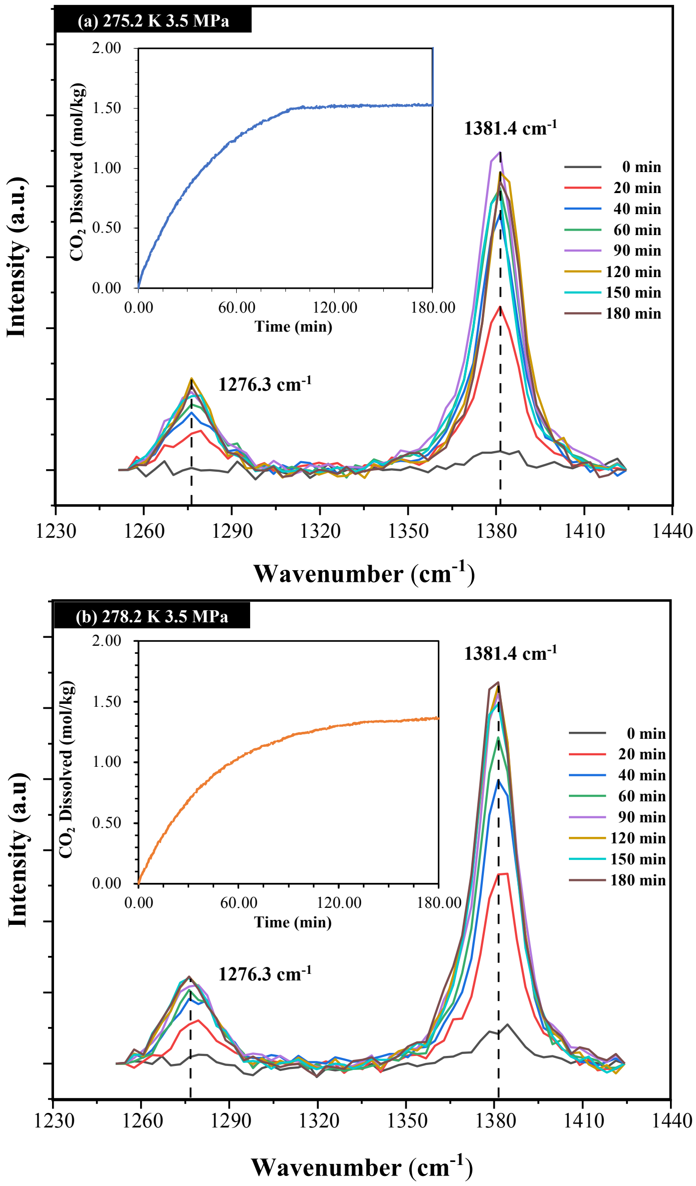

Figure 5.6 Raman peak positions of dissolved CO_2 in different conditions (a) 275.2 K and 3.5 MPa and (b) 278.2 K and 3.5 MPa.

Raman spectra of water molecules displays two overlapping broad bands (around 3225.0 cm^{-1} and 3400.0 cm^{-1}) corresponding to the vibrations of the O–H bond. In the absence of L–Trp, the O–H Raman band in Figure 5.7 (a1) exhibits a two-stage pattern similar to CO_2 hydrate formation, reflecting the growth profiles of the hydrates. Over time, three distinct behaviours are observed: (1) a decrease in spectral intensity, (2) a shift towards lower wavenumbers, and (3) an increase in the proportion of the peak at 3225.0 cm^{-1} with a decrease in the proportion of the peak at 3400.0 cm^{-1}, as shown in Figure 5.7 (a2). In the presence of 500 ppm L–Trp, the water Raman spectra in Figure 5.7 (b1) also demonstrate the three stages of CO_2 hydrate formation associated with L–Trp. These behaviours are more pronounced and distinct, as illustrated in Figure 5.7 (b2).

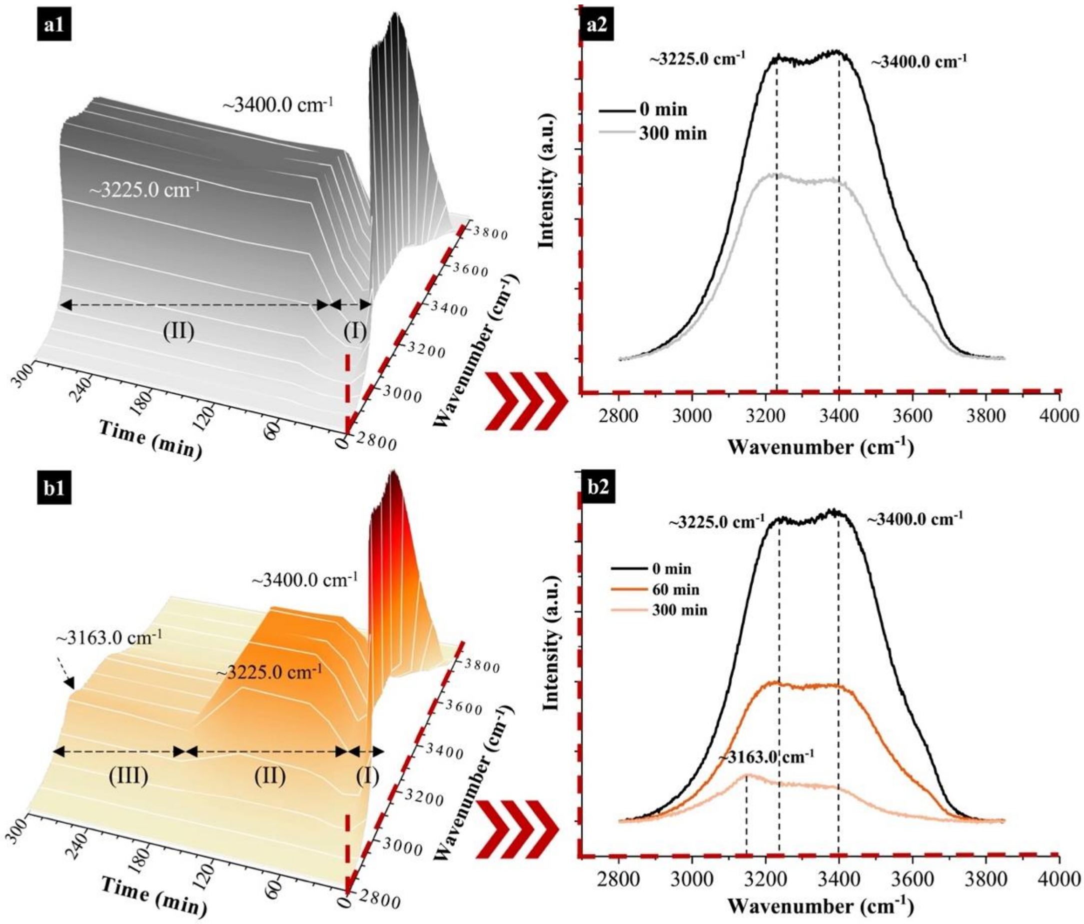

Figure 5.7 3D and 2D Plots representing the Raman spectra of the O–H bond in water molecules during CO_2 hydrate formation at 275.2 K and 3.5 MPa: (a) without L–Trp and (b) with 500 ppm L–Trp.

In order to gain a clearer understanding of the relationship between water Raman spectra and CO_2 hydrate formation, the observed water band was deconvoluted into five sub–bands, using a Gaussian function, representing different stretching modes of water O–H groups involved in distinct hydrogen bonding patterns (Sun, 2013). These sub-bands ranging from 3000 cm^{-1} to 3800 cm^{-1} include DAA O–H (single donor–double acceptor), DDAA O–H (double donor–double acceptor), DA O–H (single donor–single acceptor), DDA O–H (double donor–single acceptor), and Free O–H hydrogen bonding of water molecules, respectively, as shown in Figure 5.8. After deconvoluting the water Raman band, the shifting of the Raman spectra became more apparent. The dashed lines representing significant O–H sub–bands (DDAA at 3225 cm^{-1} and DA at 3400 cm^{-1}) clearly demonstrate that the Raman bands shift to lower wavenumbers in both cases, with and without L-Trp, as shown in Figure 5.9 and Figure 5.10, respectively. Without L–Trp, a slight red shift from 3214 cm^{-1} to 3199 cm^{-1} is observed during CO_2 hydrate formation, while with 500 ppm L–Trp, a significant shift from 3215 cm^{-1} to 3159 cm^{-1} is observed. This larger shift can be attributed to the secondary hydrate growth exclusively in the system with L–Trp, leading to the immobilization of most water molecules through the hydrogen bonding network of water cages.

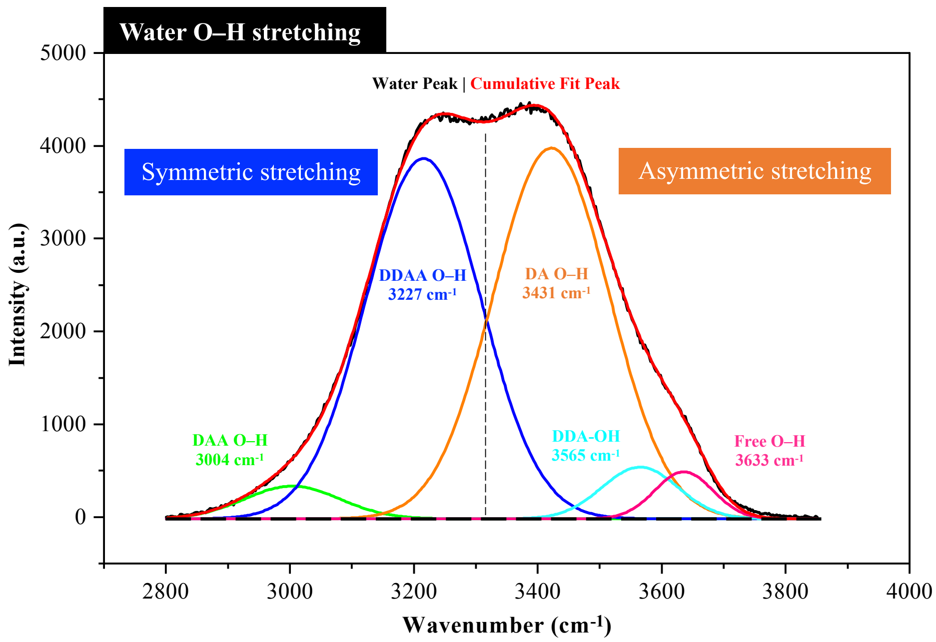

Figure 5.8 Deconvolution of Raman spectra of H_2O at 275.2 K, showing five sub-bands of O–H stretching: DAA (single donor–double acceptor), DDAA (double donor–double acceptor), DA (single donor–single acceptor), DDA (double donor–single acceptor), and Free O–H.

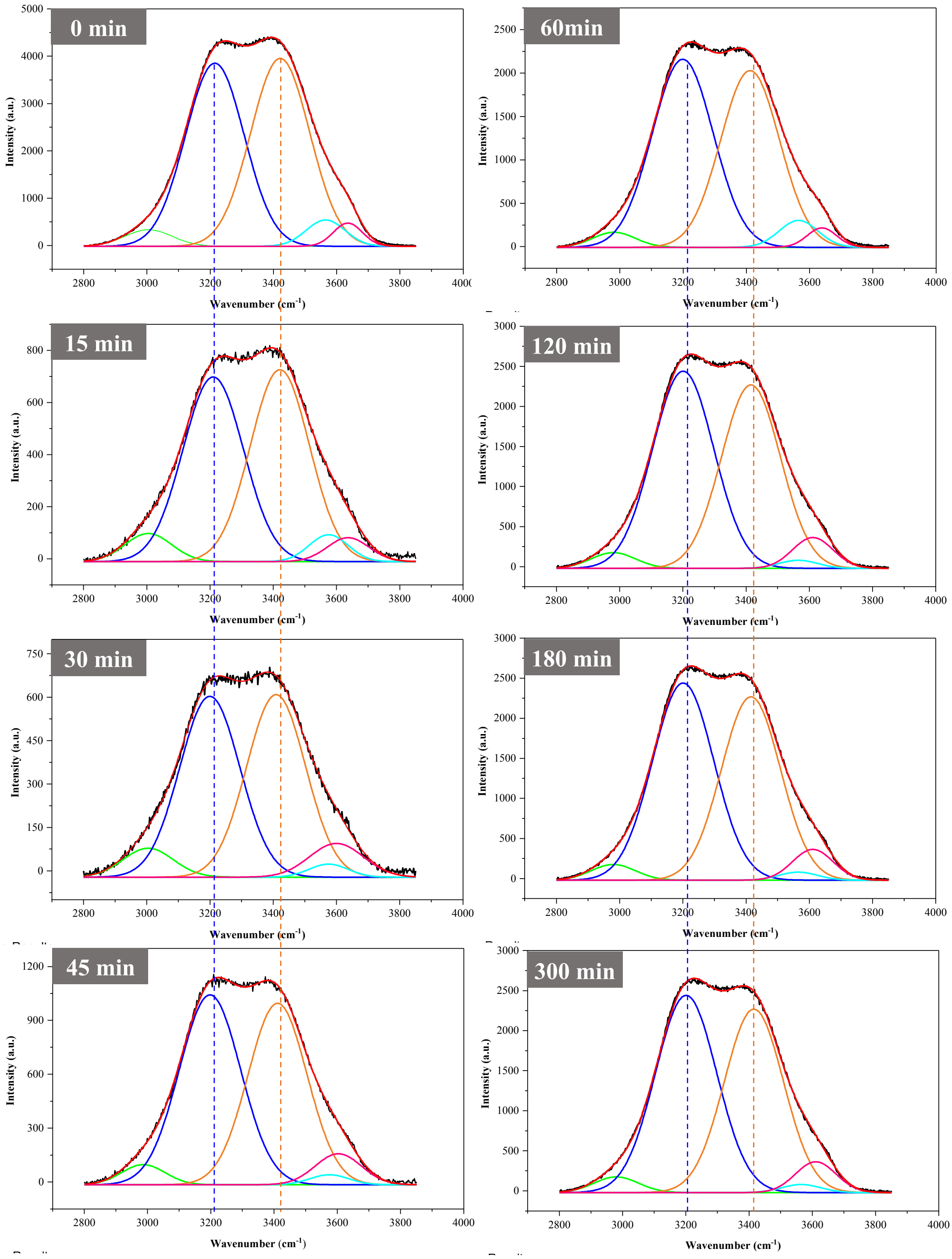

Figure 5.9 Deconvolution of Raman spectra of H_2O during CO_2 hydrate formation in the absence of L–Trp.

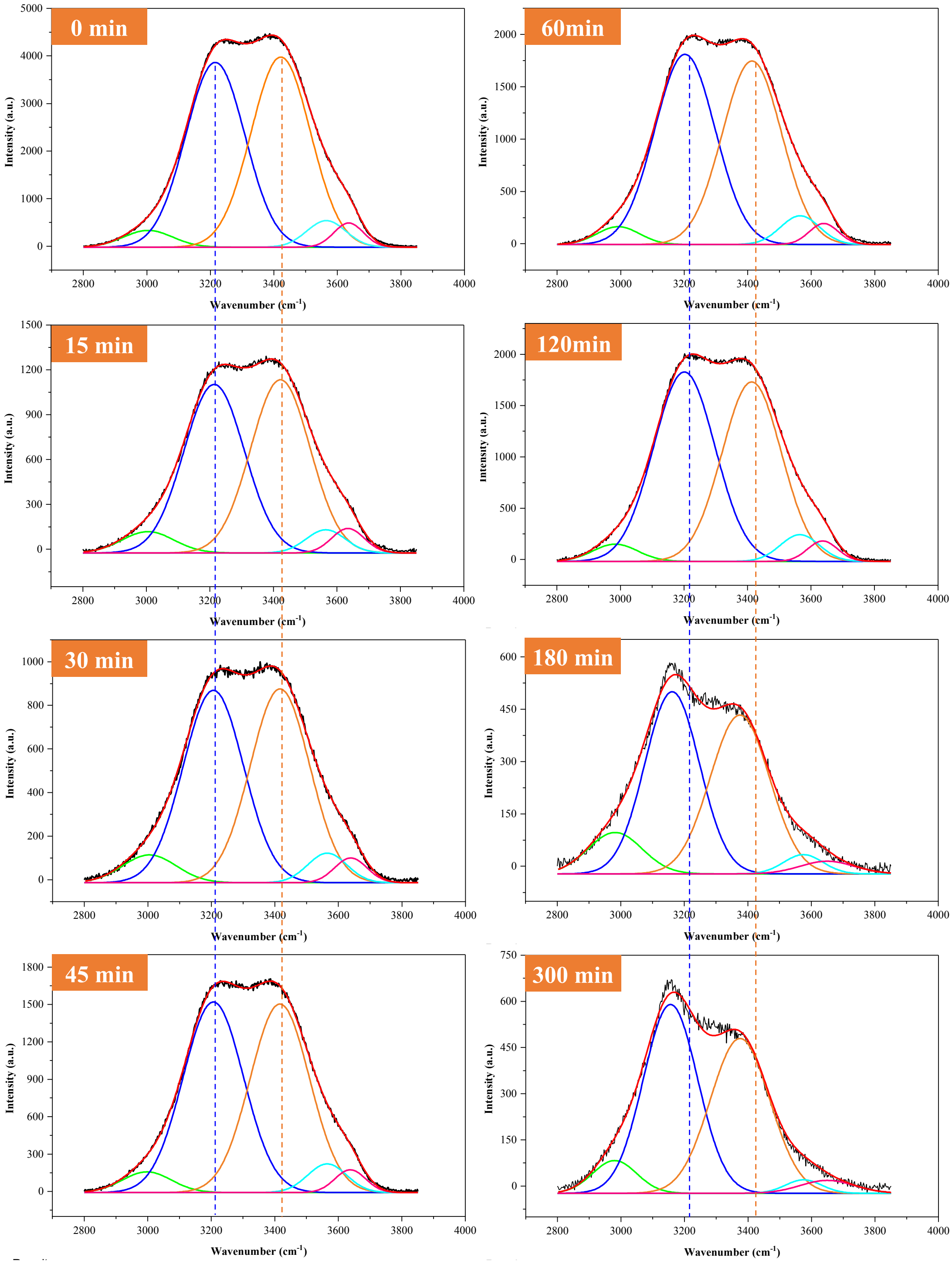

Figure 5.10 Deconvolution of Raman spectra of H_2O during CO_2 hydrate formation in the presence of 500 ppm L–Trp.

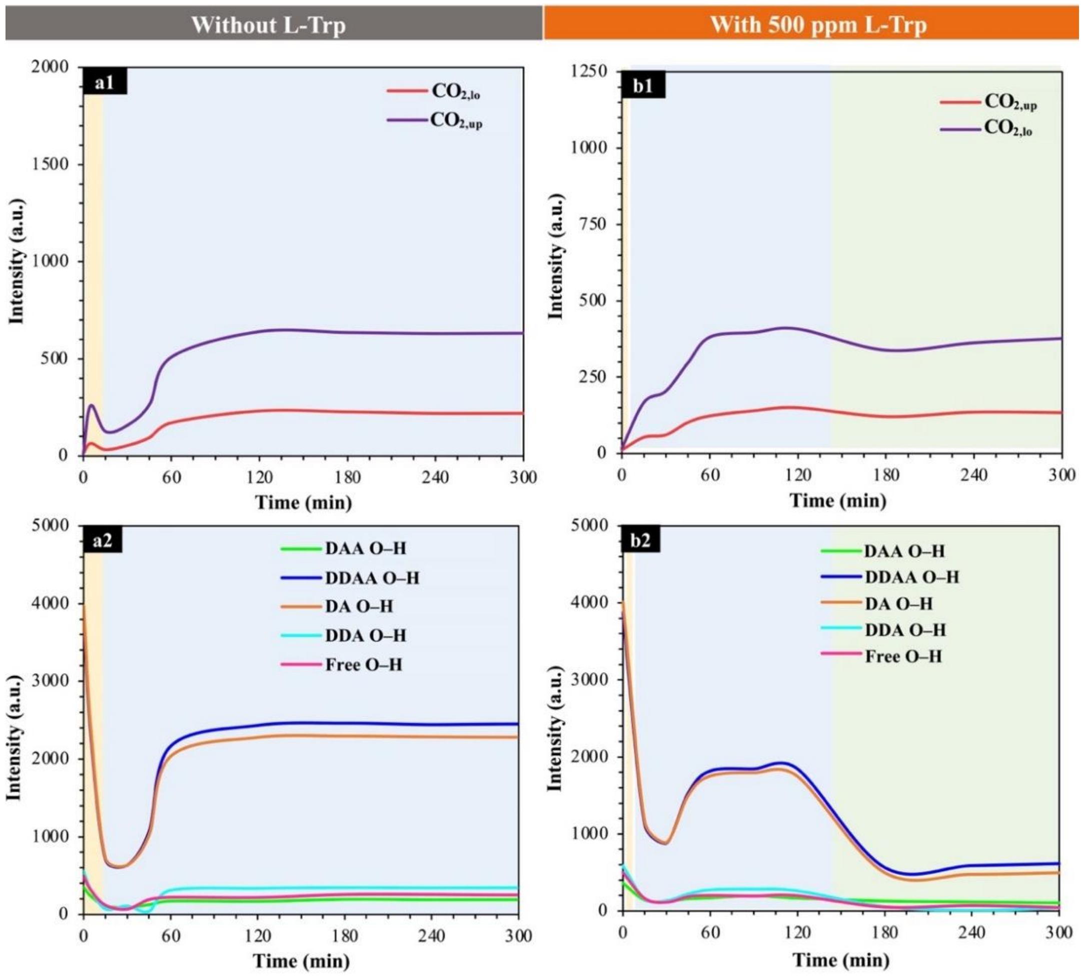

Figure 5.11 Intensity of Raman spectra for (1) CO_2 and (2) H_2O sub-bands in (a) absence of L–Trp (0 ppm) and (b) presence of 500 ppm L–Trp.

Figure 5.11 illustrates the intensity profiles of the CO_2 hydrate and water sub-bands. As CO_2 hydrate formation progresses, the intensity of each CO_2 Raman band shows an increase, likely indicating the gradual accumulation of CO_2 within the hydrate structure (Figure 5.11 (a1) and (b1)). Meanwhile, the Raman band associated with O–H stretching exhibits distinct behavior: it displays two stages during CO_2 hydrate formation in the absence of L–Trp, and three stages when 500 ppm L–Trp is present (Figure 5.11 (a2) and (b2)). Conversely, as hydrate nucleation and formation occur, the intensity of each Raman band decreases. This decrease is attributed to the reduction in water concentration due to the formation of the hydrate structure (Truong-Lam *et al.*, 2019). Furthermore, an intriguing observation includes the increase in the proportion of the sub-peak corresponding to DDAA, coupled with a decrease in the proportion of the peak corresponding to DA. This change indicates a strengthening of the hydrogen bonding within the aqueous solution systems (Li *et al.*, 2021). Consequently, the positions and proportions of these five sub-peaks can serve as indicators for changes in the hydrogen bond network of water.

Among the various water O–H stretching modes, the DDAA motif corresponds to the symmetric stretching of four hydrogen bonds, forming a tetrahedral geometric structure. Considering that the hydrogen bonding network in gas hydrate structures primarily consists of tetrahedral hydrogen bonds between neighbouring water molecules (Sloan Jr and Koh, 2007), an increase in the intensity of DDAA suggests an increase in the number of tetrahedral H–bonds resulting from hydrate cage formation. DDAA and DA represent predominant hydrogen bonding configurations within water and are likely the key contributors to the phase transition that occurs during hydrate formation. The relative intensity comparison from Raman spectroscopy between dissolved gas and water has been employed to predict gas solubilities in water under varying conditions (Guo *et al.*, 2014; Ou *et al.*, 2015). This ratio is typically derived by dividing the intensity of the primary gas peak by that of water. Specifically for CO_2, it involves the ratio between $I_{CO_{2,up}}$ and I_{DA} of water. However, during hydrate formation, the dominant primary peak shifts to DDAA due to the prevalence of tetrahedrally bonded water in cage structures. In order to adapt to this scenario, a modification is proposed by using I_{DDAA} as the denominator, resulting in a CO_2 hydrate ratio designed to monitor changes in the formation process, as outlined in equation (5.3). Analyzing these relative intensities offers insights into the transformations unfolding during CO_2 hydrate formation and the intricate interactions between CO_2 and water molecules.

$$CO_2 \text{ Hydrate Ratio} = \frac{I_{CO_{2,(up)}}}{I_{DDAA\ O\text{–}H}} \tag{5.3}$$

Furthermore, the intensity ratio of water between the DDAA and DA modes can be established as an indicative measure of water activity in the process of CO_2 hydrate formation, as equation (5.4) (Đuričković *et al.*, 2011).

$$\text{Water Activity Ratio} = \frac{I_{\text{DDAA O–H}}}{I_{\text{DA O–H}}} \tag{5.4}$$

The relative intensity of CO_2 hydrate and water activity ratios in DI water are presented in Figure 5.12 (a). The relative intensity for CO_2 hydrate starts from zero, indicating no CO_2 present initially. The ratio rapidly increases to a value of 0.25 at first and then slightly further to 0.26, indicating the progressive accumulation of CO_2 within the hydrate structure. Meanwhile, the water activity ratio starts at 0.97 and increases over time until it saturates at 1.07. The increase in water activity likely suggests an increase in tetrahedrally bonded water (DDAA) and a decrease in DA motif, which signifies the formation of the hydrate cage structure. In contrast, the system containing 500 ppm L–Trp exhibits three stages of hydrate formation, as shown in Figure 5.12 (b), with the CO_2 hydrate ratio initially increasing to 0.21 at a hydrate conversion of about 23%. After a momentary saturation, the ratio starts increasing again, reaching 0.625 at a hydrate conversion of 97%. Similarly, the water activity ratio in the L–Trp system starts at 0.97, increases to 1.05, and reaches saturation at 1.25. The magnitudes of CO_2 hydrate and water activity ratios are in good agreement with the stage of formation in hydrate formation profiles, Figure 5.3.

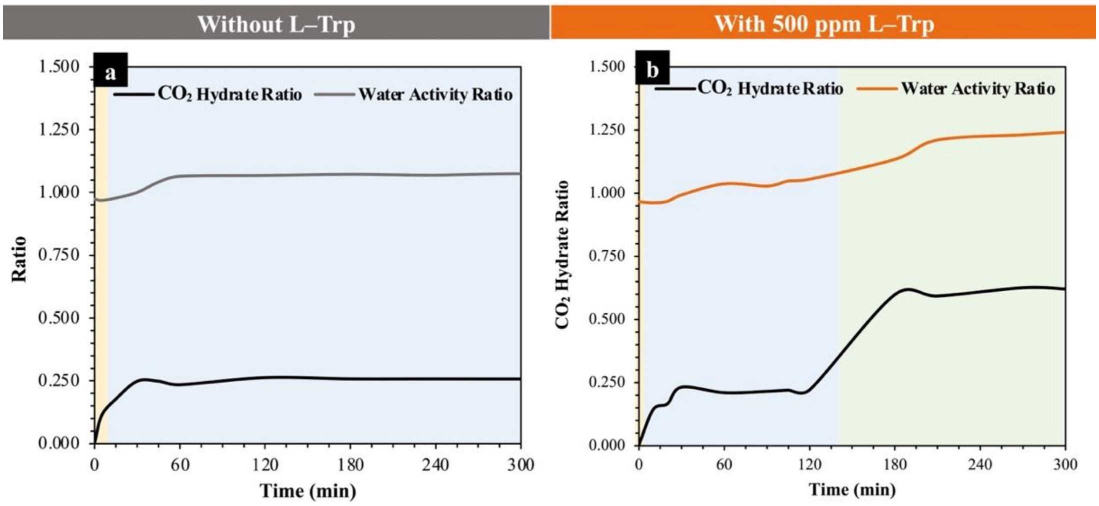

Figure 5.12 Raman spectra relative intensity (CO_2 hydrate ratio and water activity ratio) results for (a) the system without L–Trp and (b) the system with the addition of 500 ppm L–Trp.

5.4.1.2 Effect of L–Trp Concentration on CO_2 Hydrate Formation in DI Water Systems

The addition of 500 ppm L–Trp significantly enhances CO_2 hydrate formation, leading to increased CO_2 uptake within the hydrate structure. To explore the impact of L–Trp further, other L–Trp concentrations (1000 and 2000 ppm) were investigated. The CO_2 uptake profiles for all L–Trp concentrations reveal three distinct stages of CO_2 hydrate formation, showing higher CO_2 uptake than the system without L–Trp, as depicted in Figure 5.13 (a). It is noted that at 2000 ppm L–Trp, the final CO_2 uptake is slightly lower than that of 500 and 1000 ppm, Figure 5.13 (b). This might be attributed to the fact that dissolving 2000 ppm L–Trp likely disrupts the hydrogen bonding network of water due to solvation. Therefore, 2000 ppm L–Trp might need more water molecules for solvating themselves, resulting in less available water molecules to form hydrates. The effect of L–Trp not only increases the CO_2 uptake but also enhances the formation kinetics. The average CO_2 uptake and kinetic parameters, along with their standard errors, are summarized in Table 5.2.

During the first and second stages of hydrate formation, the induction time to start CO_2 hydrate formation (t_{ind}) remains consistent across all L–Trp concentrations. The average initial rate in the first 15 minutes (NIR_{15}) for the DI water system is 0.88 ± 0.21 mmol/mol·min. With the addition of 500 and 1000 ppm L–Trp, the rate increases to 1.59 ± 0.08 and 1.54 ± 0.25 mmol/mol·min. Moreover, the rate further increases with 2000 ppm L–Trp, resulting in the rate of 2.30 ± 0.41 mmol/mol·min. For stage–III of hydrate formation, the presence of secondary hydrate growth is observed in the systems with L–Trp. The rate after the secondary growth ($NR_{15,sg}$) slightly increases with higher L–Trp concentrations. Additionally, the time to start the secondary hydrate growth (t_{sg}) also varies with the L–Trp concentrations. Increasing L–Trp concentration to 1000 ppm reduces t_{sg} by approximately 2.6 times compared to 500 ppm L–Trp. Further increasing concentration to 2000 ppm, there is no significant reduction in the t_{sg}.

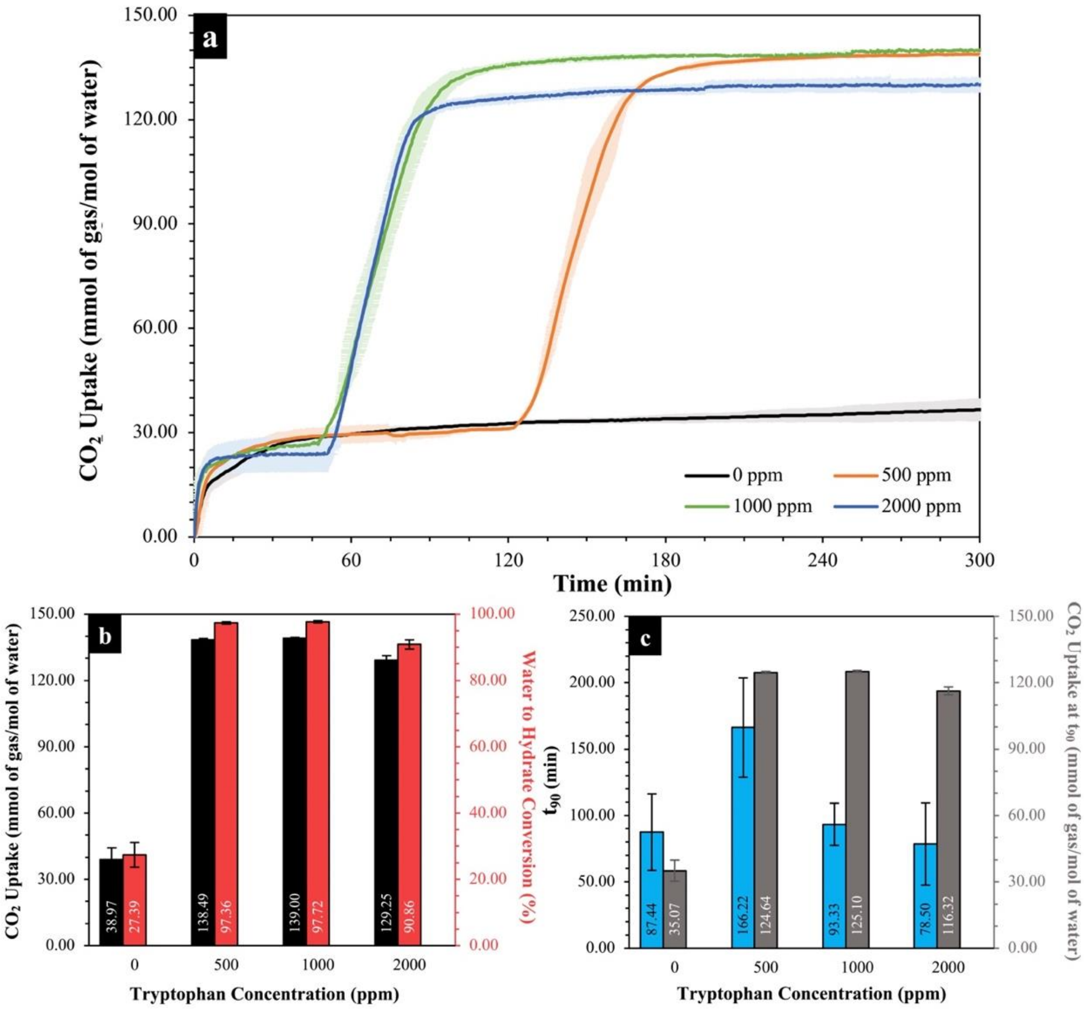

Figure 5.13 Effect of L–Trp concentration on CO_2 hydrate formation in DI water at 275.2 K and 3.5 MPa: (a) CO_2 uptake vs. time, (b) total CO_2 uptake and water to hydrate conversion at CO_2 hydrate completion, and (c) t_{90} and CO_2 uptake at t_{90}.

To obtain a comprehensive view of the kinetics of the formation process, the time taken to achieve 90% of overall uptake (t_{90}) and the gas uptake at t_{90} are typically presented Figure 5.13 (c). The data reveals that an increase in amino acid concentration leads to a reduction in t_{90}. In order to ensure a fair comparison across systems with varying CO_2 uptake, t_{90} is normalized by its corresponding 90% overall uptake, denoted as $t_{90,norm}$, Table 5.2. The system without L–Trp exhibits the longest $t_{90,norm}$. With the addition of 500 ppm L–Trp, $t_{90,norm}$ is reduced by about half compared to the DI water system. Increasing the concentration to 1000 ppm further reduces the $t_{90,norm}$ by about half. Doubling the L–Trp concentration to 2000 ppm insignificantly decreases the $t_{90,norm}$. These findings demonstrate the significant impact of L–Trp in accelerating hydrate formation. Based on these results, the optimal L–Trp concentration is chosen to be 1000 ppm, as it compromises a balance between CO_2 uptake and formation kinetics.

Table 5.2 Summary of CO_2 uptake, conversion, and kinetic parameters for *CO_2* hydrate formation in DI water systems

		L–Trp concentration			
		0 ppm	**500 ppm**	**1000 ppm**	**2000 ppm**
Formation stage–I&II	CO_2 **uptake** (mmol/mol)	38.97 ± 5.29	32.33 ± 0.26	27.14 ± 0.52	24.89 ± 5.56
	Water to hydrate conversion (%)	27.39 ± 3.72	22.73 ± 0.19	19.08 ± 0.37	17.50 ± 3.91
	t_{ind} (min)	4.00 ± 3.17	1.39 ± 1.97	5.67 ± 7.2	3.33 ± 2.45
	NIR_{15} (mmol/mol min)*	0.88 ± 0.21	1.59 ± 0.08	1.54 ± 0.25	2.30 ± 0.41
Formation stage–III	CO_2 **uptake** (mmol/mol)	–	106.15 ± 0.71	112.18 ± 0.94	103.62 ± 5.93
	Water to hydrate conversion (%)	–	74.63 ± 0.5	78.86 ± 0.66	72.84 ± 4.17
	t_{sg} (min)	–	122.22 ± 34.05	47.50 ± 13.66	51.55 ± 19.44
	$NR_{15,sg}$ (mmol/mol min)**	–	1.98 ± 0.14	2.05 ± 0.49	3.06 ± 0.31
Overall formation	CO_2 **uptake** (mmol/mol)	38.97 ± 5.29	138.49 ± 0.49	139.00 ± 0.48	129.25 ± 1.98
	Water to hydrate conversion (%)	27.39 ± 3.72	97.36 ± 0.34	97.72 ± 0.34	90.86 ± 1.39
	t_{90} (min)	87.44 ± 28.79	166.22 ± 37.42	93.33 ± 15.86	78.50 ± 30.93
	CO_2 **uptake at** t_{90} (mmol/mol)	35.07 ± 4.76	124.64 ± 0.44	125.10 ± 0.43	116.32 ± 1.78
	$t_{90,norm}$ (min/(mmol/mol))	2.21 ± 0.55	1.20 ± 0.27	0.67 ± 0.12	0.61 ± 0.23

*,** NIR_{15} and $NR_{15,sg}$ use the same method as the normalized rate of hydrate formation (NR) in previous research (Khandelwal *et al.*, 2020), but NIR_{15} is computed for the first 15 minutes from nucleation, while $NR_{15,sg}$ is computed for the first 15 minutes from the secondary hydrate growth.

Raman spectra were used to analyze the formation process at various L–Trp concentrations. The relative intensity of CO_2 hydrates and water activity ratios, as described earlier, were studied. Figure 5.14 (a1) illustrates the CO_2 hydrate ratio over time at different L–Trp concentrations. The ratios begin at zero and increase as hydrate growth progresses. Without L–Trp, the ratio saturates at about 0.26, whereas the systems with L–Trp show a further increase due to secondary hydrate growth. The ratios become constant upon completion of hydrate formation. The final CO_2 hydrate ratios are consistent with their conversions: the system without L–Trp exhibits the smallest ratio, but that with 500 and 1000 ppm L–Trp achieve similar values, and with 2000 ppm L–Trp, the ratio has a value between those without L–Trp and with 500 and 1000 ppm L–Trp. In order to confirm this, a scatter plot was made, displaying the CO_2 hydrate ratio against the hydrate conversion upon completion, Figure 5.14 (a2). It's important to note that at zero conversion, CO_2 solubility data are employed for this assessment. A notably robust positive correlation is found, evidenced by a Pearson's correlation coefficient (R) of +0.9990. This underlines the potential utility of the CO_2 hydrate ratio as an indicative measure for CO_2 hydrate formation.

In Figure 5.14 (b), the water activity ratio for the systems at different L–Trp concentrations follows a pattern similar to the CO_2 hydrate ratio. It starts at around 0.97 and briefly increases before reaching saturation in the presence of L–Trp. These patterns align with the hydrate formation profile, with the final water activity value corresponding to the hydrate conversion. Although the final water activity values differ with different L–Trp concentrations, the initial water activity remains consistent at approximately 0.97. It appears that the concentration of L–Trp may not significantly affect the ratio, but it slightly reduces the overall intensity, as shown in Figure 5.15 (a). To confirm this observation, an analysis of variance (ANOVA) was conducted with the null hypothesis that the L–Trp concentration has no significant relationship with the water activity ratio. The obtained p–value of 0.5128 exceeds the 0.05 significance level at a 95% confidence level, Table 5.3, indicating that the null hypothesis is accepted. Moreover, the correlation coefficient of –0.1998 suggests that there is no meaningful correlation between the water activity ratio and the concentration of L–Trp, Figure 5.15 (b).

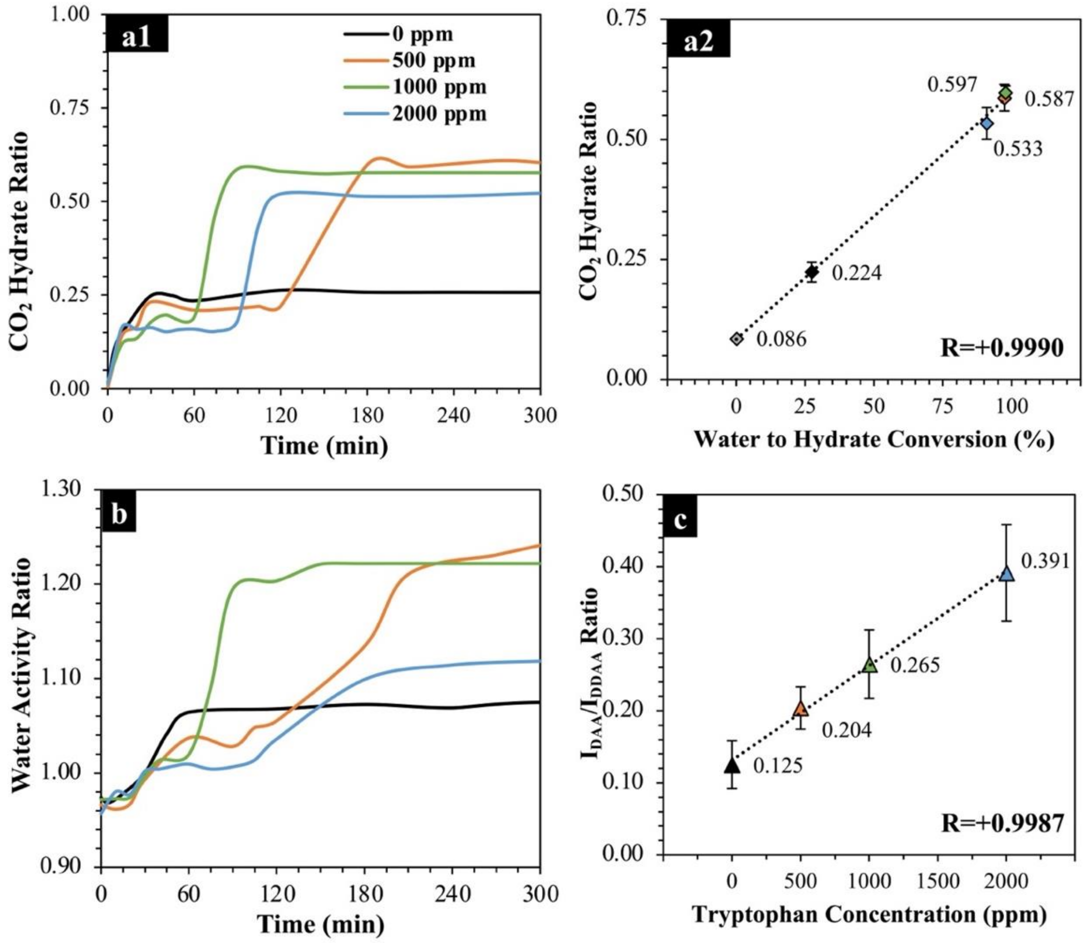

Figure 5.14 Visualization of Raman spectra for CO_2 hydrate formation in DI water system with different L–Trp concentrations: (a1) CO_2 hydrate ratio during hydrate formation, (a2) scatter plot of final CO_2 hydrate ratio against overall water to hydrate conversion, (b) water activity ratio during hydrate formation, and (c) scatter plot of final I_{DAA}/I_{DDAA} ratio against L–Trp concentration.

It's worth highlighting that the relative proportions of DAA and DDAA hydrogen bond motifs within the Raman spectra of hydrates exhibit variations across different L–Trp concentrations upon the completion of the formation process, as observed in Figure 5.16. Consequently, the relative intensities of DAA and DDAA were computed for each system and are illustrated in Figure 5.14 (c). Surprisingly, a notably strong positive correlation between the ratio and L–Trp concentrations is observed, with a correlation coefficient of R=+0.9987. This intriguing outcome could be attributed to the interactions occurring between water molecules and L–Trp. In the absence of L–Trp, water molecules predominantly form tetrahedral hydrogen bonds, resulting in the creation of water cages with a minor presence of DAA hydrogen bonds. However, with the presence of L–Trp, it appears that the hydrogen bonding motif undergoes a transition from predominantly tetrahedrally bonded (DDAA) via four hydrogen bonds to a three-hydrogen-bond configuration (DAA). This transition seems to amplify with higher L–Trp concentrations. Furthermore, this ratio might provide insights into the quantification of H–bond defect sites, which could facilitate the mass transfer of gas molecules into hydrate cages, consequently enhancing hydrate formation.

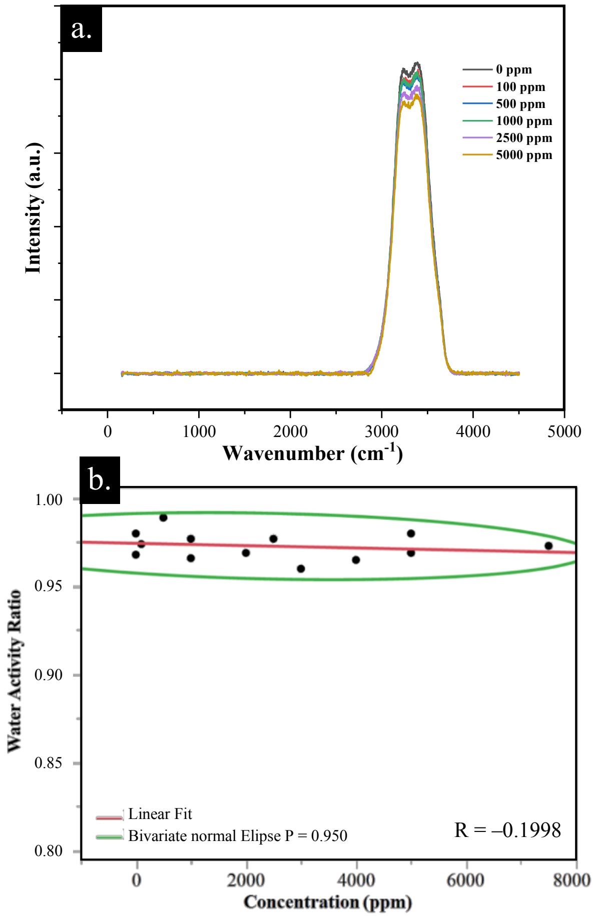

Figure 5.15 (a) Raman spectra of H_2O at various L–Trp concentrations. (b) A plot illustrating the water activity ratio at different L–Trp concentrations with Pearson's correlation (R).

Table 5.3 ANOVA results for the water activity ratio at various L–Trp concentrations

Source of Variation	df	Sum of Squares	Mean Square	F Ratio	P-value
Between groups	1	0.00002897	0.000029	0.4574	0.5128
Within groups	11	0.00069672	0.000063		
Total	12	0.00072569			

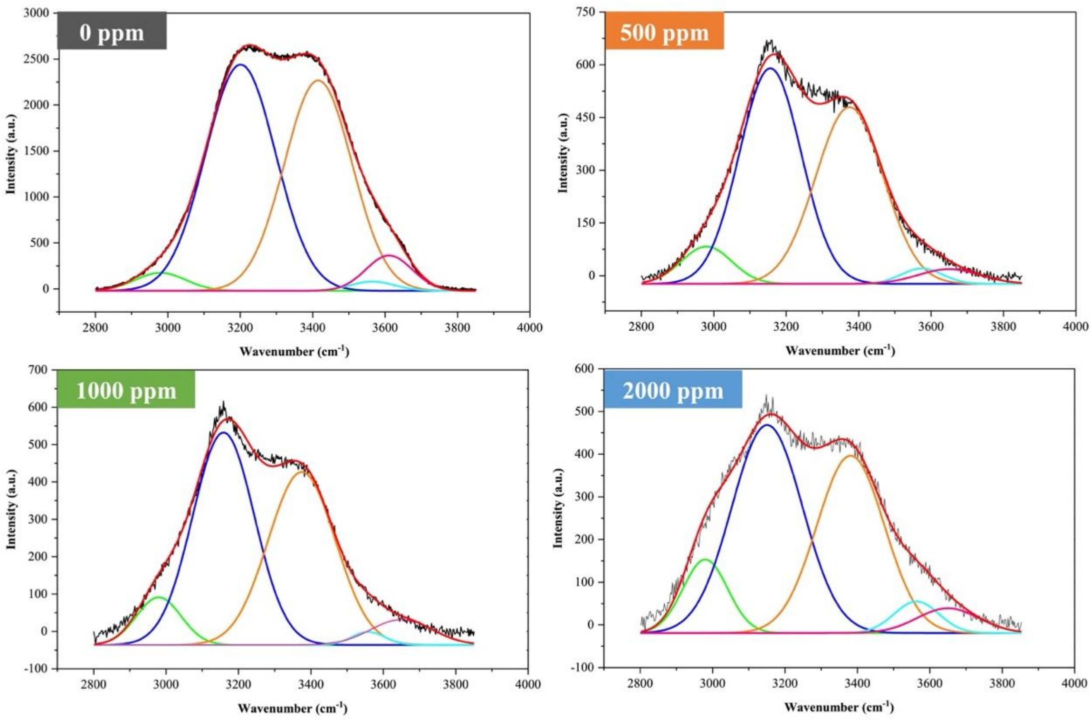

Figure 5.16 Deconvolution of Raman spectra of H_2O after CO_2 hydrate formation completion at various L–Trp concentrations.

5.4.2 CO_2 Hydrate Formation with and without L–Trp in Brine Systems

5.4.2.1 Promoting Effect of L–Trp on CO_2 Hydrate Formation in the Presence of 3.5 wt% NaCl

Many potential CO_2 storage sites, such as depleted oil and gas reservoirs, saline aquifers, and deep geological formation contain brine solutions (Ferroudji *et al.*, 2022; M. Qureshi *et al.*, 2020; Qureshi *et al.*, 2017). In order to achieve more accurate representations of real-world CO_2 storage scenarios, it is essential to study hydrate-based CO_2 sequestration in brine conditions. In this study, CO_2 hydrate formation was investigated in aqueous solutions containing 3.5 wt% NaCl to simulate subsurface environments. The presence of NaCl has been proven to act as an inhibitor, influencing the thermodynamics and kinetics of formation (Naseh *et al.*, 2022). Additionally, the impact of different L–Trp concentrations on the CO_2 hydrate formation in brine was explored.

The experiments were set up with 3.5 wt% NaCl by varying L–Trp concentrations (0, 1000, 2000, and 3000 ppm). The CO_2 uptake profiles of each system over time are depicted in Figure 5.17 (a). Notably, the CO_2 uptake pattern of brine condition without L–Trp resemble that of DI water (Figure 5.3 (a)), indicating no significant secondary hydrate growth. The final CO_2 uptake is around 35 mmol/mol, similar to that of DI water system (39 mmol/mol). Surprisingly, the addition of L–Trp has only a slight effect on enhancing CO_2 uptake. All systems reach saturation within 600 minutes, except for the one with 2000 ppm L–Trp. Thus, the observed time on the condition of 2000 ppm L–Trp is extended to 2880 minutes, Figure 5.17 (b). As a result, the system with 2000 ppm L–Trp achieves the highest CO_2 uptake at 85.40 ± 0.54 mmol/mol, equivalent to a conversion of 60.04 ± 0.38%, Figure 5.17 (c). This demonstrates the promoting effect of L–Trp in the brine system, increasing the final CO_2 uptake by approximately 2.5 times compared to the system without L–Trp. However, it is worth noting that the promoting effect is relatively lighter in the brine system than in the DI water. In the case of 3000 ppm L–Trp, the final CO_2 uptake is lower than that at 2000 ppm. This could be attributed to the fact that L–Trp's solubility in water is approximately 2300 ppm at 0°C (O'Neil, 2001), and its solubility in brine is lower than in water (Aliyeva *et al.*, 2023). As a result, L–Trp might precipitate in the brine environment, reducing its promoting effect on CO_2 hydrate formation.

An intriguing observation during the 2000 ppm L–Trp experiment is the temperature monitored during the formation process. In DI water systems (Figure 5.3), sharp temperature spikes indicated hydrate formation. However, in the brine solution, after an initial spike, numerous small spikes follow. Similar observations are found in the experiments with 1000 and 3000 ppm L–Trp, as shown in Figure 5.18. This suggests that CO_2 hydrates form distinct small clusters, as supported by the morphology illustrated in Figure 5.19.

In contrast to the homogeneous formation in DI water, the presence of NaCl, dissociating into ions, significantly affects the hydrogen bonding network of water molecules. These ions are solvated via ion-dipole interactions with water molecules, limiting the available hydrogen bond donor and acceptor sites for hydrate growth continuously. Consequently, the hydration of Na^+ and Cl^- ions causes the separation of water molecules into clusters, inhibiting and leading to separated clusters of CO_2 hydrates (Al-Bazali, 2021).

Table 5.4 Summary of CO_2 uptake, conversion, and kinetic parameters for CO_2 hydrate formation in brine containing 3.5 wt% NaCl system

		L–Trp concentration			
		0 ppm	**1000 ppm**	**2000 ppm**	**3000 ppm**
Overall formation	**CO_2 uptake** (mmol/mol)	34.35 ± 6.71	42.44 ± 3.31	85.40 ± 0.54	59.17 ± 2.41
	Water to hydrate conversion (%)	24.15 ± 4.72	29.84 ± 2.33	60.04 ± 0.38	41.60 ± 1.70
	t_{ind} (min)	4.17 ± 5.89	11.28 ± 3.85	12.95 ± 3.42	9.06 ± 1.69
	NIR_{15} (mmol/mol min)	1.49 ± 0.35	1.16 ± 0.11	1.20 ± 0.18	1.53 ± 0.13
	t_{90} (min)	159.22 ± 114.43	209.33 ± 111.70	1909.25 ± 80.82	326.33 ± 28.23
	CO_2 uptake at t_{90} (mmol/mol)	30.91 ± 6.04	36.78 ± 3.05	76.86 ± 0.49	53.25 ± 2.17
	$t_{90,norm}$ (min/(mmol/mol))	4.22 ± 2.98	5.15 ± 2.66	22.36 ± 0.93	5.51 ± 0.30

Considering formation kinetics, summarized in Table 5.4, both t_{ind} and NIR_{15} consistently maintain their values across different L–Trp concentrations. However, it's noteworthy that all t_{ind} values in the brine systems at different L–Trp concentrations surpass those observed in the DI water systems. This observation solidifies the inhibitory effect of NaCl on the process. The overall formation kinetics is represented by t_{90}, Figure 5.17 (d). The longest t_{90} observed in the 2000 ppm L–Trp system is consistent with $t_{90,norm}$. This could potentially be attributed to the formation of hydrate clusters induced by salt ions, which might impede continuous growth and consequently delay the CO_2 hydrate formation process.

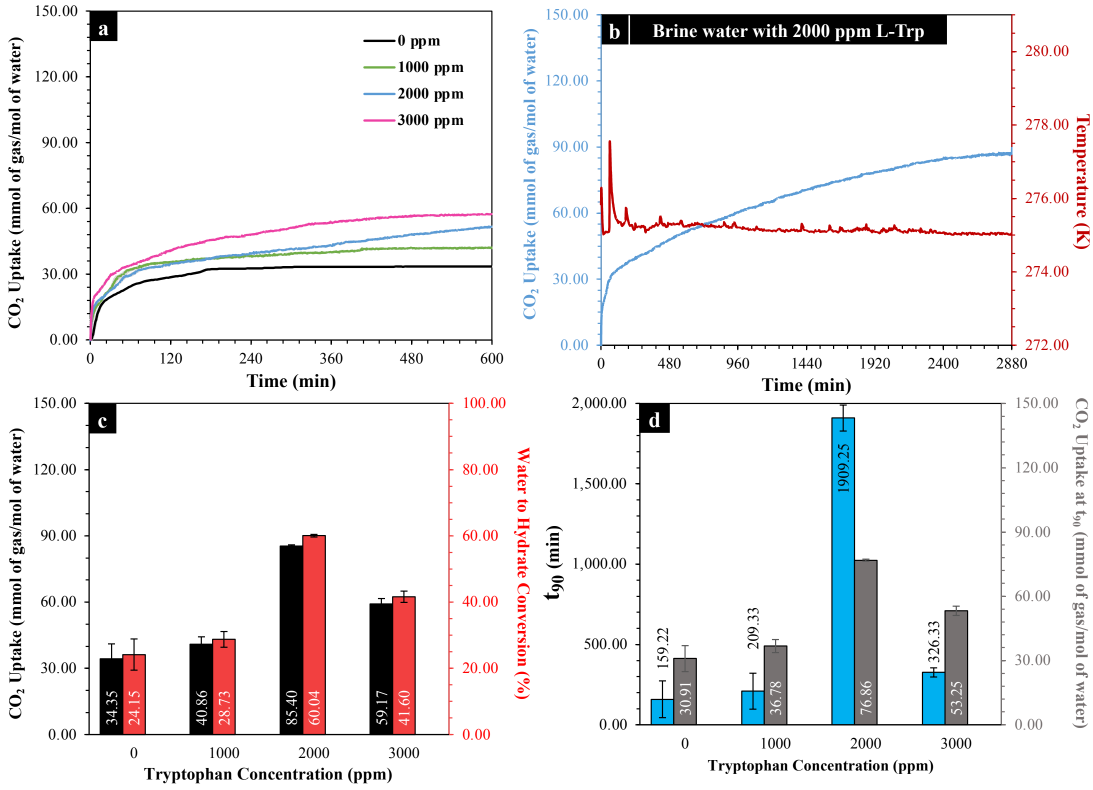

Figure 5.17 Effect of L–Trp concentration on CO_2 hydrate formation in 3.5 wt% NaCl solution at 275.2 K and 3.5 MPa: (a) CO_2 uptake vs. time, (b) temperature profile during CO_2 hydrate formation with 2000 ppm L–Trp, (c) total CO_2 uptake and water-to-hydrate conversion at CO_2 hydrate completion, and (d) t_{90} and CO_2 uptake at t_{90}.

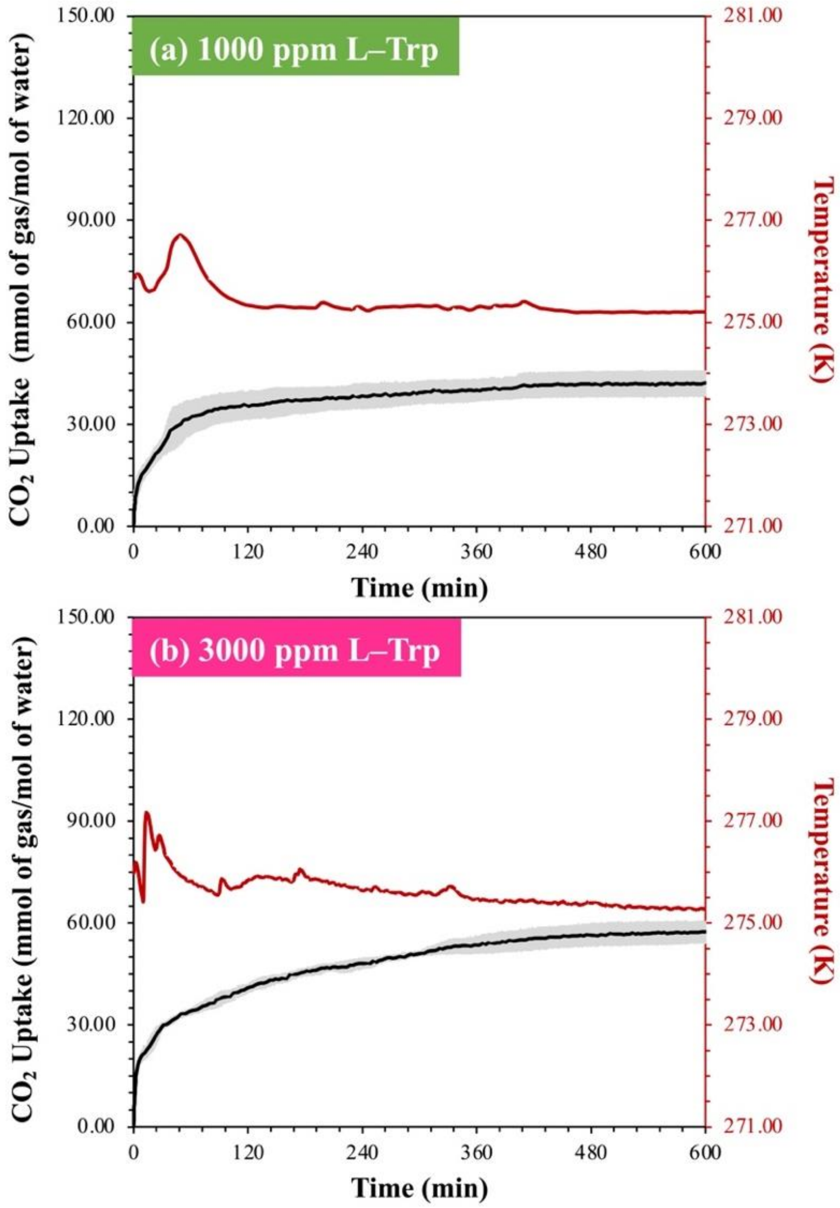

Figure 5.18 Profiles of CO_2 uptake and temperature during CO_2 hydrate formation in brine containing 3.5 wt% NaCl in the presence of: (a) 1000 ppm L–Trp and (b) 3000 ppm L–Trp.

Figure 5.19 Morphological photographs of CO_2 hydrates obtained at 275.2 K and 3.5 MPa with the addition of 2000 ppm L-Trp in brine containing 3.5 wt% NaCl.

Figure 5.20 (a1) depicts the CO_2 hydrate ratio over time at different L–Trp concentrations in the brine system. The ratio without L–Trp saturates at approximately 0.20, which is lower than the DI water system (0.26), despite having similar conversions. This difference could be attributed to the influence of NaCl, which alters the water hydrogen bond network, leading to a decrease in the I_{DDAA} and an increase in the I_{DA}. With varying L–Trp concentrations, the CO_2 hydrate ratios exhibit an ascending trend, closely mirroring their respective conversion trends akin to observations in the DI water system. This behavior is substantiated by the significant correlation between CO_2 hydrate ratio and conversion, as evident in Figure 5.20 (a2), characterized by a robust positive coefficient of +0.9893. In Figure 5.20 (b), the water activity ratio for all experiments in the brine solution starts at around 0.875, which is lower than that in the DI water system. Additionally, all final water activity values in the presence of L–Trp are lower than those in the DI water systems (Figure 5.14 (b)). This suggests that the presence of NaCl exerts a detrimental impact on water activity by disrupting the hydrogen bonding network of water molecules through the formation of hydration shells. Moreover, the final values almost correspond to the hydrate conversion, except for the 3000 ppm concentration, which reaches a saturation value around 1.025, similar to the 2000 ppm although 3000 ppm has lower conversion. In Figure 5.20 (c), examining the I_{DAA}/I_{DDAA} ratio, no significant correlation emerges between the ratio and the L–Trp concentration. This observation could potentially be attributed to the influence of salt ions, which might overshadow the impact of L–Trp in disordering the hydrogen bonding network of water molecules.

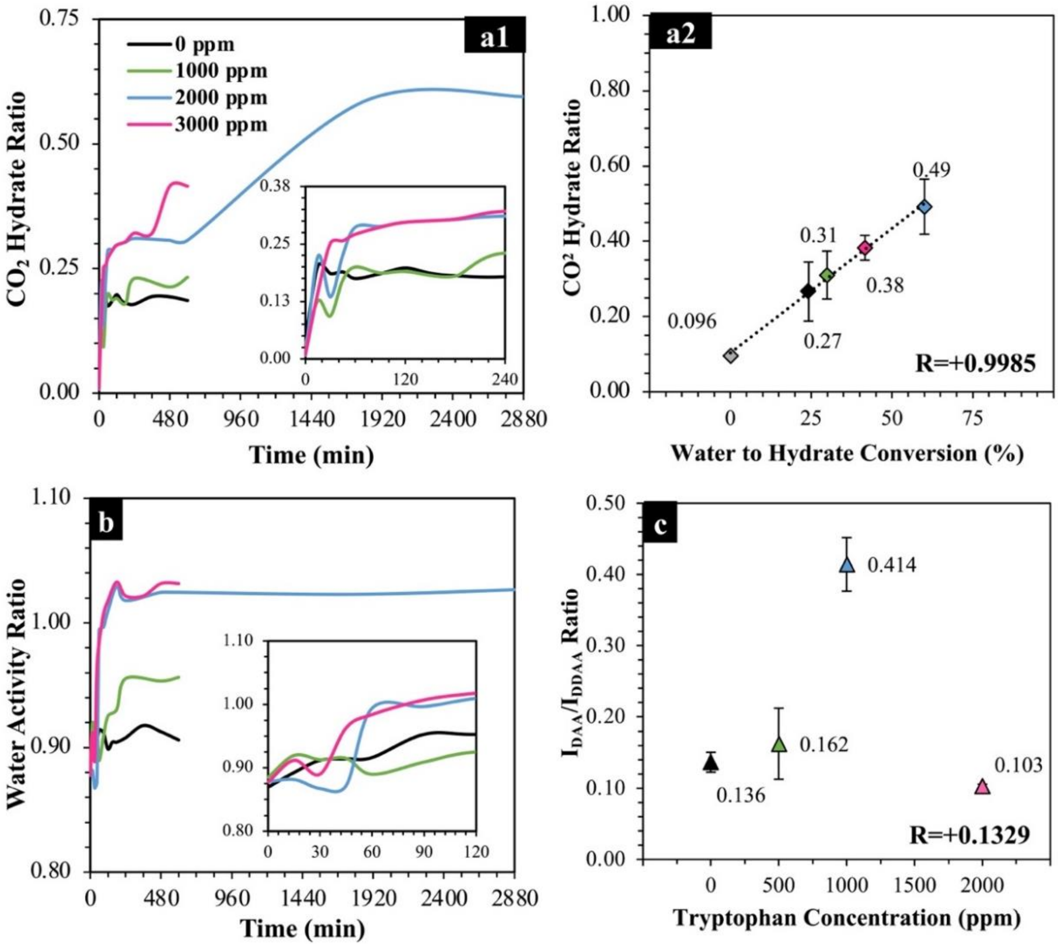

Figure 5.20 Visualization of Raman spectra for CO_2 hydrate formation in the 3.5 wt% NaCl solution with different L–Trp concentrations: (a1) CO_2 hydrate ratio during hydrate formation, (a2) scatter plot of final CO_2 hydrate ratio against overall water to hydrate conversion, (b) water activity ratio during hydrate formation, and (c) scatter plot of final I_{DAA}/I_{DDAA} ratio against L–Trp concentration.

5.4.2.2 Effect of NaCl Concentration on CO_2 Hydrate Formation in the Presence of 2000 ppm L–Trp

In comparison to CO_2 hydrate formation in pure DI water, the introduction of Na^+ and Cl^- ions significantly influences both CO_2 uptake and the formation kinetics. In this context, the influence of different NaCl concentrations (0, 1.75, and 3.5 wt%) on the CO_2 hydrate formation with the presence of 2000 ppm L–Trp was investigated. The CO_2 uptake patterns, Figure 5.21 (a), reveal distinctive behaviours. Notably, the CO_2 uptake profile associated with 1.75 wt% NaCl exhibits secondary hydrate growth akin to that of the DI water system. The final CO_2 uptake, quantified at approximately 92.33 ± 2.79 mmol/mol (equivalent to 64.91 ± 1.96% conversion), is 1.4 times lower than that of the pure DI water but only slightly different from that of 3.5 wt% NaCl, Figure 5.21 (b). Regarding the formation kinetics, the increase in the salt concentration is associated with a noticeable increase in the t_{90} values. Specifically, the t_{90} values are 6.3-fold greater for 1.75 wt% NaCl and 24.3-fold higher for 3.5 wt% NaCl than in the absence of NaCl. This observation indicates the adverse influence of salt on both CO_2 uptake and formation kinetics, as demonstrated in Figure 5.21 (c). The promoting effect of L–Trp is somewhat inhibited with increasing salt concentration. Furthermore, as illustrated in Figure 5.21 (d), a clear and strong negative correlation of -0.9730 emerges between the water activity ratio at the initiation of the process and the concentration of NaCl. This finding is in line with the theoretical perspective that salt ions disrupt the hydrogen bonding network of water molecules by forming hydration shells (Al-Bazali, 2021). This leads to a reduction in the number of DDAA–bonded water molecules (lowering I_{DDAA}) and an increase in the proportion of DA water molecules (increasing I_{DA}), resulting in lower water activity.

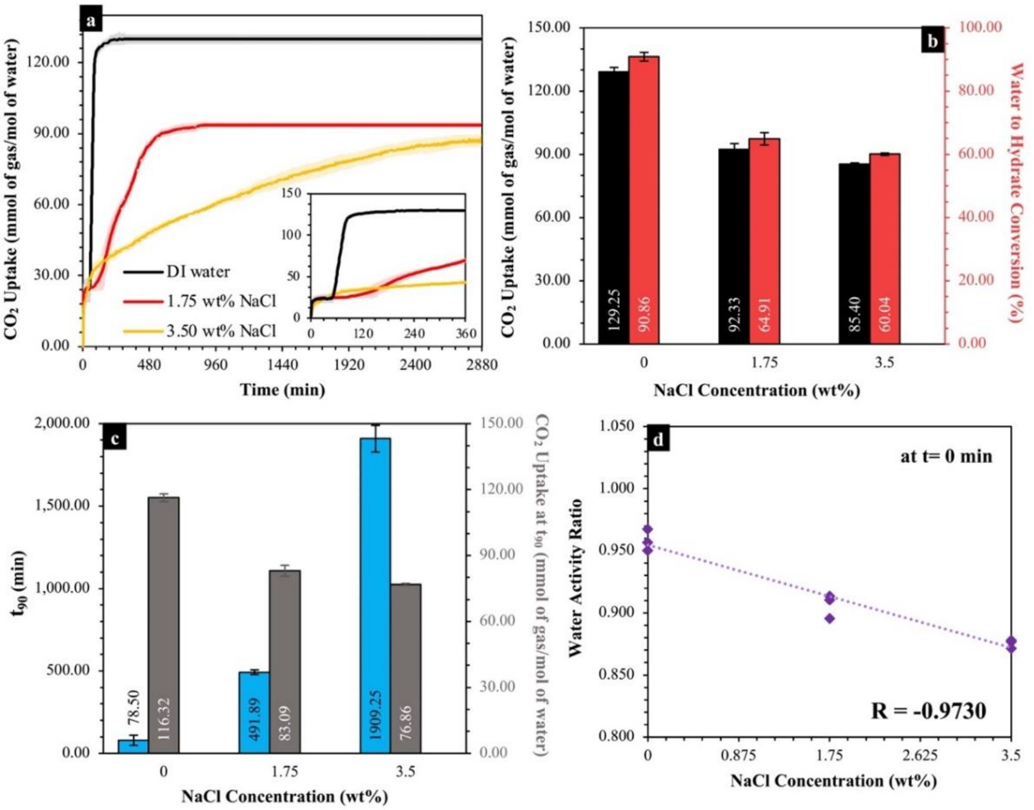

Figure 5.21 Effect of NaCl concentration on CO_2 hydrate formation with 2000 ppm L–Trp at 275.2 K and 3.5 MPa; (a) CO_2 uptake vs. time, (b) total CO_2 uptake and water-to-hydrate conversion at CO_2 hydrate completion, (c) t_{90} and CO_2 uptake at t_{90}, and (d) the water activity ratio at the starting point (0 min).

5.4.3 Effect of L–Trp on CO_2 Hydrate Dissociation in DI Water and Brine Systems

Insights in the dissociation process are of great importance for engineering applications, as it is one of the critical factors for hydrate technology. In this study, the dissociation process was investigated by heating the hydrates to 293.2 K. The pressure changes during this process provide insights into the release of CO_2 from the hydrates. The results in Figure 5.22 (a1) show that, in the DI water systems, the final CO_2 recovery without L–Trp is approximately 90%, while that with L–Trp exhibits higher final CO_2 recovery at around 95% (Table 5.5). The lower CO_2 recovery in the pure DI water can be attributed to its ability to be supersaturated with CO_2, causing some CO_2 release from the hydrates to be retained in the water. The addition of L–Trp appears to disrupt the interaction of water molecules, altering the solution's ability to retain CO_2 molecules (Al-Bazali, 2021). Alternatively, L–Trp might influence the metastability of the supersaturation state of water, allowing more CO_2 to be released from the solution than pure water.

Furthermore, the dissociation kinetics are assessed based on the time taken to achieve 90% CO_2 recovery (t_{90d}), Figure 5.22 (a2). The systems without L–Trp exhibit faster dissociation, while those with L–Trp have longer dissociation times. As hydrates with higher conversion ratios require more latent heat to be disintegrated, they take longer to dissociate at the same heating rate. In order to isolate the effect of hydrate conversion on dissociation kinetics, the time normalized by the percentage hydrate conversion ($t_{90d,norm}$) was calculated as summarized in Table 5.5. The results indicate a positive correlation between the L–Trp concentration and the dissociation kinetics. This confirms the promoting effect of L–Trp on the dissociation kinetics. The role of L–Trp in providing a hydrophobic area within the solution is crucial in this context (Zhu *et al.*, 2022). The hydrophobic area facilitates the formation of nanobubbles of CO_2 gas molecules (Chen *et al.*, 2021; Yagasaki *et al.*, 2014). These nanobubbles effectively reduce the concentration of CO_2 in the solution phase, leading to a larger concentration gradient between CO_2 in the hydrate phase and CO_2 in the solution phase. As a result, the diffusion of CO_2 from the hydrate phase is enhanced, contributing to the faster dissociation kinetics observed in the presence of L–Trp.

The impact of L–Trp as a kinetic promoter was further studied in the brine system (3.5 wt% NaCl). Compared to DI water, the systems with 3.5 wt% NaCl, irrespective of L–Trp concentration, achieved approximately 97% CO_2 recovery (Figure 5.22 (b1)). However, the t_{90d} values still follow the hydrate conversion ratio, Figure 5.22 (b2). Interestingly, the addition of L–Trp in the presence of 3.5 wt% NaCl shows no noticeable effect on $t_{90d,norm}$. This suggests that the promoting effect of L–Trp is masked by the presence of 3.5 wt% NaCl. In the presence of 2000 ppm L–Trp, the NaCl concentrations did not affect the CO_2 recovery (Figure 5.22 (c1)), but it led to an increase in the t_{d90} (Figure 5.22 (c2)) and $t_{d90,norm}$ (Table *5.5*). This indicates that higher NaCl concentrations result in a more substantial masking effect on L–Trp, leading to slower dissociation kinetics.

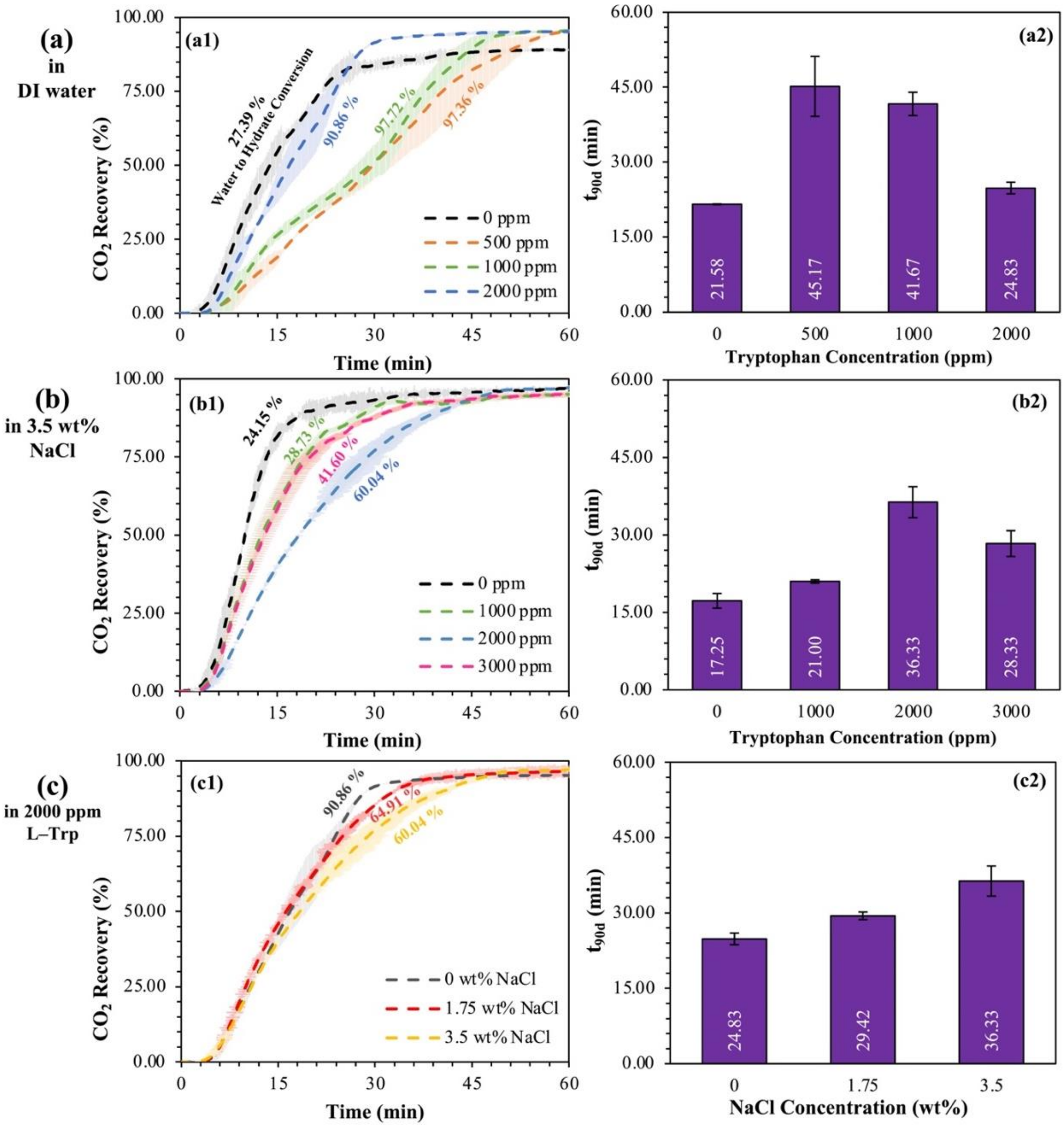

Figure 5.22 CO_2 recovery profiles and t_{90d} during hydrate dissociation in different solutions (a) DI water, (b) 3.5 wt% NaCl with various L–Trp concentrations, and (c) 2000 ppm L–Trp with various NaCl concentrations.

Table 5.5 Summary of CO_2 recovery and kinetic parameters for CO_2 hydrate dissociation in different solutions (a) DI water, (b) 3.5 wt% NaCl, and (c) 2000 ppm L–Trp

System		CO_2 **Recovery** (%)	t_{90d} (min)	$t_{90d,norm}$ (min/(%))
(a) DI water	**0 ppm L–Trp**	90.21 ± 0.28	21.58 ± 45.17	0.76 ± 0.10
	500 ppm L–Trp	97.29 ± 0.43	45.17 ± 6.00	0.48 ± 0.07
	1000 ppm L–Trp	96.82 ± 0.01	41.67 ± 2.33	0.43 ± 0.02
	2000 ppm L–Trp	95.86 ± 0.72	24.83 ± 1.17	0.27 ± 0.01
(b) 3.5 wt% NaCl	**0 ppm L–Trp**	97.61 ± 0.11	17.25 ± 1.42	0.63 ± 0.03
	1000 ppm L–Trp	97.16 ± 0.16	21.00 ± 0.33	0.69 ± 0.03
	2000 ppm L–Trp	98.10 ± 0.84	36.33 ± 3.00	0.61 ± 0.05
	3000 ppm L–Trp	97.15 ± 0.16	28.33 ± 2.50	0.66 ± 0.06
(c) 2000 ppm L–Trp	**0 wt% NaCl**	95.86 ± 0.72	24.83 ± 1.17	0.27 ± 0.01
	1.75 wt% NaCl	97.03 ± 0.09	29.42 ± 0.75	0.45 ± 0.03
	3.5 wt% NaCl	98.10 ± 0.84	36.33 ± 3.00	0.61 0.05

5.5 Conclusion

This study provides valuable insights into the influence of L–Tryptophan (L–Trp), an environmentally friendly kinetic promoter, on the formation and dissociation of CO_2 hydrates in deionized water (DI) and brine systems. Through comprehensive investigations using in situ Raman spectroscopy, both macro and micro perspectives were explored. The change in CO_2 hydrate formation was detected via the CO_2 hydrate ratio, which positively correlates with the water-to-hydrate conversion. In DI water, the addition of L–Trp at an optimal concentration of 1000 ppm had a significant impact on CO_2 hydrate formation. It facilitated higher hydrate formation by promoting secondary growth, resulting in a remarkable 3.6-fold increase in CO_2 uptake. The kinetics of formation was significantly enhanced by a factor of 3.3. Additionally, L–Trp exhibited an acceleration effect on the dissociation process in DI water. In the presence of 3.5 wt% NaCl, the addition of 2000 ppm L–Trp led to a 1.5-fold increase in CO_2 uptake. The presence of salt ions in solution likely reduces the concentration of water available for hydrate formation, resulting in a decrease in water activity. This may likely decrease the water-to-CO_2 hydrate conversion and delay the hydrate formation and dissociation kinetics. Overall, this work demonstrates the great potential of L–Trp employing in situ Raman spectroscopy in improving CO_2 hydrate formation kinetic to foster the development of hydrate-based CO_2 sequestration technology.

5.6 CRediT Authorship Contribution Statement

Kan Jeenmuang: Conceptualization, Methodology, Formal analysis, Investigation, Data curation, Writing - Original Draft, Visualization. **Phuwadej Pornaroontham:** Validation, Formal analysis, Writing – review & editing, Visualization. **M. Fahed Qureshi:** Conceptualization, Validation, Writing – review & editing. **Praveen Linga:** Validation, Supervision, Funding acquisition, Writing – review & editing. **Pramoch Rangsunvigit:** Validation, Writing – review & editing, Supervision, Funding acquisition.

5.7 Acknowledgments

The authors would like to acknowledge the financial support received from the following organizations: Second Century Fund (C2F), Thailand Science Research and Innovation Fund and Ratchadaphiseksomphot Endowment Fund, Chulalongkorn University; The authors also acknowledge the funding support from the Agency of Science, Technology and Research (A*STAR) under the low carbon energy research (LCER) funding initiatives (project ID: U2102d2010).

CHAPTER 6

INSIGHT FINDING AND OPTIMIZATION ON THE IMPACT OF CRYSTALLIZER AND EXPERIMENTAL SETUP FOR THE ROOM TEMPERATURE SII HYDRATE FORMATION KINETICS USING RESPONSE SURFACE METHODOLOGY

6.1 Abstract

Gas hydrate formation is a complex process influenced by factors like gas-liquid interfacial area, solution volume, and gas surplus, resulting in varied outcomes in capacity and kinetics. This study employs Design of Experiment (DOE) analysis to understand these complexities, investigating primary factors and their interactions, affecting mixed methane-THF hydrate formation at 298.2 K and 9.2 MPa, using 0.03 wt% L-Tryptophan (L-Trp) as a kinetic promoter. Employing a 2^k Factorial Design to identify significant factors and their interactions influencing four desirable responses: water to hydrate conversion, mole gas consumption, the normalized rate of hydrate formation (NR_{30}), and the time taken to achieve 90% of overall gas uptake (t_{90}). Subsequently, employing the face-centered central composite design response surface methodology (FCCCD-RSM) to add the nonlinear term of these factors and fully develop models for all four responses, forming the basis for system design and scaling. Notably, V_S/V_R has a significant role in shaping the process, influencing all four responses. However, V_{res} and crystallizer length also play essential roles, impacting gas consumption and hydrate formation kinetics. The optimization process seeks a balanced compromise influence factors and desirable responses, aiming for equilibrium in these complex interactions. The resulting optimized setup, guided by a V_S/V_R of 0.54, achieves high hydrate formation capacity while minimizing the formation time to within three hours. Model validation affirms the model's reliability with small percentage errors, providing a solid foundation for system design, upscaling, and applications in methane hydrate-based energy storage technology.

Keywords: Methane Hydrates, Hydrate Formation Kinetics, Response Surface Methodology, Optimization.

6.2 Introduction

Clathrate hydrates are solid, crystalline structures similar to ice, originating from water molecules' hydrogen bonding. These unique structures have the ability to trap molecules of light gases within their framework, giving rise to what are known as gas hydrates. Gas hydrates can hold up to 170 volumes of natural gas per unit volume of hydrate (Sloan Jr and Koh, 2007). This exceptional gas-trapping ability has opened the door to a wide array of potential engineering applications including energy storage and transportation (Bhattacharjee *et al.*, 2021; Siažik and Malcho, 2017), gas separation (Partoon *et al.*, 2018; Sun *et al.*, 2014), methane capture (Babu *et al.*, 2014; Dashti *et al.*, 2015), and desalination (Babu *et al.*, 2018; Kang *et al.*, 2014; Seo *et al.*, 2019) etc. To improve the viability and competitiveness of hydrate technology, researchers are actively working on enhancing several key aspects of gas hydrate formation. Specifically, they aim to achieve milder formation conditions, faster formation rates, and higher water to hydrate conversion rates (Veluswamy *et al.*, 2018). Currently, in applications related to energy storage and transportation, the formation of natural gas hydrates typically requires compression to around 10 MPa and cooling to approximately 274.2 K [8].

However, the addition of certain thermodynamic promoters can modify the structure of gas hydrates and enable their formation under less extreme conditions (Lee *et al.*, 2012). Tetrahydrofuran (THF) at a 5.56 mol% concentration is a promising thermodynamic promoter facilitates the formation of sII hydrates, notably achievable at room temperature without the necessity for high pressures or low temperatures (Seo *et al.*, 2001; Veluswamy, 2019). By enabling gas hydrates to form under milder conditions, researchers are paving the way for more efficient and cost-effective utilization of this innovative material in various engineering contexts. Nevertheless, An increase in temperature reduces the driving force for hydrate formation, impacting kinetics and water-to-hydrate conversion (Veluswamy *et al.*, 2016b). This is where kinetic promoters come into play, as they can diminish the interfacial tension between gas and liquid, facilitating more effective gas dissolution (He *et al.*, 2017; Veluswamy *et al.*, 2016b) and thereby expediting hydrate nucleation and gro1wth (Bavoh *et al.*, 2018; Chaturvedi *et al.*, 2018). The presence of amino acids has demonstrated the ability to augment hydrate formation kinetics within a THF co-promoted solution (Jeenmuang *et al.*, 2021). L-Tryptophan demonstrates significant hydrophobic properties, making it a promising kinetic promoter that enhances gas uptake and formation rate during hydrate formation at room temperature (298.2 K) (Jeenmuang *et al.*, 2023).

Previous studies under similar conditions showed distinct results. Veluswamy *et al.* (2016b) observed four times faster hydrate nucleation (induction time) at 5.56 mol% THF, 293.2 K, and 7.2 MPa compared to Inkong *et al.* (2019a) study at the same temperature but 8 MPa. Surprisingly, Veluswamy's lower pressure conditions didn't hinder hydrate formation, resulting in a faster t_{90}. Despite the lower pressure in Veluswamy's study, hydrate formation was not more challenging; in fact, the time taken to achieve 90% of overall gas uptake (t_{90}) was faster. However, methane uptake was 1.5 times higher in Inkong's study, potentially due to the higher pressure or differences in crystallizer setup. A closer look at their crystallizers reveals distinctions: Veluswamy used a 142 cm^3 crystallizer with 53 cm^3 solution and no additional gas supply, while Inkong used a 180 cm^3 crystallizer with 90 cm^3 solution and an additional 100 cm^3 gas vessel. Although specific crystallizer diameters weren't provided, making it challenging to discuss the precise impact. However, it is evident that these variations likely played a role in influencing the dynamics of hydrate formation. Furthermore, employing the 142 cm^3 crystallizer setup (Bhattacharjee *et al.*, 2020b) at conditions of 5.56 mol% THF + 0.03 wt% Tryptophan, 298.2 K, and 9.2 MPa resulted in faster hydrate formation, indicated by lower t_{90} values compared to using the 180 cm^3 crystallizer (Jeenmuang *et al.*, 2023). Veluswamy *et al.* (2016c) explored the impact of crystallizer dimensions and solution setup specifics (such as gas-liquid interface area, solution volume, solution height, gas excess percentage, etc.). They noted that larger-scale crystallizers led to a slight decrease in gas uptake capacity and hydrate formation rate, primarily due to an increase in the solution height. However, they also observed a significant enhancement in induction time due to the larger gas-liquid interface area. Moreover, it's evident that certain crystallizer dimensions and solution setup details are interconnected. Zheng *et al.* (2016) noted that an increase in gas uptake and hydrate formation rate was observed with an increase in gas-liquid interfacial area, resulting from a change in crystallizer orientation from vertical to horizontal. Additionally, a decrease in liquid saturation (amount of solution) also led to an increase in both gas uptake and hydrate formation rate. For instance, in a horizontal tubular crystallizer, the solution volume may impact the gas-liquid interface area, while the solution amount might influence the solution height or gas volume used. To ascertain scalability and optimize crystallizer design for hydrate formation, comprehensive investigations that explore the impact of diverse crystallizer dimensions and solution setup specifics are imperative. Gaining insights into these correlations will pave the way for more efficient and feasible large-scale applications of hydrate technology.

In this study, the primary focus was to assess the influence of multi-input factors, namely crystallizer dimensions (gas-liquid interface area), crystallizer setup (percentage of excess gas), and solution setup details (volume of the solution) on a mixed methane-5.56 mol% THF hydrate formation, using 0.03 wt% tryptophan as a kinetic promoter at 298.2 K and 9.2 MPa. The 2^k factorial design was employed to identify a significant factors and their interactions through a minimal number of runs (Sarabia and Ortiz, 2009). The face-centered central composite design response surface model (FCCCD-RSM) was employed to optimize the experimental setup and develop quadratic equation models for predicting optimal conditions related to desired responses. The responses to optimize included the water to hydrate conversion percentage, the mole gas consumption, the normalized rate of hydrate formation (NR_{30}), and the time taken to achieve 90% of overall gas uptake (t_{90}). Through the integration of 2k factorial design and response surface methodology (RSM), this experiment offers a robust framework for interpreting results, identifying key factors and interactions, and optimizing process parameters in hydrate formation. Simultaneously investigating three factors marks a novel approach in hydrate research, potentially introducing a groundbreaking methodology. This advancement could reduce capital and operating costs, bolstering the viability of hydrate-based energy storage, positioning it competitively against conventional methods.

6.3 Experimental

6.3.1 Materials

Ultra-high purity methane (99.99 %) supplied by Linde Public Company, Thailand was used for hydrate formation with distilled deionized water. Tetrahydrofuran (THF), AR grade, from RCI Labscan, Thailand, was utilized as the promoter. L-Tryptophan, an amino acids as kinetic promoters were purchased from Sigma-Aldrich, Singapore.

6.3.2 Hydrate Formation

The apparatus used in this study was divided into two segments: one for the preliminary evaluation of hydrate formation and the other for conducting response surface analysis on hydrate formation. The preliminary evaluation, a mixed methane-5.56 mol% THF hydrate with the addition of 0.03 wt% L–Tryptophan (L–Trp) was formed in three different crystallizers, including two vertical orientation crystallizers, the 50 cm^3 (3 cm diameter (ID)) vertical (Crystallizer 1), the 180 cm^3 (5 cm ID) crystallizer (Crystallizer 2), and 365 cm^3 (4.5 cm ID) horizontal crystallizer (Crystallizer 3). These experiments aimed to assess diverse hydrate formation outcomes and identify the factors significantly influencing the process. Detailed descriptions of the crystallizer setups can be found in a previous study (Jeenmuang *et al.*, 2023).

The main focus of this study is the Response Surface Analysis, the same solution was formed in an adjustable-length horizontal tubular crystallizer as shown in Figure 6.1. The crystallizer has a 4 cm diameter equipped with an electric screw motor and piston (Model L42078A1, Hiwin Mikrosystem Corp., Taiwan), which allows for adjusting the crystallizer length from 15 cm to 29 cm which is equivalent to 188-365 cm^3 crystallizer volume. The crystallizer was connected to an extra variable-sized gas reservoir (400 - 600 cm^3) in order to provide excess gas. all hydrate formation experiments were done at temperature of 298.2 K and a pressure of 9.2 MPa. Prior work (Qureshi *et al.*, 2017; Skovborg *et al.*, 1993), the stirring configuration, which was initially used to disrupt hydrate metastability (sub cooling) and induce the hydrate nucleation, was replaced by an electric screw motor and piston within the crystallizer. These components effectively induced motion in the solution, thereby rapidly initiating hydrate nucleation within the metastable zone. Temperature control was achieved using a refrigerated bath circulator (Model NESLAB RTE7, Thermo Fisher Scientific, U.S.A.), circulating a coolant mixture of ethylene glycol and water through the crystallizer jacket. A K-type thermocouple (TC) with 1.0 K precision and a pressure transmitter (PT) throughout the range of 0 to 10 MPa (Model ZG-PT9200, ZEGA, Thailand) were used to measure temperature and pressure, respectively. The pressure and temperature were monitored and recorded by a data logger (DL, 4xthermocouple Phidget and VINT Hub Phidget, Canada) for five hours or until the pressure decrease did not exceed 100 kPa within an hour. The pressure and temperature data were used to calculate various parameters, including the water to hydrate conversion percentage, the mole gas consumption, the normalized rate of hydrate formation (NR_{30}), and the time taken to achieve 90% of overall gas uptake (t_{90}). The calculation details were follow previous sections.

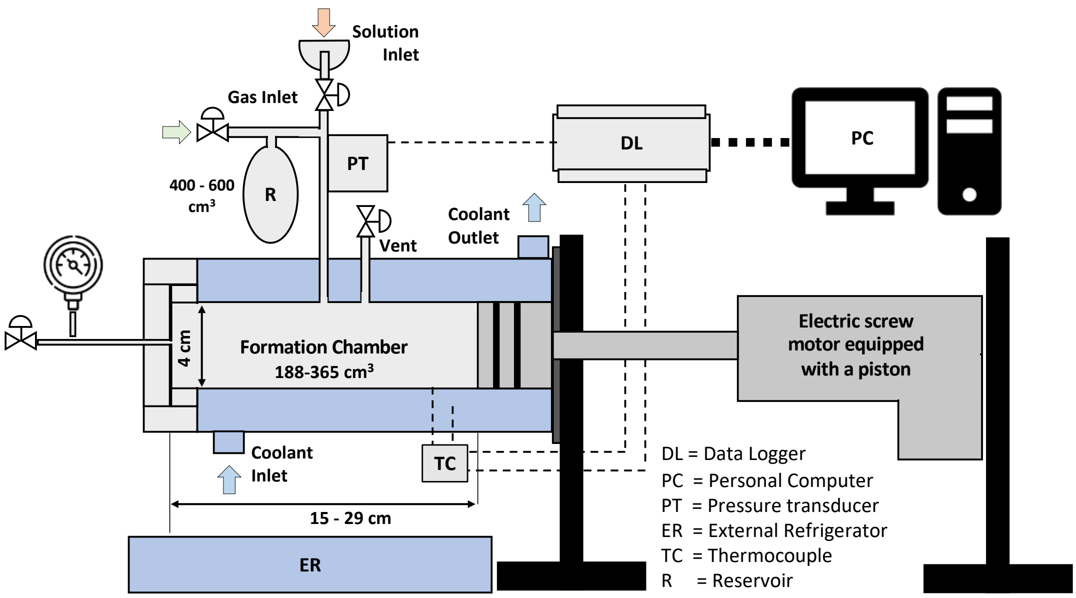

Figure 6.1 Schematic of the adjustable-length horizontal tubular batch crystallizer with adjustable volume of reservoir.

6.3.3 Design of Experiment (DOE) and Optimization

The optimization Face-Centered Central Composite Design Response Surface Methodology (FCCCD-RSM) was performed based on experimental runs generated with Design-Expert software V13.0 (Stat-Ease Inc). The experimental setup encompassed three key factors: gas-liquid interface areas, solution volume, and percentage of excess gas. Due to limitations, the factors of the study were transformed into adjustable factors for enhanced control: (A) crystallizer length, (B) solution to crystallizer volume ratio (V_S/V_R), and (C) volume of supplementary gas reservoir (V_{res}). The responses to optimize included the water to hydrate conversion percentage, the mole gas consumption, the normalized rate of hydrate formation (NR_{30}), and the time taken to achieve 90% of overall gas uptake (t_{90}). The three levels of the FCCCD were designated as "+1" (maximum actual value), "0" (mean value), and "-1" (minimum actual value) for each study factor. The experimental levels for each factor are presented in Table 6.1, with other potentially influencing factors held constant.

Table 6.1 Experimental levels of each factor

Factors	**level**		
	-1	**0**	**1**
A: crystallizer length (cm)	15	22	29
B: V_S/V_R ratio	0.25	0.5	0.75
C: V_{res} (cm^3)	400	500	600

The stepwise procedure for full RSM statistical analysis is presented in Figure 6.2. The implementation of FCCCD-RSM transpired in a two-step sequence. Initially, methane hydrate formations were conducted using a screening design, specifically a 2^3 factorial design with center points, to reveal the main factors and their interactions. To enhance the design study's statistical power, two replications were employed plus three center points, resulting in a total of 19 trials. By incorporating two replications for each code set, the statistical power surged from the initial 68.1% achieved with single replications to exceed the 96.2% threshold. The main factors obtained from the 2^3 factorial design was analyzed using analysis of variance (ANOVA) to obtain a significant P-value while ensuring the model had no significant lack of Fit (LOF). Subsequently, the model underwent diagnostic validation, checking for normally distributed and heteroscedastic residuals and ensuring no outliers in the experimental results. This section also involved analyzing model transformations and assessing their curvature.

Subsequently, an additional two replications of the six axial points, along with two central points, were introduced into the design to assess the polynomial effects of the factors during the second stage of the Response Surface Methodology (RSM). The model selection process entailed comparing a full quadratic model to a reduced model, achieved by excluding insignificant terms (P-value > 0.05) through ANOVA analysis, fit statistics evaluation, and diagnostic validation. This comprehensive approach aimed to prevent overfitting, ensuring the model captured meaningful relationships without incorporating random noise from the data.

The optimal model was employed for optimization, with a focus on carefully balancing operational and capital costs related to methane hydrate formation. Subsequently, model validation was performed using the optimized experimental setup and alternate conditions in methane hydrate formation experiments to evaluate the accuracy of the predictive model.

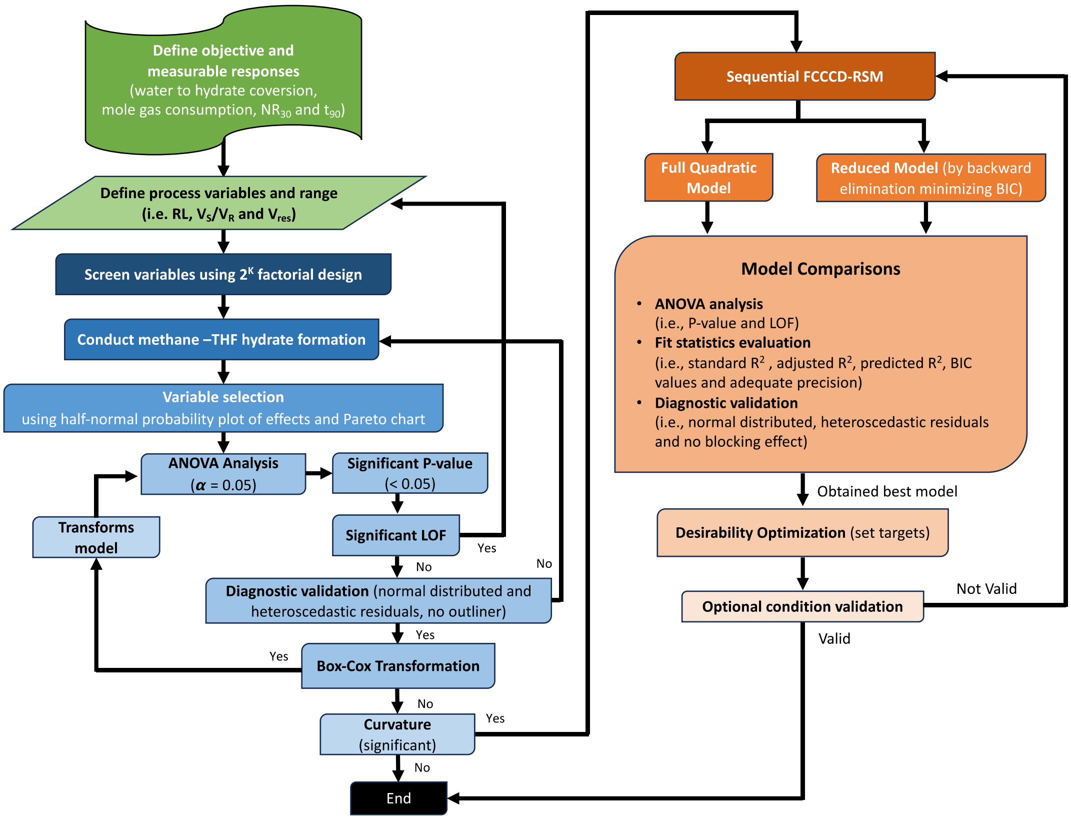

Figure 6.2 Flowchart of full response surface methodology (RSM) analysis.

6.4 Result and Discussion

Prior to this study, preliminary studies indicated significant differences in hydrate formation kinetics for mixed methane-5.56 mol% THF at 298.2 K and 9.2 MPa across three different crystallizers. The differences of their orientation, gas-liquid interface areas by different inside diameter (ID), the volume of used solution, and the percentage of excess gas. These varying factors likely contributed to the disparities observed in hydrate formation kinetics. Crystallizer 1, a vertical orientation crystallizer with a volume (V) of 50 cm^3 and 3 cm diameter (~7 cm^2 interfacial area (IFA)), exhibited the fastest hydrate completion, evident in its t_{90} values, Figure 6.3. Despite the larger size of the vertical crystallizer (180 cm^3) with a 5 cm diameter (~20 cm^2 IFA), it achieved the lowest normalized rate of hydrate formation (NR_{30}) and took the longest time to reach 90% of overall gas uptake (t_{90}). Interestingly, the increase in solution volume from 7 to 90 cm³ in both crystallizer 1 and crystallizer 2 might be the crucial factor contributing to the decreased hydrate formation rate (NR_{30}). This led to a deceleration in hydrate completion, evident in the increase in t_{90}. Meanwhile, applying the same conditions utilizing crystallizer 3, a 370 cm³, 4.5 cm diameter horizontal crystallizer with 100 cm³ solution (~110 cm² IFA), showcased the impact of the horizontal orientation. This setup amplified the gas-liquid interfacial area, leading to an increased NR_{30} and consequently a shorter t_{90} compared to crystallizer 1. What's intriguing is that despite the different setups between the crystallizer 1 and 3, they yield nearly the same hydrate formation kinetics. This raises questions about the influential power of the crystallizer's gas-liquid interfacial area and solution volume, directly affecting hydrate formation kinetics. To comprehend these factors, a new series of experiments delved into three key factors: gas-liquid interfacial areas, solution volume, and percentage of excess gas. Owing to constraints, the study's factors were transformed into adjustable factors to ensure improved control: (A) crystallizer length, (B) solution to crystallizer volume ratio (V_S/V_R), and (C) volume of supplementary gas reservoir (V_{res}).

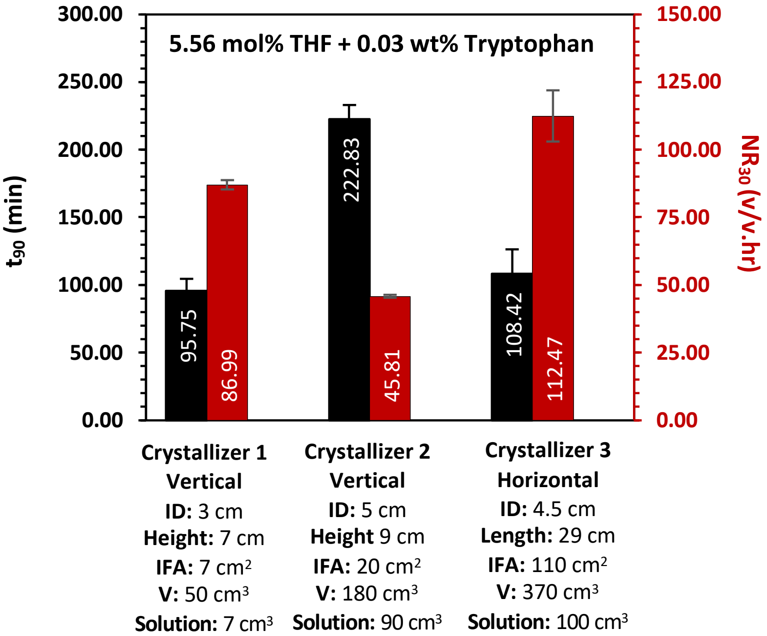

Figure 6.3 Comparison of mixed methane-THF hydrate formation kinetic in various size crystallizer.

Table 6.2 Effects of various parameters on methane-THF hydrate formation: experimental setup and results

Study Parameters						Desirable Responses			
A		B		C		[y_1] water to hydrate conversion	[y_2] mole gas consumption	[y_3] NR_{30}	[y_4] t_{90}
reactor length (cm)	IFA (cm^2)	V_S/V_R	Vs (cm^3)	V_{res} (cm^3)	%excess	(%)	(mol)	(v/v/hr)	(min)
Effect of crystallizer length									
15	60 cm^2	0.50	93 cm^3	500	178	99.19 ± 0.36	0.480 ± 0.003	90.92 ± 1.46	91.09 ± 7.09
22	88 cm^2	0.50	138 cm^3	500	120	98.64 ± 0.02	0.699 ± 0.001	61.39 ± 11.44	130.83 ± 16.50
29	116 cm^2	0.50	182 cm^3	500	88	97.89 ± 0.96	0.911 ± 0.013	58.83 ± 6.96	149.92 ± 1.25
Effect of solution to crystallizer volume ratio (V_S/V_R)									
22	80 cm^2	0.25	69 cm^3	500	283	98.69 ± 0.15	0.350 ± 0.001	172.72 ± 2.05	55.09 ± 10.09
22	88 cm^2	0.50	138 cm^3	500	120	98.64 ± 0.02	0.699 ± 0.001	61.39 ± 11.44	130.83 ± 16.50
22	80 cm^2	0.75	207 cm^3	500	46	96.18 ± 1.51	1.009 ± 0.024	33.99 ± 0.33	296.33 ± 5.50
Effect of volume of supplementary gas reservoir (V_{res})									
22	88 cm^2	0.50	138 cm^3	400	96	96.69 ± 0.5	0.678 ± 0.005	66.83 ± 0.56	120.67 ± 4.17
22	88 cm^2	0.50	138 cm^3	500	120	98.64 ± 0.02	0.699 ± 0.001	61.39 ± 11.44	130.83 ± 16.50
22	88 cm^2	0.50	138 cm^3	600	144	98.61 ± 0.38	0.698 ± 0.004	68.30 ± 0.60	133.83 ± 9.50

6.4.1 Investigation on Factors Affecting on the Methane-THF Hydrate Formation by One-Factor-at-a-Time (OFAT) Method

A traditional investigation was done to study the effect of each factor on the methane-THF hydrate formation, the variation of three factors was studied individually while the other two factors were set constant. The hydrates were formed using a specified volume of solution in a horizontal tubular crystallizer connected with an electric screw motor and a piston. This setup offered the flexibility to modify the length of the hydrate formation, directly impacting the gas-liquid interfacial areas and the solution height. Additionally, this setup also included an adaptable gas supply reservoir. The experiments were conducted using the same solution and formation conditions, consistent with our previous study (Jeenmuang *et al.*, 2023). The experimental setup of each set of experiment and their results are summarized in Table 6.2.

6.4.1.1 Effect of Crystallizer Length

Initially, the influence of the gas-liquid interfacial area was examined by varying the length of the crystallizer to 15, 22, and 29 cm. As the crystallizer featured a horizontal orientation, the gas-liquid interface area increased with the elongation of the crystallizer, corresponding to of 60, 88, and 116 cm^2, respectively. As mentioned earlier, the other factors were held constant with a setup featuring a 0.50 V_S/V_R ratio and 500 cm^3 of V_{res}. However, to maintain the consistent 0.50 V_S/V_R ratio, three different solution volumes (93, 138, and 182 cm^3) were prepared for 15, 22, and 29 cm crystallizer lengths, respectively. Figure 6.4 (a1) illustrates the effect of different crystallizer length on the water to hydrate conversion (blue) and the mol gas consumption (orange), along with their respective standard deviations. The results indicate that water to hydrate conversion remains consistently high, exceeding 97 percent across all crystallizer lengths. This suggests that the system can achieve a high conversion even when the crystallizer configuration is altered, and the increase in the solution volume does not appear to have a significant impact. However, the gas consumption is 0.480 ± 0.003 mol for a 15 cm long crystallizer and increases as the crystallizer length is extended. This increase can be attributed to the larger solution volume required to maintain a constant 0.5 V_S/V_R ratio in each experimental setup. Therefore, more water, more hydrates and more gas trapped Table 6.2. In terms of hydrate formation kinetics, the NR_{30} (green) and the t_{90} (purple) are shown in Figure 6.4 (a2). The results show that the 22 and 29 cm long crystallizers show almost the same NR_{30} and t_{90} (around 60 mmol/mol·min and 140 min, respectively). While the 15 cm long crystallizer results in the highest NR_{30} (90.92 ± 1.46 mmol/mol·min) which is almost 1.5 times higher than both 22 and 29 cm long crystallizer. The 15 cm long crystallizer also results in the fastest hydrate completion as observed in the t_{90} (91.09 ± 7.09 min), while the gas-liquid interface area tends to increase with the extension of crystallizer length, which is generally favorable to enhance the hydrate formation kinetics. There is a counterbalancing effect due to the increased amount of solution as the crystallizer length is extended. This, in turn, leads to a delay in the hydrate formation, resulting in the decrease in the NR_{30} and the increase in the t_{90}. Therefore, it becomes evident that both the gas-liquid interfacial area and the amount of solution exert significant influence on these outcomes, though their effects vary in magnitude and direction. Additionally, as the solution increases to maintain a 0.5 V_S/V_R ratio and the constant V_{res}, the percentage excess of methane decreases, registering at 178, 120, and 88% excess for crystallizer lengths of 15, 22, and 29 cm, respectively. This factor could influence both conversion and hydrate formation kinetics, however, it's challenging to identify which factor holds more impact on hydrate formation.

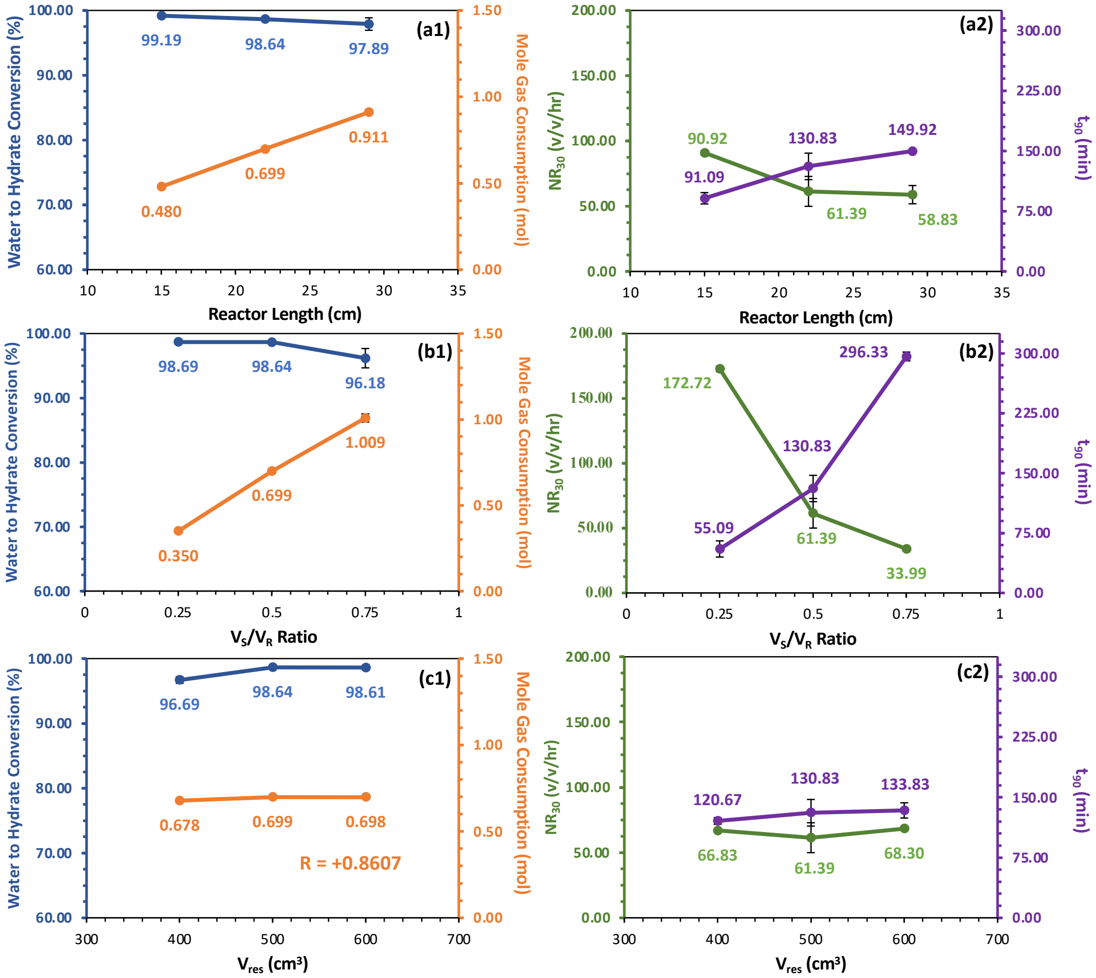

Figure 6.4 Effects of three different factors on the crystallizer design; (a) crystallizer length, (b) V_S/V_R ratio, and (c) V_{res} on water to hydrate conversion (blue), mole gas consumption (orange), NR_{30} (green) and the t_{90} (purple) through the OFAT method.

6.4.1.2 Effect of Solution to Crystallizer Volume Ratio (V_S/V_R)

Next, the study focused on the influence of the V_S/V_R ratio, which enabled the examination of the effects related to the solution volume, the solution height, and the utilization of space within the crystallizer. To investigate this ratio, the study maintained a constant crystallizer length of 15 cm and V_{res} of 500 cm^3, while considering three V_S/V_R ratios: 0.25 (equivalent to 69 cm^3), 0.50 (138 cm^3), and 0.75 (207 cm^3), Table 6.2. Figure 6.4 (b1) shows that the water to hydrate conversion of the 0.25 and 0.5 V_S/V_R reach up to around 98% conversion. However, further increases in the V_S/V_R to 0.75 decreases the conversion to 96.18 ± 1.51 % conversion.

These could be because the increase in the of solution within the same crystallizer volume increases the solution level in crystallizer. This height increase then increases the difficulty for gas and liquid below interface to contact which might result in a solution trapped remaining inside the methane hydrates. The gas consumption also increases with the increase in the amount of solution. The hydrate formation kinetics are also influenced by the solution level, which increases with increase in the V_S/V_R ratio, potentially preventing efficient contact between gas and liquid phases. Consequently, an increase in the V_S/V_R ratio tends to slow down hydrate formation kinetics, leading to the decrease in the NR_{30} and the increase in the t_{90}, Figure 6.4 (b2). Furthermore, it is reasonable that high solution volume may need more time to complete the formation. Notably, at ratios of 0.25 and 0.75, the interfacial area measures 80 cm^3, slightly decreasing from the 88 cm^2 observed at a ratio of 0.5, while the percentage of methane excess also decreases with the increase in V_S/V_R, as detailed in Table 6.2. These variations in interfacial area might have a subtle impact on hydrate formation, its influence appears too small to be clearly identified.

6.4.1.3 Effect of Volume of Supplementary Gas Reservoir (V_{res})

Finally, the study explored the effects of varying the V_{res} in the range of 400 to 600 cm^3, while keeping the crystallizer length and V_S/V_R ratio constant at 22 cm and 0.5, respectively. This setup provided ease compared to prior studies, enabling focused examination due to the constant crystallizer length and V_S/V_R ratio, which exert influence across multiple aspects. The variation was designed to represent the impact of different percentages of excess supply methane on the hydrate formation. Figure 6.4 (c1) shows that the 400 cm^3 V_{res} (96% excess) has 96.69 ± 0.50% conversion and 0.678 ± 0.006 mol gas consumption, while the addition of 500 cm^3 V_{res} (120% excess) increases the conversion and gas consumption to 98.64 ± 0.02% conversion or 0.699 ± 0.001 mol, respectively, and remains constant with 600 cm^3 V_{res} (144% excess). Interestingly, no significant difference is observed from different V_{res} in terms of hydrate formation kinetics Figure 6.4 (c2).

These results indicate that the modification in the studied factors does indeed impact both the quantity of hydrate formation and its kinetics. However, the effect of this influence appears to vary, and there may be potential interactions between them. Achieving this understanding requires refining the experimental design.

6.4.2 Effect Crystallizer Factors Through the Design of Experiment (DOE)

A more advanced and systematic design of experiment, the 2^k factorial design and the response surface methodology (RSM) were employed. They involve creating a mathematical model (response surface) that approximates the relationship between the input factors and the desirable response parameters. This approach allows for the exploration of interactions between input factors and helps in finding the optimal conditions that maximize or minimize the desirable response.

6.4.2.1 Screening Factors Using a 2^3 Factorial Design with Center Points

The study began with an initial screening using a 2^k factorial design as the block 1 of study to identify crucial factors and their interactions. The experiment's sequence was randomized to reduce the potential bias from systematic variations or external factors. Coded values from Table 6.3 were utilized in the 2^3 factorial design, encompassing the full range of factor variations. This design included two replications for each set of codes and incorporated three central points to investigate methane-THF hydrate formation. The study involved evaluating four experimental responses, as outlined in the preceding section. The experimental levels for each factor together with the experimental results of the 2^3 factorial designs are also listed in Table 6.3.

Table 6.3 Experimental factors in coded values and their desirable responses for the 2^3 factorial design with three central points (Block 1)

Standard order[a]	Coded level			Actual level			Desirable Responses			
	A	B	C	A crystallizer length (cm)	B V_S/V_R Ratio	C $V_{res}(cm^3)$	[y_1] water to hydrate conversion (%)	[y_2] mole gas consumption (mol)	[y_3] NR_{30} (v/v/hr)	[y_4] t_{90} (min)
1	-1	-1	-1	15	0.25	400	97.25	0.23	52.50	157.93
2	-1	-1	-1	15	0.25	400	98.31	0.24	37.00	186.87
3	1	-1	-1	29	0.25	400	97.63	0.45	55.33	160.63
4	1	-1	-1	29	0.25	400	99.08	0.46	53.83	145.66
5	-1	1	-1	15	0.75	400	92.94	0.65	249.00	35.50
6	-1	1	-1	15	0.75	400	93.81	0.66	223.33	38.60
7	1	1	-1	29	0.75	400	94.36	1.29	363.50	24.84
8	1	1	-1	29	0.75	400	93.49	1.27	384.83	25.35
9	0	0	0	22	0.5	500	98.31	0.70	148.50	60.18
10	0	0	0	22	0.5	500	98.54	0.68	127.33	69.04
11	0	0	0	22	0.5	500	98.18	0.69	137.00	65.05
12	-1	-1	1	15	0.25	600	98.91	0.2389	44.67	170.20
13	-1	-1	1	15	0.25	600	99.44	0.2409	42.33	179.65
14	1	-1	1	29	0.25	600	99.36	0.4657	46.50	161.63
15	1	-1	1	29	0.25	600	97.39	0.452	47.50	150.35
16	-1	1	1	15	0.75	600	98.13	0.7085	217.33	47.48
17	-1	1	1	15	0.75	600	96.89	0.6949	233.33	50.26
18	1	1	1	29	0.75	600	95.83	1.3224	414.33	25.70
19	1	1	1	29	0.75	600	98.31	1.3748	380.50	25.20

[a] The actual run order has been randomized

Initially, linear regression with least square method was used to analyze the effects of factors on the water to methane hydrate conversion [y_1] after completing of hydrate formation. The half-normal probability plot of effects on Figure 6.5 (a) indicates that the V_S/V_R ratio (B) and the V_{res} (C), along with the interaction of V_S/V_R and V_{res} (BC) deviate from the line of normality, suggesting a significant effect on the water to hydrate conversion. The V_S/V_R ratio (B) is represented in blue, indicating a negative effect on conversion. Meanwhile, V_{res} (C) and the interaction of V_S/V_R and V_{res} (BC) are depicted in orange, also signaling a negative impact on the conversion. Furthermore, the crystallizer length (A) and the interactions of crystallizer length with both V_S/V_R (AB) and V_{res} (AC) appear to align with a normal distribution, suggesting an unaffecting on conversion. The Pareto chart for the t-value of |Effect| confirms the significance of B, C, and BC, as their t-values are larger in the magnitude than both the t-value critical value (2.132) and the Bonferroni limit (3.187), Figure 6.5 (b). Using t-value critical and Bonferroni limits ensures accurate significance assessment in 2^k factorial screenings, reducing the risk of false factor selection across multiple factors. Consistent with the previous analysis, the ANOVA results reveal that both main factors and the interactions of BC exhibit the p-values lower than the significance threshold of 0.05, within a 95% confidence level. This observation implies a statistically significant impact on the water to methane hydrate conversion, as indicated in Table 6.4. The P-value for lack of fit (LOF) is non-significant as desired and no more term was needed. Furthermore, the ANOVA results also highlight the significance of curvature (or nonlinearity) within the relationship between factors. This implies that the linear model may not adequately capture the intrinsic relationships between factors. The introduction of curvature or nonlinear terms could potentially enhance the model's fitness and predictive accuracy.

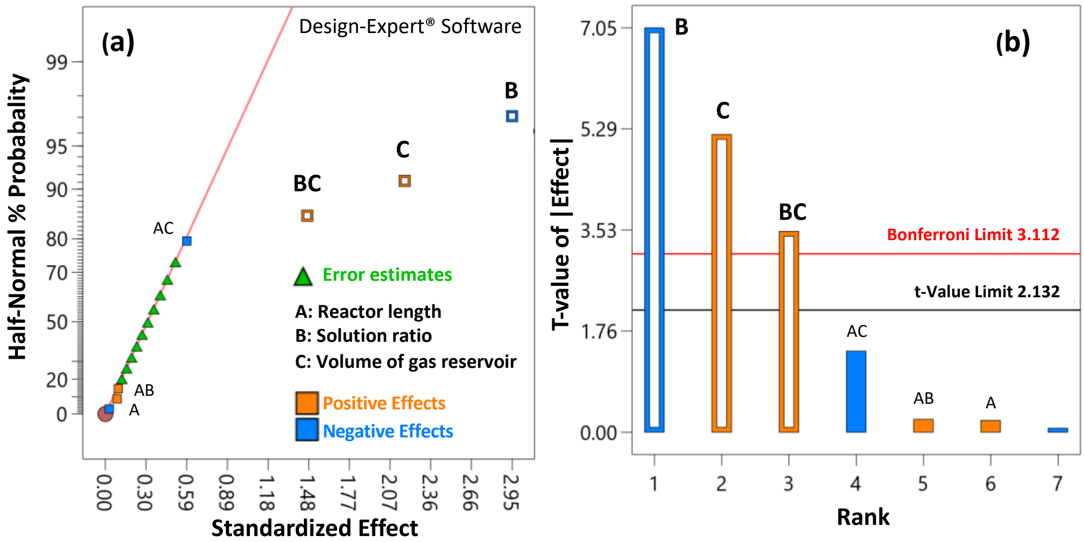

Figure 6.5 Half-normal probability plot of effects (a) and the Pareto chart of the factors for the 2^3 factorial design (b) on the desirable responses: water to hydrate conversion [y_1].

Table 6.4 ANOVA table of the significant terms for the [y_1] water to methane hydrate conversion in 2^3 factorial design with three central points

Source of variation	Sum of Squares	DF[a]	Mean Square	F-value	P-value
Model	2.37	3	20.79	29.67	< 0.0001*
A	0.0032	1	0.0032	0.0043	0.9492
B	34.87	1	34.87	49.77	< 0.0001*
C	18.9	1	18.90	26.97	0.0001*
AB	0.0293	1	0.0293	0.0385	0.848
AC	1.4	1	1.4	1.84	0.2024
BC	8.6	1	8.60	12.27	0.0035*
Curvature	4.93	1	4.93	7.04	0.0189*
Residual	9.81	14	0.70		
Lack of fit	1.47	4	0.37	0.44	0.7775
Pure error	8.34	10	0.83		
Total	77.11	18			

* This factor significant
[a] Degree of freedom

Indeed, the result must undergo diagnostic validation to ensure its accuracy and reliability. In diagnostic validation for a 2^k factorial design, anticipate a straight-line alignment for normal probability plots, identification and management of influential data points using Cook's Distance, and absence of discernible patterns in residual plots. Figure 6.6 (a) illustrates the normal probability plot for water to methane hydrate conversion, indicating the model's reasonable accuracy as the residuals closely align with the straight line, implying normal distribution of errors. None of the experiments exceed the Cook's distance limit, indicating that individual data points have minimal impact on the regression model, and no outliers are identified, Figure 6.6 (b). Thus, the model is well-fitted and not overly influenced by noise or irrelevant factors. Furthermore, the residuals vs. predicted plot depicted in Figure 6.6 (c) exhibits homoscedasticity, featuring a random dispersion of points around the y-axis (residual = 0). This signifies that the model's predictions are unbiased, devoid of outliers or influential points, and the residuals lack any discernible systematic pattern. Given the observed homoscedasticity, the Box-Cox plot for power transformations revealing that no transformation is needed (Figure 6.6 (d)). Notably, the current λ value of 1 (blue line) signifies that the data is in a form where no major transformation is needed. The data may already exhibit some degrees of normality and stable variance. While the best λ of -2 (green line) is not considered applicable because it's quite different from the current λ of 1. So, the Box-Cox transformation is not necessary in this case. Certainly, although the model's diagnostic validation confirms its reliability, the presence of curvature necessitates the addition of further nonlinear terms.

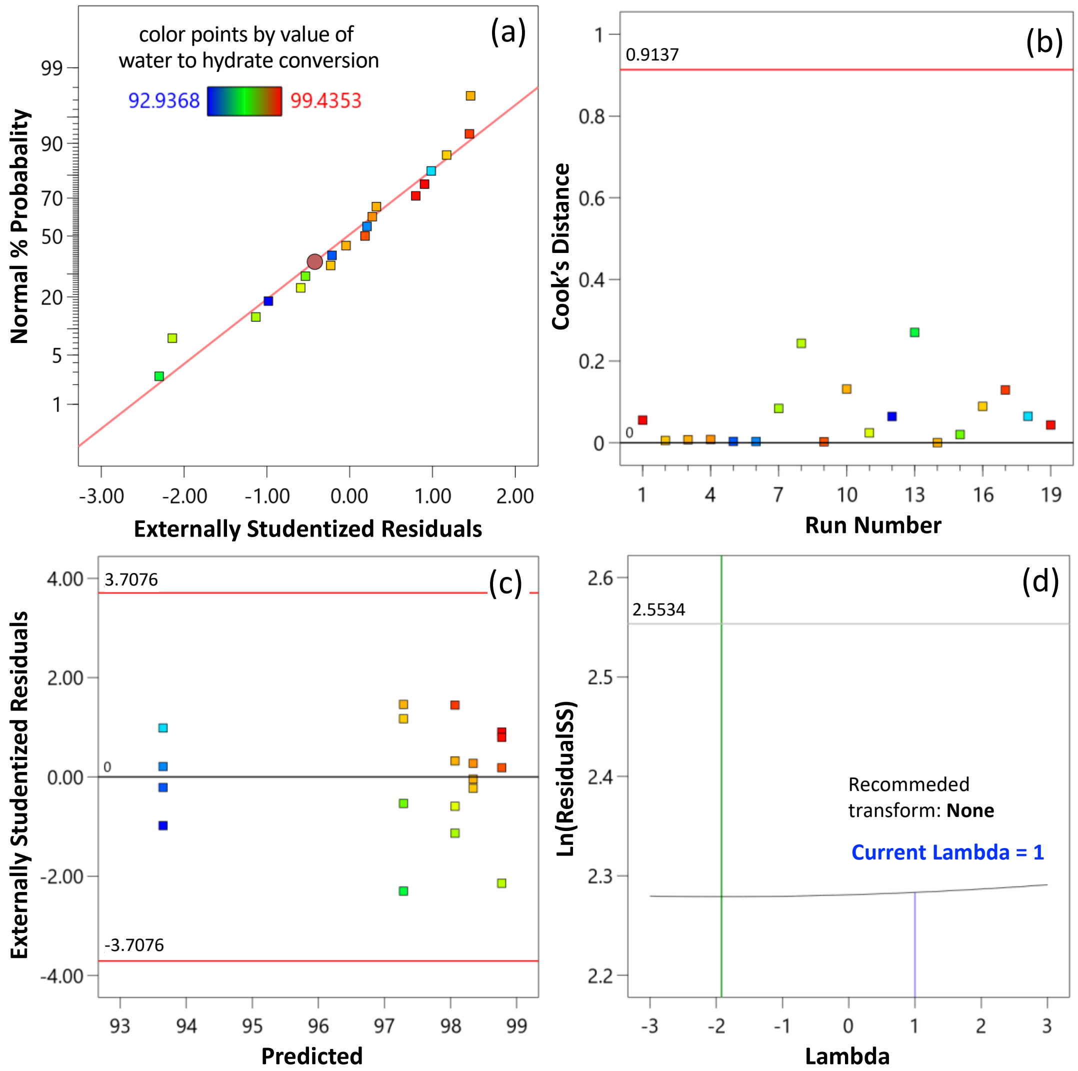

Figure 6.6 Diagnostic plots of the model for the desirable response, water to methane hydrate conversion [y_1], encompass the following: the normal probability plot (a), Cook's distance (b), residuals vs. predicted plot (c), and the Box-Cox plot (d).

In term of mole gas consumption [y_2], The half-normal probability plot of effects on Figure 6.7 (a) revealed significant positive effects on mole gas consumption from all main factors A, B, and C, as well as the interactions of AB and BC. Supported by the ANOVA results in Table 6.5 (a), these factors exhibited statistically significant impacts on mole gas consumption. Additionally, the lack of fit (LOF) p-value was non-significant. Notably, the absence of significant curvature in factor relationships suggested no necessity for non-linear factors. While the model's diagnostic validation, as shown in Figure 6.8 (a), the residuals vs. predicted plot exhibits a funnel-shaped pattern, indicating heteroscedasticity Figure 6.8 (a-3). This pattern suggests varying error variance across predicted values, potentially requiring an alternative modeling approach or transformation. Given this observation, the Box-Cox plot recommends a $\log_{10}$ transformation to address mole gas consumption, emphasizing the potential need for a different modeling approach, Figure 6.8 (a-4).

After applying a $\log_{10}$ transformation to mole gas consumption, the half-normal probability plot of effects, the Pareto chart for the T-value of |Effect| Figure 6.7 (b), and the ANOVA analysis Table 6.5 (b) collectively indicate the same significant impact of all main factors, however only the interactions of BC was significant on mole gas consumption. The lack of fit (LOF) p-value was also non-significant, however, curvature in factor relationships became significant indicating the need of nonlinear terms. The model's diagnostic validation all met criteria, normal distribution alignment for normal probability plots, none of the desirable responses exceed the Cook's distance limit Figure 6.8 (b-1) and 6.8 (b-2). Additionally, the residuals vs. predicted plot indicates homoscedasticity Figure 6.8 (b-3). the Box-Cox plot didn't recommend a transformation, Figure 6.8 (b-4).

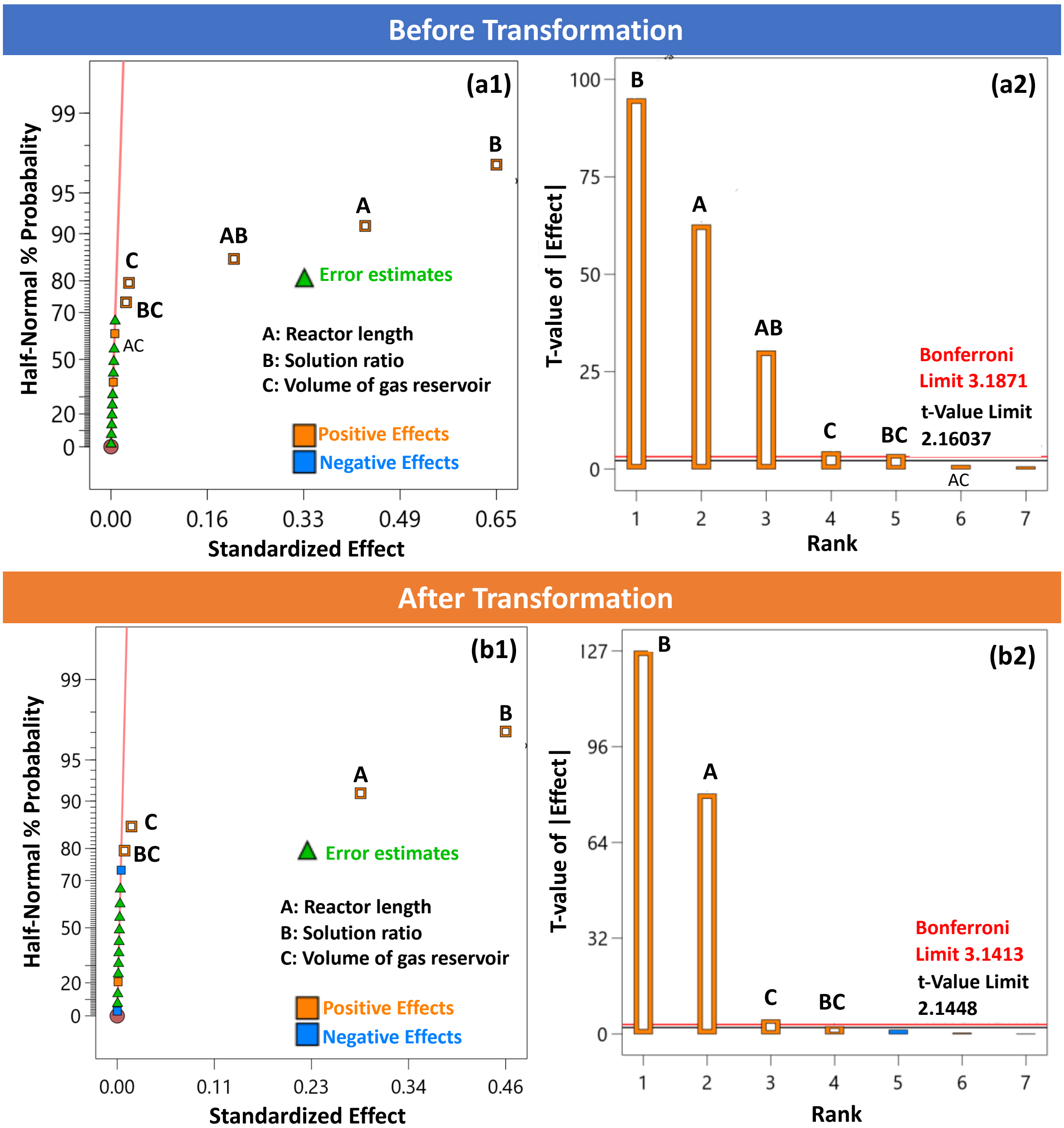

Figure 6.7 Half-normal probability plot of effects (1) and the Pareto chart of the factors for the 2^3 factorial design (2) on the desirable responses: mole gas consumption [y_2] before (a) and after (b) transformed.

Table 6.5 ANOVA table of the significant parameters for mole gas consumption [y_2] (a) before and (b) after transformed in 2^3 factorial design with three central points

Source of variation	Sum of Squares	DF[a]	Mean Square	F-value	P-value
(a) Mole gas consumption before transformation					
Model	2.61	6	0.4344	2188.99	< 0.0001*
A	0.7358	1	0.7358	3708.11	< 0.0001*
B	1.69	1	1.69	8525.8	< 0.0001*
C	0.0037	1	0.0037	18.78	0.0012*
AB	0.1722	1	0.1722	867.91	< 0.0001*
AC	0.0001	1	0.0001	0.3266	0.5792
BC	0.0026	1	0.0026	13.03	0.0041*
Curvature	0.0009	1	0.0009	4.42	0.0593
Residual	0.0022	11	0.0002		
Lack of fit	0.0002	1	0.0002	0.8322	0.3831
Pure error	0.002	10	0.0002		
Total	2.61	18			
(b) Mole gas consumption after transformation					
Model	1.17	6	0.1954	3663.18	< 0.0001*
A	0.3301	1	0.3301	6187.95	< 0.0001*
B	0.841	1	0.841	15762.61	< 0.0001*
C	0.0011	1	0.0011	21.31	0.0007*
AB	1.97E-09	1	1.97E-09	0	0.9953
AC	0.0001	1	0.0001	1.63	0.2283
BC	0.0003	1	0.0003	5.56	0.0379*
Curvature	0.022	1	0.022	411.91	< 0.0001*
Residual	0.0006	11	0.0001		
Lack of fit	4.49E-06	1	4.49E-06	0.0771	0.787
Pure error	0.0006	10	0.0001		
Total	1.2	18			

* This factor significant

[a] Degree of freedom

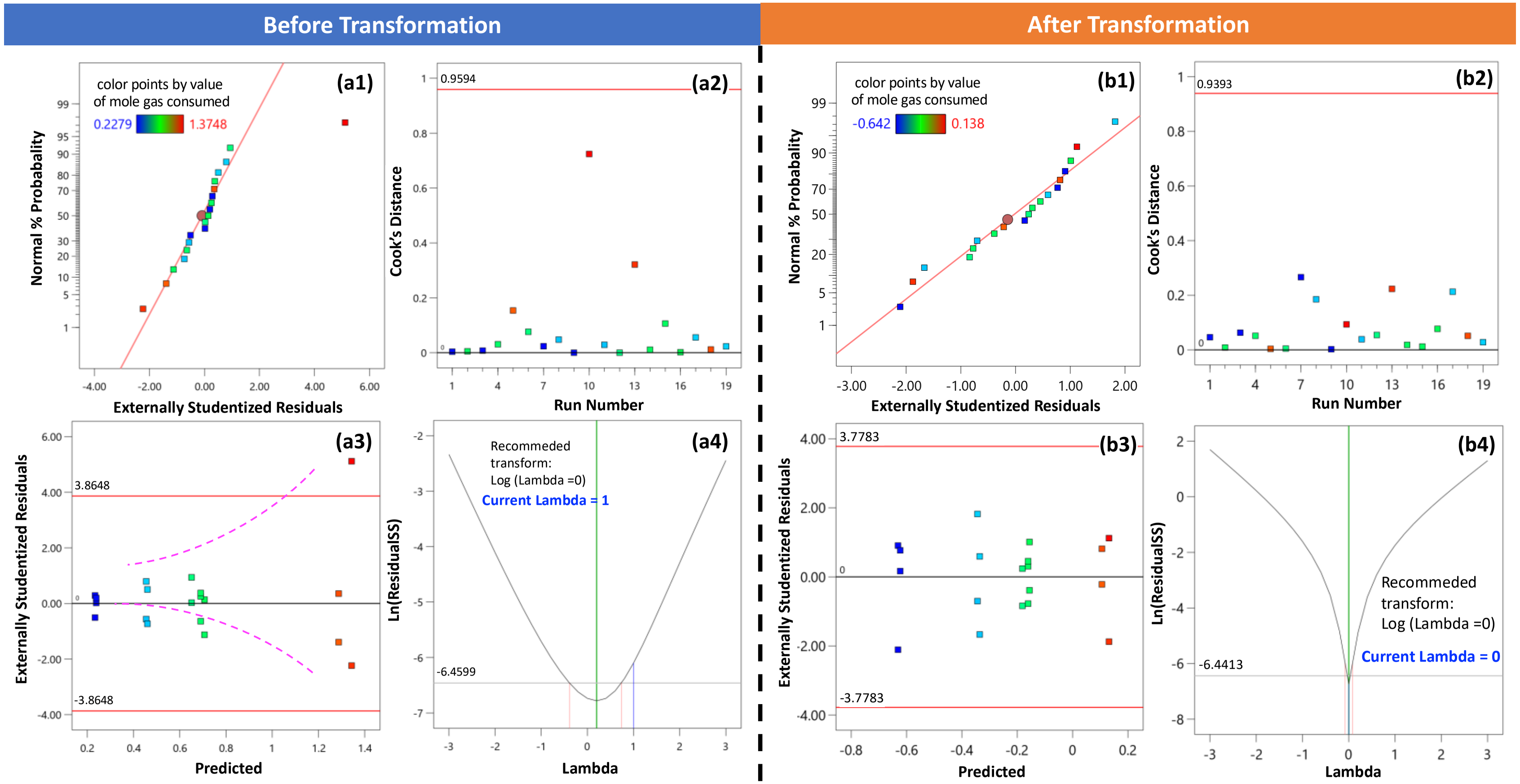

Figure 6.8 Diagnostic plots of the model for the desirable response, water to mole gas consumption [y_2] (a) before and (b) after transformed, encompass the following: the normal probability plot (1), Cook's distance (2), residuals vs. predicted plot (3), and the Box-Cox plot (4).

The remaining desirable responses (NR_{30} [y_3] and t_{90} [y_4]) were analyzed following a similar approach as previous two desirable responses (half-normal probability plot and Pareto chart in Figure 6.9). The diagnostic plots for these responses also suggest the need for data transformation. Based on the residuals vs. predicted plot and the Box-Cox plot, it was found that both NR_{30} and t_{90} require a square root transformation. The ANOVA analysis results and the diagnostic plots for NR_{30}, and t_{90} before the transformations are presented in the Table 6.6 and Figure 6.10, respectively.

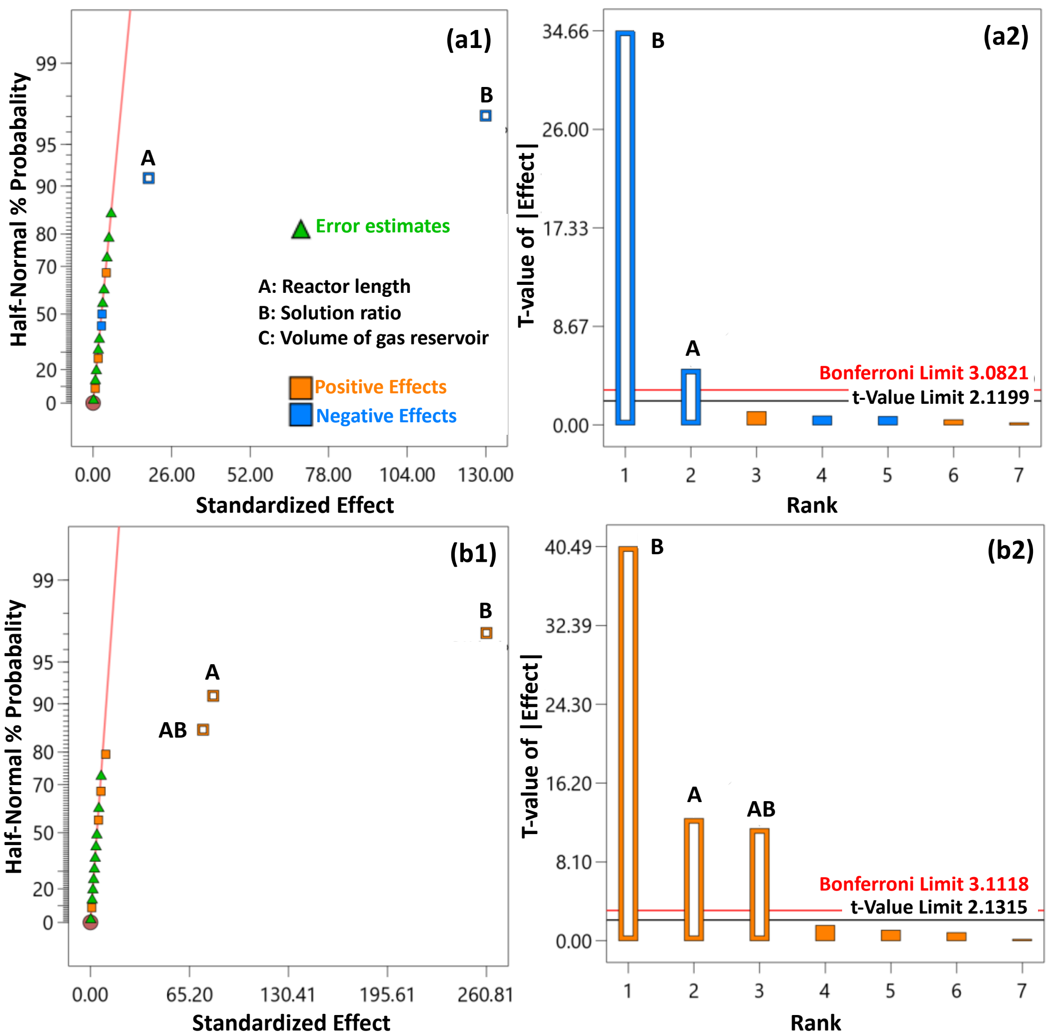

Figure 6.9 Half-normal probability plot of effects (1) and the Pareto chart (2) of the factors for the 2^3 factorial design on the desirable responses before transformation in 2^3 factorial design with three central points: (a) NR_{30} and (b) t_{90}.

Table 6.6 ANOVA table of the significant parameters for desirable responses before transformation; NR_{30} and t_{90} in 2^3 factorial designs with three central points

Source of variation	**Sum of Squares**	**DF[a]**	**Mean Square**	**F-value**	**P-value**
			[y_3] NR_{30}		
Model	68951.15	2	34475.57	612.84	< 0.0001*
A	1352.98	1	1352.98	24.05	0.0002*
B	67598.16	1	67598.16	1201.63	< 0.0001*
Curvature	2981.94	1	2981.94	53.01	< 0.0001*
Residual	843.83	15	56.26		
Lack of fit	156.28	5	31.26	0.4546	0.8012
Pure error	687.55	10	68.75		
Total	72776.92	18			
			[y_4] t_{90}		
Model	3.20E+05	3	1.07E+05	643.28	< 0.0001*
A	26149.32	1	26149.32	157.57	< 0.0001*
B	2.72E+05	1	2.72E+05	1,639.59	< 0.0001*
AB	22,015.88	1	22,015.88	132.67	< 0.0001*
Curvature	4,093.43	1	4,093.43	24.67	0.0002*
Residual	2,323.3	14	165.95		
Lack of fit	716.98	4	179.24	1.12	0.4018
Pure error	1,606.32	10	160.63		
Total	3.27E+05	18			

* This factor significant

[a] Degree of freedom

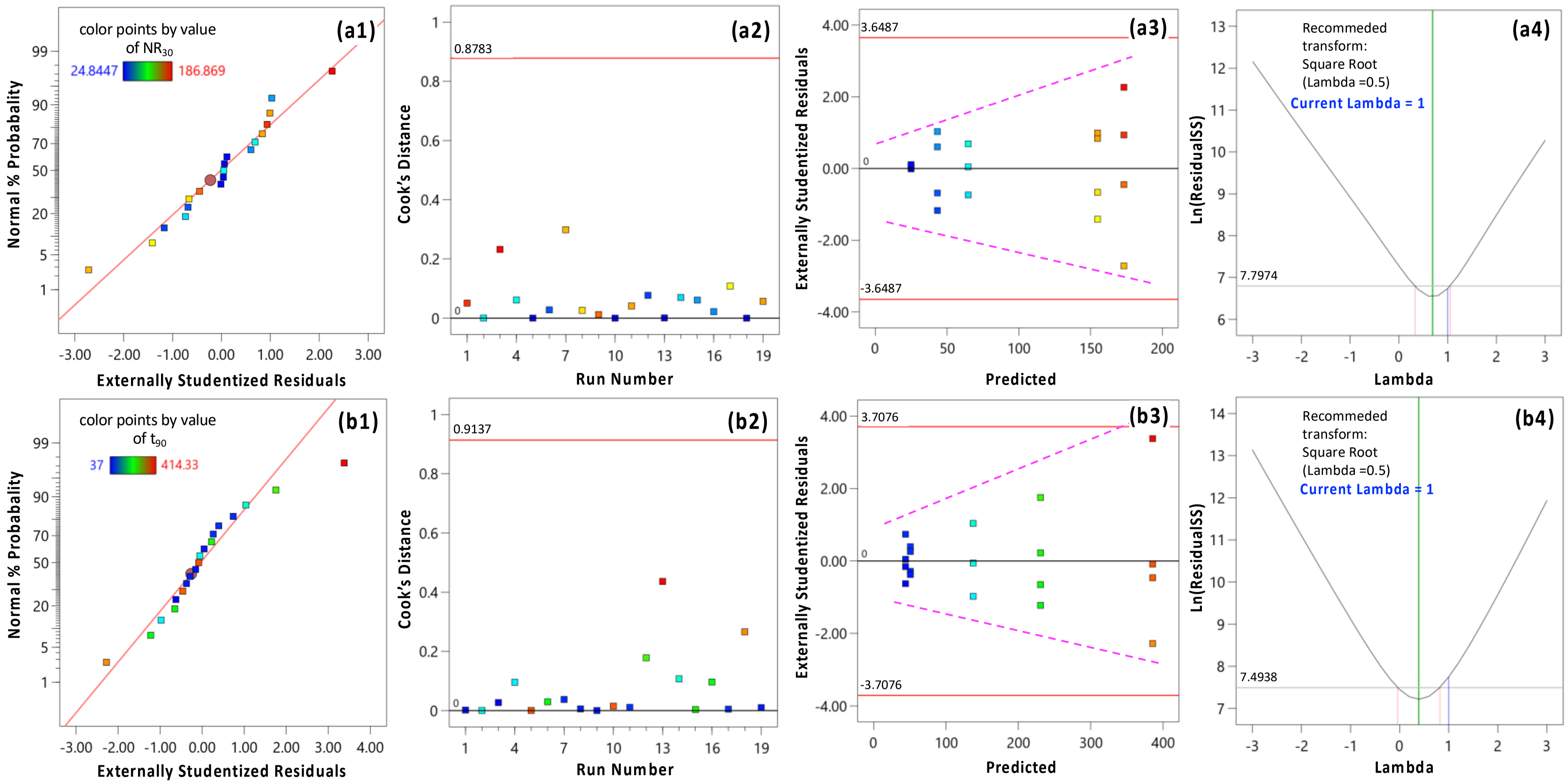

Figure 6.10 Diagnostic plots of the model for the desirable response, (a) NR_{30} and (b) t_{90} before transformation, encompass the following: the normal probability plot (1), Cook's distance (2), residuals vs. predicted plot (3), and the Box-Cox plot (4).

After transformation, the half-normal probability plot of effects, the Pareto chart for the T-value of |Effect|, and the ANOVA analysis collectively indicate the significant impact of factors A and B on NR_{30} [y_3], while for t_{90} [y_4], factors A, B, and AB are significant, Figure 6.11. Furthermore, the ANOVA results emphasize the significance of curvature or nonlinearity in the relationships between factors of NR_{30}. However, for t_{90}, this significance was not observed (Table 6.7). Notably, the LOF (Lack of Fit) is found to be non-significant. Furthermore, the model's diagnostic validation confirms its reliability, Figure 6.12. The normal probability plots indicate a normal distribution of errors. None of the desirable responses exceeds the Cook's distance limit, signifying minimal influence of individual points. Additionally, the residuals vs. predicted plot indicates homoscedasticity. the Box-Cox plot does not recommend a transformation. Based on these findings, NR_{30} requires the incorporation of additional nonlinear terms, whereas for t_{90}, the model is deemed suitable for immediate use.

In summary, Table 6.8 presents the various significant factors, factor interactions and model curvature for each desired response before and after model transformation. After the transformation, there are notable changes in the significant factors and curvature of mole gas consumption, while the curvature of t_{90} also disappears after the transformation. The results indicate that the V_S/V_R has an impact on all responses, as it can influence the total amount of water, solution height, and the gas-liquid interfacial area within the crystallizer, all of which directly affect the responses. Additionally, the crystallizer length can alter mole gas consumption and hydrate formation kinetics by changing the solution volume and gas-liquid surface area. Finally, the increase in the gas supply (V_{res}) only affects water to hydrate conversion and mole gas consumption. Given these findings, it is not possible to eliminate any factor to obtain a perfect model. The results also indicate that three out of four responses exhibit nonlinear relationships in their results, as observed in the recommended model transformation. Furthermore, the results highlight the significant curvature in most of desired responses. Therefore, considering the importance of curvature in each of these responses, it is advisable to opt for a model that incorporates nonlinear terms, such as a quadratic model from axial point, to enhance the modeling of these responses. Although the t_{90} model is currently usable, the inclusion of the nonlinear term for t_{90} remains an extension stemming from further exploration in other response studies.

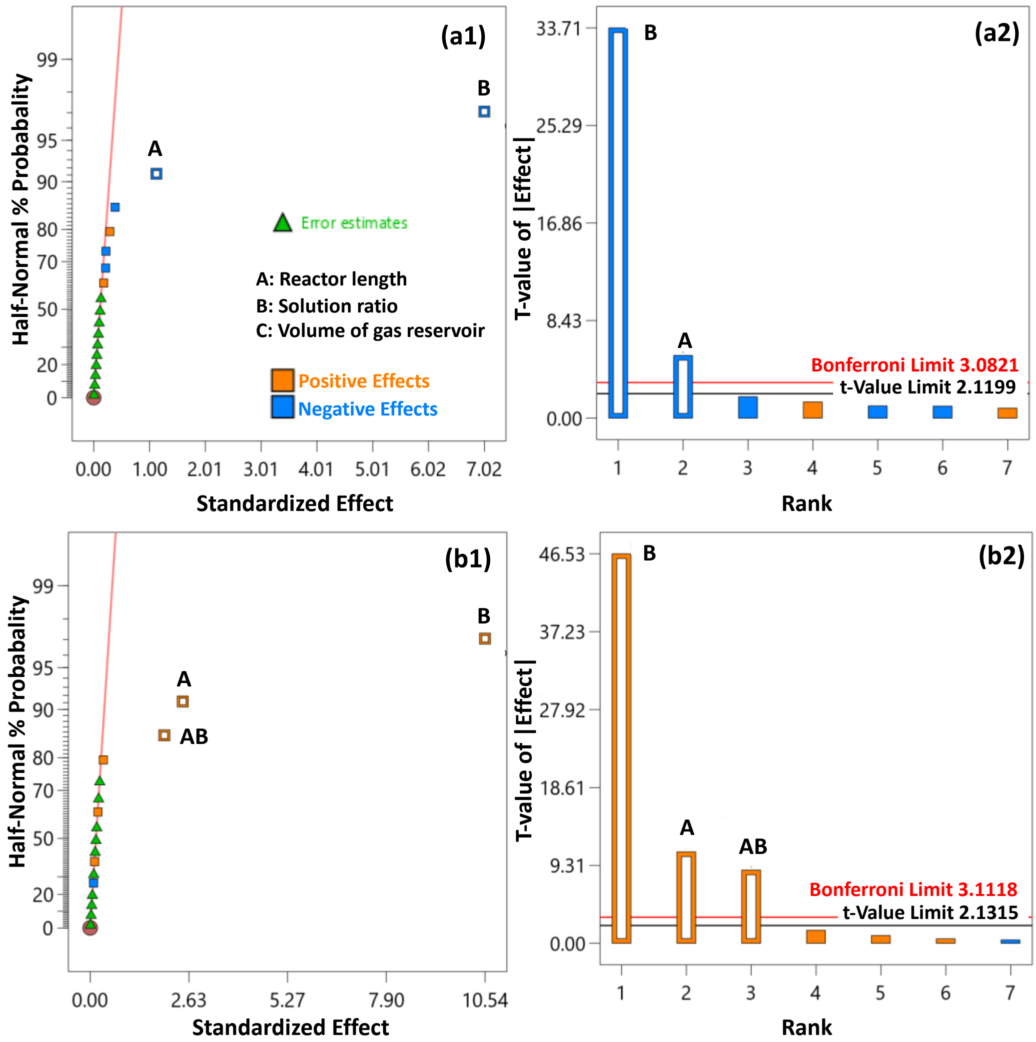

Figure 6.11 Half-normal probability plot of effects (1) and the Pareto chart (2) of the factors for the 2^3 factorial design on the desirable responses after transformation in 2^3 factorial design with three central points: (a) NR_{30} and (b) t_{90}.

Table 6.7 ANOVA table of the significant parameters for desirable responses after transformation; (a) NR_{30} and (b) t_{90} in 2^3 factorial designs with three central points

Source of variation	Sum of Squares	DF[a]	Mean Square	F-value	P-value
Square root (NR_{30}): $\sqrt{y_3}$					
Model	202.09	2	101.05	582.98	< 0.0001*
A	5.08	1	5.08	29.28	< 0.0001*
B	197.02	1	197.02	1136.67	< 0.0001*
Curvature	3.93	1	3.93	22.68	0.0003*
Residual	2.6	15	0.1733		
Lack of fit	1.43	5	0.287	2.46	0.1055
Pure error	1.17	10	0.1165		
Total	208.62	18			
Square root (t_{90}): $\sqrt{y_4}$					
Model	484.06	3	161.35	730.68	< 0.0001*
A	24.43	1	24.43	110.64	< 0.0001*
B	443.95	1	443.95	2010.43	< 0.0001*
AB	15.67	1	15.67	70.97	< 0.0001*
Residual	3.31	15	0.2208		
Lack of fit	1.2	5	0.2404	1.14	0.4009
Pure error	2.11	10	0.211		
Total	487.37	18			

* This factor significant

[a] Degree of freedom

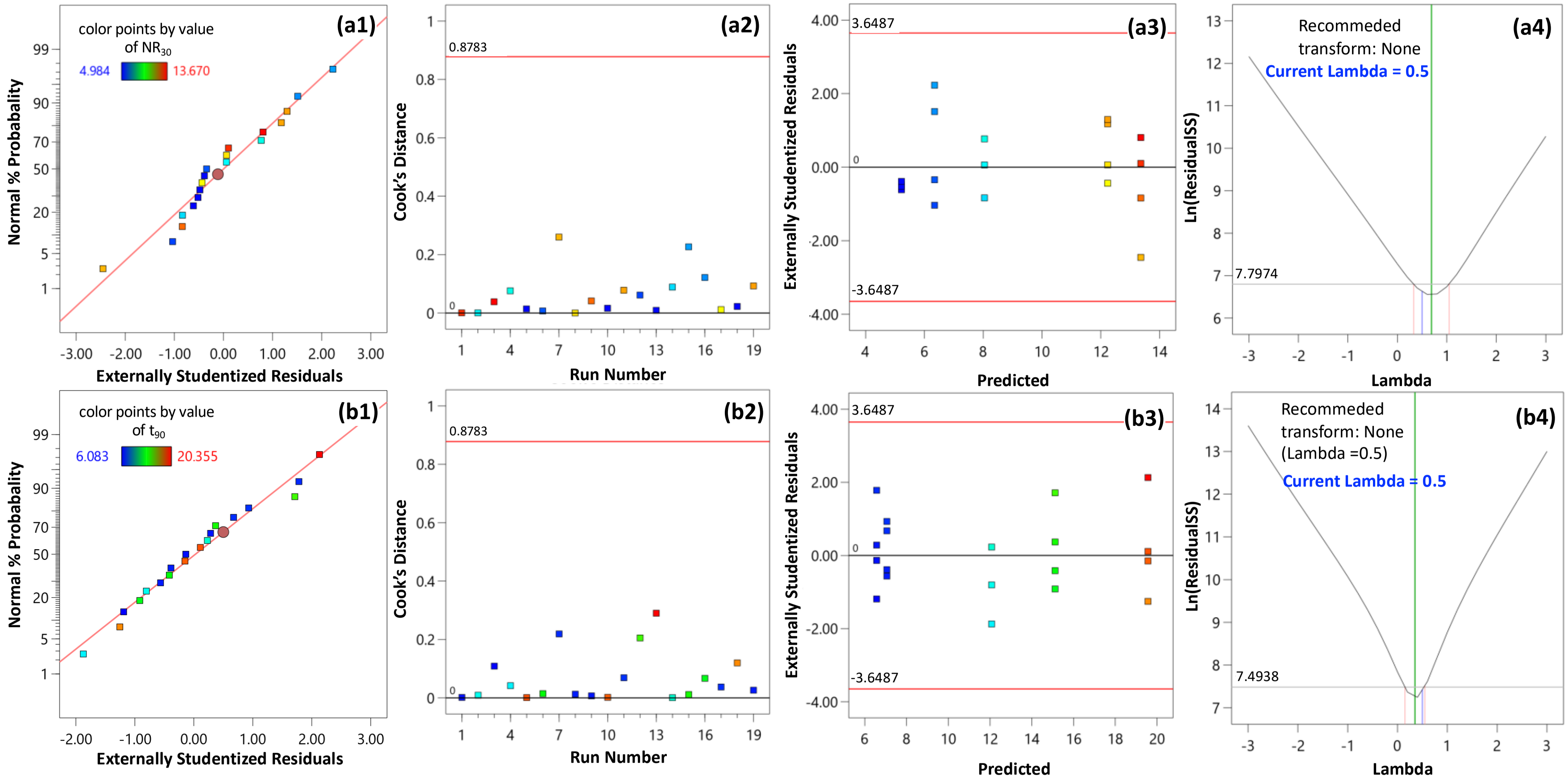

Figure 6.12 Diagnostic plots of the model for the desirable response, (a) NR_{30} and (b) t_{90} after transformation, encompass the following: the normal probability plot (1), Cook's distance (2), residuals vs. predicted plot (3), and the Box-Cox plot (4).

Table 6.8 Summary of significant factors for each desirable response in screening factors using a 2^3 factorial design with center points

Desirable Response	A	B	C	AB	AC	BC	Curvature	Transformation
[y_1] Water to hydrate conversion								-
Model before transformation								
[y_2] Mole gas consumption								-
[y_3] NR_{30}								-
[y_4] t_{90}								-
Model after transformation								
[y_2] Mole gas consumption								Log_{10}
[y_3] NR_{30}								Square root
[y_4] t_{90}								Square root

6.4.2.2 Optimization by Face-Centered Central Composite Design with Response Surface Methodology (FCCCD-RSM) Analysis

Having identified key factors, along with their interactions and the noteworthy curvature of the data derived from the 2^k factorial design, the utilization of a more advanced experimental design becomes imperative. The integration of the FCCCD-RSM offers the opportunity to delve into the curvature and the interactions that are not be fully captured within the confines of the 2^k design. To achieve this enhancement, the original factorial design is elevated to an RSM context by introducing axial points into the design space, thus crafting a comprehensive FCCCD-RSM configuration. This expanded design incorporates six axial points, facilitating the estimation of quadratic terms (A^2, B^2, and C^2) by the model. Additionally, supplementary center points are introduced to serve as control runs, ensuring the stability of the process across different blocks. Leveraging the FCCCD-RSM framework, an ANOVA analysis is executed for the quadratic model, encompassing various elements. This includes main effects (A, B, and C), two-factor interactions (AB, AC, and BC), as well as quadratic effects for each individual factor (A^2, B^2, and C^2). The experimental results of the additional axial points are listed in in Table 6.9.

Table 6.9 Experimental factors in coded values and their desirable responses for the addition axial points for FCCCD-RSM (Block 2)

Standard order[a]	Code level			Actual level			Desirable Responses			
	A	B	C	A crystallizer length (cm)	B V_S/V_R Ratio	C V_{res} (cm^3)	[y_1] water to hydrate conversion (%)	[y_2] mole gas consumption (mol)	[y_3] NR_{30} (v/v/hr)	[y_4] t_{90} (min)
20	0	0	-1	22	0.5	400	96.19	0.6723	124.83	67.39
21	0	0	-1	22	0.5	400	97.19	0.6833	116.5	66.27
22	0	-1	-1	22	0.25	500	98.54	0.3487	65.17	170.67
23	0	-1	-1	22	0.25	500	98.84	0.3505	45	174.77
26	-1	0	0	15	0.5	500	99.55	0.4824	84	92.38
27	-1	0	0	15	0.5	500	98.83	0.4774	98.17	89.46
28	0	0	0	22	0.5	500	98.62	0.6983	114.33	72.83
29	0	0	0	22	0.5	500	98.67	0.6988	147.33	49.95
24	1	0	0	29	0.5	500	98.85	0.9242	148.67	51.86
25	1	0	0	29	0.5	500	96.94	0.8976	151.17	65.79
30	0	1	0	22	0.75	500	97.69	1.0325	301.83	33.66
31	0	1	0	22	0.75	500	94.67	0.9846	290.83	34.31
32	0	0	1	22	0.5	600	98.23	0.6941	124.33	67.7
33	0	0	1	22	0.5	600	98.98	0.7025	143.33	68.9

[a] The actual run order has been randomized

The ANOVA results for the inclusion of the axial point are presented in Table 6.10 through Table 6.13 for the responses of [y_1] water to hydrate conversion, [$\log_{10}(y_2)$] $\log_{10}$(mole gas consumption), [$\sqrt{y_3}$] square root (NR_{30}), and [$\sqrt{y_4}$] square root (t_{90}), respectively. All the models for desirable responses exhibit significant p-values, all below 0.05, and the lack of fit term is also non-significant. However, the ANOVA of factors in the full FCCCD-RSM model includes a large number of terms, and some of them are statistically insignificant ($p > 0.05$).

Table 6.10 ANOVA table of t variables in the full FCCCD-RSM model for water to hydrate conversion

Source of variation	**Sum of Squares**	**DF**[a]	**Mean Square**	**F-value**	**P-value**
Block	5.4	1	5.4		
Model	82.51	9	9.17	11.53	< 0.0001*
A	0.3972	1	0.3972	0.4997	0.487
B	41.02	1	41.02	51.6	< 0.0001*
C	22.52	1	22.52	28.33	< 0.0001*
AB	0.0293	1	0.0293	0.0369	0.8494
AC	1.4	1	1.4	1.76	0.1981
BC	8.6	1	8.6	10.81	0.0034*
A^2	0.1554	1	0.1554	0.1956	0.6626
B^2	4.13	1	4.13	5.2	0.0326*
C^2	2.46	1	2.46	3.09	0.0925
Residual	17.49	22	0.7949		
Lack of fit	1.68	5	0.3351	0.3603	0.8685
Pure error	15.81	17	0.9301		
Total	105.4	32			
Fit statistics	**Std. Dev.**[b]	**Mean**	**C.V. %**[c]		
	0.8916	97.51	0.91		

* This factor significant

[a] Degree of freedom, [b] Standard of deviation, [c] Coefficient of variation

Table 6.11 ANOVA table of variables in the full FCCCD-RSM model for mole gas consumption

Source of variation	Sum of Squares	DF[a]	Mean Square	F-value	P-value
Block	0.024	1	0.024		
Model	1.49	9	0.1661	3576.47	< 0.0001*
A	0.4075	1	0.4075	8777.31	< 0.0001*
B	1.05	1	1.05	22670.93	< 0.0001*
C	0.0013	1	0.0013	27.83	< 0.0001*
AB	1.97E-09	1	1.97E-09	0	0.9949
AC	0.0001	1	0.0001	1.87	0.1852
BC	0.0003	1	0.0003	6.39	0.0191*
A^2	0.0022	1	0.0022	47.8	< 0.0001*
B^2	0.0224	1	0.0224	482.28	< 0.0001*
C^2	0.0001	1	0.0001	1.82	0.1912
Residual	0.001	22	0		
Lack of fit	0.0001	5	0	0.3468	0.8773
Pure error	0.0009	17	0.0001		
Total	1.52	32			
Fit statistics	**Std. Dev.**[b]	**Mean**	**C.V. %**[c]		
	0.0068	-0.22	3.15		

* This factor significant

[a] Degree of freedom, [b] Standard of deviation, [c] Coefficient of variation

Table 6.12 ANOVA table of variables in the full FCCCD-RSM model for NR_{30}

Source of variation	Sum of Squares	DF[a]	Mean Square	F-value	P-value
Block	1.75	1	1.75		
Model	268.22	9	29.8	167.49	< 0.0001*
A	8.15	1	8.15	45.81	< 0.0001*
B	250.42	1	250.42	1407.38	< 0.0001*
C	0.3132	1	0.3132	1.76	0.1982
AB	0.5908	1	0.5908	3.32	0.0821
AC	0.1848	1	0.1848	1.04	0.3193
BC	0.1287	1	0.1287	0.7231	0.4043
A^2	0.3856	1	0.3856	2.17	0.1551
B^2	6.63	1	6.63	37.27	< 0.0001*
C^2	0.0418	1	0.0418	0.2347	0.6329
Residual	3.91	22	0.1779		
Lack of fit	1.23	5	0.246	1.56	0.2249
Pure error	2.68	17	0.1579		
Total	273.88	32			
Fit statistics	**Std. Dev.[b]**	**Mean**	**C.V. %[c]**		
	0.4218	8.90	4.74		

* This factor significant

[a] Degree of freedom, [b] Standard of deviation, [c] Coefficient of variation

Table 6.13 ANOVA table of variables in the full FCCCD-RSM model for t_{90}

Source of variation	Sum of Squares	DF[a]	Mean Square	F-value	P-value
Block	2.9	1	2.9		
Model	592.38	9	65.82	235.93	< 0.0001*
A	31.72	1	31.72	113.69	< 0.0001*
B	540.04	1	540.04	1935.79	< 0.0001*
C	0.009	1	0.009	0.0324	0.8588
AB	15.67	1	15.67	56.17	< 0.0001*
AC	0.0576	1	0.0576	0.2065	0.654
BC	0.1753	1	0.1753	0.6285	0.4364
A^2	1.03	1	1.03	3.7	0.0673
B^2	4.33	1	4.33	15.54	0.0007*
C^2	0.0318	1	0.0318	0.1141	0.7388
Residual	6.14	22	0.279		
Lack of fit	1.31	5	0.2619	0.9223	0.4904
Pure error	4.83	17	0.284		
Total	601.41	32			
Fit statistics	**Std. Dev.**[b]	**Mean**	**C.V. %**[c]		
	0.5282	11.82	4.47		

* This factor significant

[a] Degree of freedom, [b] Standard of deviation, [c] Coefficient of variation

Consequently, the extensive model appears to suffer from overfitting, capturing not only meaningful relationships but also random noise from the data. In such cases, it is essential to seek a more robust modeling approach (Frank E. Harrell, 2015). Bayesian Information Criterion (BIC) is a valuable tool often employed in combination with stepwise regression to aid in factor selection (Hocking, 1976). In the context of stepwise regression, specifically the backward elimination method, BIC values are calculated and compared at each step. The stepwise begins with a full model including all potential predictor factors. The BIC values are then calculated and compared for various combinations of factors, removing one at a time until reaching the lowest BIC value, indicating a better-fitting model (Frank E. Harrell, 2015). So, the final model comprises the selected factors, providing a balance between model fit and simplicity (Zhang, 2016). So, the ANOVA results for the reduced model, which exhibits significance in all desirable responses, as well as insignificance in residuals and a lack of fit, are presented in Table 6.14 through Table 6.17. Although, the adequate precision value of all models significantly exceeds 4, indicating the model's reliability, the fit statistics must be evaluated to check the prediction performance of the models.

Table 6.14 ANOVA table of variables in the reduced FCCCD-RSM model for water to hydrate conversion

Source of variation	**Sum of Squares**	**DF**[a]	**Mean Square**	**F-value**	**P-value**
Block	5.4	1	5.4		
Model	80.53	5	16.11	21.51	< 0.0001*
B	41.02	1	41.02	54.78	< 0.0001*
C	22.52	1	22.52	30.08	< 0.0001*
BC	8.6	1	8.6	11.48	0.0023*
B^2	3.98	1	3.98	5.31	0.0294*
C^2	2.31	1	2.31	3.08	0.0909
Residual	19.47	26	0.7488		
Lack of fit	3.66	9	0.4064	0.4369	0.8963
Pure error	15.81	17	0.9301		
Total	105.4	32			
Fit statistics	**Std. Dev.**[b]	**Mean**	**C.V. %**[c]		
	0.8653	97.51	0.89		

* This factor significant

[a] Degree of freedom, [b] Standard of deviation, [c] Coefficient of variation

Table 6.15 ANOVA table of variables in the reduced FCCCD-RSM model for mole gas consumption

Source of variation	Sum of Squares	DF[a]	Mean Square	F-value	P-value
Block	0.024	1	0.024		
Model	1.49	6	0.2491	5220.19	< 0.0001*
A	0.4075	1	0.4075	8541.83	< 0.0001*
B	1.05	1	1.05	22062.72	< 0.0001*
C	0.0013	1	0.0013	27.09	< 0.0001*
BC	0.0003	1	0.0003	6.22	0.0196*
A^2	0.0025	1	0.0025	52.49	< 0.0001*
B^2	0.024	1	0.024	502.19	< 0.0001*
Residual	0.0012	25	0		
Lack of fit	0.0003	8	0	0.6094	0.7581
Pure error	0.0009	17	0.0001		
Total	1.52	32			
Fit statistics	**Std. Dev.**[b]	**Mean**	**C.V. %**[c]		
	0.0069	-0.22	3.20		

* This factor significant

[a] Degree of freedom, [b] Standard of deviation, [c] Coefficient of variation

Table 6.16 ANOVA table of variables in the reduced FCCCD-RSM model for NR_{30}

Source of variation	**Sum of Squares**	**DF**[a]	**Mean Square**	**F-value**	**P-value**
Block	1.75	1	1.75		
Model	267.2	4	66.8	365.62	< 0.0001*
A	8.15	1	8.15	44.62	< 0.0001*
B	250.42	1	250.42	1370.62	< 0.0001*
AB	0.5908	1	0.5908	3.23	0.0833
B^2	8.04	1	8.04	44.01	< 0.0001*
Residual	4.93	27	0.1827		
Lack of fit	2.25	10	0.2249	1.42	0.2507*
Pure error	2.68	17	0.1579		
Total	273.88	32			
Fit statistics	**Std. Dev.**[b]	**Mean**	**C.V. %**[c]		
	0.4274	8.90	4.80		

* This factor significant

[a] Degree of freedom, [b] Standard of deviation, [c] Coefficient of variation

Table 6.17 ANOVA table of variables in the reduced FCCCD-RSM model for t_{90}

Source of variation	Sum of Squares	DF[a]	Mean Square	F-value	P-value
Block	2.9	1	2.9		
Model	592.11	5	118.42	480.24	< 0.0001*
A	31.72	1	31.72	128.62	< 0.0001*
B	540.04	1	540.04	2190.05	< 0.0001*
AB	15.67	1	15.67	63.55	< 0.0001*
A^2	1.16	1	1.16	4.69	0.0397*
B^2	4.37	1	4.37	17.71	0.0003*
Residual	6.41	26	0.2466		
Lack of fit	1.58	9	0.1759	0.6195	0.765
Pure error	4.83	17	0.284		
Total	601.41	32			
Fit statistics	**Std. Dev.**[b]	**Mean**	**C.V. %**[c]		
	0.4966	11.82	4.2		

* This factor significant

[a] Degree of freedom, [b] Standard of deviation, [c] Coefficient of variation

Table 6.18 Summary of fit statistics of the studied models

	Full model				Reduced Model			
Desirable Response	**R^2**	**Adjusted R^2**	**Predicted R^2**	***BIC**	**R^2**	**Adjusted R^2**	**Predicted R^2**	***BIC**
Water to hydrate conversion	0.8251	0.7536	0.5866	111.15	0.8053	0.7679	0.6849	100.71
Mole gas consumption	0.9993	0.9990	0.9983	-210.53	0.9992	0.9990	0.9986	-215.90
NR_{30}	0.9856	0.9797	0.9716	61.76	0.9819	0.9792	0.9742	51.91
t_{90}	0.9897	0.9856	0.9778	76.60	0.9893	0.9872	0.9830	64.06

* Bayesian Information Criterion

As shown in Table 6.18, the standard R^2 values of the simplified models are less than those of the full model. Typically, the R^2 value tends to rise as more factors are added to the model because additional terms can capture more variability. Therefore, comparing the adjusted R^2 of the models, it becomes evident that all the reduced models exhibit increased adjusted R^2 values, suggesting the better fit of the models through stepwise regression. Additionally, the predicted R^2 values of all the reduced models improve and are now in closer alignment with their respective adjusted R^2 values. This alignment indicates that there are no apparent signs of overfitting. Furthermore, the BIC values for the reduced models have decrease compared to those of the full model. Subsequently, diagnostic assessments of the reduced models were conducted, revealing that the models satisfy key requirements. The residuals exhibit an approximately normal distribution (Figure 6.13). They also display random scattering around predicted values (Figure 6.14) and show no discernible trend over runs, as all residuals fall within the Bonferroni limits delineated by red lines (Figure 6.15). There is exhibit no blocking effect, with residuals evenly distributed around the zero-line at both ends of the range (Figure 6.16).

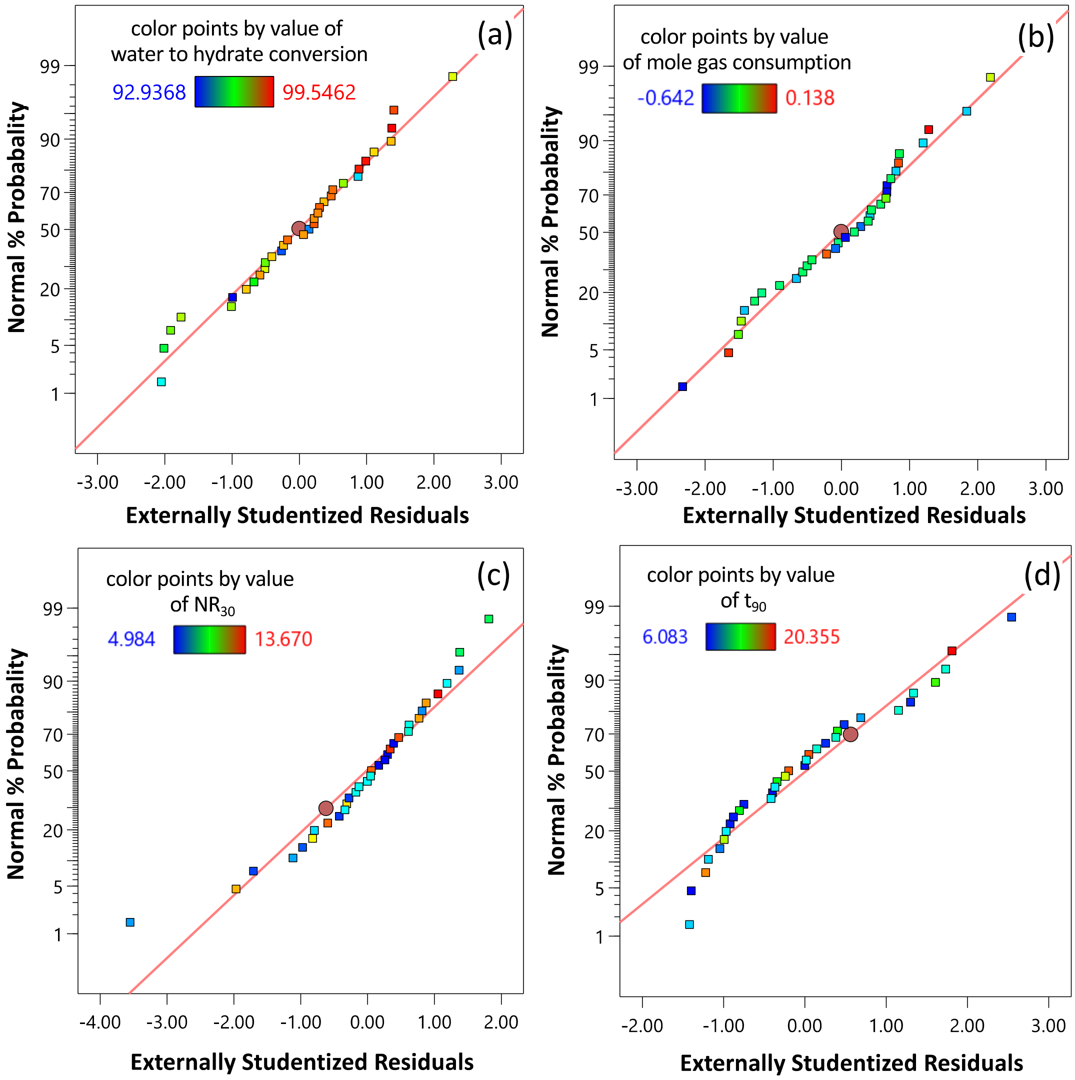

Figure 6.13 Normal probability plot for the desirable response from the reduced FCCCD-RSM model; (a) water to hydrate conversion, (b) mole gas consumption, (c) NR_{30} and (d) t_{90}.

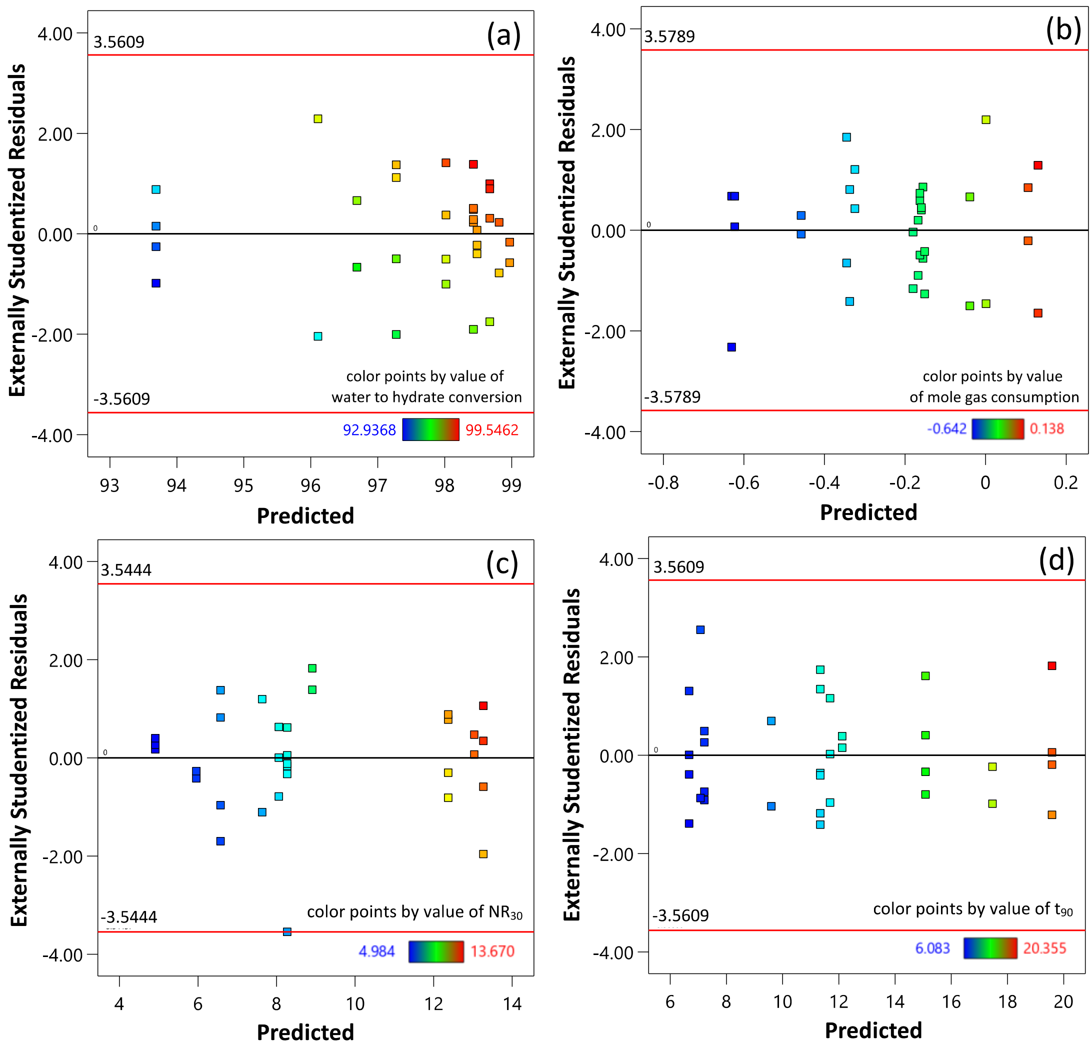

Figure 6.14 Residuals vs. predicted plot for the desirable response from the reduced FCCCD-RSM model; (a) water to hydrate conversion, (b) mole gas consumption, (c) NR_{30} and (d) t_{90}.

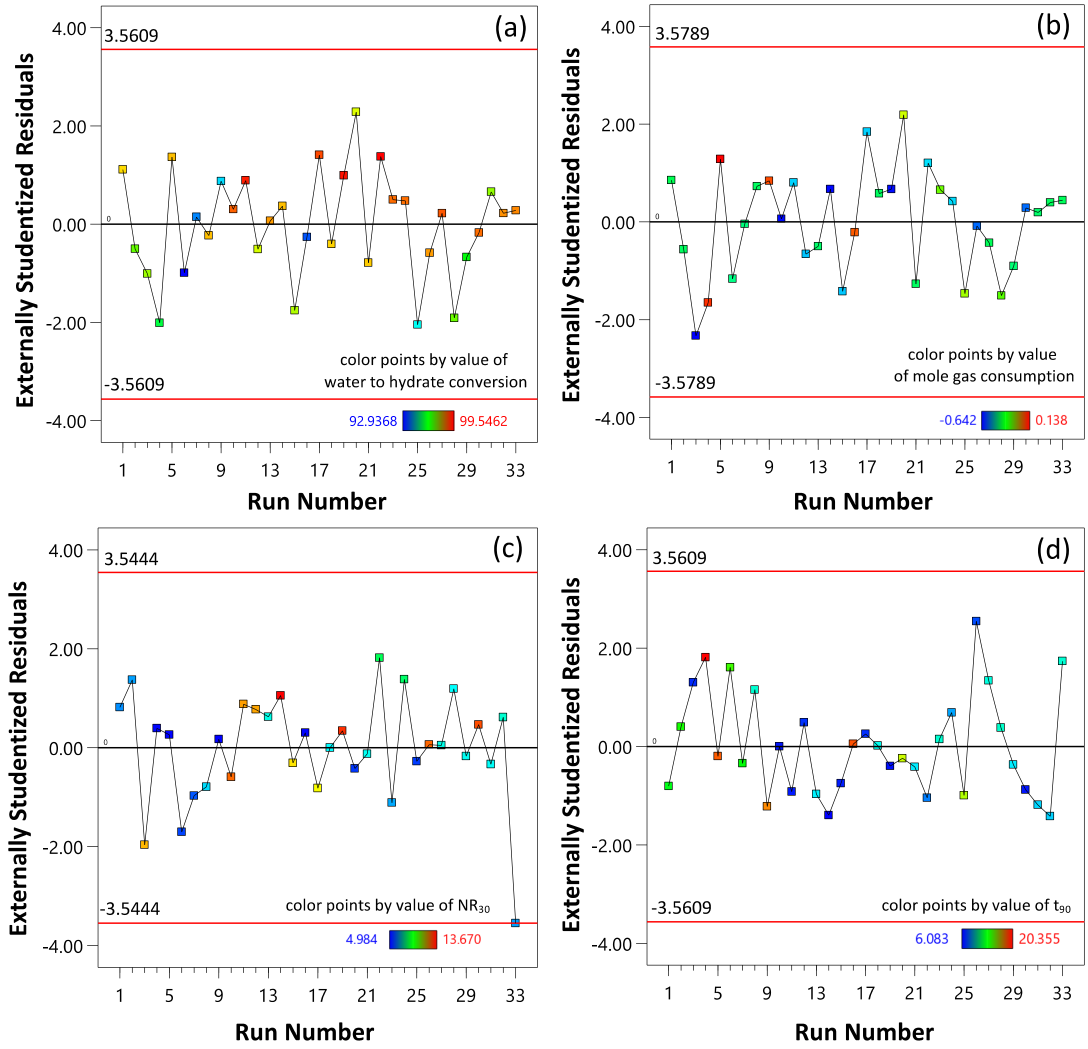

Figure 6.15 Residuals vs. run plot for the desirable response from the reduced FCCCD-RSM model; (a) water to hydrate conversion, (b) mole gas consumption, (c) NR_{30} and (d) t_{90}.

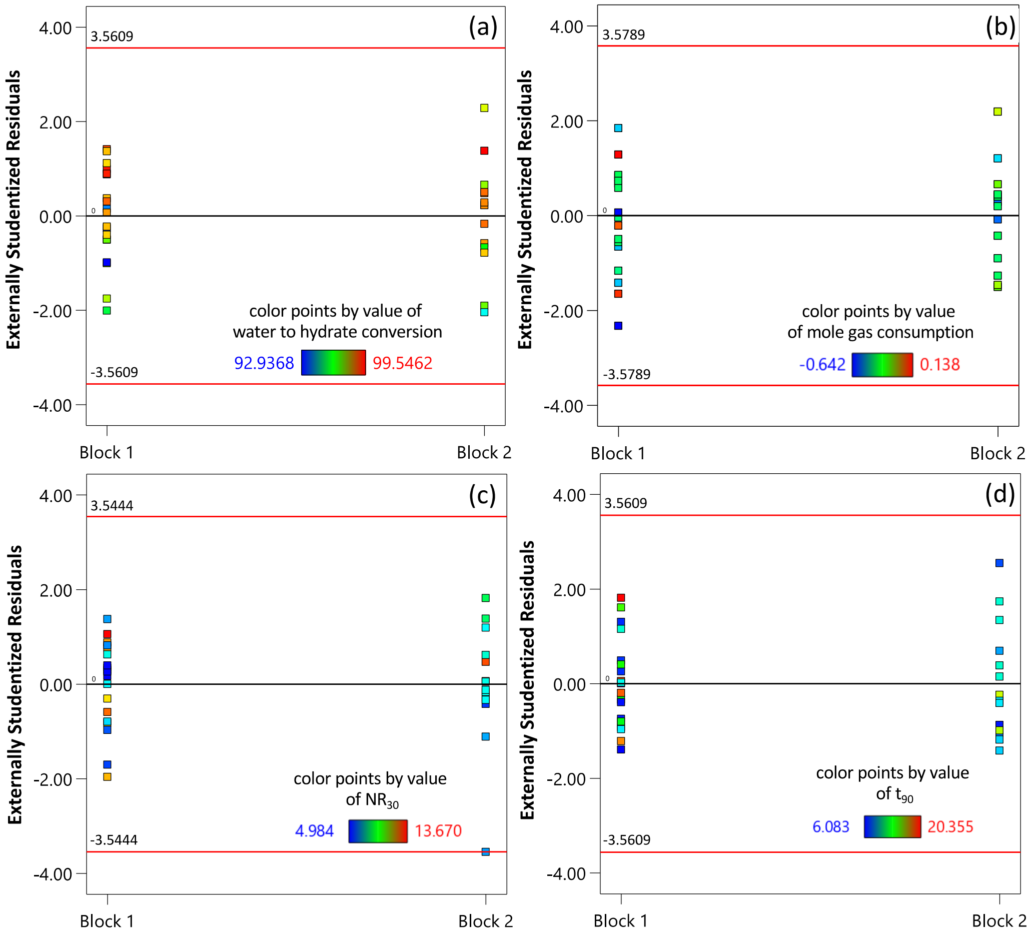

Figure 6.16 Residuals vs. blocks for the desirable response from the reduced FCCCD-RSM model; (a) water to hydrate conversion, (b) mole gas consumption, (c) NR_{30} and (d) t_{90}.

Table 6.19 Summary of significant factors and their coefficient sign for each desirable response FCCCD-RSM

Desirable Response	**A**	**B**	**C**	**AB**	**AC**	**BC**	**A^2**	**B^2**	**C^2**	**Transformation**
[y_1] Water to hydrate conversion		(-)	(+)			(+)		(-)	(-)	-
[y_2] Mole gas consumption	(+)	(+)	(+)			(+)	(-)	(-)		Log_{10}
[y_3] NR_{30}	(-)	(-)		(-)				(+)		Square root
[y_4] t_{90}	(+)	(+)		(+)			(-)	(+)		Square root

Table 6.19 offers a summary of the included factors associated with each desirable response. The inclusion of quadratic terms in all desirable responses is in accordance with the proposal that curvature is significant in the context of the 2^k factorial design. For water to hydrate conversion, the model incorporates five factors: B, C, their interaction BC, as well as their quadratic terms, B^2 and C^2. Although the impact of C^2 is not highly significant due to its p-value (0.0909), its inclusion is necessary to establish a hierarchical model structure. Such a hierarchy aids in enhancing model interpretability and gaining a deeper understanding of the relationships among factors. The mole gas consumption model includes six factors, four factors are included in the NR_{30} model, and five factors are part of the t_{90} model. So, the regression equation (in terms of coded factors) of all desirable responses could be expressed by Eq. (6.1), (6.2), (6.3), and (6.4),

$$\mathbf{y_1} = 98.46 - 1.43(B) + 1.06\,(C) + 0.7329\,(BC) - 0.8896\,(B^2) - 0.6777\,(C^2) \tag{6.1}$$

$$\mathbf{log_{10}(y_2)} = -\,0.1605 + 0.1427\,(A) + 0.2294\,(B) + 0.0080\,(C) + 0.0043\,(BC) - 0.0223\,(A^2) - 0.069\,(B^2) \tag{6.2}$$

$$\sqrt{\mathbf{y_3}} = 8.17 - 0.6384\,(A) - 3.54\,(B) - 0.1922\,(AB) + 1.22\,(B^2) \tag{6.3}$$

$$\sqrt{\mathbf{y_4}} = 11.52 + 1.26\,(A) + 5.20\,(B) + 0.9897\,(AB) - 0.4797\,(A^2) + 0.9320\,(B^2) \tag{6.4}$$

The model equation demonstrates consistent factor coefficients across all desirable responses, aligning with the outcomes observed in the one-factor-at-a-time (OFAT) section, as depicted in Figure 6.4. Beginning with water to hydrate conversion, it's evident that the V_S/V_R ratio (B) exerts a notably more pronounced impact, as indicated by its coefficient of -1.43, in contrast to V_{res} (C) with a coefficient of 1.06. These coefficients indicate that an increase in V_S/V_R leads to a decrease in conversion, primarily due to the increased solution height, which makes gas-liquid contact more challenging. Conversely, an increase in gas supply doesn't significantly contribute but tends to slightly enhance conversion. The interaction term BC suggests that when there is a concurrent rise in both V_S/V_R and V_{res}, it tends to counterbalance the negative trend induced by higher V_S/V_R, potentially resulting in a more moderate decrease or even an increase in conversion. In terms of quadratic terms, B^2 indicates diminishing returns, indicating that excessively high V_S/V_R values can nonlinearly impede conversion. Conversely, C^2 implies that larger gas supplies, despite their negative impact, can still contribute to conversion rates, although this effect may not be as pronounced as the linear term.

Regarding mole gas consumption, the V_S/V_R ratio (B) exhibits the most significant contribution, represented by a coefficient of 0.2294, followed by crystallizer length (A) with a coefficient of 0.1427, and V_{res} (C) with a coefficient of 0.0080. This suggests that a higher V_S/V_R ratio corresponds to increased gas consumption because it involves adding more solution to the crystallizer. Similarly, an increase in crystallizer length, which provides more volume for the solution, shows a positive coefficient, indicating an associated rise in gas consumption. The small positive coefficient for V_{res} implies a higher gas supply, which provides a greater driving force for gas molecules, leads to a slight increase in gas consumption. The interaction term BC (0.0043) suggests that when both B and C increase concurrently, there is a slight additive effect on gas consumption. As for the quadratic terms, A^2 signifies diminishing returns for extremely long crystallizer lengths, while B^2 suggests that excessively high ratios result in diminishing increases in gas consumption. It's worth noting that the relationship between all factors and mole gas consumption follows a logarithmic pattern.

In the case of NR_{30}, it's notable that the V_S/V_R (A) makes a more substantial contribution (3.54), compared to the crystallizer length (B) (0.6384). Both B and A exhibit negative coefficients, indicating that a higher V_S/V_R (B) and a longer crystallizer length (A) have a significant negative impact on NR_{30}, meaning that both factors tend to reduce NR_{30}. The interaction term AB further complicates this relationship, as it also contributes negatively to NR_{30} when both crystallizer length and V_S/V_R increase simultaneously. Interestingly, the quadratic term B^2, which suggests that very high V_S/V_R can, actually increase NR_{30}. Additionally, it's important to note that the relationship between all factors and NR_{30} follows a square root pattern.

In case of t_{90}, V_S/V_R also exhibits the higher contribution (5.20) to t_{90} than the crystallizer length (1.26). The positive coefficient of A and B corresponds to a higher t_{90}, the interaction between AB has a positive impact on t_{90}, implying that simultaneous increases in both factors result in a synergistic effect on t_{90}. Additionally, the quadratic terms A^2 suggesting diminishing returns for extremely long crystallizer lengths and B^2 indicating that very high V_S/V_R can significantly increase t_{90}. These trends might be attributed to changes in the solution volume.

To summarize, V_S/V_R plays the most significant role in each desirable response. Changes in V_S/V_R impact methane hydrate formation through various dimensions, including the amount of solution, changes in solution height, and alterations in the gas-liquid contact surface area within the horizontal crystallizer. These interactions further emphasize the significance of the interaction between V_S/V_R and the other two factors. However, we cannot overlook the importance of these two factors. V_{res} contributes to an increase in gas uptake and the overall amount of gas consumption. On the other hand, the increase in gas-liquid contact surface area, influenced by the crystallizer length, plays a vital role in hydrate formation kinetics, including NR_{30} and t_{90}.

To provide a clearer illustration of how the desirable responses depend on their significant factors, we've utilized Figure 6.17. In this figure, you'll find 3D response surface plots and corresponding 2D contours. The x and y-axes in these plots represent the two factors with the highest contributions, while the z-axis represents the desirable responses. These visuals effectively demonstrate the significant impact of V_S/V_R, along with other factors and their interactions, on the desirable responses. The non-linear shapes of the desirable response surfaces and the influence of different factors on these responses become evident through these graphics. Additionally, these images help identify optimal factor settings for achieving the best results in each desirable response. For example, 0.35 of V_S/V_R and 500 cm^3 of V_{res} can give and 99% conversion while 0.75 V_S/V_R and 29 cm crystallizer length give highest gas consumption. In term of hydrate formation kinetics, low V_S/V_R and high crystallizer length give a high NR_{30} and low t_{90}. Indeed, within the realm of hydrate formation, an interesting phenomenon emerges. Despite the significance of these four factors, they occasionally counteract each other, leading to varying optimal conditions for different aspects of hydrate formation within the same process. To optimize the hydrate formation setup, it's essential to establish a set of acceptable result criteria from different perspectives. These criteria serve as benchmarks for evaluating the effectiveness and efficiency of the process.

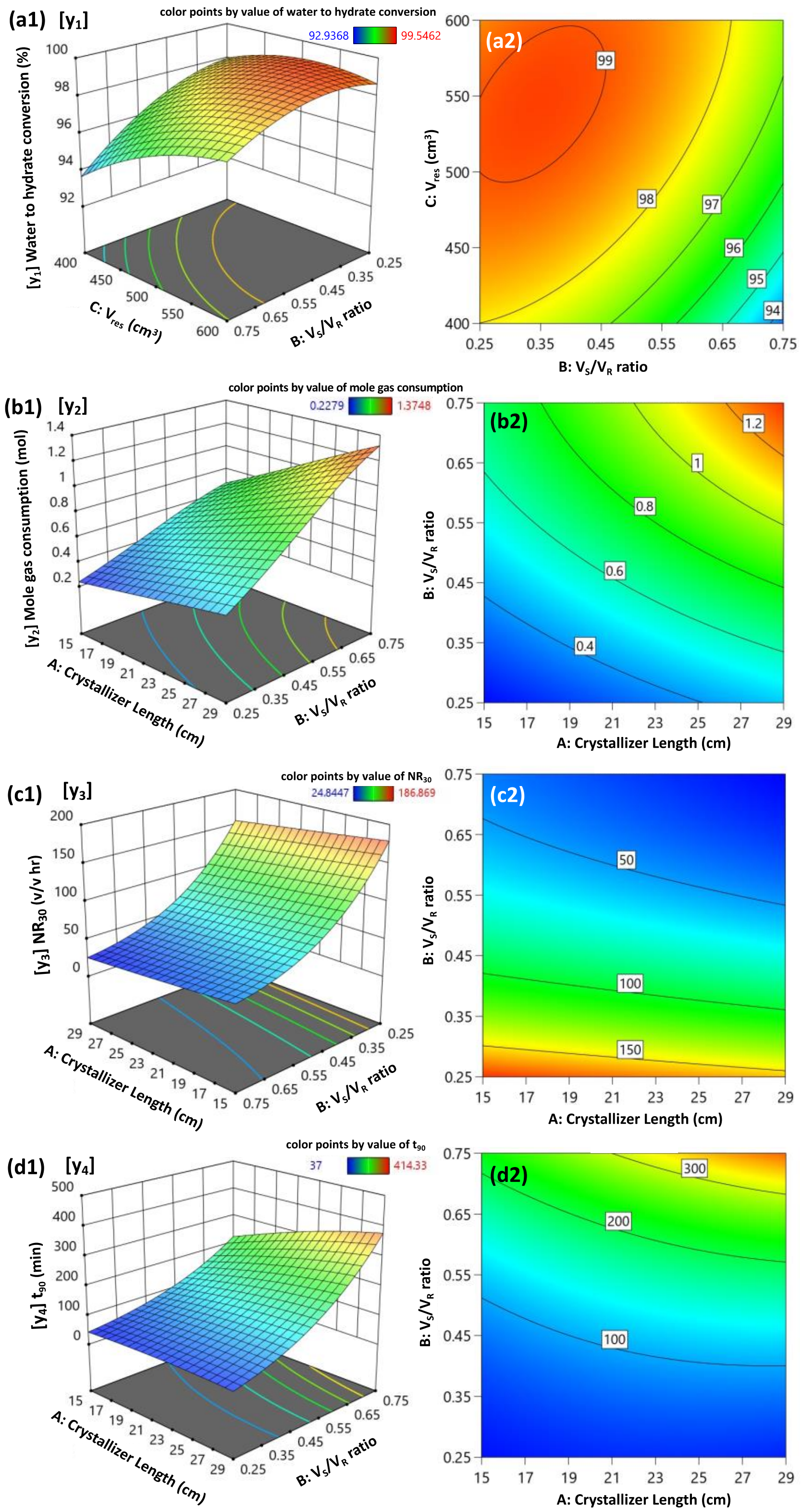

Figure 6.17 Response surface 3D plot (1) and 2D contour (2) of desirable responses; (a) water to hydrate conversion, (b) mole gas consumption, (c) NR_{30}, and (d) t_{90}.

6.4.3 Optimizing Hydrate Formation and Model Validation

To enhance the efficiency and economic feasibility of energy storage using hydrate technology, it is essential to carefully balance the operational and capital costs associated with methane hydrate formation. In terms of operational efficiency, the primary goals are to maximize water to hydrate conversion and mole gas consumption per batch, while optimizing hydrate formation kinetics, particularly by minimizing the t_{90}. From the capital cost perspective, the focus is on minimizing gas supply usage and maximizing crystallizer space utilization. The crystallizer size can be varying based on its purpose. The optimization constraints are detailed in Table 6.20.

Table 6.20 Constraints detail for the optimizing methane-THF hydrate formation

Name	Goal	Lower Limit	Upper Limit	Importance*
Desirable Hydrate Formation Responses				
Water to hydrate conversion	maximize	92.94	99.55	3
Mole gas consumption	maximize	0.50	1.375	5
NR_{30}	maximize	24.84	186.87	2
t_{90}	minimize	37.00	180.00	4
Factors of Crystallizer setup				
A: Crystallizer length	is in range	15	29	1
B:V_S/V_R ratio	maximize	0.25	0.75	5
C: V_{res}	minimize	400	600	3

*Highest = 5, Lowest = 1

In prioritizing aspects of the process, the maximization of mole gas consumption per batch and the V_S/V_R ratio were ranked as the most critical (highest = level 5) for efficient hydrate formation. Setting the goal to minimize t_{90} was designated at level 4 to have a fast hydrate formation. Prioritizing the maximization of water to hydrate conversion was positioned at level 3, considering that the lowest achieved result was already sufficiently high for effective hydrate formation.

Simultaneously, the minimization of gas supply usage (V_{res}) was also ranked at level 3 to ensure an adequate gas supply for the process. NR_{30} was assigned level 2, recognizing its relatively lower significance compared to overall process kinetics like t_{90}. Finally, crystallizer length was set at level 1, acknowledging its variability based on user and space availability. The upper and lower limits for factors and responses were established across a comprehensive range, except for mole gas consumption and t_{90}. The lower limit for Mole gas consumption was set at 0.50 to ensure sufficient gas capture, while the upper limit for t_{90} was fixed at 180 minutes to maintain an acceptable duration for hydrate formation.

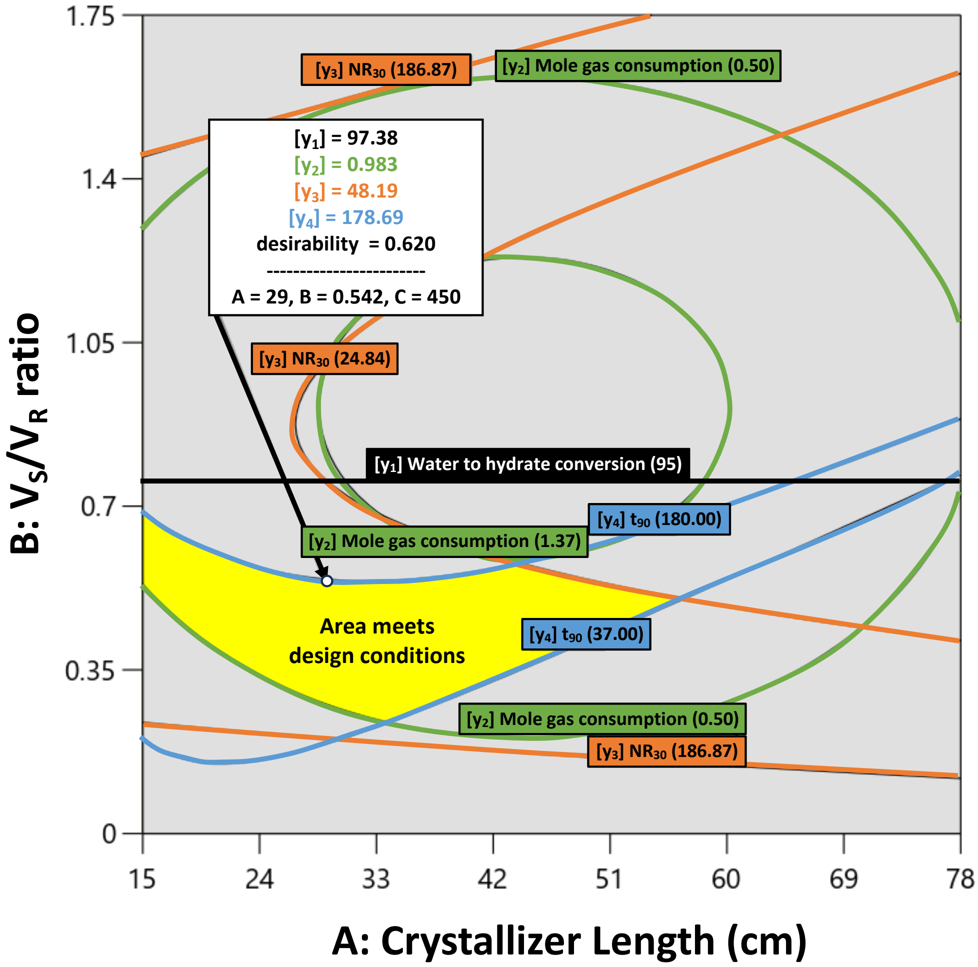

Figure 6.18 Optimal design space and sweet point at setup constraint of mixed methane-THF hydrate formation.

The results indicate that an optimized crystallizer setup consists of 29 cm crystallizer length (A), 0.542 V_S/V_R ratio (B), and 450 cm³ V_{res} (C) leading to 97.38% water to hydrate conversion, 0.983 mole of gas consumption, 48.19 v/v/hr NR_{30}, and 178.69 minutes t_{90}, as illustrated in Figure 6.18. Considering the complexity of the objectives and constraints, the c value achieved through optimization is 0.620 closely aligns with the predefined goals for the mentioned objectives. Furthermore, this figure depicts the optimal design space within the setup constraints. It demonstrates the diverse range of results achievable by varying the hydrate formation factors within this designated design space.

The last step involves model validation through confirmation runs for comparison with experimental values. To assess the predictive model's accuracy, the optimized setup and three new factor values were tested within a range that does not overlap with the dataset. Table 6.21 displays the experimental and predicted values for each desirable response, along with their respective percentage errors. In terms of water to hydrate conversion and the mole gas consumption, the percentage errors are within a ±5.00% range, indicating an excellent predictivity of the model. For the stochastic hydrate formation kinetics, percentage errors are somewhat larger but still fall within an acceptable range of ±10.00%. This highlights the successful utilization of the statistical experimental design by FCCCD-RSM in creating a predictive model for methane-THF hydrate formation within specific crystallizer setups. This optimization presents an approach to for economically effective operation of hydrate formation. However, a thorough economic analysis of the hydrate formation process is necessary to precisely determine the importance of each factor and response. Moreover, this dataset of statistical results provides opportunities for optimization from various perspectives, depending on the important of each response. Ultimately, the model offers valuable insights for the design of new hydrate formation systems and proves beneficial for scaling up efforts, thereby enhancing the feasibility of hydrate-based technology for energy storage.

Table 6.21 Comparison of model validation results from FCCCD-RSM

Actual level			Water to hydrate conversion (%)			Mole gas consumption (mol)			*NR_{30} (v/v/hr)			t_{90} (min)		
A	B	C	Experimental	Estimated	% Error	Experimental	Estimated	% Error	Experimental	Estimated	% Error	Experimental	Estimated	% Error
29	0.542	450	95.90	97.38	1.55	0.958	0.983	-2.61	44.11	48.19	9.26	184.17	178.69	2.97
18	0.800	575	96.84	96.08	0.79	0.593	0.590	0.46	57.23	61.56	7.56	148.33	133.97	2.92
17	0.563	400	95.98	96.46	0.49	0.879	0.864	1.69	38.04	38.23	0.49	320.50	307.83	3.95

6.5 Conclusion

This study utilized Design of Experiment (DOE) statistical analysis to uncover the primary factors and their interactions impacting the capacity and formation kinetics of mixed methane-THF hydrate formation. The subsequent 2^k factorial experiment revealed key factors influencing each response, highlighting the significant role of the solution to crystallizer volume ratio (V_S/V_R) in shaping various process aspects. Crystallizer length and the volume of the supplementary gas reservoir (V_{res}) were also influential but in specific ways. Additionally, the factorial design uncovered a significant absence of nonlinear terms, suggesting their necessity. The face-centered central composite design response surface methodology (FCCCD-RSM) was recommended to incorporate these terms, further elucidating the dominant impact of V_S/V_R on each desirable response. It illustrated how changes in V_S/V_R ripple throughout the system, impacting solution volume, height adjustments, and gas-liquid contact surface areas in the horizontal crystallizer. These insights underscore the substantial impact of the interaction between V_S/V_R and the other two factors. Nevertheless, this doesn't diminish the significance of V_{res}, which enhances gas uptake and overall consumption, or crystallizer length, a key player in hydrate formation kinetics, including NR_{30} and t_{90}. These are corresponded to a traditional investigation method one-factor-at-a-time (OFAT) but with more efficient examines multiple variables simultaneously, capturing interactions. The optimization process led to a well-balanced crystallizer setup that seeks equilibrium between operational and capital costs. This approach navigates the complexity of these interactions to achieve an economically viable process. Model validation affirms the model's reliability, with small percentage errors. Consequently, this comprehensive analysis establishes a strong foundation for designing innovative hydrate formation systems and enhancing existing processes, offering a promising path to improving the feasibility of energy storage technology rooted in methane hydrates.

6.6 CRediT Authorship Contribution Statement

Kan Jeenmuang: Conceptualization, Methodology, Formal analysis, Investigation, Data curation, Writing - Original Draft, Visualization. **Phuwadej Pornaroontham:** Methodology, Validation, Formal analysis, Writing – review & editing, Visualization. **Hari Prakash Veluswamy:** Writing – review & editing, Visualization. **Benjapon Chalermsinsuwan:** Validation, Software. **Praveen Linga:** Validation, Supervision. **Pramoch Rangsunvigit:** Validation, Writing – review & editing, Supervision, Funding acquisition.

6.7 Acknowledgments

The authors would like to acknowledge the financial support received from the following organizations: Second Century Fund (C2F), Thailand Science Research and Innovation Fund and Ratchadaphiseksomphot Endowment Fund, Chulalongkorn University.

CHAPTER 7
INVESTIGATING THE IMPACT OF AMINO ACID ADDITIVES ON THE MIXED METHANE-THF HYDRATE FORMATION: REUSABILITY ASSESSMENT

7.1 Abstract

Amino acids have been proven to serve as potent kinetic promoters enhancing methane hydrate formation. Expanding the viability of hydrate technology requires considering factors beyond capacity and formation kinetics. The reusability of hydrate formation solutions is crucial for its economic feasibility, yet information on this aspect remains insufficient. To explore the reusability aspect, five amino acids including glutamic acid, valine, leucine, methionine, and tryptophan, arranged in increasing order of hydrophobicity, were employed. Their impact on methane hydrate formation parameters was studied across three methane hydrate formation cycles under low driving force conditions (298.2K and 9.2 MPa). It is interesting to note that several amino acid solutions are reusable, enhancing the formation of hydrates in a second cycle of hydrate formation. However, the findings suggested a reduction in the amino acid ability to enhance methane hydrate formation across multiple cycles. Additionally, a correlation was observed between the hydrophobicity of amino acids and their reusability performance, indicating that higher hydrophobicity allows for more cycles of solution usage. This study helps eliminate amino acid degradation as the cause of the observed reduction in enhancement performance, as evidenced by similar hydrate formation behavior observed during normal operation at a dissociation temperature of 308.2 K after a 3-hour preheat for hydrate formation. Furthermore, High-Performance Liquid Chromatography (HPLC) results also indicated that there was no loss of amino acid concentration across the hydrate formation cycles. This could aid future studies in uncovering hidden information regarding amino acids as hydrate formation kinetic promoters.

Keywords: Methane Hydrate Formation, Amino acid, Reusability, Degradation, High-Performance Liquid Chromatography.

7.2 Introduction

Solidified natural gas technology (SNG), utilizing gas hydrate-based storage, has been developed as a strong and practical alternative for natural gas storage. The gas hydrates resemble ice-like crystalline solids, forming under suitable pressure and temperature conditions by fostering hydrogen bonds between water molecules, resulting in ice cages that trap gas molecules (Sloan Jr and Koh, 2007). This hydrates technology offers increased energy storage capacity in a compact form, especially under lower pressure and higher temperature conditions. Furthermore, these hydrates can efficiently store natural gas under milder operating conditions, leading to cost-effective operations compared to alternative technologies. SNG also allows for easy gas recovery and incorporates enhanced safety measures to address pressure-related concerns (Veluswamy *et al.*, 2018). Due to these properties, gas hydrates able to used in others variety of applications, including hydrogen storage (Zhang *et al.*, 2022), CO_2 capture, storage and sequestration (Qureshi *et al.*, 2022b; Zheng *et al.*, 2020), gas separation (Partoon *et al.*, 2018; Zheng *et al.*, 2019), and desalination (Seo *et al.*, 2019; Truong-Lam *et al.*, 2022). However, hydrate-based technology always faces the challenge of operating conditions (high pressure and low temperature) required to generate a high enough driving force for inducing hydrate nucleation and formation (Khurana *et al.*, 2017).

To generate the necessary driving force, researchers have explored changes in the hydrate structure. This involves the addition of thermodynamic promoters (THPs) that influence the transformation of the hydrate structure, shifting it from sI (the structure of pure water and gas) to sII when these thermodynamic promoters are introduced (Lee *et al.*, 2012). As a result of the entrapment of THPs (thermodynamic promoters) in the hydrate structure, there is an extension of the temperature and pressure stability range for gas hydrates. This shift in the hydrate phase equilibrium leads to lower pressure and higher temperature conditions. Tetrahydrofuran (THF), Dioxolane, and Dioxane represent innovative thermodynamic promoters. They extend the hydrate phase equilibrium, allowing hydrate formation under more moderate conditions (Seo *et al.*, 2001; Veluswamy, 2019). Nevertheless, transitioning to hydrate formation at higher temperatures results in a reduction in its formation kinetics, primarily due to the decreased gas dissolution caused by the driving force (Veluswamy *et al.*, 2016b).

Chemical promoters that have the ability to increase the amount of gas dissolved in the solution were introduced, and they play a crucial role in promoting hydrate formation kinetics (He *et al.*, 2017). The introduction of protein-based substances, such as amino acids, has been found to enhance the kinetics of both sI and sII methane hydrate formation (Bavoh *et al.*, 2018; Asheesh Kumar *et al.*, 2019a; Sa *et al.*, 2013). Amino acids contribute to an increase in the dissolved gas quantity due to their unique chemical properties, which include the formation of a hydrophobic pocket promoting hydrophobic interactions between amino acids and methane molecules, leading to an increase in the quantity of dissolved gas (Bhattacharjee and Linga, 2021; Jeenmuang *et al.*, 2023). Indeed, the varying hydrophobicity of different amino acids leads to differing effects on hydrate formation (i.e., gas uptake, conversion, induction time, normalized rate of hydrate formation) (Jeenmuang *et al.*, 2021). Reusability and the memory effect of the solution is another factor could be influenced by the varying hydrophobicity of amino acids. However, it's important to note that the findings from the previous study may not offer a clear understanding of the reusability of amino acids concerning both the quantity and kinetics of hydrate formation. In previous study, Bhattacharjee *et al.* (2020b) observed an 11.3% reduction in gas uptake when reusing an amino acid-THF solution (with 500 ppm L-Trp). Additionally, they noted that it required more time to complete hydrate formation compared to the fresh solution, as indicated by the increases in t_{90} results. These findings were consistent with our prior research, which also showed unfavorable results in terms of both gas uptake and hydrate formation kinetics (Jeenmuang *et al.*, 2021). However, it's worth noting that the co-promotion of amino acid and dioxolane resulted in an unchanged gas uptake for hydrate formation over ten cycle reused solution (Bhattacharjee *et al.*, 2020a). Understanding the reusability of the solution is crucial in making hydrate-based energy storage more feasible and economical. Therefore, it's equally important to explore alternative perspectives that might provide insights into the effect of amino acids on methane hydrate formation. These differing viewpoints could offer a more comprehensive understanding of the complex interactions involved in this process.

Therefore, the primary goal of this study was to investigate the role of different amino acids as kinetic promoters, focusing particularly on their reusability on the methane-THF hydrates. The reusability of amino acids was investigated with a stoichiometric ratio of THF concentration at 5.56 mol% and included different concentrations of amino acids, such as tryptophan, methionine, leucine, valine, and glutamic acid. The study examined the amino acid reusability on hydrate at various formation condition in order to cover a large range of hydrate formation temperature and pressure driving force (298.2 K and 9.2 MPa, 293.2 K and 8.2 MPa, and 293.2 K and 7.0 MPa). The aim was to shed light on the influence of amino acid hydrophobicity in another aspects, extending beyond quantity and hydrate formation kinetics, to include the reusability of mixed methane-THF hydrate formation. Additionally, High-Performance Liquid Chromatography (HPLC) was utilized to analyze the composition of the solution after hydrate formation, providing further confirmation of the findings in this study.

7.3 Experimental

7.3.1 Materials

Ultra-high purity methane (99.99%) supplied by Linde Public Company, Thailand, was employed for hydrate formation in conjunction with distilled deionized water. Tetrahydrofuran (THF) of analytical reagent (AR) grade from RCI Labscan, Thailand, was used as a thermodynamic promoter. Amino acids, serving as kinetic promoters, which included tryptophan, methionine, leucine, valine, and glutamic acid, were obtained from Sigma-Aldrich, Singapore, with a purity level of ≥ 98%. Trifluoroacetic acid (TFA) HPLC grade was from Sigma-Aldrich, Singapore, with a purity level of ≥ 99%.

7.3.2 Hydrate Formation and Dissociation

7.3.2.1 Apparatus

Figure 7.1 depicts the experimental setup, which were modified from the previous work (Jeenmuang *et al.*, 2021). It comprises a batch-type 180 cm^3

high-pressure stainless-steel crystallizer (CR) with a magnetic bar stirring system and a 150 cm^3 supply vessel to enhance the methane supply for hydrate formation. To initiate hydrate nucleation, a hybrid stirred configuration was employed. Stirring commenced at the initiation of methane feed and ceased upon the first observation of hydrate nucleation (Jeenmuang *et al.*, 2023). These components are immersed in a cooling bath containing a mixture of glycol and water, with an external refrigerator (ER) (Model RC-20, Daeyang, Korea). The experimental pressure and temperature were monitored using a pressure transmitter (PT) (Model 68073-68074, Cole Parmer®, Singapore) with a 0.13% MPa accuracy, and a K-type thermocouple (TC) with ± 1.0 K accuracy. Both instruments were connected to a data logger (DL) (AI210, Wisco Industrial Instruments, Thailand), which was linked to a computer (PC). The system apparatus.

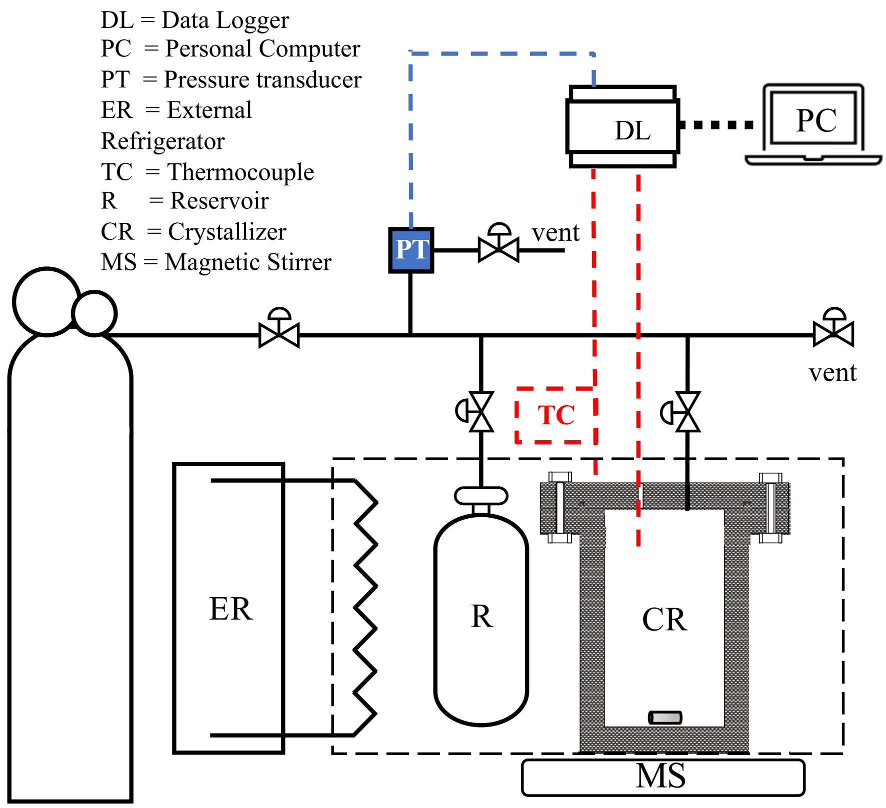

Figure 7.1 Experimental setup schematic.

7.3.2.2 Procedures

The procedures were adapted from our prior study (Jeenmuang *et al.*, 2023). In brief, a 90 cm^3 solution of amino acids with 5.56 mol% THF was introduced into the crystallizer. To eliminate any air within the crystallizer, the system was purged with methane gas three times. The hybrid stirred configuration was employed during the stirring process. The operating temperature remained constant at each set point, while the operating pressure was initially set at the desired pressure. Following hydrate formation, the system's temperature was elevated to 308.2 K to induce hydrate dissociation. After the hydrates fully dissociated, all the methane was released. The remaining solution was then reused for the next cycle of hydrate formation. This solution was reused two more times, allowing us to study its reusability within a three-cycle process. Temperature and pressure were continuously monitored and recorded over a 10-hour period, ensuring that the pressure drop did not exceed 100 kPa per hour. Each experiment was triplicated to confirm reproducibility. The calculations incorporated a new parameter drawn from previous research (Jeenmuang *et al.*, 2023). The normalized time required to achieve 90% completion of hydrate formation, referred to as $t_{90,norm}$, which was determined using equation (7.1).

$$t_{90,norm}\ (\text{min/(v/v)}) = \frac{t_{90}\ (\text{min})}{\text{methane uptake}_{\text{at }90\%}\ (\text{v/v})} \qquad 7.1)$$

7.3.3 <u>High-Performance Liquid Chromatography (HPLC) Investigation</u>

7.3.3.1 Solution Preparation

A 1 mL standard solution containing 5.56 mol% THF, both with and without 0.25 wt% methionine, were initially prepared using the same procedure employed for hydrate formation. while 1 mL of reused solution was sampling from each cycle of hydyrate formation. Subsequently, these solutions underwent dilution and filtration through a 0.22 μm filter to remove unwanted particles for calibration and application.

7.3.3.2 Apparatus and Procedures

The HPLC setup included an Alltech Model 525 binary gradient pump, a Rheodyne 8125 injection valve, and the Alltech Model 500 Evaporative Light Scattering Detector (ELSD), Alltech Associates, Inc. For chromatography, an Alltech Alltima^{TM} C18 column with a particle size of 5μm and dimensions of 250 x 4.6mm ID was utilized.

The procedures were modified from an equipment Application Note 0040EP: Underivatized Amino Acids from Alltech Associates, Inc. A 50μL injection of a prepared solution containing the amino acid mixture was chromatographed onto a C18 column using the following chromatographic conditions: Mobile Phase A consisted of 0.1% TFA in Water, and Mobile Phase B comprised 0.1% TFA in Acetonitrile. The flow rate was set at 0.8mL/min, temperature maintained at 25°C, and the gas flow rate was 2.5 SLPM. The 5.56 mol% THF standard served as a blank experiment. Subsequently, when analyzing the methionine mixed solution, any additional peaks observed were attributed to methionine.

7.4 Result and Discussion

The kinetics and morphology of mixed methane-THF hydrate formation with the addition of amino acids have been thoroughly investigated in previous studies (Jeenmuang *et al.*, 2023; Jeenmuang *et al.*, 2021). These investigations have shed light on the synergistic effects of amino acids and THF in high temperature hydrate formation, which have enhanced methane hydrate formation in terms of both quantity and formation kinetics. However, the role of amino acid reusability remains a crucial aspect that could further explain the effects of the presence of amino acids.

7.4.1 Reusability of 5.56 mol% THF Mixed with Amino Acids at 293.2 K and 8.0 MPa for Methane Hydrate Formation

The impact of several amino acids (valine, leucine, and methionine) on the mixed methane–THF hydrate formation and dissociation was thoroughly investigated at 293.2 K, 8.0 MPa hydrate formation and the 308.2 K hydrate dissociation in a previous study (Jeenmuang *et al.*, 2021). Hydrophobic amino acids like leucine and methionine demonstrated not only high methane uptake but also enhanced hydrate formation kinetics, observed in the decreased hydrate formation induction time, increased normalized rate of hydrate formation 30 minutes after the first nucleation (NR_{30}), the decrease of time required to achieve 90% of methane uptake (t_{90}) compared to without amino acid (only 5.56 mol% THF). Moreover, the reusability of these amino acids was also investigated and discussed in this previous work, Figure 7.2.

The reusability of the solution after dissociation at 308.2 K, Figure 7.2 shows no significant difference in methane uptake across the solution system and its cycles of hydrate formations, as illustrated in Figure 7.2 (a). In regard to the hydrate formation kinetics, the cycle of hydrate formation directly affects the hydrate formation. In terms of hydrate nucleation observed by the induction time, Figure 7.2 (b), all solutions result in the decrease of induction time across the cycle of hydrate formations which could be the water molecules retain a memory on the hydrogen bond of hydrate cage formation, which facilitates and promotes the next hydrate formation (Bhattacharjee *et al.*, 2020b; Wu and Zhang, 2010). In terms of t_{90}, the THF solution exhibits a decreasing trend in t_{90} values across the cycles of hydrate formation (Figure 7.2 (c)), potentially indicating the presence of a memory effect during the hydrate formation process. However, this phenomenon was not observed in the NR_{30} value, as it demonstrated consistent results across the cycles of hydrate formation, Figure 7.2 (d). Regarding to the addition of amino acid, the t_{90} increase and NR_{30} decreases across the hydrate formation cycles Figure 7.2 (c) and 7.2 (d), which is directly opposite to the trend observed in the THF solution. It has been proposed that the observed phenomenon is likely attributed to the accelerated degradation of amino acids at higher temperatures (Larsen, 1980) which surpasses the memory effect in water molecules. Although the t_{90} of the amino acid co-promoted systems increases with reused solution, it still reaches this threshold faster than in the fresh THF solution. This suggests that the amino acid's effectiveness decreases across the hydrate formation cycle until its impact becomes almost equivalent to that of the fresh THF solution.

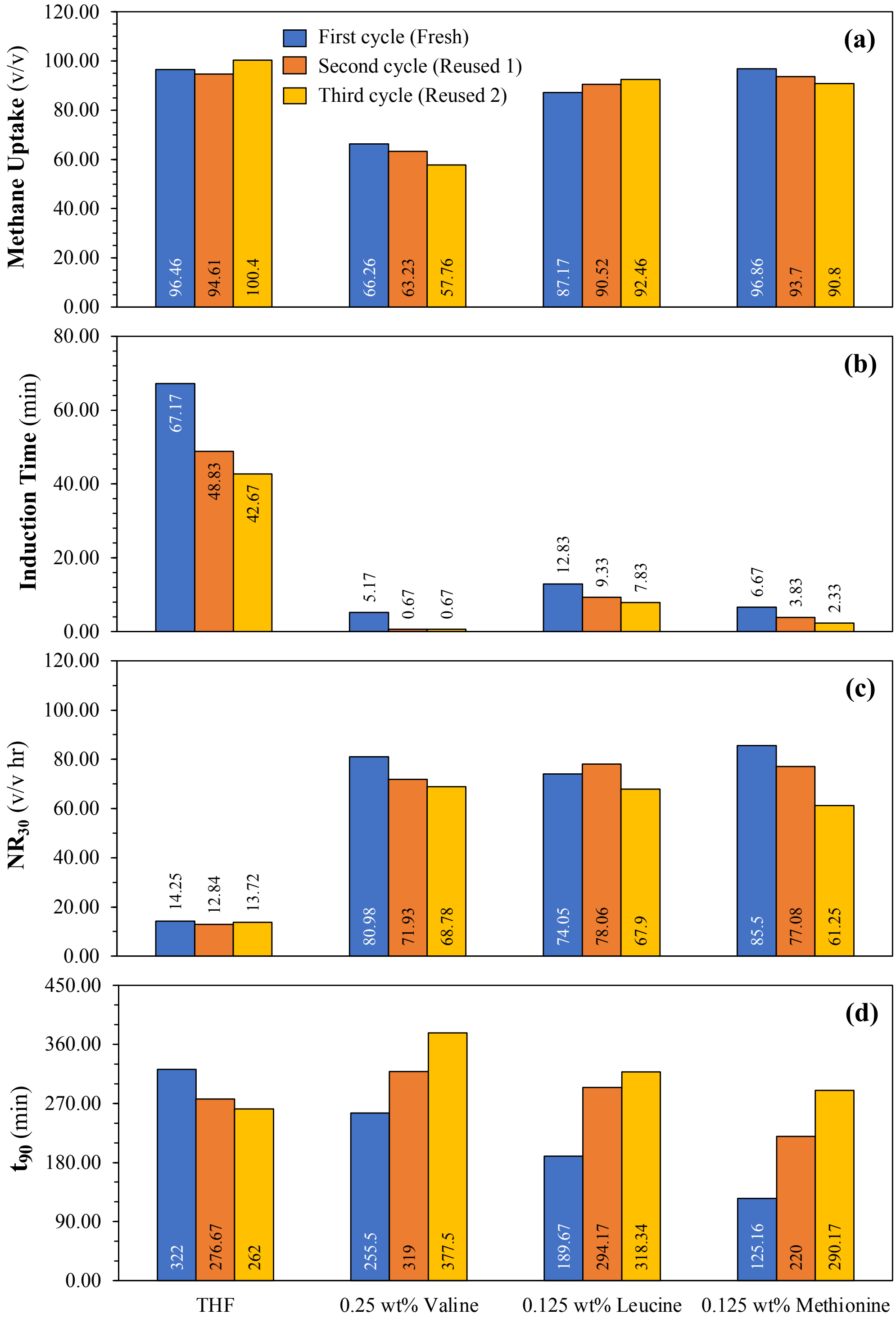

Figure 7.2 Comparison of methane uptake (a), induction time (b), NR_{30} (c) and the t_{90} (d) during methane hydrate formation cycles using 5.56 mol% THF and 5.56 mol% THF with three amino acids at 293.2 K and 8.0 MPa (refer to the data presented in Table 4 from Jeenmuang *et al.* (2021)).

7.4.2 Reusability of 5.56 mol% THF Mixed with Amino Acids at 298.2 K and 9.2 MPa for Methane Hydrate Formation

At 293.2 K and 8 MPa, the potential reusability of amino acid solutions appears promising. However, the degradation of amino acids across the cycle of hydrate formation is not clearly understood. To further investigate, the effects of amino acids were examined under more extreme hydrate formation conditions at 298.2 K and 9.2 MPa, where lower temperatures and pressure driving were applied, as shown in Figure 7.3. These reduced driving forces, from 9.25 K to 5.00 K and 5.88 MPa to 4.77 MPa, directly increase the difficulty of hydrate formation. Additionally, as hydrate formation is an exothermic process (Sloan Jr, 2003), higher formation temperatures can favor a reverse reaction, potentially lowering hydrate formation efficiency.

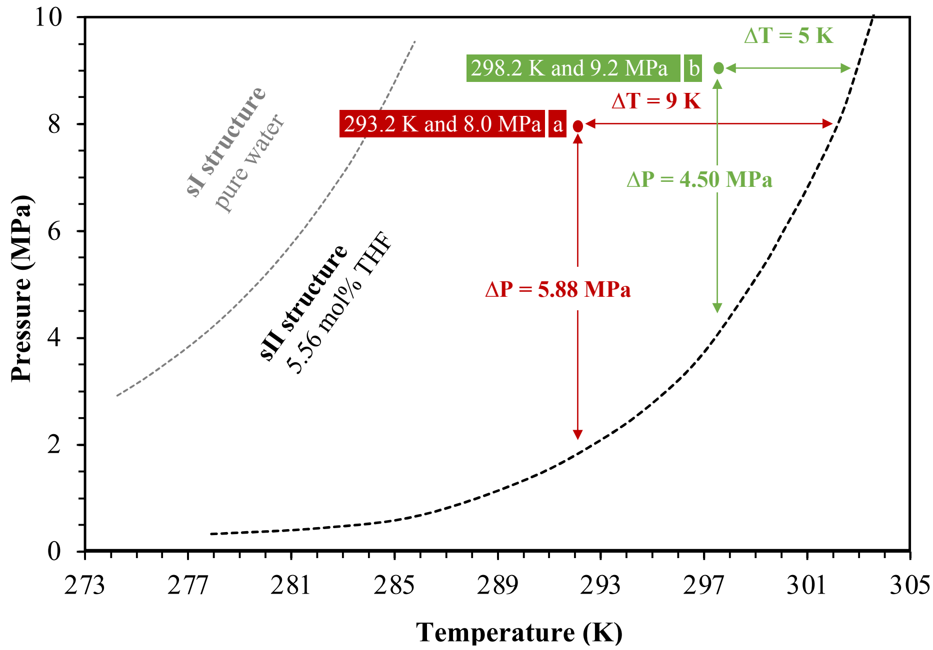

Figure 7.3 Pressure and temperature plot showing driving forces used at different formation conditions of (a) 293.2 K and 8.0 MPa and at (b) 298.2 K and 9.2 MPa.

The fresh solution (first cycle solution) of the mixed methane-THF with the addition of amino acids for hydrate formation at 298.2 K and 9.2 MPa has been previously investigated. The low driving force under these conditions clearly demonstrates the impact of amino acids compared to only THF solution. Their methane hydrate formation profiles in the fresh solution (Figure 7.4) emphasize the significant role of amino acid hydrophobicity, particularly with tryptophan, methionine, and leucine, enhancing both the quantity of methane uptake and the kinetics of hydrate formation (time required to achieve 90% completion of hydrate formation, t_{90}). However, the addition of valine and glutamic acid did not enhance hydrate formation, yielding similar results to the case without amino acids. Moreover, the impact on hydrate formation follows the amino acid hydrophobicity ranking: tryptophan, methionine, leucine, valine, and glutamic acid, respectively. Therefore, given the low hydrate formation driving force at this condition and the inclusion of five different amino acids with varying hydrophobicity, there is potential for revealing the concealed reusability of amino acids in methane hydrate formation.

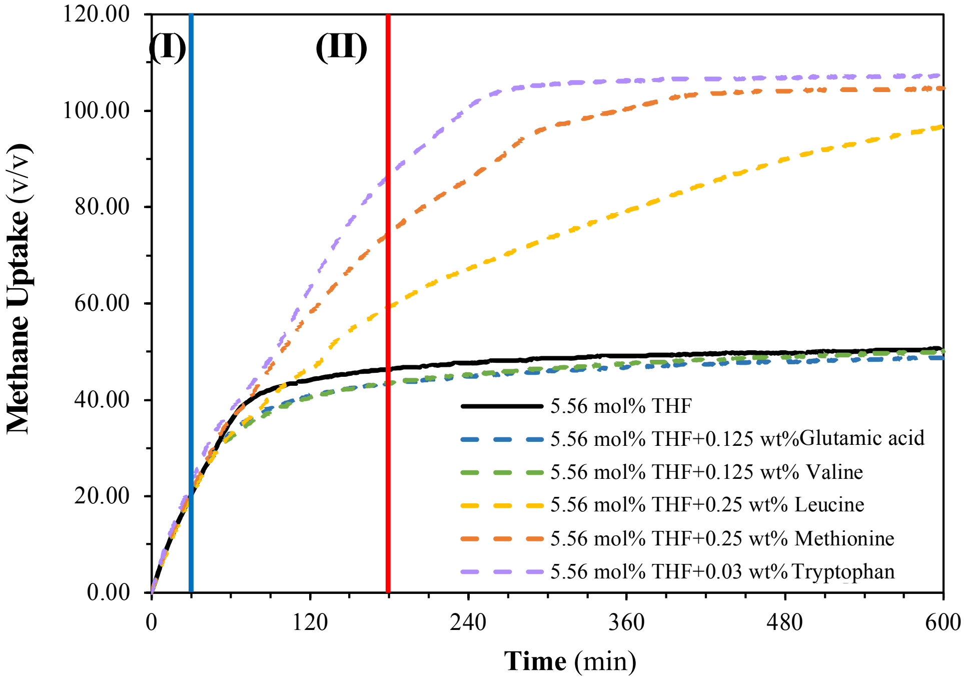

Figure 7.4 Plots of methane uptake against time on the 298.2 K and 9.2 MPa hydrate forming systems with different amino acids and concentrations; 0.125 wt% glutamic acid, 0.125 wt% valine, 0.25 wt% leucine, 0.25 wt% methionine, and 0.03 wt% tryptophan (reprinted with permission from Jeenmuang *et al.* (2023)).

7.4.2.1 Methane Uptake During the Hydrate Formation Cycle

Table 7.1 compiles methane uptake and water to hydrate conversion data during hydrate formation cycles at 298.2 K and 9.2 MPa. It involves 5.56 mol% THF and the same concentration of THF with five amino acids (glutamic acid, valine, leucine, methionine, and tryptophan) chosen based on optimal hydrate formation results observed in a previous study (Jeenmuang *et al.*, 2023). While Figure 7.5 also illustrates the changes in the hydrate formation profile, Figure 7.5 (a) and the average methane uptake, along with their standard deviations, Figure 7.5 (b), observed across three hydrate formation cycles from two replicates.

Without the addition of amino acids, the methane uptake profiles (Figure 7.5 (a-1)) indicate that all three cycles of solution behave similarly in the initial 30 minutes. However, beyond this point, hydrate growth is hindered in the second (reused 1) and third (reused 2) cycle solutions, differing from the behavior observed in the first cycle (fresh solution). The fresh solution results in the highest methane uptake 54.19 ± 0.05 volume of methane per volume of water (v/v) which equivalent to 64.78 ± 0.02 % water to hydrate conversion. While the second cycle of the THF solution results in a reduction of methane uptake and conversion by approximately 20% and 25% in the second and third cycle compared to the first cycle (43.30 ± 0.78 v/v or 58.46 ± 0.44 % conversion and 41.39 ± 1.71 v/v or 57.36 ± 1.02 % conversion), respectively. In contrast to the previous conditions at 293.2 K and 8.0 MPa, where the reuse of THF solution showed unchanged methane uptake, the difference at 298.2 K and 9.2 MPa suggests a unique scenario. This phenomenon might be due to the low driving force at these conditions, making methane diffusion through the hydrate film layer more challenging and thereby impeding hydrate crystal growth.

Table 7.1 Individual results for methane uptake and water to hydrate conversion during methane hydrate formation cycles using 5.56 mol% THF and 5.56 mol% THF with three amino acids at 298.2 K and 9.2 MPa

System	Experiment	Cycle	Methane Uptake (mol/mol)	Methane Uptake (v/v)	Water to Hydrate Conversion (%)
5.56 mol% THF	A1	F1C1	0.0555	54.24	64.78
	A2	F1C2	0.0451	44.08	58.9
	A3	F1C3	0.0441	43.10	58.37
	A4	F2C1	0.0554	54.15	64.81
	A5	F2C2	0.0435	42.51	58.02
	A6	F2C3	0.0406	39.68	56.34
0.125 wt% Glutamic acid	B1	F1C1	0.0503	49.16	61.85
	B2	F1C2	0.0461	45.06	59.47
	B3	F1C3	0.0446	43.59	58.64
	B4	F2C1	0.045	43.98	58.84
	B5	F2C2	0.0374	36.55	54.51
	B6	F2C3	0.0309	30.20	50.83
0.125 wt% Valine	C1	F1C1	0.0514	50.24	62.44
	C2	F1C2	0.0493	48.18	61.29
	C3	F1C3	0.0457	44.67	59.26
	C4	F2C1	0.0543	53.07	64.1321
	C5	F2C2	0.0492	48.09	61.2346
	C6	F2C3	0.0418	40.85	57.0604
0.25 wt% Leucine	D1	F1C1	0.1051	102.72	92.92
	D2	F1C2	0.0518	50.63	62.73
	D3	F1C3	0.0466	45.54	59.79
	D4	F2C1	0.103	100.67	91.7307
	D5	F2C2	0.0651	63.63	70.2428
	D6	F2C3	0.0351	34.31	53.2448
0.25 wt% Methionine	E1	F1C1	0.1067	104.28	93.82
	E2	F1C2	0.094	91.87	86.64
	E3	F1C3	0.0469	45.84	59.93
	E4	F2C1	0.1086	106.14	94.9
	E5	F2C2	0.0617	60.30	68.29
	E6	F2C3	0.047	45.94	59.96
0.03 wt% Tryptophan	F1	F1C1	0.1102	107.70	95.83
	F2	F1C2	0.1004	98.13	90.27
	F3	F1C3	0.055	53.75	64.52
	F4	F2C1	0.1103	107.80	95.86
	F5	F2C2	0.1024	100.08	91.37
	F6	F2C3	0.064	62.55	69.61

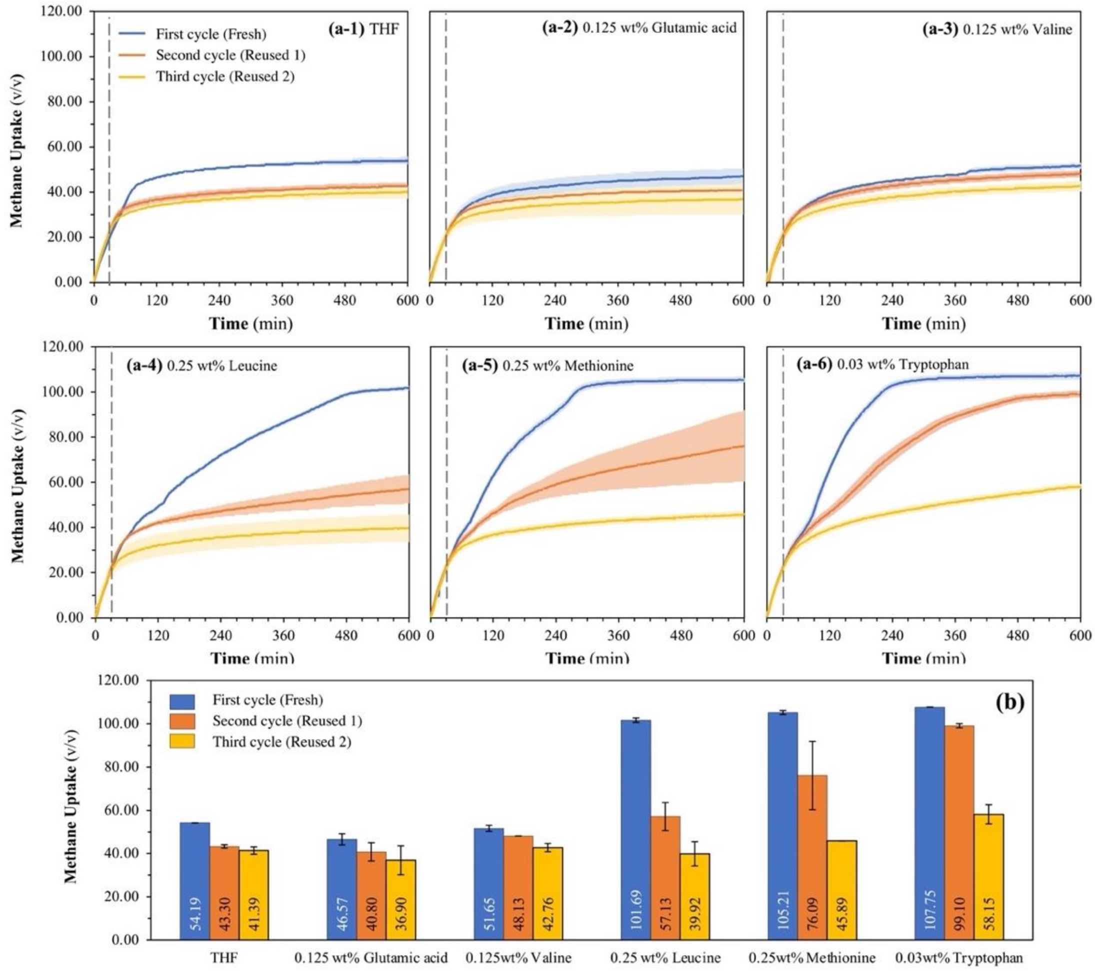

Figure 7.5 Profiles depicting methane uptake during hydrate formation cycles (a) and the methane uptake at 600 min after hydrate nucleation (b) with 5.56 mol% THF and 5.56 mol% THF with five amino acids at 298.2 K and 9.2 MPa.

In the presence of amino acids that initially enhance hydrate formation during the first cycle, methane uptake profiles demonstrate a decreasing trend in methane uptake along the increase cycle of solution the same as only THF solution. The highest uptake is observed in the first cycle, followed by a reduction across subsequent solution cycles, as depicted in Figure 7.5 (a-2) to 7.5 (a-6). There was no promotional effect observed in the reused solution. However, these profiles differ in the extent of methane uptake reduction.

The methane uptake reduction in the solution with 0.125 wt% glutamic acid and valine, which did not promote methane hydrate formation in the first cycle, Figure 7.5 (a-2) and 7.5 (a-3), are slightly reduced the methane uptake the same as only THF. In the presence of hydrophobic amino acids (leucine, methionine, and tryptophan), the methane uptake profile of the reused solution appears to decrease more significantly. The methane uptake for the addition of 0.25 wt% leucine in the fresh solution is 101.69 ± 1.03 v/v, equivalent to 92.33 ± 0.59 water to hydrate conversion. This uptake is then reduced by 28% in the second cycle and further to 61% in the third cycle Figure 7.5 (a-4). Similarly, the methane uptakes are reduced by 28% and 57% in the second and third cycle of 0.25 wt% methionine solution Figure 7.5 (a-5) and by 8% and 46% in the second and third cycle of 0.03 wt% tryptophan solution Figure 7.5 (a-6).

The comparison of methane uptake among various amino acids is presented in Figure 7.5 (b). It is evident that there is no discernible difference in methane uptake profiles when comparing the solutions containing glutamic acid and valine with the THF solution. The reduction observed in methane uptake is comparable to that observed with THF, suggesting that this reduction might solely originate from THF and not from the impact of glutamic acid and valine. Regarding the addition of hydrophobic amino acids that enhance methane hydrate formation, the fresh solution (first cycle) exhibits higher methane uptake than pure 5.56 mol% THF, aligning with previous findings. Similarly, the second cycle also displays higher uptake than the fresh THF solution, indicating the continued promoting effect of amino acids. However, the enhancing power of the amino acids diminishes in the second cycle compared to the fresh solution, evident in the reduced methane uptake. Furthermore, a more significant decrease is observed in the third cycle of every amino acid. Only tryptophan shows a promoting effect in the third cycle, with methane uptake slightly higher than in the fresh THF solution. These decreases in the promoting effect could imply the loosing of amino acid performance which could cause by the loosing of their concentration or changing of their structure. Figure 7.5 (b) also illustrates the order of methane uptake among the hydrophobic amino acids in each cycle: leucine < methionine < tryptophan. Surprisingly, this order directly aligns with the amino acid hydrophobicity ranking proposed by Trinquier and Sanejouand (1998) as mention in previous work (Jeenmuang *et al.*, 2023). This strongly suggests that the power of amino acid hydrophobicity significantly impacts the reusability of their solutions. Based on these findings, tryptophan emerges as the most promising amino acid, exerting the most pronounced promoting effect in both fresh and reused solutions.

7.4.2.2 Hydrate Formation Kinetics During the Hydrate Formation Cycle

The kinetics of hydrate formation is another crucial factor. Figure 7.6 displays the mean and error bars of key kinetic parameters including the induction time, the normalized rate of hydrate formation 30 minutes after the first nucleation (NR_{30}), the time required to achieve 90% of methane uptake (t_{90}) and the normalized of t_{90} by the 90%methane uptake ($t_{90,norm}$) across various amino acids and hydrate formation cycles.

Figure 7.6 (a) illustrates the induction time of the methane hydrate formation in each solution system. With only 5.56 mol% THF, showing no difference across the different hydrate formation cycles in terms of mean and standard deviation. Similarly, the addition of glutamic acid and valine does not exhibit any noticeable change in induction time across the cycles. In terms of hydrophobic amino acids (leucine, methionine, and tryptophan), the hydrate formation induction time increases across the cycle of hydrate formation. In addition, most of these amino acid formation cycles exhibit shorter induction times compared to the only THF solution. This might suggest that the promoting effect remains active; however, there seems to be a subtle decline in the effectiveness of hydrophobic amino acids in the second and third formation cycles. Nevertheless, it is too early to conclude on the reusability of amino acids in terms of hydrate formation kinetics.

Figure 7.6 (b) illustrates the NR_{30} of hydrate formation, which remains consistent across the methane hydrate formation cycles, showing no noticeable differences among the various amino acids. This consistency might suggest that stirring system plays a more pivotal role in the initial formation than the specific amino acid promoters.

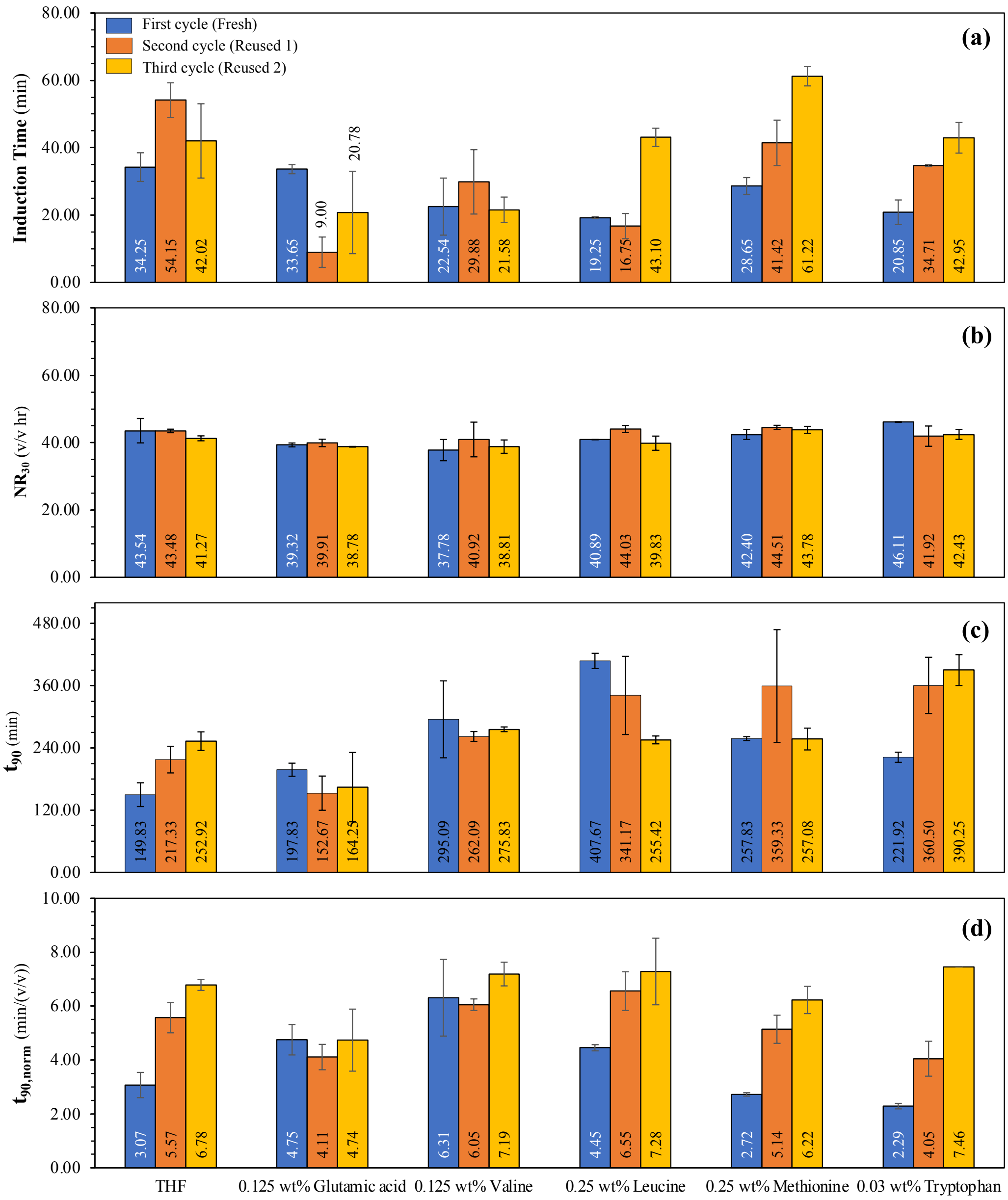

Figure 7.6 Hydrate formation kinetic parameter including (a) the induction time, (b) the normalized rate of hydrate formation 30 minutes after the first nucleation (NR_{30}), (c) the time required to achieve 90% of methane uptake (t_{90}) and (d) the normalized of t_{90} by the 90%methane uptake ($t_{90,norm}$).

When considering hydrate completion indicated by t_{90}, representing the time taken for hydrates to achieve 90% of methane uptake with each amino acid, no distinct trend is observed Figure 7.6 (c). As there are varying methane uptakes, t_{90} should be normalized by their respective methane uptake to ensure a fair comparison. Figure 7.6 (d) showcases the normalized t_{90} ($t_{90,norm}$) for each solution system across their hydrate formation cycles. In the THF system, the $t_{90,norm}$ increases throughout the hydrate formation cycle, possibly due to the increased challenge of methane diffusion through the hydrate film layer, as discussed earlier. With the addition of glutamic acid and valine, there is no significant difference in the norm t_{90} across the formation cycles. This suggests a consistent capability along the cycle of hydrate formation. However, the hydrophobic amino acid like leucine, methionine, and tryptophan, the $t_{90,norm}$ increases throughout their respective hydrate formation cycles. Notably, with the addition of leucine, the least hydrophobic among these three, the $t_{90,norm}$ remains seemingly constant during the second and third cycles of hydrate formation. When also considering the methane uptake during these cycles, a decreasing trend is noticeable. This trend might imply a diminishing promoting effect of leucine, resulting in a similar $t_{90,norm}$. This differs from the higher hydrophobicity amino acids, methionine, and tryptophan, where the $t_{90,norm}$ noticeably increases from the first to the second and from the second to the third cycle. Remarkably, the $t_{90,norm}$ in the tryptophan solution appears to have doubled compared to the previous cycle.

The comparison of amino acid reusability based on their hydrophobicity in Figure 7.6 (d) reveals an inverse relationship: as amino acid hydrophobicity increases (leucine < methionine < tryptophan), the $t_{90,norm}$ decreases notably in the first and second cycles. This trend signifies the significant role of amino acid hydrophobicity in enhancing hydrate formation kinetics along the cycle of hydrate formation. Unexpectedly, in the third cycle, tryptophan exhibits a longer $t_{90,norm}$ instead of the anticipated shorter value compared to methionine, despite being less hydrophobic. When also considering the methane uptake during their third cycle, it is notable that only tryptophan maintains a promotion in methane uptake, despite demonstrating a shorter $t_{90,norm}$ compared to methionine and leucine, which have ceased to enhance hydrate formation. Furthermore, upon comparing the $t_{90,norm}$ of methionine and tryptophan to that of the THF solution, both amino acids exhibit shorter $t_{90,norm}$ values in the second cycle compared to that of THF. this indicating of the existing of kinetic enhancement of methionine and tryptophan. This suggests the presence of kinetic enhancement attributed to methionine and tryptophan.

Considering both methane uptake and the kinetics of hydrate formation, the reusability of amino acids becomes a crucial factor. Findings suggest a decline in amino acid performance across the cycle of hydrate formation. However, employing highly hydrophobic amino acids such as methionine and tryptophan still demonstrates higher performance in the second cycle of hydrate formation compared to other amino acids. It seems that the second cycle represents the maximum number of cycles, resulting in good performance in both capacity and kinetics. With these findings, there is a need to explore the changes in amino acid performance during the cycles of hydrate formation, which might be attributed to a decrease in amino acid concentration or changes in amino acid structure.

7.4.3 Amino Acid Degradation Investigation

7.4.3.1 Preheat Solution Before Hydrate Formation for Possible Amino Acid Thermal Degradation

In assessing the reusability of the amino acid solution for the formation of mixed-methane THF hydrate across multiple cycles, a process involving cooling for hydrate formation and subsequent heating for dissociation was conducted. The primary objective was to eliminate the possibility of any decrease observed in performance, impacting both storage capacity and hydrate formation kinetics during the solution's reuse were not attributed to the thermal stimulation. This necessitated a comprehensive investigation to isolate and comprehend the factors contributing to these effects, ensuring they were not exclusively due to thermal conditions. To investigate this, a new set of experiments was designed. Initially, the fresh amino acid solution (first cycle) was preheated to the hydrate dissociation temperature of 308.2 K. Subsequently, it was maintained at this temperature for specified durations of 1.5 and 3 hours before being cooled down to the hydrate formation temperature. Methionine and tryptophan were the focus amino acids in this investigation.

The results depicted in Figure 7.7 indicate that there were no significant differences observed in the methane uptake profile of the preheat experiment compared to the standard mixed methane-THF hydrate formation process. Upon the addition of tryptophan, the methane uptake profile for the 1.5 hours preheat duration closely resembled the normal operation profile, as shown in Figure 7.7 (a).

Similarly, the addition of methionine also exhibited a methane uptake profile akin to normal operation, even when the solution was preheated for durations of 1.5 and 3 hours (Figure 7.7 (b)). Furthermore, the hydrate formation capacity and kinetics showed no significant differences in the preheat experiment compared to the standard mixed methane-THF hydrate formation, as observed in Table 7.2. This finding suggests that the high temperature during hydrate dissociation does not damage or reduce the amount of amino acids, which eliminates a potential reason for a decrease in the enhancement performance of the amino acids.

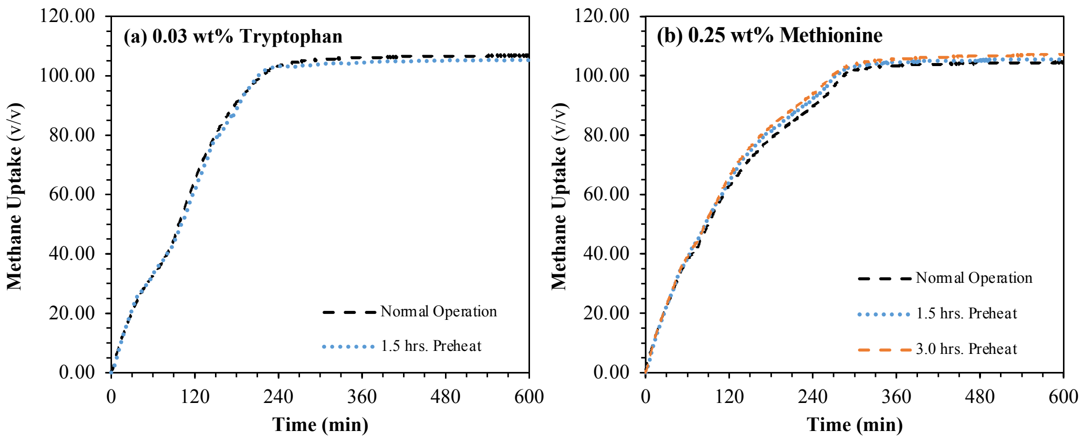

Figure 7.7 Profiles depicting methane uptake during preheat solution hydrate formation; (a) 0.03 wt% Tryptophan and (b) 0.25wt% Methionine.

7.4.3.2High-Performance Liquid Chromatography (HPLC) Investigation for Possible Amino Acid Degradation Across Cycles of Hydrate Formation

To confirm that the high temperature during hydrate dissociation is not a potential cause for the decrease in the enhancement performance of the amino acids, high-performance liquid chromatography (HPLC) was employed to measure the remaining amino acid concentration throughout the cycle of hydrate formation. Initially, a standard 5.56 mol% THF solution was measured as part of a blank experiment, identifying a peak of THF. Subsequently, any additional peaks observed with the amino acid standard were attributed to the added amino acid. Figure 7.8 illustrates the HPLC chromatogram of the 5.56 mol% THF standard alongside three standard concentrations of added methionine (0.0625, 0.1250, and 0.2500 wt%). The chromatogram distinctly shows that the peak within the retention time of 4.400 - 4.600 corresponds to the 5.56 mol% THF, whereas the peak within the retention time of 5.050 – 5.200 is attributed to methionine. Additionally, there's a noticeable increase in the peak area of methionine corresponding to the concentration increase of methionine.

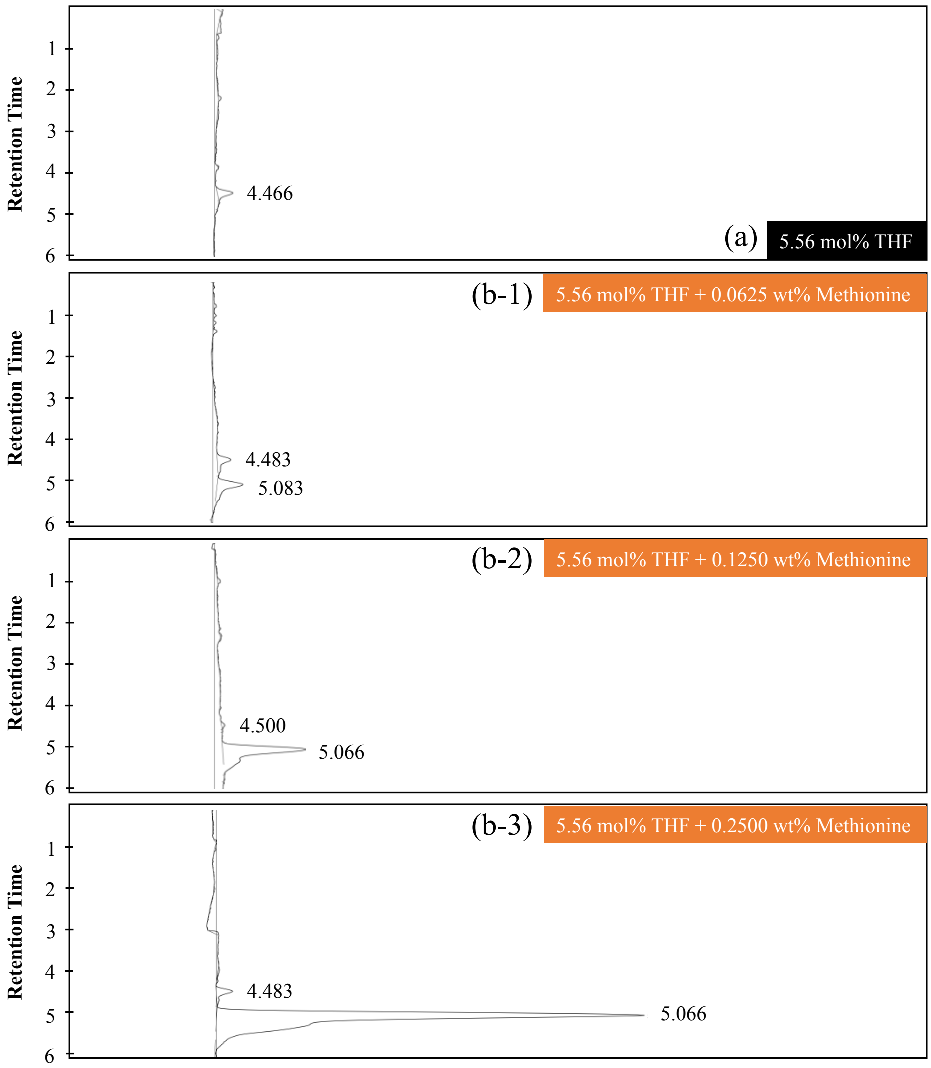

Figure 7.8 HPLC chromatogram of the standard 5.56 mol% THF (a) and three standard concentrations of added methionine including (b-1) 0.0625, (b-2) 0.1250, and (b-3) 0.2500 wt%.

Table 7.2 Summary of methane uptake, water to hydrate conversion, and kinetic parameters for methane hydrate formation in DI preheat solution hydrate formation

System	Condition	Methane Uptake (v/v)	Water to hydrate conversion (%)	Induction Time (min)	NR_{15} (v/v min)	t_{90} (min)	$t_{90,norm}$ (min/(v/v))
5.56 mol% THF + 0.03 wt% Tryptophan	Normal Operation (no preheat)	107.75 ± 0.05	95.85 ± 0.02	20.85 ± 3.66	46.11 ± 0.11	221.92 ± 9.74	2.29 ± 0.10
	1.5 hrs. Preheat	105.86 ± 0.59	94.74 ± 0.34	20.19 ± 1.95	46.27 ± 4.17	202.17 ± 8.00	2.12 ± 0.07
5.56 mol% THF + 0.25 wt% Methionine	Normal Operation (no preheat)	105.21 ± 0.93	94.36 ± 0.54	28.65 ± 2.48	42.40 ± 1.46	257.83 ± 3.83	2.72 ± 0.06
	1.5 hrs. Preheat	105.05 ± 0.45	94.28 ± 0.27	27.75 ± 2.58	44.52 ± 0.50	258.17 ± 5.00	2.73 ± 0.06
	3 hrs. Preheat	104.93 ± 2.21	94.21 ± 1.29	23.50 ± 7.5	45.09 ± 1.08	248.33 ± 5.33	2.63 ± 0.01

After evaluating the chromatogram of the standard solution, the concentration of methionine in the reused solutions from hydrate formation was assessed. Table 7.3 illustrates the retention time and peak area of both THF and methionine obtained from different cycles of reused hydrate formation at 298.2 K and 9.2 MPa (solution were sampling from the same experiment in section 4.2). The comparison of both the retention time and the percentage of peak area across the cycles of hydrate formation indicates that there was no significant decrease with the increasing number of reused cycles. The values across all cycles remained similar to those of the 0.25 wt% methionine standard solution, and they still markedly differed from the values of the 0.125 wt% methionine standard solution. This finding strongly suggests that the decrease in the enhancement performance of amino acids during the second and third cycles of hydrate formation did not result from amino acid degradation, as there was no loss of amino acid concentration across the hydrate formation cycle. This implies that factors beyond a reduction in amino acid concentration might be influencing their behavior, potentially contributing to the decrease in enhancement performance. Further investigation is required to evaluate other aspects in which amino acids may exhibit changes or alterations, beyond degradation or concentration loss.

Table 7.3 Summary of retention times and peak areas for THF and methionine observed in the HPLC chromatogram of the methionine standard solution and methionine solution across different hydrate formation cycles

System	Experiment	Cycle	THF			Methionine		
			Retention time	Area	Area %	Retention time	Area	Area %
0.0625 wt% Methionine	Standard solution		4.483	21.879	31.245	5.083	48.144	68.755
0.125 wt% Methionine	Standard solution		4.500	22.833	12.262	5.066	163.383	87.738
0.25 wt% Methionine	Standard solution		4.483	18.209	2.509	5.066	707.491	97.491
0.25 wt% Methionine	Start solution		4.550	8.318	1.393	5.133	588.803	98.607
	E4	F2C1	4.566	6.303	1.100	5.150	566.914	98.900
	E5	F2C2	4.550	14.597	2.468	5.116	576.921	97.532
	E6	F2C3	4.583	15.669	5.032	5.200	673.135	97.725

7.5 Conclusion

This study delved into the impact of amino acid hydrophobicity on their reusability in mixed methane-THF hydrate formation cycles. Five distinct amino acids with different hydrophobicity, glutamic acid, valine, leucine, methionine, and tryptophan, were evaluated. The presence of hydrophobic amino acids like leucine, methionine, and tryptophan showed enhanced performance beyond THF alone in the second cycle, signifying the reusability of the amino acid solution. However, there was an observed decrease in enhancement performance across subsequent cycles in both hydrate formation capacity and kinetics. Interestingly, amino acids with higher hydrophobicity maintained their enhancing performance for longer durations compared to those with lower hydrophobicity. Tryptophan, being the most hydrophobic, demonstrated particular effectiveness in enhancing methane hydrate formation over multiple cycles compared to other amino acids. Nevertheless, in the second and third cycles of a 0.03 wt% tryptophan solution, methane uptake reduced by 8% and 46%, respectively, while the formation kinetics ($t_{90,norm}$) increased by 180% and 330%. Notably, this study found that high temperatures during hydrate dissociation did not lead to amino acid degradation, evidenced by similar behaviors observed between normal and 3-hour and 308.2 K preheated hydrate formations. Additionally, the HPLC chromatogram revealed no loss of amino acid concentration over the three cycles of hydrate formation, dismissing amino acid degradation as the cause of declining performance in methane hydrate formation.

7.6 CRediT Authorship Contribution Statement

Kan Jeenmuang: Conceptualization, Methodology, Formal analysis, Investigation, Data curation, Writing - Original Draft, Visualization. **Praveen Linga:** Validation, Supervision, Funding acquisition, Writing – review & editing. **Pramoch Rangsunvigit:** Validation, Writing – review & editing, Supervision, Funding acquisition.

7.7 Acknowledgments

The authors would like to acknowledge the financial support received from the following organizations: Second Century Fund (C2F), Thailand Science Research and Innovation Fund and Ratchadaphiseksomphot Endowment Fund, Chulalongkorn University.

CHAPTER 8
CONCLUSIONS AND RECOMMENDATIONS

8.1 Conclusions

This study has shed light on the significant role of amino acid hydrophobicity in methane and carbon dioxide hydrate formation and dissociation. The introduction of hydrophobic amino acids significantly enhances both capacity and kinetics of hydrate formation. Notably, the introduction of amino acids, in collaboration with a stirred system, enables the high-capacity room temperature (298.2 K) mixed methane-THF hydrate formation, with similar behavior observed in 275.2 K CO_2 hydrate formation. The observed enhanced in hydrate formation is directly promoted with the increased amino acid hydrophobicity. The correlation between the increased amino acid hydrophobicity and the enhanced hydrate formation is evident, and optimal concentrations for maximizing CH_4 and CO_2 hydrate formation were identified. This correlation underscores the crucial role of hydrophobic-hydrophobic interactions between amino acids and gases, fostering enriched gas areas that accelerate the formation of hydrates. Additionally, in situ Raman spectroscopy reveals lattice defects caused by dissolved CO_2 hydronium ions, accelerating CO_2 hydrate formation. The CO_2 hydrate Raman ratio correlates with the amount of CO_2 hydrate formed, aiding in quantifying hydrate formation via Raman spectroscopy. In the presence of NaCl, the introduction of amino acids results in a 2.5-fold enhancement of CO_2 hydrate formation compared to conditions without amino acids, thereby facilitating CO_2 sequestration, particularly in deep-sea environments. Furthermore, scalability insights reveal that three crystallizer design factors interact with each other, with solution to reactor volume ratio (V_S/V_R) resulting in the most influential factor on hydrate formation. Model predictions of four hydrate formation responses encompass optimized crystallizer design. Stability tests review the storage stability of hydrate pellets at 283.2 K with minimal gas release (800 kPa), which occurs within the first 15 days before stabilizing at this pressure. Additionally, amino acid solutions can be reused with minimal performance reduction under high temperature and pressure driving force conditions, presenting practical advancements in energy storage and carbon capture technologies. However, performance reduction was observed at low driving force conditions. Nonetheless, at this condition, the possibility of losing amino acids due to thermal degradation was eliminated as the amino acids remained in solution. These findings not only bridge critical gaps but also underscore the potential for further exploration and innovation in this field, laying a robust foundation for future research endeavors.

8.2 Recommendations

Based on the experimental results and the writer's understanding, it is recommended to explore further aspects of amino acid influence and their hydrophobicity on hydrate formation. For instance, investigating the impact on the metastable zone of amino acid solutions, which could significantly affect hydrate formation. Establishing the correlation between the enhancing effect of amino acids and the driving force of hydrate formation could help identify an optimal operating point considering temperature and pressure utilization costs. Additionally, exploring various aspects of hydrate formation optimization, such as the impact of temperature and pressure on hydrate formation kinetics, is suggested. Furthermore, conducting research to understand the reasons behind the diminishing effect of amino acid enhancement in reused solutions would be beneficial.

APPENDIX

Appendix A GRAPHICAL ABSTRACT

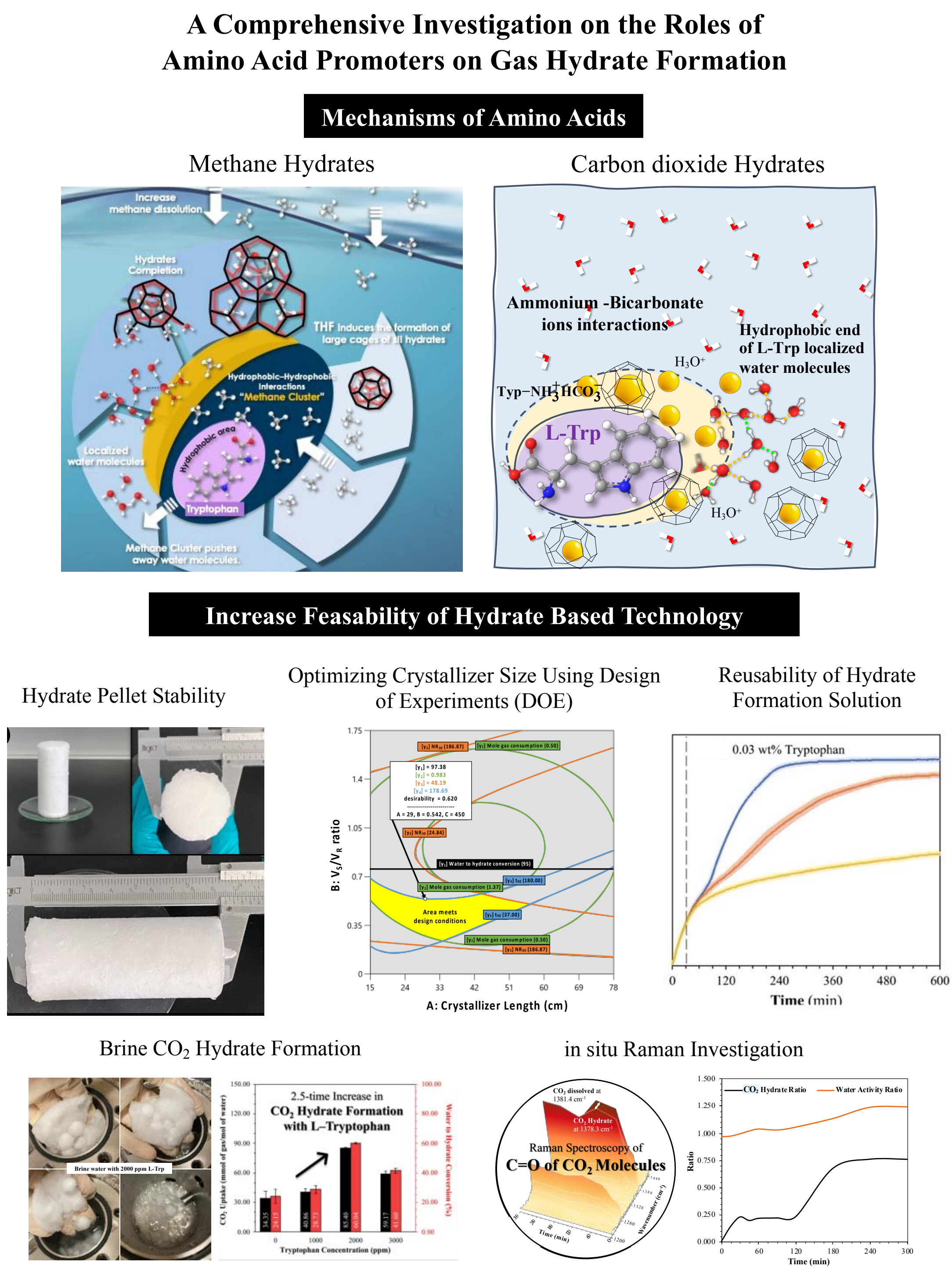

REFERENCES

Abdul, Q. M., Haider, J., Qadeer, K., and Lee, M. (2019). Performance Enhancement of Offshore LNG Processes by Introducing Optimal Mixed Refrigerant Self-Cooling Recuperator. Paper presented at the International Conference on Applied Energy 2019, Västerås, Sweden.

Al-Bazali, T. (2021). Insight on the inhibitive property of potassium ion on the stability of shale: a diffuse double-layer thickness (κ−1) perspective. Journal of Petroleum Exploration and Production Technology, 11(6), 2709-2723.

Al-Sowadi, A., Roosta, H., Dashti, A., Pakzad, S. A., Ghasemian, R., and Rajaei, M. (2019). The effects of SDS, SLES and THF on the growth rate, kinetic behaviors and energy consumption during ethylene hydrate formation process. Journal of Molecular Liquids, 294, 111608.

Aliyeva, M., Brandão, P., Gomes, J. R. B., Coutinho, J. A. P., Held, C., Ferreira, O., and Pinho, S. P. (2023). Salt effects on the solubility of aromatic and dicarboxylic amino acids in water. The Journal of Chemical Thermodynamics, 177, 106929.

Altamash, T., Qureshi, M. F., Aparicio, S., Aminnaji, M., Tohidi, B., and Atilhan, M. (2017). Gas hydrates inhibition via combined biomolecules and synergistic materials at wide process conditions. Journal of Natural Gas Science and Engineering, 46, 873-883.

Atta, D. Y., Negash, B. M., Yekeen, N., Habte, A. D., and Abdul Malik, A. B. (2021). Influence of natural L-amino acids on the interfacial tension of an oil-water system and rock wettability alterations. Journal of Petroleum Science and Engineering, 199, 108241.

Babu, P., Ho, C. Y., Kumar, R., and Linga, P. (2014). Enhanced kinetics for the clathrate process in a fixed bed reactor in the presence of liquid promoters for pre-combustion carbon dioxide capture. Energy, 70, 664-673.

Babu, P., Kumar, R., and Linga, P. (2013). Pre-combustion capture of carbon dioxide in a fixed bed reactor using the clathrate hydrate process. Energy, 50, 364-373.

Babu, P., Nambiar, A., He, T., Karimi, I. A., Lee, J. D., Englezos, P., and Linga, P. (2018). A Review of clathrate hydrate based desalination to strengthen energy–water nexus. ACS Sustainable Chemistry & Engineering, 6(7), 8093-8107.

Baek, S., Lee, W., Min, J., Ahn, Y.-H., Kang, D. W., and Lee, J. W. (2020). Hydrate seeding effect on the metastability of CH4 hydrate. Korean Journal of Chemical Engineering, 37(2), 341-349.

Basile, A., Gugliuzza, A., Iulianelli, A., and Morrone, P. (2011). Membrane technology for carbon dioxide (CO2) capture in power plants. In Advanced Membrane Science and Technology for Sustainable Energy and Environmental Applications (pp. 113-159). United Kingdom: Woodhead Publishing.

Bavoh, C. B., Nashed, O., Khan, M. S., Partoon, B., Lal, B., and Sharif, A. M. (2018). The impact of amino acids on methane hydrate phase boundary and formation kinetics. The Journal of Chemical Thermodynamics, 117, 48-53.

Beheshtimaal, A., and Haghtalab, A. (2018). Thermodynamic modeling of hydrate formation conditions using different activity coefficient models in the presence of tetrahydrofuran (THF). Chemical Engineering Research and Design, 129, 150-159.

Bhamidi, V., Kenis, P. J. A., and Zukoski, C. F. (2017). Probability of Nucleation in a Metastable Zone: Induction Supersaturation and Implications. Crystal Growth & Design, 17(3), 1132-1145.

Bhattacharjee, G., Goh, M. N., Arumuganainar, S. E. K., Zhang, Y., and Linga, P. (2020a). Ultra-rapid uptake and the highly stable storage of methane as combustible ice. Energy & Environmental Science, 13(12), 4946-4961.

Bhattacharjee, G., Kushwaha, O. S., Kumar, A., Khan, M. Y., Patel, J. N., and Kumar, R. (2017). Effects of Micellization on Growth Kinetics of Methane Hydrate. Industrial & Engineering Chemistry Research, 56(13), 3687-3698.

Bhattacharjee, G., and Linga, P. (2021). Amino Acids as Kinetic Promoters for Gas Hydrate Applications: A Mini Review. Energy & Fuels, 35(9), 7553-7571.

Bhattacharjee, G., Prakash Veluswamy, H., Kumar, R., and Linga, P. (2020b). Rapid methane storage via sII hydrates at ambient temperature. Applied Energy, 269, 115142.

Bhattacharjee, G., Veluswamy, H. P., Kumar, A., and Linga, P. (2021). Stability analysis of methane hydrates for gas storage application. Chemical Engineering Journal, 415, 115142.

Cai, Y., Chen, Y., Li, Q., Li, L., Huang, H., Wang, S., and Wang, W. (2017). CO2 Hydrate Formation Promoted by a Natural Amino Acid l-Methionine for Possible Application to CO2 Capture and Storage. Energy Technology, 5(8), 1195-1199.

Caumon, M.-C., Robert, P., Laverret, E., Tarantola, A., Randi, A., Pironon, J., Dubessy, J., and Girard, J.-P. (2014). Determination of methane content in NaCl–H2O fluid inclusions by Raman spectroscopy. Calibration and application to the external part of the Central Alps (Switzerland). Chemical Geology, 378-379, 52-61.

Chanakro, W., Jaikwang, C., Inkong, K., Kulprathipanja, S., and Rangsunvigit, P. (2020). Comparative Study of Tetra-N-Butyl Ammonium Bromide and Cyclopentane on the Methane Hydrate Formation and Dissociation. Energies, 13(24), 6518.

Chaturvedi, E., Prasad, N., and Mandal, A. (2018). Enhanced formation of methane hydrate using a novel synthesized anionic surfactant for application in storage and transportation of natural gas. Journal of Natural Gas Science and Engineering, 56, 246-257.

Chen, C., Hu, W., Yang, L., Zhao, J., and Song, Y. (2021). Gas supersaturation and diffusion joint controlled CH_4 nanobubble evolution during hydrate dissociation. Journal of Molecular Liquids, 323, 114614.

Chen, L., Lu, H., and Ripmeester, J. A. (2015). Raman spectroscopic study of CO_2 in hydrate cages. Chemical Engineering Science, 138, 706-711.

Choe, C., Lademann, J., and Darvin, M. E. (2016). Depth profiles of hydrogen bound water molecule types and their relation to lipid and protein interaction in the human stratum corneum in vivo. Analyst, 141(22), 6329-6337.

Choi, S., Park, J., Park, J. H., Kim, S.-C., Won, S. O., and Kang, Y. T. (2021). Study on CO_2 hydrate formation characteristics with promoters for CO_2 capture and cold thermal energy transportation. Journal of Cleaner Production, 295, 126392.

Dashti, H., Zhehao Yew, L., and Lou, X. (2015). Recent advances in gas hydrate-based CO_2 capture. Journal of Natural Gas Science and Engineering, 23, 195-207.

de Deugd, R. M., Jager, M. D., and de Swaan Arons, J. (2001). Mixed hydrates of methane and water-soluble hydrocarbons modeling of empirical results. AIChE Journal, 47(3), 693-704.

Dhamu, V., Qureshi, M. F., Abubakar, S., Usadi, A., Barckholtz, T. A., Mhadeshwar, A. B., and Linga, P. (2023). Investigating High-Pressure Liquid CO_2 Hydrate Formation, Dissociation Kinetics, and Morphology in Brine and Freshwater Static Systems. Energy & Fuels, 37(12), 8406-8420.

Du, J., Li, H., and Wang, L. (2014). Effects of ionic surfactants on methane hydrate formation kinetics in a static system. Advanced Powder Technology, 25(4), 1227-1233.

Duan, L., and Li, L. (2023). OCAC Technology in Oxy-Fuel Combustion for Carbon Capture. In Oxygen-Carrier-Aided Combustion Technology for Solid-Fuel Conversion in Fluidized Bed (pp. 65-77). Singapore: Springer Nature Singapore.

Đuričković, I., Claverie, R., Bourson, P., Marchetti, M., Chassot, J.-M., and Fontana, M. D. (2011). Water-ice phase transition probed by Raman spectroscopy. Journal of Raman Spectroscopy, 42(6), 1408-1412.

Englezos, P., and Lee, J. D. (2005). Gas hydrates: A cleaner source of energy and opportunity for innovative technologies. Korean Journal of Chemical Engineering, 22(5), 671-681.

Fahed Qureshi, M., Zheng, J., Khandelwal, H., Venkataraman, P., Usadi, A., Barckholtz, T. A., Mhadeshwar, A. B., and Linga, P. (2022). Laboratory demonstration of the stability of CO2 hydrates in deep-oceanic sediments. Chemical Engineering Journal, 432, 134290.

Ferroudji, H., Hadjadj, A., Ofei, T. N., Gajbhiye, R. N., Rahman, M. A., and Qureshi, M. F. (2022). Effect of drill pipe orbital motion on non-Newtonian fluid flow in an eccentric wellbore: a study with computational fluid dynamics. Journal of Petroleum Exploration and Production Technology, 12(5), 1383-1402.

Frank E. Harrell, J. (2015). Regression Modeling Strategies: With Applications to Linear Models, Logistic and Ordinal Regression, and Survival Analysis. Switzerland: Springer Cham.

Gabitto, J. F., and Tsouris, C. (2010). Physical properties of gas hydrates: A Review. Journal of Thermodynamics, 2010, 1-12.

Ganji, H., Manteghian, M., and Rahimi Mofrad, H. (2007). Effect of mixed compounds on methane hydrate formation and dissociation rates and storage capacity. Fuel Processing Technology, 88(9), 891-895.

Gudmundsson, J. S., Parlaktuna, M., and Khokhar, A. A. (1994). Storage of Natural Gas as Frozen Hydrate. SPE Production & Facilities, 9(01), 69-73.

Guo, G.-J., and Zhang, Z. (2021). Open questions on methane hydrate nucleation. Communications Chemistry, 4(1), 102.

Guo, H., Chen, Y., Hu, Q., Lu, W., Ou, W., and Geng, L. (2014). Quantitative Raman spectroscopic investigation of geo-fluids high-pressure phase equilibria: Part I. Accurate calibration and determination of CO2 solubility in water from 273.15 to 573.15 K and from 10 to 120 MPa. Fluid Phase Equilibria, 382, 70-79.

He, Y., Sun, M.-T., Chen, C., Zhang, G.-D., Chao, K., Lin, Y., and Wang, F. (2019). Surfactant-based promotion to gas hydrate formation for energy storage. Journal of Materials Chemistry A, 7(38), 21634-21661.

He, Z., Linga, P., and Jiang, J. (2017). What are the key factors governing the nucleation of CO2 hydrate? Physical Chemistry Chemical Physics, 19(24), 15657-15661.

Hocking, R. R. (1976). A Biometrics Invited Paper. The Analysis and Selection of Variables in Linear Regression. Biometrics, 32(1), 1-49.

Hütz, U., and Englezos, P. (1996). Measurement of structure H hydrate phase equilibrium and the effect of electrolytes. Fluid Phase Equilibria, 117(1), 178-185.

Inkong, K., Rangsunvigit, P., Kulprathipanja, S., and Linga, P. (2019a). Effects of temperature and pressure on the methane hydrate formation with the presence of tetrahydrofuran (THF) as a promoter in an unstirred tank reactor. Fuel, 255, 115705.

Inkong, K., Veluswamy, H. P., Rangsunvigit, P., Kulprathipanja, S., and Linga, P. (2019b). Investigation on the kinetics of methane hydrate formation in the presence of methyl ester sulfonate. Journal of Natural Gas Science and Engineering, 71, 102999.

Jager, M., De Deugd, R., Peters, C., de Swaan Arons, J., and Sloan, E. (1999). Experimental determination and modeling of structure II hydrates in mixtures of methane + water + 1, 4-dioxane. Fluid Phase Equilibria, 165(2), 209-223.

Jeenmuang, K., Pornaroontham, P., Inkong, K., Bhattacharjee, G., Kulprathipanja, S., Linga, P., and Rangsunvigit, P. (2023). Roles of amino acid hydrophobicity on methane-THF hydrates in the context of storage and stability. Chemical Engineering Journal, 454, 140326.

Jeenmuang, K., Viriyakul, C., Inkong, K., Prakash Veluswamy, H., Kulprathipanja, S., Rangsunvigit, P., and Linga, P. (2021). Enhanced hydrate formation by natural-like hydrophobic side chain amino acids at ambient temperature: A kinetics and morphology investigation. Fuel, 299, 120828.

Jin, J., Wang, J., Shen, Y., Lin, C., Pan, Z., and Chou, I. M. (2014). Visual and Raman spectroscopic observations of hot compressed water oxidation of guaiacol in fused silica capillary reactors. The Journal of Supercritical Fluids, 95, 546-552.

Kang, K. C., Linga, P., Park, K.-n., Choi, S.-J., and Lee, J. D. (2014). Seawater desalination by gas hydrate process and removal characteristics of dissolved ions (Na+, K+, Mg2+, Ca2+, B3+, Cl−, SO42−). Desalination, 353, 84-90.

Khandelwal, H., Qureshi, M. F., Zheng, J., Venkataraman, P., Barckholtz, T. A., Mhadeshwar, A. B., and Linga, P. (2020). Effect of l-Tryptophan in Promoting the Kinetics of Carbon Dioxide Hydrate Formation. Energy & Fuels, 35(1), 649-658.

Khokhar, A. A., Gudmundsson, J. S., and Sloan, E. D. (1998). Gas storage in structure H hydrates. Fluid Phase Equilibria, 150-151, 383-392.

Khurana, M., Yin, Z., and Linga, P. (2017). A Review of clathrate hydrate nucleation. ACS Sustainable Chemistry & Engineering, 5(12), 11176-11203.

Kirchner, M. T., Boese, R., Billups, W. E., and Norman, L. R. (2004). Gas Hydrate Single-Crystal Structure Analyses. Journal of the American Chemical Society, 126(30), 9407-9412.

Kumar, A., Kumar, R., and Linga, P. (2019). Sodium Dodecyl Sulfate Preferentially Promotes Enclathration of Methane in Mixed Methane-Tetrahydrofuran Hydrates. iScience, 14, 136-146.

Kumar, A., Sakpal, T., Linga, P., and Kumar, R. (2015). Enhanced carbon dioxide hydrate formation kinetics in a fixed bed reactor filled with metallic packing. Chemical Engineering Science, 122, 78-85.

Kumar, A., Veluswamy, H. P., Kumar, R., and Linga, P. (2019a). Kinetic promotion of mixed methane-THF hydrate by additives: Opportune to energy storage. Energy Procedia, 158, 5287-5292.

Kumar, A., Veluswamy, H. P., Linga, P., and Kumar, R. (2019b). Molecular level investigations and stability analysis of mixed methane-tetrahydrofuran hydrates: Implications to energy storage. Fuel, 236, 1505-1511.

Kyte, J., and Doolittle, R. F. (1982). A simple method for displaying the hydropathic character of a protein. Journal of Molecular Biology, 157(1), 105-132.

Lang, X., Fan, S., and Wang, Y. (2010). Intensification of methane and hydrogen storage in clathrate hydrate and future prospect. Journal of Natural Gas Chemistry, 19(3), 203-209.

Larsen, P. O. (1980). Physical and Chemical Properties of Amino Acids. In Amino Acids and Derivatives (pp. 225-269). USA: Academic Press.

Le, Q.-D., Rodriguez, C. T., Legoix, L. N., Pirim, C., and Chazallon, B. (2020). Influence of the initial CH4-hydrate system properties on CO2 capture kinetics. Applied Energy, 280, 115843.

Lee, J. D., Susilo, R., and Englezos, P. (2005). Kinetics of Structure H Gas Hydrate. Energy & Fuels, 19(3), 1008-1015.

Lee, Y.-J., Kawamura, T., Yamamoto, Y., and Yoon, J.-H. (2012). Phase equilibrium studies of tetrahydrofuran (THF) + CH4, THF + CO2, CH4 + CO2, and THF + CO2 + CH4 Hydrates. Journal of Chemical & Engineering Data, 57(12), 3543-3548.

Lenz, A., and Ojamae, L. (2011). Structures of the I-, II- and H-methane clathrates and the ice-methane clathrate phase transition from quantum-chemical modeling with force-field thermal corrections. the Journal of Physical Chemistry, 115(23), 6169-6176.

Li, D., Zhu, Z., and Sun, D.-W. (2021). Quantification of hydrogen bonding strength of water in saccharide aqueous solutions by confocal Raman microscopy. Journal of Molecular Liquids, 342, 117498.

Li, D.-L., Du, J.-W., Fan, S.-S., Liang, D.-Q., Li, X.-S., and Huang, N.-S. (2007). Clathrate Dissociation Conditions for Methane + Tetra-n-butyl Ammonium Bromide (TBAB) + Water. Journal of Chemical & Engineering Data, 52(5), 1916-1918.

Liang, Z., Rongwong, W., Liu, H., Fu, K., Gao, H., Cao, F., Zhang, R., Sema, T., Henni, A., Sumon, K., Nath, D., Gelowitz, d., Srisang, W., Saiwan, C., Benamor, A., Al-Marri, M., Shi, H., Supap, T., Chan, C., and Tontiwachwuthikul, P. (2015). Recent progress and new developments in post-combustion carbon-capture technology with amine based solvents. International Journal of Greenhouse Gas Control, 40, 26-54.

Lin, Y., Veluswamy, H. P., and Linga, P. (2018). Effect of eco-friendly cyclodextrin on the kinetics of mixed methane–tetrahydrofuran hydrate formation. Industrial & Engineering Chemistry Research, 57(17), 5944-5950.

Linga, P., and Clarke, M. A. (2016). A Review of Reactor Designs and Materials Employed for Increasing the Rate of Gas Hydrate Formation. Energy & Fuels, 31(1), 1-13.

Liu, X., Li, Y., Chen, G.-J., Chen, D.-Y., Sun, B., and Yin, Z. (2023). Coupling Amino Acid with THF for the Synergistic Promotion of CO2 Hydrate Micro Kinetics: Implication for Hydrate-Based CO2 Sequestration. ACS Sustainable Chemistry & Engineering, 11(15), 6057-6069.

Liu, Y., Chen, B., Chen, Y., Zhang, S., Guo, W., Cai, Y., Tan, B., and Wang, W. (2015). Methane Storage in a Hydrated Form as Promoted by Leucines for Possible Application to Natural Gas Transportation and Storage. Energy Technology, 3(8), 815-819.

Luo, Y. T., Zhu, J. H., Fan, S. S., and Chen, G. J. (2007). Study on the kinetics of hydrate formation in a bubble column. Chemical Engineering Science, 62(4), 1000-1009.

Mainusch, S., Peters, C. J., de Swaan Arons, J., Javanmardi, J., and Moshfeghian, M. (1997). Experimental determination and modeling of methane hydrates in mixtures of acetone and water. Journal of Chemical & Engineering Data, 42(5), 948-950.

Majid, A. A. A., and Koh, C. A. (2021). Self-preservation Phenomenon in Gas ydrates and Its Spplication for Energy Storage. In Intra- and Intermolecular Interactions Between Non-covalently Bonded Species (pp. 267-285). Netherland: Elsevier.

Makogon, Y. F. (2007). Hydrate of Natural Gas. In Petroleum Science and Engineering (Vol. 4, pp. 24). France: Encyclopedia of Life Support Systems.

McGlade, C., and Ekins, P. (2015). The geographical distribution of fossil fuels unused when limiting global warming to 2 C. Nature, 517(7533), 187-190.

Mech, D., Gupta, P., and Sangwai, J. S. (2016). Kinetics of methane hydrate formation in an aqueous solution of thermodynamic promoters (THF and TBAB) with and without kinetic promoter (SDS). Journal of Natural Gas Science and Engineering, 35, 1519-1534.

Miller, S., Lesk, A. M., Janin, J., and Chothia, C. (1987). The accessible surface area and stability of oligomeric proteins. Nature, 328(6133), 834-836.

Mimachi, H., Takahashi, M., Takeya, S., Gotoh, Y., Yoneyama, A., Hyodo, K., Takeda, T., and Murayama, T. (2015). Effect of Long-Term Storage and Thermal History on the Gas Content of Natural Gas Hydrate Pellets under Ambient Pressure. Energy & Fuels, 29(8), 4827-4834.

Mitarai, M., Kishimoto, M., Suh, D., and Ohmura, R. (2015). Surfactant Effects on the Crystal Growth of Clathrate Hydrate at the Interface of Water and Hydrophobic-Guest Liquid. Crystal Growth & Design, 15(2), 812-821.

Moon, C. P., and Fleming, K. G. (2011). Side-chain hydrophobicity scale derived from transmembrane protein folding into lipid bilayers. Proceedings of the National Academy of Sciences, 108(25), 10174-10177.

Motahari, A., Omrani, A., Rostami, A. A., and Ehsani, M. (2013). Preparation and characterization of a novel epoxy based nanocomposite using tryptophan as an eco-friendly curing agent. Thermochimica Acta, 574, 38-46.

Nakamura, T., Makino, T., Sugahara, T., and Ohgaki, K. (2003). Stability boundaries of gas hydrates helped by methane—structure-H hydrates of methylcyclohexane and cis-1,2-dimethylcyclohexane. Chemical Engineering Science, 58(2), 269-273.

Naseh, M., Falamaki, C., and Mohebbi, V. (2022). Equilibrium conditions of CO2+C3H8 hydrates in pure and saline water solutions of NaCl. Journal of Natural Gas Science and Engineering, 106, 104734.

Nguyen, N. N., La, V. T., Huynh, C. D., and Nguyen, A. V. (2022). Technical and economic perspectives of hydrate-based carbon dioxide capture. Applied Energy, 307, 118237.

Nguyen, N. N., and Nguyen, A. V. (2017). Hydrophobic Effect on Gas Hydrate Formation in the Presence of Additives. Energy & Fuels, 31(10), 10311-10323.

O'Neil, M. J. (2001). The Merck index : an Encyclopedia of Chemicals, Drugs, and Biologicals (13th ed ed.). New Jersey: Merck Whitehouse Station.

Okutani, K., Kuwabara, Y., and Mori, Y. H. (2008). Surfactant effects on hydrate formation in an unstirred gas/liquid system: An experimental study using methane and sodium alkyl sulfates. Chemical Engineering Science, 63(1), 183-194.

Ou, W., Geng, L., Lu, W., Guo, H., Qu, K., and Mao, P. (2015). Quantitative Raman spectroscopic investigation of geo-fluids high-pressure phase equilibria: Part II. Accurate determination of CH4 solubility in water from 273 to 603 K and from 5 to

140 MPa and refining the parameters of the thermodynamic model. Fluid Phase Equilibria, 391, 18-30.

Pan, Z., Wu, Y., Shang, L., Zhou, L., and Zhang, Z. (2020). Progress in use of surfactant in nearly static conditions in natural gas hydrate formation. Frontiers in Energy, 14(3), 463-481.

Pandey, G., Bhattacharjee, G., Veluswamy, H. P., Kumar, R., Sangwai, J. S., and Linga, P. (2018). Alleviation of Foam Formation in a Surfactant Driven Gas Hydrate System: Insights via a Detailed Morphological Study. ACS Applied Energy Materials, 1(12), 6899-6911.

Pandey, G., Poothia, T., and Kumar, A. (2022). Hydrate based carbon capture and sequestration (HBCCS): An innovative approach towards decarbonization. Applied Energy, 326, 119900.

Partoon, B., Sabil, K. M., Lau, K. K., Lal, B., and Nasrifar, K. (2018). Production of gas hydrate in a semi-batch spray reactor process as a means for separation of carbon dioxide from methane. Chemical Engineering Research and Design, 138, 168-175.

Pasteris, J. D., Wopenka, B., Freeman, J. J., Brewer, P. G., White, S. N., Peltzer, E. T., and Malby, G. E. (2004). Raman spectroscopy in the deep ocean: successes and challenges. Applied Spectroscopy, 58(7), 195a-208a.

Perchard, J. P. (2001). Anharmonicity and hydrogen bonding. III. Analysis of the near infrared spectrum of water trapped in argon matrix. Chemical Physics, 273(2), 217-233.

Qureshi, M., Khraisheh, M., and AlMomani, F. (2020). Experimentally measured methane hydrate phase equilibria and ionic liquids inhibition performance in Qatar's seawater. Scientific reports, 10(1), 1-14.

Qureshi, M. F., Atilhan, M., Altamash, T., Aparicio, S., Aminnaji, M., and Tohidi, B. (2017). High-pressure gas hydrate autoclave hydraulic experiments and scale-up modeling on the effect of stirring RPM effect. Journal of Natural Gas Science and Engineering, 38, 50-58.

Qureshi, M. F., Dhamu, V., Usadi, A., Barckholtz, T. A., Mhadeshwar, A. B., and Linga, P. (2022a). CO2 Hydrate Formation Kinetics and Morphology Observations Using High-Pressure Liquid CO2 Applicable to Sequestration. Energy & Fuels, 36(18), 10627-10641.

Qureshi, M. F., Khandelwal, H., Usadi, A., Barckholtz, T. A., Mhadeshwar, A. B., and Linga, P. (2022b). CO2 hydrate stability in oceanic sediments under brine conditions. Energy, 256, 124625.

Qureshi, M. F., Khraisheh, M., and Almomani, F. (2020). Doping amino acids with classical gas hydrate inhibitors to facilitate the hydrate inhibition effect at low dosages. Greenhouse Gases: Science and Technology, 10(4), 783-794.

Qureshi, M. F., Khraisheh, M., and AlMomani, F. (2021). Probing the effect of various water fractions on methane (CH4) hydrate phase equilibria and hydrate inhibition performance of amino acid L-proline. Journal of Molecular Liquids, 333, 115888.

Raza, M. A., Hallett, P. D., Liu, X., He, M., and Afzal, W. (2019). Surface Tension of Aqueous Solutions of Small-Chain Amino and Organic Acids. Journal of Chemical & Engineering Data, 64(12), 5049-5056.

Rodriguez Machine, C. T. (2021). Raman spectroscopic study of CO2 capture and separation by semi-clathrate hydrates crystallization and investigation of exchange processes in hydrates. Ph.D. Thesis, Université de Lille, Lille, France.

Sa, J. H., Kwak, G. H., Han, K., Ahn, D., Cho, S. J., Lee, J. D., and Lee, K. H. (2016). Inhibition of methane and natural gas hydrate formation by altering the structure of water with amino acids. Sci Rep, 6, 31582.

Sa, J. H., Kwak, G. H., Lee, B. R., Park, D. H., Han, K., and Lee, K. H. (2013). Hydrophobic amino acids as a new class of kinetic inhibitors for gas hydrate formation. Scientific Reports, 3, 2428.

Sarabia, L. A., and Ortiz, M. C. (2009). Response Surface Methodology. In Comprehensive Chemometrics (pp. 345-390). Oxford: Elsevier.

Schicks, J. M. (2022). Gas Hydrates in Nature and in the Laboratory: Necessary Requirements for Formation and Properties of the Resulting Hydrate Phase. In ChemTexts (Vol. 8). Germany: Springer Nature.

Schicks, J. M., Erzinger, J., and Ziemann, M. A. (2005). Raman spectra of gas hydrates--differences and analogies to ice 1h and (gas saturated) water. Spectrochim Acta A Mol Biomol Spectrosc, 61(10), 2399-2403.

Seo, S. D., Hong, S. Y., Sum, A. K., Lee, K.-H., Lee, J. D., and Lee, B. R. (2019). Thermodynamic and kinetic analysis of gas hydrates for desalination of saturated salinity water. Chemical Engineering Journal, 370, 980-987.

Seo, Y.-T., Lee, H., Moudrakovski, I., and Ripmeester, J. A. (2003). Phase Behavior and Structural Characterization of Coexisting Pure and Mixed Clathrate Hydrates. ChemPhysChem, 4(4), 379-382.

Seo, Y. T., Kang, S. P., and Lee, H. (2001). Experimental determination and thermodynamic modeling of methane and nitrogen hydrates in the presence of THF, propylene oxide, 1,4-dioxane and acetone. Fluid Phase Equilibria, 189(1), 99-110.

Shi, B.-H., Yang, L., Fan, S.-S., and Lou, X. (2017). An investigation on repeated methane hydrates formation in porous hydrogel particles. Fuel, 194, 395-405.

Shi, L., Shen, X., Ding, J., and Liang, D. (2017). Experimental Study on the Formation Kinetics of Methane Hydrates in the Presence of Tetrabutylammonium Bromide. Energy & Fuels, 31(8), 8540-8547.

Siangsai, A., Rangsunvigit, P., Kitiyanan, B., Kulprathipanja, S., and Linga, P. (2015). Investigation on the roles of activated carbon particle sizes on methane hydrate formation and dissociation. Chemical Engineering Science, 126, 383-389.

Siažik, J., and Malcho, M. (2017). Accumulation of primary energy into natural gas hydrates. Procedia Engineering, 192, 782-787.

Skovborg, P., Ng, H. J., Rasmussen, P., and Mohn, U. (1993). Measurement of induction times for the formation of methane and ethane gas hydrates. Chemical Engineering Science, 48(3), 445-453.

Sloan Jr, E. D. (2003). Fundamental principles and applications of natural gas hydrates. Nature, 426, 353–359.

Sloan Jr, E. D., and Koh, C. A. (2007). Clathrate Hydrates of Natural Gases (Third ed.). Boca Raton, FL: CRC Press.

Smith, J. M., Van Ness, H. C., and Abbott, M. (2005). Introduction to Chemical Engineering Thermodynamics (7th International Edition ed.). Boston: McGraw-Hill Education.

Suess, E. (2020). Marine Cold Seeps: Background and Recent Advances. In Hydrocarbons, Oils and Lipids: Diversity, Origin, Chemistry and Fate (pp. 747-767). Cham: Springer International Publishing.

Sun, Q. (2013). Local statistical interpretation for water structure. Chemical Physics Letters, 568-569, 90-94.

Sun, Q., Chen, G., Guo, X., and Liu, A. (2014). Experiments on the continuous separation of gas mixtures via dissolution and hydrate formation in the presence of THF. Fluid Phase Equilibria, 361, 250-256.

Sun, Z., Xin, Y., Sun, Q., Ma, R., Zhang, J., Lv, S., Cai, M., and Wang, H. (2016). Numerical Simulation of the Depressurization Process of a Natural Gas Hydrate Reservoir: An Attempt at Optimization of Field Operational Factors with Multiple Wells in a Real 3D Geological Model. Energies, 9(9), 714.

Theo, W. L., Lim, J. S., Hashim, H., Mustaffa, A. A., and Ho, W. S. (2016). Review of pre-combustion capture and ionic liquid in carbon capture and storage. Applied Energy, 183, 1633-1663.

Tomé, L. I. N., Catambas, V. R., Teles, A. R. R., Freire, M. G., Marrucho, I. M., and Coutinho, J. A. P. (2010). Tryptophan extraction using hydrophobic ionic liquids. Separation and Purification Technology, 72(2), 167-173.

Trinquier, G., and Sanejouand, Y. H. (1998). Which effective property of amino acids is best preserved by the genetic code? Protein Engineering, 11(3), 153-169.

Truong-Lam, H. S., Cho, S. J., and Lee, J. D. (2019). Simultaneous in-situ macro and microscopic observation of CH4 hydrate formation/decomposition and solubility behavior using Raman spectroscopy. Applied Energy, 255, 113834.

Truong-Lam, H. S., Seo, S. D., Jeon, C., Lee, G.-p., and Lee, J. D. (2022). A gas hydrate process for high-salinity water and wastewater purification. Desalination, 529.

Tsuji, H., Ohmura, R., and Mori, Y. H. (2004). Forming Structure-H Hydrates Using Water Spraying in Methane Gas: Effects of Chemical Species of Large-Molecule Guest Substances. Energy & Fuels, 18(2), 418-424.

Veluswamy, H. P., Ang, W. J., Zhao, D., and Linga, P. (2015). Influence of cationic and non-ionic surfactants on the kinetics of mixed hydrogen/tetrahydrofuran hydrates. Chemical Engineering Science, 132, 186-199.

Veluswamy, H. P., Hong, Q. W., and Linga, P. (2016a). Morphology study of methane hydrate formation and dissociation in the presence of amino acid. Crystal Growth & Design, 16(10), 5932-5945.

Veluswamy, H. P., Kumar, A., Kumar, R., and Linga, P. (2017a). An innovative approach to enhance methane hydrate formation kinetics with leucine for energy storage application. Applied Energy, 188, 190-199.

Veluswamy, H. P., Kumar, A., Seo, Y., Lee, J. D., and Linga, P. (2018). A review of solidified natural gas (SNG) technology for gas storage via clathrate hydrates. Applied Energy, 216, 262-285.

Veluswamy, H. P., Kumar, S., Kumar, R., Rangsunvigit, P., and Linga, P. (2016b). Enhanced clathrate hydrate formation kinetics at near ambient temperatures and moderate pressures: Application to natural gas storage. Fuel, 182, 907-919.

Veluswamy, H. P., Lee, P. Y., Premasinghe, K., and Linga, P. (2017b). Effect of biofriendly amino acids on the kinetics of methane hydrate formation and dissociation. Industrial & Engineering Chemistry Research, 56(21), 6145-6154.

Veluswamy, H. P., and Linga, P. (2013). Macroscopic kinetics of hydrate formation of mixed hydrates of hydrogen/tetrahydrofuran for hydrogen storage. International Journal of Hydrogen Energy, 38(11), 4587-4596.

Veluswamy, H. P., Wong, A. J. H., Babu, P., Kumar, R., Kulprathipanja, S., Rangsunvigit, P., and Linga, P. (2016c). Rapid methane hydrate formation to develop a cost effective large scale energy storage system. Chemical Engineering Journal, 290, 161-173.

Verrett, J., Posteraro, D., and Servio, P. (2012). Surfactant effects on methane solubility and mole fraction during hydrate growth. Chemical Engineering Science, 84, 80-84.

Villar-Muñoz, L. (2019). Gas Hydrate in Sediments on the Southern Chile Continental Slope. Ph.D. Thesis, University of Kiel, Germany.

Viriyakul, C., Jeenmuang, K., Inkong, K., Kulprathipanja, S., and Rangsunvigit, P. (2021). A detailed morphology investigation on the effects of mixed anionic and nonionic surfactants on methane hydrate formation and dissociation. Journal of Natural Gas Science and Engineering, 90, 103904.

Vysniauskas, A., and Bishnoi, P. R. (1983). A kinetic study of methane hydrate formation. Chemical Engineering Science, 38(7), 1061-1072.

Wang, X., French, J., Kandadai, S., and Chua, H. T. (2010). Adsorption measurements of methane on activated carbon in the temperature range (281 to 343) K and pressures to 1.2 MPa. Journal of Chemical & Engineering Data, 55(8), 2700-2706.

Wimley, W. C., and White, S. H. (1996). Experimentally determined hydrophobicity scale for proteins at membrane interfaces. Nature Structural Biology, 3(10), 842-848.

Wu, Q., and Zhang, B. (2010). Memory effect on the pressure-temperature condition and induction time of gas hydrate nucleation. Journal of Natural Gas Chemistry, 19(4), 446-451.

Xu, N., Liu, Y., Cheng, Z., Wang, S., Jiang, L., and Song, Y. (2020). Morphology-Based Kinetic Study of the Formation of Carbon Dioxide Hydrates with Promoters. Energy & Fuels, 34(6), 7307-7315.

Yagasaki, T., Matsumoto, M., Andoh, Y., Okazaki, S., and Tanaka, H. (2014). Effect of bubble formation on the dissociation of methane hydrate in water: a molecular dynamics study. Journal of Physical Chemistry B, 118(7), 1900-1906.

Yao, Y., Yin, Z., Niu, M., Liu, X., Zhang, J., and Chen, D. (2023). Evaluation of 1,3-dioxolane in promoting CO2 hydrate kinetics and its significance in hydrate-based CO2 sequestration. Chemical Engineering Journal, 451, 138799.

Yin, Z., Chong, Z. R., Tan, H. K., and Linga, P. (2016). Review of gas hydrate dissociation kinetic models for energy recovery. Journal of Natural Gas Science and Engineering, 35, 1362-1387.

Zhang, J., Xing, X., Yin, Z., Mao, N., and He, T. (2023). Evaluating CO2+C3H8 hydrate kinetics with cyclopentane and graphite for sustainable hydrate-based desalination. Journal of Cleaner Production, 384, 135365.

Zhang, J. S., Lee, S., and Lee, J. W. (2007). Does SDS micellize under methane hydrate-forming conditions below the normal Krafft point? Journal of Colloid and Interface Science, 315(1), 313-318.

Zhang, Y., Bhattacharjee, G., Kumar, R., and Linga, P. (2022). Solidified Hydrogen Storage (Solid-HyStore) via Clathrate Hydrates. Chemical Engineering Journal, 431.

Zhang, Z. (2016). Variable selection with stepwise and best subset approaches. Ann Transl Med, 4(7), 136.

Zhao, G., and London, E. (2006). An amino acid "transmembrane tendency" scale that approaches the theoretical limit to accuracy for prediction of transmembrane helices: relationship to biological hydrophobicity. Protein Science, 15(8), 1987-2001.

Zhao, G., Yang, M., Pang, W., Gong, G., Zheng, J.-n., Zhang, P., and Chen, B. (2022). Effects of hydrate cap on leakage prevention and capacity improvement of sub-seabed CO2 sequestration. Chemical Engineering Journal, 450, 138493.

Zheng, J., Chong, Z. R., Qureshi, M. F., and Linga, P. (2020). Carbon Dioxide Sequestration via Gas Hydrates: A Potential Pathway toward Decarbonization. Energy & Fuels, 34(9), 10529-10546.

Zheng, J., Lee, Y. K., Babu, P., Zhang, P., and Linga, P. (2016). Impact of fixed bed reactor orientation, liquid saturation, bed volume and temperature on the clathrate hydrate process for pre-combustion carbon capture. Journal of Natural Gas Science and Engineering, 35, 1499-1510.

Zheng, J., Loganathan, N. K., Zhao, J., and Linga, P. (2019). Clathrate hydrate formation of CO2/CH4 mixture at room temperature: Application to direct transport of CO2-containing natural gas. Applied Energy, 249, 190-203.

Zhong, D.-L., Lu, Y.-Y., Sun, D.-J., Zhao, W.-L., and Li, Z. (2015). Performance evaluation of methane separation from coal mine gas by gas hydrate formation in a stirred reactor and in a fixed bed of silica sand. Fuel, 143, 586-594.

Zhu, J., Li, X., Liu, Z., Sun, X., Zhao, L., Shi, Y., Zhou, G., Rui, Z., and Lu, G. (2022). Effect of biofriendly amino acids on methane hydrate decomposition: Insights from molecular dynamics simulations. Fuel, 325, 124919.

Brunning, A. “A Brief Guide to the Twenty Common Amino Acids.” Compound Interest. Novermber 4, 2023 <https://www.compoundchem.com/2014/09/16/ aminoacids/>

Energy Educatio University of Calgary. “Natural Gas Vehicle Fuel Storage.” Energy Educatio University of Calgary. <https://energyeducation.ca/encyclopedia/Natural_gas_vehicle _fuel_storage>

Hannah, R., Max, R., and Pablo, R. “CO_2 and Greenhouse Gas Emissions.” Our World in Data. 19 April 2022 <https://ourworldindata.org/co2-and-greenhouse-gas-emissions>

Harrison, S. E. “Natural Gas Hydrates.” Stanford University. 22 May 2022 <http://large .stanford.edu/courses/2010/ph240/harrison1/>

International Energy Agency. “World Energy Outlook 2021.” International Energy Agency. 20 September 2021 <https://www.iea.org/reports/world-energy-out look-2021>

International Energy Agency. “IEA: Global short-term gas demand growth comes to a halt.” Oil & Gas Journal. 06 September 2023 < https://www.ogj.com/general-interest/economics-markets/article/14283648/iea-global-shortterm-gas-demand-growth-comes-to-a-halt>

International Energy Agency. “World Energy Outlook 2023.” International Energy Agency. 28 August 2023 <https://www.iea.org/reports/world-energy-outlook-2023, >

LibreTexts. “Temperature Effects on the Solubility of Gases.” LibreTexts. 22 Feburary 2022 <https://chem.libretexts.org/@go/page/1615>

Mettler Toledo. “Metastable Zone Width (MSZW) in Crystallization the Building Blocks of Crystallization.” Mettler Toledo. 2 November 2023 <https://www.mt.com/ca/en /home/applications/L1_AutoChem_Applications/L2_Crystallization/Metastable_zone .html#publications>

Schmidt Ocean Institute. “Hunting Bubbles: Understanding Plumes of Seafloor Methane.” Schmidt Ocean Institute. 24 February 2023 <https://schmidtocean.org/cruise/hunting-bubbles-understanding-plumes-of-seafloor-methane/>

U.S. Energy Information Administration. “How much carbon dioxide is produced when different fuels are burned?” U.S. Energy Information Administration. 13 December 2021 <https://www.eia.gov/tools/faqs/faq.php?id=73&t=11>

U.S. Energy Information Administration. “Natural Gas - Energy Explained.” U.S. Energy Information Administration. 24 March 2022 <https://www.eia.gov/energyexplained /print.php?page=natural_gas_home>

United Nations Framework Convention on Climate Change. “The Paris Agreement.” United Nations Framework Convention on Climate Change. 25 Novermber 2023 <https://unfccc.int/process-and-meetings/the-paris-agreement>

Veluswamy, H. P. “SNG Technology.” New Gen Gas. 16 January 2021 <http://www .newgengas.com/index.php/our-technology-1>

VITA

NAME	Kan Jeenmuang
DATE OF BIRTH	27 October 1995
PLACE OF BIRTH	Bangkok
INSTITUTIONS ATTENDED	2020 - 2024 Doctor of Philosophy (Ph.D.), Petrochemical Technology (International Program), The Petroleum and Petrochemical College (PPC), Chulalongkorn University, Bangkok, Thailand. 2018- 2020 Master of Science (M.S.), Petroleum and Energy Technology (International Program), The Petroleum and Petrochemical College (PPC), Chulalongkorn University, Bangkok, Thailand. 2014 - 2018: Bachelor of Science (B.Sc.), Department of Chemical Technology, Faculty of Science, Chulalongkorn University, Bangkok, Thailand.
HOME ADDRESS	49, Rat Burana 26, Rat Burana, Bangkok, Thailand, 10140
PUBLICATION	1. Jeenmuang, K., Pornaroontham, P., Fahed Qureshi, M., Linga, P., and Rangsunvigit, P. (2024). Micro kinetic analysis of the CO_2 hydrate formation and dissociation with L-tryptophan in brine via high pressure in situ Raman spectroscopy for CO_2 sequestration. Chemical Engineering Journal, 479, 147691. 2. Jennmuang, K., Pornaroontham, P., Inkong, K., Bhattacharjee, G., Kulprathipanja, S., Linga, P., Rangsunvigit, P., (2023). Roles of amino acid hydrophobicity on methane-THF hydrates in the context of storage and stability, Chemical Engineering Journal, 454, 140326. 3. Jeenmuang, K., Viriyakul, C., Inkong, K., Kulprathipanja, S., Rangsunvigit, P., (2021). Enhanced hydrate formation by natural-like hydrophobic side chain amino acids at ambient temperature: A kinetics and morphology investigation, Fuel, 299, 120828. 4. Viriyakul, C., Jeenmuang, K., Inkong, K., Kulprathipanja, S., Rangsunvigit, P., (2021). A detailed morphology investigation on the effects of mixed anionic and nonionic surfactants on methane hydrate formation and dissociation, Journal of Natural Gas Science and Engineering, 90, 103904.

AWARD RECEIVED

1. Best Presentation Award for the oral presentation titled "Brand New Natural Gas Storage Using Clathrate Technology: Enhanced Formation at Ambient Temperature" at the 30th Thai Institute of Chemical Engineering and Applied Chemistry Conference (TIChE2021), May 6-7, 2021, Nakhon Ratchasima, Thailand.
2. Best Poster Award for the poster presentation titled "In-situ Raman Spectroscopy of CO_2 Hydrate Formation and Dissociation in the Presence of L-Tryptophan" at the 10th International Conference on Gas Hydrates (ICGH10) July 9-14, 2023, Singapore.